Search for a new charged gauge boson decaying to charged lepton and neutrino with the ATLAS detector at the LHC

Magnar Kopangen Bugge

THESIS SUBMITTED FOR THE DEGREE
MASTER OF SCIENCE

Department of Physics
University of Oslo

May 2010

Acknowledgements

Thanks first of all to my supervisor Prof. Farid Ould-Saada, who has been inspiring both as lecturer in two particle physics courses, and as supervisor of my master work.

Thanks also to the rest of the EPF group at UiO. The group is both scientifically and socially a great place to work, where people are always happy to help and answer questions. In addition, the group has given me the opportunity to travel to CERN several times, and to the nordic particle physics conference at Spåtind.

Finally, I would like to thank my family and my girlfriend Vanja Morisbak.

Introduction

The LHC is a particle accelerator which collides protons on protons at high energy, and which will within short time open up a whole new range of potential physics discoveries. The ATLAS detector is a multi-purpose detector which will be used, and is currently used, to detect the final state particles emerging from the LHC collisions.

In this thesis, the possibility for the discovery of a certain kind of new physics, namely a new charged gauge boson, with the ATLAS detector is evaluated. This is done using simulated data, but as the ATLAS detector has already taken both cosmic data and LHC collision data, the opportunity has been taken to include also analyses of these data in the thesis.

This thesis contains one chapter on particle physics theory, one chapter on the ATLAS detector, one chapter on cosmic ATLAS data, one chapter on the potential for discovery of a new charged gauge boson with ATLAS, and one chapter on the first LHC collision data taken by ATLAS. We begin with a review of the current state of particle physics theory.

Contents

Chapter 1

The Standard Model and Beyond

The Standard Model (SM) is a theory which successfully describes the interactions of elementary particles through the weak, electromagnetic, and strong forces. Its main ingredients are relativity, quantum mechanics, and gauge invariance. The predictions of the SM have been exhaustively tested, and no experimental data to date shows significant deviation from the SM predictions.

1.1 Particle content

The fermions (matter particles) of the SM appear in three generations. In each generation there is a negatively charged lepton and a corresponding neutral neutrino, as well as two quarks. The fermions are all spin-1/2 particles. The SM particles interact through forces mediated by gauge bosons; the gluons (strong force), the photon (electromagnetic force), and the $W^{\pm}$ and Z^0 massive gauge bosons (weak force). The gauge bosons are all spin-1 particles. In addition, the SM contains one spin-0 particle, namely the Higgs particle H responsible for giving mass to all the elementary particles.

All the SM particles have their respective antiparticles of opposite quantum numbers (e.g. opposite electric charge). The antiparticle of the electron e^- is the positron e^+. An electrically neutral particle may be its own antiparticle, as is the case for the Z^0 and the photon γ.

The leptons are particles which do not feel the strong force, but only the electroweak forces, and are situated in the top left corner of table 1.1. The quarks, situated in the bottom left corner of table 1.1, feel the strong and electroweak forces and are confined inside hadrons. The hadrons are grouped in baryons, consisting of three (valence) quarks, and mesons, consisting of two (valence) quarks. The quarks have fractional electric charges of $+2e/3$ for u, c, and t, and $-e/3$ for d, s, and b (where e is the elementary charge).

1st generation	2nd generation	3rd generation	Bosons
e^-	μ^-	τ^-	H
ν_e	ν_μ	ν_τ	$W^{\pm}, Z^0$
u	c	t	γ
d	s	b	g

Table 1.1: The particles of the Standard Model.

The e^-, μ^- and τ^- all have charge $-e$. The neutrinos are electrically neutral, and feel effectively only the weak force.

The masses of the leptons and quarks are smallest for the 1st generation, and heaviest for the 3rd generation. This means for example that the τ lepton can decay to the muon, and that the muon can decay to the electron,

$$\tau^- \to \nu_\tau \, \mu^- \, \overline{\nu_\mu} \quad \text{and} \quad \mu^- \to \nu_\mu \, e^- \, \overline{\nu_e}. \tag{1.1}$$

An exception to this rule may be the neutrinos, for which the mass hierarchy is not really known. This is beacuse neutrino oscillations experiments are only sensitive to $|\Delta m^2| = \left|m_i^2 - m_j^2\right|$, so that one cannot know whether $m_i > m_j$ or vice versa.

1.2 Formalism

This section is based mainly on reference [1].

1.2.1 Lagrangian field theory

The formalism of particle physics is Lagrangian field theory. In classical mechanics, the Lagrangian is a function of the generalized coordinates of a system and their time derivatives, from which the equations of motion of the system may be derived. Each generalized coordinate corresponds to a degree of freedom of the system. In field theory, the degrees of freedom are the fields $\phi_i = \phi_i(x)$. The Lagrangian is replaced by the Lagrangian density $\mathcal{L} = \mathcal{L}(\phi_i, \partial_\mu \phi_i)$ which depends on the fields and their derivatives. The Euler-Lagrange equations,

$$\frac{\partial \mathcal{L}}{\partial \phi_i} - \partial_\mu \left(\frac{\partial \mathcal{L}}{\partial(\partial_\mu \phi_i)} \right) = 0 \quad \text{for all } i, \tag{1.2}$$

lead to the equations of motion for the system.

In the classical case, the Lagrangian is $L = T - V$ where T (V) is the kinetic (potential) energy of the system. The resulting Euler-Lagrange-equations are equivalent to Newton's laws. For example, the Euler-Lagrange-equations for a particle of mass m moving in a potential V is simply Newton's second law:

$$m \frac{d^2 \mathbf{r}}{dt^2} = -\nabla V. \tag{1.3}$$

Consider the Dirac equation:

$$(i\gamma^\mu \partial_\mu - m)\, \psi = 0 \tag{1.4}$$

where $\psi = \psi(x)$ is a four-component spinor and γ^μ are the γ-matrices. This equation is the equation of motion of a free, relativistic spin-1/2 particle of mass m. The Dirac equation may be obtained through the Euler-Lagrange-equations from the Dirac Lagrangian density,

$$\mathcal{L}_{\text{Dirac}} = \overline{\psi}\, (i\gamma^\mu \partial_\mu - m)\, \psi \tag{1.5}$$

where $\overline{\psi} = \psi^\dagger \gamma^0$. Thus, $\mathcal{L}_{\text{Dirac}}$ is a Lagrangian density describing a free spin-1/2 particle.

1.2.2 Second Quantization

In relativistic quantum field theory, the theoretical framework of particle physics, the fields (such as ϕ_i and ψ in section 1.2.1) are in fact operators. They contain creation and annihilation operators, which create and annihilate particles when acting on quantum mechanical states. A quantum mechanical state is in particle physics characterized by the particles present. An example is the vaccuum state $|0\rangle$, in which no particles are present.

1.2.3 Time evolution

The time evolution of the quantum mechanical states is calculated in the interaction picture. The Lagrangian density is separated in the part describing the free fields $\mathcal{L}_0$ and an interaction part $\mathcal{L}_{\text{int}}$, $\mathcal{L} = \mathcal{L}_0 + \mathcal{L}_{\text{int}}$. The Hamiltonian density is derived from the Lagrangian density, and is thus separated in the same way, $\mathcal{H} = \mathcal{H}_0 + \mathcal{H}_{\text{int}}$. In the interaction picture, the operators evolve according to $\mathcal{L}_0$ (free field time evolution), while the states evolve according to the equation

$$i\frac{d}{dt}\left|\Phi(t)\right\rangle = H_{\text{int}}(t)\left|\Phi(t)\right\rangle \tag{1.6}$$

where

$$H_{\text{int}} = \int \mathcal{H}_{\text{int}}\, d^3\mathbf{x}. \tag{1.7}$$

Eq. (1.6) can only be solved perturbatively. One then inserts[1] $|\Phi(-\infty)\rangle$ as a zeroth order approximation to $|\Phi(t)\rangle$ on the right hand side of eq. (1.6) and integrates. This gives a first order approximation to $|\Phi(t)\rangle$ which can then be inserted into eq. (1.6) and integrated to obtain a second order approximation etc. The result is that the S-matrix, defined by $|\Phi(+\infty)\rangle = S\,|\Phi(-\infty)\rangle$, can be written as [1]

$$S = \sum_{n=0}^{\infty} \frac{(-i)^n}{n!} \int \cdots \int d^4x_1\, d^4x_2 \cdots d^4x_n\, \mathrm{T}\{\mathcal{H}_{\text{int}}(x_1)\mathcal{H}_{\text{int}}(x_2)\cdots\mathcal{H}_{\text{int}}(x_n)\} \tag{1.8}$$

where T denotes a time ordered product (note that the interaction Hamiltonian densities at different space-time points do not commute as they contain fields which are operators after second quantization). The sum (1.8) will turn out to be a power series in the coupling constant of the force under study. This implies that such a perturbative solution is only applicable when the coupling constant is small, such that one can truncate the series after a finite number of terms and still obtain a good approximation.

1.2.4 Feynman rules

With the time evolution known, one can in principle obtain measurable quantities such as cross sections and lifetimes. The basic idea is to start with an initial state (often given by an experimental setup), apply the time evolution, and then project the resulting state onto an eigenstate of some measurable quantity to obtain a probability amplitude. The probability amplitude is $\langle f|\, S\,|i\rangle$ where $|i\rangle$ is the initial state and $|f\rangle$ is the eigenstate of the measurable quantity.

[1] Note that the time evolution problem in quantum field theory is solved from the initial time $t = -\infty$ to the final time $t = +\infty$.

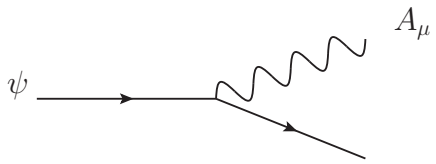

Figure 1.1: The basic vertex of QED in which a fermion couples to a photon. The vertex can be oriented as to represent a fermion emitting a photon (shown), an anti-fermion emitting a photon, a fermion and an anti-fermion combining to a photon, or a photon splitting into a fermion and an anti-fermion.

Going from the Lagrangian density to a cross section or a lifetime is a technically very complicated process. Feynman discovered that the result of this complicated calculation can be anticipated from the Lagrangian density. To each term in the interaction Lagrangian density one can associate a graphical vertex, and to each free field Lagrangian density one can associate a propagator. These vertices and propagators can be combined into Feynman diagrams. The Feynman diagrams of a given process can be translated into the Feynman amplitude $\mathcal{M}$ by following the so-called Feynman rules. This amplitude is then combined with known factors to obtain a cross section or a decay width.

1.3 Gauge theories

With the aid of Feynman rules, one can obtain measurable quantities from a given Lagrangian[2]. The problem now is to obtain the Lagrangian which correctly describes the interactions between elementary particles. This is done by requiring that the Lagrangian must be invariant under certain local (meaning space-time dependent) transformations. These are called gauge transformations. This section is based mainly on references [1], [2], and [3].

1.3.1 The QED example

Consider the Lagrangian for a free electron or other charged fermion:

$$\mathcal{L}_0 = \overline{\psi}\left(i\gamma^\mu\partial_\mu - m\right)\psi. \tag{1.9}$$

This Lagrangian is trivially invariant under the transformation

$$\psi \;\rightarrow\; e^{iQ\alpha}\psi \tag{1.10}$$

where α is a real constant, since then $\overline{\psi} \rightarrow \overline{\psi}e^{-iQ\alpha}$ and $e^{-iQ\alpha}e^{iQ\alpha} = 1$. If α is space-time dependent, $\alpha = \alpha(x)$, then

$$\mathcal{L}_0 \;\rightarrow\; \mathcal{L}_0 - Q\overline{\psi}\gamma^\mu\psi\partial_\mu\alpha \tag{1.11}$$

under the transformation (1.10). The Lagrangian $\mathcal{L}_0$ is *not* invariant under such a *local* transformation, called a gauge transformation.

[2]Actually Lagrangian density, but from here on the Lagrangian density will be referred to simply as the Lagrangian.

The Lagrangian can be made invariant under local phase transformations by adding a term involving a new vector field $A_\mu = A_\mu(x)$:

$$\mathcal{L} = \mathcal{L}_0 - Q\overline{\psi}\gamma^\mu\psi A_\mu = \mathcal{L}_0 + \mathcal{L}_{\text{int}} \tag{1.12}$$

where $\mathcal{L}_{\text{int}} = -Q\overline{\psi}\gamma^\mu\psi A_\mu$ and where the field A_μ transforms as

$$A_\mu \;\rightarrow\; A_\mu - \partial_\mu\alpha. \tag{1.13}$$

The parameter Q is the electric charge of the fermion, and the vector field A_μ is nothing but the electromagnetic 4-potential. The interaction Lagrangian in eq. (1.12) gives rise to the basic vertex of quantum electrodynamics (QED) in which a fermion couples to a photon (see figure 1.1). The strength of the coupling is given by the electric charge Q of the fermion.

The Lagrangian (1.12) can alternatively be written

$$\mathcal{L} = \overline{\psi}\left(i\gamma^\mu D_\mu - m\right)\psi \tag{1.14}$$

where the covariant derivative $D_\mu = \partial_\mu + iQA_\mu$ has been defined. The "minimal substitution" $\partial_\mu \rightarrow D_\mu$ is the recipe for introducing electromagnetic interactions in non-relativistic quantum mechanics.

The transformation rule (1.13) is known from classical electrodynamics as a gauge transformation of the electromagnetic 4-potential. This means that if A_μ changes according to eq. (1.13), then the electric and magnetic fields $\mathbf{E}$ and $\mathbf{B}$ do not change. It corresponds to an unphysical degree of freedom of the electromagnetic 4-potential.

The quantity

$$F_{\mu\nu} = \partial_\nu A_\mu - \partial_\mu A_\nu \tag{1.15}$$

is also invariant under the gauge transformation (1.13). Thus, adding some term involving $F_{\mu\nu}$ to the Lagrangian does not destroy its gauge invariance, and indeed such a term must be added. The complete QED Lagrangian can be written

$$\mathcal{L} = \mathcal{L}_0 + \mathcal{L}_{\text{int}} = \overline{\psi}\left(i\gamma^\mu\partial_\mu - m\right)\psi - \frac{1}{4}F_{\mu\nu}F^{\mu\nu} - Q\overline{\psi}\gamma^\mu\psi A_\mu \tag{1.16}$$

where

$$\mathcal{L}_0 = \overline{\psi}\left(i\gamma^\mu\partial_\mu - m\right)\psi - \frac{1}{4}F_{\mu\nu}F^{\mu\nu} \tag{1.17}$$

describes the free fermion and the free electromagnetic field and

$$\mathcal{L}_{\text{int}} = -Q\overline{\psi}\gamma^\mu\psi A_\mu \tag{1.18}$$

describes the interaction between the fermion and the electromagnetic field. The Euler-Lagrange equations for the field A_μ derived from the Lagrangian (1.16) are Maxwell's equations.

1.4 Quantum chromodynamics

Historically, it was a problem that the baryon Δ^{++}, consisting of three up-quarks, all with the same spin projection, seemed to violate the Pauli exclusion principle. The solution to this problem was to postulate a new quantum number, color, carried by the quarks.

With three colors, the three up-quarks of the Δ^{++} can carry different colors, and thus not violate the exclusion principle. Color is also the basis of quantum chromodynamics (QCD), which is the gauge theory of the strong interaction.

In QCD, the Lagrangian for a free quark of one specific flavor is

$$\mathcal{L}_0 = \sum_{i=1}^{3} \overline{\psi_i} \left(i\gamma^\mu \partial_\mu - m\right) \psi_i = \overline{\psi} \left(i\gamma^\mu \partial_\mu - m\right) \psi \tag{1.19}$$

where

$$\psi = \begin{pmatrix} \psi_1 \\ \psi_2 \\ \psi_3 \end{pmatrix} \quad \text{and} \quad \overline{\psi} = \begin{pmatrix} \overline{\psi_1} & \overline{\psi_2} & \overline{\psi_3} \end{pmatrix} \tag{1.20}$$

and where ψ_i is a regular Dirac spinor for a quark of color i. This Lagrangian is invariant under SU(3) transformations of the kind

$$\psi \;\rightarrow\; U\psi \quad \text{where} \quad U = e^{\frac{1}{2} i g_\mathrm{s} \alpha_k \lambda_k}, \tag{1.21}$$

where λ_k $(k = 1, 2, \ldots, 8)$ are the Gell-Mann matrices and g_s is the strong coupling constant, as long as the real numbers α_k are constants. This invariance follows from $\overline{\psi} \rightarrow \overline{\psi} U^\dagger$ and $U^\dagger U = 1$ (the SU(3) matrices are unitary).

If we consider a *local* SU(3) transformation, i.e. eq. (1.21) with $\alpha_k = \alpha_k(x)$, then the Lagrangian $\mathcal{L}_0$ is no longer invariant, but transforms as

$$\mathcal{L}_0 \;\rightarrow\; \mathcal{L}_0 + \overline{\psi} i\gamma^\mu U^\dagger (\partial_\mu U) \psi. \tag{1.22}$$

Invariance of the Lagrangian can be restored by the introduction of eight gluon fields $A^k_\mu = A^k_\mu(x)$ through the interaction Lagrangian

$$\mathcal{L}_\mathrm{int} = -\frac{g_\mathrm{s}}{2} \overline{\psi} \gamma^\mu \lambda_k \psi A^k_\mu. \tag{1.23}$$

The fields A^k_μ transform under infinitesimal SU(3) transformations as [2]

$$A^k_\mu \;\rightarrow\; A^k_\mu - \partial_\mu \alpha_k - g_\mathrm{s} f_{klm} \alpha_l A^m_\mu \tag{1.24}$$

where f_{klm} are the SU(3) structure constants. The last term in eq. (1.24) arises because the SU(3) matrices do not commute, SU(3) is a non-Abelian group. Eq. (1.23) gives rise to the basic quark-gluon vertex.

We need also the Lagrangian describing the free gluon field. The straight forward generalization of $F_{\mu\nu}$ from eq. (1.15) is not gauge invariant because of the non-Abelian nature of SU(3). The free gluon Lagrangian takes the form [2]

$$\mathcal{L}_\mathrm{gluons} = -\frac{1}{4} F^k_{\mu\nu} F^{\mu\nu}_k \tag{1.25}$$

where

$$F^k_{\mu\nu} = \partial_\mu A^k_\nu - \partial_\nu A^k_\mu - g_\mathrm{s} f_{klm} A^l_\mu A^m_\nu. \tag{1.26}$$

When written out explicitely in terms of the gluon fields A^k_μ, the Lagrangian (1.25) contains terms involving

$$g_\mathrm{s} f_{klm} (\partial_\mu A^k_\nu - \partial_\nu A^k_\mu) A^\mu_l A^\nu_m \quad \text{and} \quad g^2_\mathrm{s} f_{klm} f_{kij} A^l_\mu A^m_\nu A^\mu_i A^\nu_j, \tag{1.27}$$

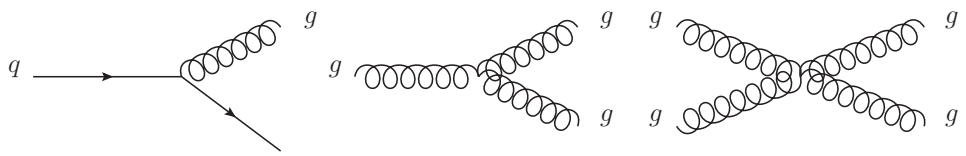

Figure 1.2: The basic vertices of QCD.

giving rise to three- and four gluon vertices. Such vertices, which are not present in QED, give a different evolution of the effective coupling constant in QCD compared to QED. In QED, the strength of the interaction increases with energy. In QCD, we have the opposite case; the coupling is weaker at high energy (asymptotic freedom) and stronger at low energy (confinement). Perturbation theory (see section 1.2.3) is only applicable to QCD in the high energy regime.

To sum up QCD, the full Lagrangian for a quark of one specific flavor is

$$\mathcal{L} = \overline{\psi}\left(i\gamma^{\mu}\partial_{\mu} - m\right)\psi - \frac{1}{4}F^{k}_{\mu\nu}F^{\mu\nu}_{k} - \frac{g_{\mathrm{s}}}{2}\overline{\psi}\gamma^{\mu}\lambda_{k}\psi A^{k}_{\mu}. \tag{1.28}$$

The basic vertices of QCD are shown in figure 1.2. Note that while quark masses are not a problem in QCD alone (meaning that the Dirac mass term is SU(3) gauge invariant), they must be omitted when fitting QCD into the SM, and they are reinserted into the Lagrangian through the Higgs mechanism (see section 1.5.1). The Dirac mass term is also invariant under the gauge transformation of QED.

1.5 The Standard Electroweak Theory

In the Standard Electroweak Theory, the concept of chirality or handedness is central. It is closely related to the concept of helicity, defined by the projection of the spin of a particle on its direction of motion:

$$\sigma_{\mathbf{p}} = \frac{\boldsymbol{\sigma}\cdot\mathbf{p}}{|\mathbf{p}|}. \tag{1.29}$$

A left-handed massless particle has helicity $\sigma_{\mathbf{p}} = -1/2$, while a right-handed one has helicity $\sigma_{\mathbf{p}} = +1/2$. The helicity and the chirality coincide in this way for massless particles, and to good approximation for all particles moving at ultrarelativistic speeds.

If the operation of space inversion, parity, was a symmetry of nature, no distinction would be made between left-handed and right-handed particles. Since this symmetry is violated in weak interactions, we will see that left-handed and right-handed particles are treated differently in the electroweak theory.

In the electroweak theory, left-handed quarks and leptons are grouped into doublets. One such doublet is the electron and its neutrino, which will be used as the example in introducing the theory. The theory is identical for the other lepton generations, and also more or less identical for the three quark generations.

We define $\psi_L = L\psi$ and $\psi_R = R\psi$, where L and R are the left-handed and right-handed chirality projection matrices:

$$L = \frac{1}{2}\left(1 - \gamma_5\right) \quad \text{and} \quad R = \frac{1}{2}\left(1 + \gamma_5\right). \tag{1.30}$$

Because $\{\gamma^\mu, \gamma_5\} = 0$, we have $\gamma^\mu L = R\gamma^\mu$ and $L\gamma^\mu = \gamma^\mu R$. Furthermore, $L^2 = L$, $R^2 = R$ and $R + L = 1$. Using these relations, we may decompose the Dirac Lagrangian as

$$\mathcal{L} = \overline{\psi_L} i\gamma^\mu \partial_\mu \psi_L + \overline{\psi_R} i\gamma^\mu \partial_\mu \psi_R - m\overline{\psi_R}\psi_L - m\overline{\psi_L}\psi_R. \tag{1.31}$$

The mass term is troublesome because it mixes the left-handed and right-handed parts of the field. Neglecting the masses, we may write the Lagrangian describing the free electron and electron-neutrino as

$$\mathcal{L}_0 = \overline{\psi_L^e} i\gamma^\mu \partial_\mu \psi_L^e + \overline{\psi_R^e} i\gamma^\mu \partial_\mu \psi_R^e + \overline{\psi_L^\nu} i\gamma^\mu \partial_\mu \psi_L^\nu + \overline{\psi_R^\nu} i\gamma^\mu \partial_\mu \psi_R^\nu. \tag{1.32}$$

In constructing the electroweak Lagrangian, one next makes a distinction between left-handed and right-handed fields, and writes the Lagrangian as

$$\mathcal{L}_0 = \overline{\chi_L} i\gamma^\mu \partial_\mu \chi_L + \overline{\psi_R^e} i\gamma^\mu \partial_\mu \psi_R^e + \overline{\psi_R^\nu} i\gamma^\mu \partial_\mu \psi_R^\nu \tag{1.33}$$

where

$$\chi_L = \begin{pmatrix} \psi_L^\nu \\ \psi_L^e \end{pmatrix} \quad \text{and} \quad \overline{\chi_L} = \begin{pmatrix} \overline{\psi_L^\nu} & \overline{\psi_L^e} \end{pmatrix}. \tag{1.34}$$

We have now grouped the left-handed fields in a weak isospin doublet, where ψ_L^ν has $I_3 = +1/2$ and ψ_L^e has $I_3 = -1/2$, while the right-handed fields are isospin singlets ($I_3 = 0$). Furthermore, we assign a weak hypercharge Y to each field (individually for right-handed and left-handed fields) such that the electric charge is $Q = (I_3 + Y/2)e$. Hence, the left-handed fields have $Y = -1$, the right-handed electron has $Y = -2$ and the right-handed neutrino has $Y = 0$.

The electroweak Lagrangian is invariant under SU(2)-transformations of the kind

$$\chi_L \to U\chi_L, \quad U = e^{\frac{1}{2} i g \omega_k \tau_k} \tag{1.35}$$

where τ_k are the Pauli matrices (see appendix B) and ω_k are real constants. Furthermore, it is invariant under U(1)-transformations of the kind

$$\psi \to e^{\frac{Y}{2} i g' \beta} \psi \tag{1.36}$$

where Y is the weak hypercharge as long as the real number β is constant.

To make the Lagrangian invariant under *local* U(1)-transformations, eq. (1.36) with $\beta = \beta(x)$, we must add a term (for each spinor)

$$\mathcal{L}_{\text{int}}^B = -\frac{Y}{2} g' \overline{\psi} \gamma^\mu \psi B_\mu \tag{1.37}$$

where the field $B_\mu = B_\mu(x)$ transforms as

$$B_\mu \to B_\mu - \partial_\mu \beta. \tag{1.38}$$

Furthermore, to make the Lagrangian invariant under local SU(2)-transformations, eq. (1.35) with $\omega_k = \omega_k(x)$, we must add a term

$$\mathcal{L}_{\text{int}}^W = -\frac{1}{2} g \overline{\chi_L} \gamma^\mu \tau_k \chi_L W_\mu^k, \tag{1.39}$$

where the three fields $W_\mu^k = W_\mu^k(x)$, $k = 1, 2, 3$, transform under infinitesimal SU(2)-transformations as [1]

$$W_\mu^i \to W_\mu^i - \partial_\mu \omega_i - g\varepsilon_{ijk}\omega_j W_\mu^k. \tag{1.40}$$

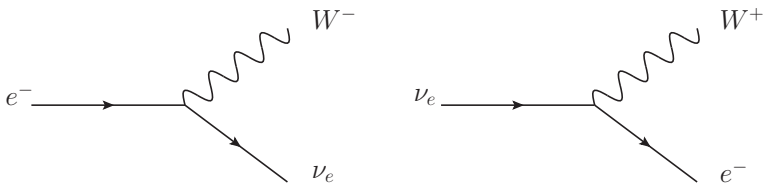

Figure 1.3: The basic charged current vertices for the electron and electron-neutrino.

The full interaction Lagrangian for the electron and electron-neutrino can now be written out, inserting the correct hypercharge values:

$$\mathcal{L}_{\text{int}} = \mathcal{L}^W_{\text{int}} + \mathcal{L}^B_{\text{int}} = -\frac{1}{2} g \overline{\chi_L} \gamma^\mu \tau_k \chi_L W^k_\mu + \frac{1}{2} g' \overline{\chi_L} \gamma^\mu \chi_L B_\mu + g' \overline{\psi^e_R} \gamma^\mu \psi^e_R B_\mu \tag{1.41}$$

We first consider the terms involving W^1_μ and W^2_μ. Defining the physical $W^\pm$-bosons

$$W^{(\pm)}_\mu = \frac{1}{\sqrt{2}} \left(W^1_\mu \pm i W^2_\mu \right) \tag{1.42}$$

and using explicit expressions for τ_1 and τ_2, we find

$$\mathcal{L}^{W^{1,2}}_{\text{int}} = -\frac{g}{\sqrt{2}} \left[\overline{\psi^\nu_L} \gamma^\mu \psi^e_L W^{(-)}_\mu + \overline{\psi^e_L} \gamma^\mu \psi^\nu_L W^{(+)}_\mu \right], \tag{1.43}$$

giving rise to the basic charged current vertices shown in figure 1.3. We see that the $W^\pm$ bosons couple only to left-handed particles (right-handed anti-particles); the symmetry of space inversion is violated 100% in charged current weak interactions.

When writing out the terms involving W^3_μ and B_μ, we define the physical photon A_μ and Z^0 boson Z_μ:

$$\begin{aligned} A_\mu &= \cos\theta_{\text{W}} B_\mu + \sin\theta_{\text{W}} W^3_\mu, \\ Z_\mu &= -\sin\theta_{\text{W}} B_\mu + \cos\theta_{\text{W}} W^3_\mu \end{aligned}$$

where θ_{W} is the weak mixing angle. Demanding that A_μ couples to the electromagnetic current, one obtains the restrictions $g \sin\theta_{\text{W}} = g' \cos\theta_{\text{W}} = e$. The resulting neutral current terms are

$$\mathcal{L}^{W^3 B}_{\text{int}} = e \overline{\psi^e} \gamma^\mu \psi^e A_\mu - \frac{g}{\cos\theta_{\text{W}}} \left(\frac{1}{2} \overline{\chi_L} \gamma^\mu \tau_3 \chi_L + \sin^2\theta_{\text{W}} \overline{\psi^e} \gamma^\mu \psi^e \right) Z_\mu. \tag{1.44}$$

These terms give the neutral current vertices shown in figure 1.4. The Z^0 couples not only to the left-handed electron, but also to the right-handed one. However, the left-handed and right-handed couplings are not equal.

The vertex factor for a fermion coupling to the Z^0 is customarily written as

$$\frac{-ig\gamma^\mu}{2\cos\theta_{\text{W}}} \left(g_{\text{V}} - g_{\text{A}} \gamma_5 \right) \tag{1.45}$$

where g_{V} (g_{A}) is the vector (axial vector) coupling. By comparison with equation (1.44), we find $g_{\text{V}} = 2\sin^2\theta_{\text{W}} - 1/2$ and $g_{\text{A}} = -1/2$ for the electron, and $g_{\text{V}} = g_{\text{A}} = 1/2$ for the

Fermion	e^-, μ^-, τ^-	ν_e, ν_μ, ν_τ	u, c, t	d, s, b
g_{V}	$2\sin^2\theta_{\mathrm{W}} - \frac{1}{2}$	$\frac{1}{2}$	$\frac{1}{2} - \frac{4}{3}\sin^2\theta_{\mathrm{W}}$	$\frac{2}{3}\sin^2\theta_{\mathrm{W}} - \frac{1}{2}$
g_{A}	$-\frac{1}{2}$	$\frac{1}{2}$	$\frac{1}{2}$	$-\frac{1}{2}$

Table 1.2: The vector and axial vector Z^0 couplings to quarks and leptons. (From [2].)

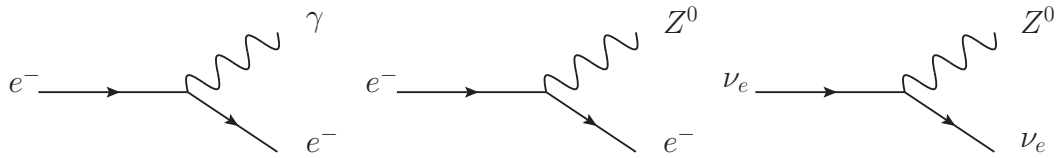

Figure 1.4: The basic neutral current vertices for the electron and electron-neutrino.

electron-neutrino. Values of g_{V} and g_{A} for quarks and leptons are given in table 1.2. The vertex factor for $W^\pm$ coupling to electron and electron-neutrino is from equation (1.43)

$$\frac{-ig\gamma^\mu}{2\sqrt{2}}\left(1-\gamma_5\right). \tag{1.46}$$

This factor is the same for $W^\pm$ coupling to the other lepton generations and the quark generations. It should be noted that in the coupling to quarks, the down-type quark coupling to the W is a linear combination of the three mass eigenstate down-type quarks. This means that the W^+ can couple for example to $u\overline{s}$, but such generation mixing is suppressed by the smallness of the off-diagonal elements of a matrix known as the CKM matrix.

We see that because it has hypercharge $Y = 0$, the right-handed neutrino has dropped out of the interaction Lagrangian. Hence, the right-handed neutrino does not take part in any SM interaction, and it is a technicality that we included it in the first place. As long as neutrinos are massless, there is no need for a right-handed neutrino in the SM. Recent experiments have, however, shown that neutrinos have mass, but it is an open question whether the neutrino is of Dirac or Majorana nature.

The complete electroweak Lagrangian contains also a free gauge field part, giving rise to gauge boson self-interactions as in the case of QCD, since SU(2) is a non-Abelian group. This part has the form [1]

$$\mathcal{L}_{\mathrm{bosons}} = -\frac{1}{4}B_{\mu\nu}B^{\mu\nu} - \frac{1}{4}F^i_{\mu\nu}F_i^{\mu\nu} \tag{1.47}$$

where

$$B_{\mu\nu} = \partial_\nu B_\mu - \partial_\mu B_\nu \tag{1.48}$$

and

$$F^i_{\mu\nu} = \partial_\nu W^i_\mu - \partial_\mu W^i_\nu + g\varepsilon_{ijk}W^j_\mu W^k_\nu. \tag{1.49}$$

Some gauge boson self interaction vertices in the electroweak theory are shown in figure 1.5.

1.5.1 The Higgs mechanism

We had to neglect the fermion mass terms in constructing the electroweak Lagrangian because they are not gauge invariant on account of the left-right mixing [1]. Furthermore,

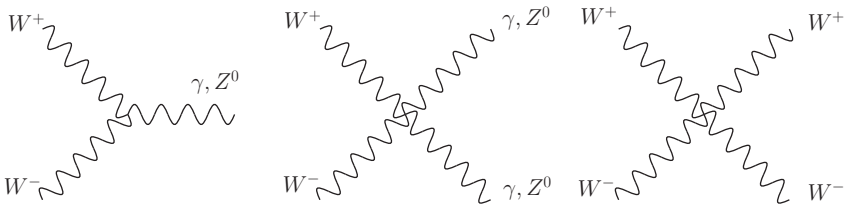

Figure 1.5: Some gauge boson self interaction vertices in the electroweak theory.

mass terms for the $W^\pm$ and Z^0 bosons,

$$m_W^2 W_\mu^{(+)} W^{(-)\mu} + \frac{1}{2} m_Z^2 Z_\mu Z^\mu, \tag{1.50}$$

are not gauge invariant either. The way gauge boson and fermion masses are incorporated into the standard electroweak theory is the Higgs mechanism.

An additional isospin doublet $\Phi = \Phi(x)$ with hypercharge $Y = 1$ is introduced in the Lagrangian through the terms

$$\mathcal{L}_\Phi = (iD^\mu \Phi)^\dagger (iD_\mu \Phi) - \left[\mu^2 \Phi^\dagger \Phi + \lambda (\Phi^\dagger \Phi)^2\right] \tag{1.51}$$

where the covariant derivative

$$D^\mu = \partial^\mu + \frac{1}{2} i g \tau_k W_k^\mu + \frac{1}{2} i g' B^\mu \tag{1.52}$$

ensures gauge invariance. The term in square brackets is the Higgs potential, which for $\mu^2 < 0$ has a minimum at $\Phi^\dagger \Phi = v^2/2$ where $v = \sqrt{-\mu^2/\lambda}$. The Higgs field will therefore choose a ground state on the circle $\Phi^\dagger \Phi = v^2/2$. In the electroweak theory, this ground state is written as

$$\Phi_0 = \frac{1}{\sqrt{2}} \begin{pmatrix} 0 \\ v \end{pmatrix}. \tag{1.53}$$

Allowing for small oscillations around the ground state value Φ_0, one writes

$$\Phi = \frac{1}{\sqrt{2}} \begin{pmatrix} \eta_1(x) + i\eta_2(x) \\ v + H(x) + i\eta_3(x) \end{pmatrix}. \tag{1.54}$$

It is possible to find an $\mathrm{SU}(2) \times \mathrm{U}(1)$ gauge transformation which brings us to the unitary gauge, in which the Higgs doublet has the form

$$\Phi = \frac{1}{\sqrt{2}} \begin{pmatrix} 0 \\ v + H(x) \end{pmatrix} \tag{1.55}$$

where $H(x)$ is the Higgs field. When writing out the kinetic term of $\mathcal{L}_\Phi$ with this expression for the Higgs doublet, mass terms for the $W^\pm$ and Z^0 bosons arise, and one finds $m_W = vg/2$ and $m_Z = vg/(2\cos\theta_\mathrm{W})$. This lead originally to a direct prediction of the $W^\pm$ and Z^0 masses, which was a great success for the theory when confirmed by experiment. Note that with our choice for the Higgs ground state, no mass term is generated for the photon.

The parameter v is related to the Fermi coupling constant G_F. Written in terms of this constant and the fine structure constant α, the $W^\pm$ and Z^0 masses are

$$m_W = \frac{1}{\sin\theta_\mathrm{W}} \sqrt{\frac{\alpha\pi}{G_\mathrm{F}\sqrt{2}}} \quad \text{and} \quad m_Z = \frac{2}{\sin 2\theta_\mathrm{W}} \sqrt{\frac{\alpha\pi}{G_\mathrm{F}\sqrt{2}}} \tag{1.56}$$

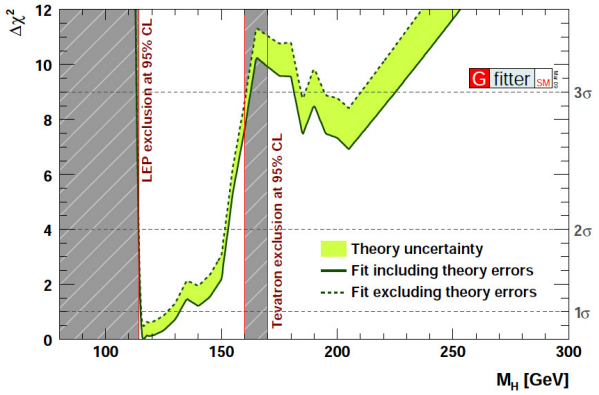

Figure 1.6: The $\Delta\chi^2$ of a global fit to precision electroweak data as function of the Higgs mass. The grey regions are excluded by direct searches. (From [5].)

giving $m_W = 76.9\,\text{GeV}$ and $m_Z = 87.9\,\text{GeV}$ with $\sin^2\theta_\text{W} = 0.235$ obtained from neutrino scattering [1]. The experimental masses for the $W^\pm$ and Z^0 are $m_W = 80.4\,\text{GeV}$ and $m_Z = 91.2\,\text{GeV}$ [4]. The electroweak prediction agrees with these values within uncertainty when radiative corrections are included [1].

Mass terms for the fermions are also introduced by the Higgs mechanism through additional terms of the form (taking the electron as an example)

$$\mathcal{L}_{e\Phi} = -G_e \left[\overline{\chi_L}\Phi\psi_R^e + \overline{\psi_R^e}\Phi^\dagger\chi_L\right]. \tag{1.57}$$

This gives rise to the electron mass term and the interaction of the electron with the Higgs boson. Note that this way of generating fermion masses does not predict the masses, since the parameter G_e is a free parameter which must be tuned to give the correct electron mass. Note also that the term above may only be used to give mass to $I_3 = -1/2$ particles. To give masses to $I_3 = +1/2$ quarks (u,c,t), similar terms involving $\tilde{\Phi} = -i(\Phi^\dagger\tau_2)^\text{T}$ are added.

The Higgs mechanism has been experimentally verified in the sense that the predictions for the $W^\pm$ and Z^0 masses turned out to be correct. The Higgs particle H has, however, not been observed in experiment, and it is regarded as the last missing piece of the SM. Figure 1.6 shows the $\Delta\chi^2$ of a global electroweak fit as function of the Higgs mass, from [5]. The grey regions are excluded by LEP and Tevatron by direct searches. As seen from the plot, a light Higgs boson just beyond the LEP exclusion limit is favored by the fit.

1.6 Summary

The SM describes the elementary particles and their interactions. The interactions are introduced through requirements of gauge invariance, and the resulting particles mediating the forces are known as gauge bosons. The SM is often schematically depicted as

$$\text{SU}(3)_\text{C} \times \text{SU}(2)_L \times \text{U}(1)_Y, \tag{1.58}$$

referring to the gauge symmetries related to color, weak isospin, and weak hypercharge respectively.

1.7 Beyond the Standard Model and New Gauge Bosons

Even though the SM satisfactory describes all experimental data within its domain to date (except neutrino masses and mixings), there are reasons to believe that it is a low energy approximation to some greater theory. The SM does not contain an explanation for dark matter, which is required to explain the motion of the galaxies. Neither does it explain dark energy, responsible for the accelerating expansion of the universe. CP violation within the SM is not great enough to explain the abundance of matter over antimatter in the universe. Furthermore, loop diagram corrections to the Higgs mass give a quadratically divergent mass unless there is some extremely precise "accidental" cancellation, a problem known as the hierarchy problem.

Exploration of beyond the Standard Model (BSM) theories are also driven by the wish for unification of the forces. The standard electroweak theory unites the electromagnetic and weak forces (although with two coupling constants, related by a parameter θ_{W} to be extracted from experiment). Unification of the electroweak force with the strong force, and finally also with gravity, is the goal of grand unification theories (GUTs). Today, gravity is not described within the quantum field theory formalism, as are the other forces.

BSM thories often involve new particles, which must be heavy and/or weakly interacting since they are not already observed. Searches for these particles are a way of experimentally exploring the BSM theories. If predicted particles are not observed, then the theory may be ruled out, and if they are observed, this is experimental support for the theory. New gauge bosons are bosons originating from new gauge symmetries in BSM theories. New charged gauge bosons are referred to as W', and neutral ones as Z'. We now consider a particular class of BSM models where new gauge bosons arise.

1.7.1 Left-Right Symmetric Models

In constructing the electroweak Lagrangian, one makes an a priori distinction between left- and right-handed fields when one groups the left-handed part according to SU(2), but not the right-handed part. This results in the parity violating nature of the weak interactions, which is an experimental fact. In left-right symmetric models, one groups also the right-handed fields according to SU(2), and arrives at a structure such as

$$\mathrm{SU}(2)_R \times \mathrm{SU}(2)_L \times \mathrm{U}(1). \tag{1.59}$$

The Lagrangian is required to be invariant under the discrete symmetry operation $L \leftrightarrow R$ (interchanging left-handed and right-handed fields). As parity is violated in weak interactions, the left-right symmetry must be broken.

As the gauge group $\mathrm{SU}(2)_L$ in the SM is associated with gauge bosons $W^{\pm}$ and Z^0, the gauge group $\mathrm{SU}(2)_R$ of the left-right symmetric theory is also associated with gauge bosons $W_R^{\pm}$ and Z'. The new gauge bosons W_R couple only to right-handed currents, in constrast to the regular W-bosons, which couple only to left-handed currents.

The left-right symmery is broken spontaneously [6] analogously to the Higgs mechanism in the standard electroweak theory. The Higgs content in left-right symmetric models is more complex than in the SM, and contains charged Higgs bosons. First, the symmetry is broken down to the symmetry of the SM:

$$\mathrm{SU}(2)_R \times \mathrm{SU}(2)_L \times \mathrm{U}(1) \quad \rightarrow \quad \mathrm{SU}(2)_L \times \mathrm{U}(1)_Y. \tag{1.60}$$

In this process, the gauge bosons W_R and Z' obtain masses. Then the SM symmetry is broken down to only the U(1) symmetry of electromagnetism, and the regular gauge bosons W and Z obtain masses. At this point, also the fermions aquire masses as in the SM.

The U(1)-symmetry in left-right symmetric models is, at least in some models, related to baryon- and lepton number (B and L). The charge formula of the SM,

$$Q = I_3 + \frac{Y}{2}, \tag{1.61}$$

where the weak hypercharge Y is rather arbitrary, chosen to give the correct charges to all particles, is then replaced by

$$Q = I_3^L + I_3^R + \frac{B-L}{2}. \tag{1.62}$$

Here, the hypercharge is replaced by the familiar baryon- and lepton numbers.

Initially, no parity violation is present in left-right symmetric models. Parity violation may only occur after the breaking of the initial left-right symmetry. The requirement that parity is violated 100% in weak interactions at the energies so far probed, translates to the right-handed gauge bosons $W_R^{\pm}$ being much heavier than the left-handed $W^{\pm}$. In this case, W_R does not play an important role at low energies, and parity is violated in this regime. The parity symmetry would in this case be restored at energies of the same order of magnitude as the mass of the W_R. Instead of parity violation being put in "by hand", as in the SM, the parity symmetry is spontaneously broken by the Higgs fields in left-right symmetric models.

A further interesting feature of left-right symmetric models is the seesaw mechanism [7]. In the SM, there is no explanation for the non-vanishing but extremely small neutrino mass. In left-right symmetric models, the breaking of the left-right symmetry gives a large Majorana mass to the right-handed neutrino. The breaking of the $\mathrm{SU}(2)_L \times \mathrm{U}(1)_Y$ symmetry relates the masses of the left-handed and right-handed neutrinos in such a way that a heavy right-handed neutrino gives a light left-handed one. The mass of the right-handed neutrino is further related to the mass of the W_R, since these masses are both given by the breaking of the left-right symmetry.

The result of this is that the left-handed neutrino acquires a mass

$$m_{\nu_l} \sim \frac{m_l^2}{m_{W_R}}. \tag{1.63}$$

Comparing to the coupling for weak $V+A$ currents, $G_{V+A} \sim g^2/m_{W_R}^2$, we see that the maximal parity violation observed in weak interactions at low energies is closely related to the very small neutrino mass. As the mass of the W_R tends to infinity, parity violation becomes maximal and the neutrino mass tends to zero.

As the left-handed neutrino mass is related to the W_R mass, one can make estimates of m_{W_R} knowing that the left-handed neutrino mass is of order eV. The mass of the W_R is, however, not determined completely by the left-handed neutrino mass, but depends on an unknown parameter. Different assumptions for this parameter, the Dirac mass term, gives masses ranging from the GUT scale 10^{14} GeV down to the TeV scale. If m_{W_R} is of order TeV, the W_R may be discovered at the LHC.

Boson	Direct search limit ($p\overline{p}$ collisions)	Electroweak fit limit	Comment
W' with SM couplings	$m > 1.000\,\mathrm{TeV}$		Decay to $e\nu$
W_R - right handed W		$m > 715\,\mathrm{GeV}$	
Z' with SM couplings	$m > 923\,\mathrm{GeV}$	$m > 1500\,\mathrm{GeV}$	
Z_{LR} of $\mathrm{SU}(2)_L \times \mathrm{SU}(2)_R \times \mathrm{U}(1)$	$m > 630\,\mathrm{GeV}$	$m > 860\,\mathrm{GeV}$	$g_L = g_R$
Z_χ of $\mathrm{SO}(10) \to \mathrm{SU}(5) \times \mathrm{U}(1)_\chi$	$m > 822\,\mathrm{GeV}$	$m > 781\,\mathrm{GeV}$	$g_\chi = e/\cos\theta_\mathrm{W}$
Z_ψ of $E_6 \to \mathrm{SO}(1) \times \mathrm{U}(1)_\psi$	$m > 822\,\mathrm{GeV}$	$m > 475\,\mathrm{GeV}$	$g_\psi = e/\cos\theta_\mathrm{W}$
Z_η of $E_6 \to \mathrm{SU}(3) \times \mathrm{SU}(2) \times \mathrm{U}(1) \times \mathrm{U}(1)_\eta$	$m > 891\,\mathrm{GeV}$	$m > 619\,\mathrm{GeV}$	$g_\eta = e/\cos\theta_\mathrm{W}$

Table 1.3: Current limits on new gauge bosons from direct searches and electroweak fits. (From [4].)

1.7.2 Current limits on new gauge bosons

Table 1.3 summarizes the current limits on new gauge bosons from direct searches and electroweak precision data. The direct search limits are obtained from $p\overline{p}$ data.

1.8 Summary

In this chapter we have reviewed the SM, which is the current theory of particle physics. We have also seen that this theory, despite its enormous success, has some important shortcomings, and that there are many theories which go beyond the SM. The testing of such theories is one of the objectives of the LHC. We now proceed to a description of the ATLAS detector and the LHC.

Chapter 2

The ATLAS detector

2.1 The LHC and ATLAS

The Large Hadron Collider (LHC) is a proton-proton and heavy ion collider at CERN. Its design center of mass energy is $E_{\mathrm{CM}} = 14\,\mathrm{TeV}$ and its design luminosity is $L = 10^{34}\,\mathrm{cm}^{-2}\,\mathrm{s}^{-1}$ (for proton-proton collisions). The luminosity essentially measures the collision rate in such a way that given a process with cross section σ, the expected number of events in a period of time is

$$N = \sigma \int L\,dt. \tag{2.1}$$

The luminosity integrated over time is a measure of the amount of data collected. Luminosity and center of mass energy are the key variables for a collider.

Around the LHC, there are four detectors (experiments) situated at four interaction points, where the protons or heavy ions are made to collide head on. The ATLAS (A Toroidal LHC ApparatuS) detector is one of these. It is a multi-purpose detector, meaning that it is not tailored specifically to only one area of physics studies, but rather constructed to be able to give good results in many different kinds of studies.

2.2 Detectors in particle physics

In particle physics, most experiments aim to study the processes taking place when particles collide (when protons or heavy ions collide, in the case of ATLAS/LHC). The only particles (known to date) living long enough to actually reach the detector after such a collision are photons, electrons, muons, and neutrinos, as well as a handful of different baryons and mesons. The neutrinos, feeling only the weak interaction, have tiny cross sections for interacting with anything, and will escape out of any detector undetected. This leaves the photons, electrons, muons, and hadrons to be measured in the detector of a collider experiment. Our detector must be constructed in such a way that it can as accurately as possible measure the momenta and energies of these particles, since all the dynamics of the initial collision must be inferred from these measurements. In addition, it should be able to identify these particles, e.g. distinguish an electron from a muon.

2.2.1 The different parts of a detector

A detector in a collider experiment is built up around the interaction point (see figure 2.2). Innermost, closest to the beam pipe, we have a tracking system. This is composed of many

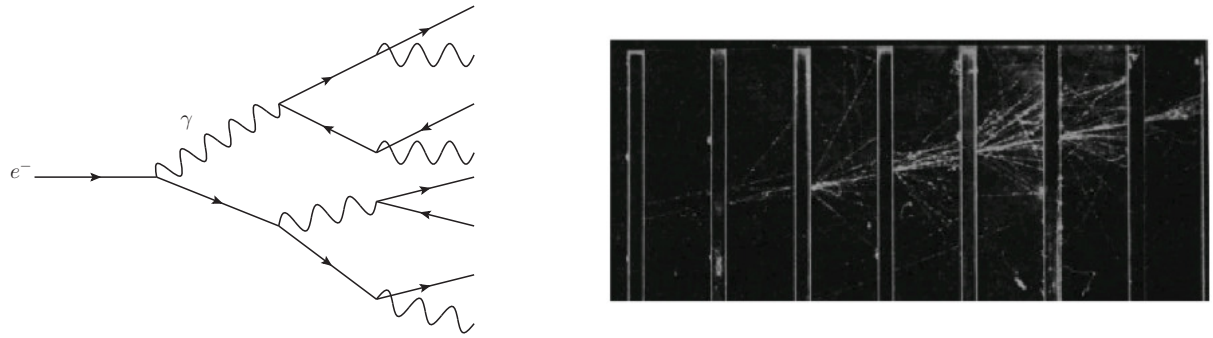

Figure 2.1: Sketch of the development of an electromagnetic shower initiated by an electron (left) and a picture of an electromagnetic shower in a bubble chamber with lead absorbers (right).

small units, e.g. pixels or strips, which each give a signal when a charged particle passes through. Such a signal is known as a hit, and gives a point or region in space where the particle has passed through. A given charged particle should make many hits when passing through the tracking system, and these hits are then combined to identify the trajectory of the particle. This trajectory, or track, allows us to identify

- the direction of the initial momentum of the particle,
- the charge and the magnitude of the momentum of the particle, based on the curvature of the track in a magnetic field,
- the primary vertex (interaction point) and secondary vertices, based on the convergence of several tracks to a common space point.

The tracking material should as little as possible change the trajectory of a particle, meaning that it should not be too dense.

If we keep moving radially outwards from the beam pipe, after the tracking system comes the electromagnetic calorimeter (ECal). The purpose of the ECal is to measure the energy of electrons and photons. Electrons and photons will create showers in the ECal, and deposit all their energy. This happens in the following way. When a high energy electron enters the ECal, the material will cause it to create a bremsstrahlung photon, $e^{\pm} \rightarrow e^{\pm}\,\gamma$ (a process which can only happen in the presence of additional particles due to conservation of energy and momentum). This photon will (again, possible because of the material) produce an e^+e^- pair, $\gamma \rightarrow e^+\,e^-$, and the initial electron will do bremsstrahlung again. In this way, the shower develops until the energies of the electrons and photons are too small for bremsstrahlung and pair production. The case is equivalent if the initial particle is a photon, but then the first process will be pair production. A sketch of an electromagnetic shower development is shown in figure 2.1.

After the ECal comes the hadronic calorimeter (HCal). The purpose of the HCal is to measure the energy of all hadrons. When a hadron enters the material of the HCal, it will interact strongly with the nuclei of the HCal material and create a hadronic shower, which is the strong interaction analogue of an electromagnetic shower. This shower is made up mainly of pions, kaons, and the lightest baryons. The material of the HCal must be dense and "deep" to be able to stop the high energy hadrons originating from a high energy collision.

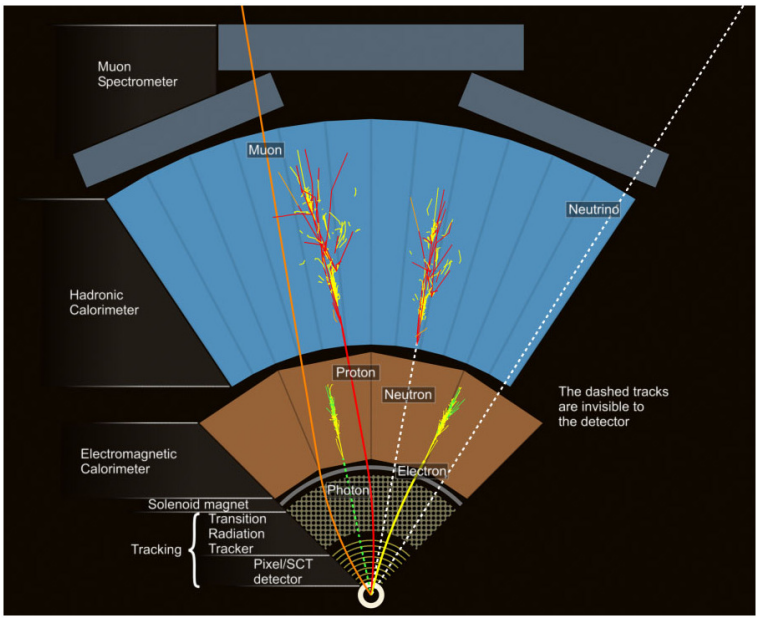

Figure 2.2: Figure showing a cross section of part of the ATLAS detector and how the different particles interact in the different parts of the detector.

The only particle (except the neutrino) which passes through both the ECal and HCal without being stopped is the muon. The muon will not do bremsstrahlung in the ECal because of its large mass (the cross section for bremsstrahlung goes as $1/m^2$ where m is the mass). In addition, it does not feel the strong interaction, so it is not stopped in the HCal. The outermost part of a detector is therefore the muon spectrometer, dedicated to detecting and measuring muons. This is an additional layer of tracking, which gives an additional measurement of the muon momentum and which gives muon identification, since only muons can reach this part of the detector.

Figure 2.2 shows how different particles are seen in the different parts of the ATLAS detector. The neutrinos are not measured. They can however to some extent be indirectly measured, since their momentum will show up as missing, in the sense that any apparent violation of the conservation of momentum may be attributed to the neutrinos (or to other, yet unknown, weakly interacting particles).

2.3 The ATLAS detector

Most of the technical details (such as resolutions of different subdetectors) and figures in this section are taken from reference [8].

2.3.1 The ATLAS coordinate system

The ATLAS coordinate system is oriented with the z-axis along the beam pipe, the positive x-direction towards the center of the LHC ring, and the positive y-direction upwards (opposite of the acceleration of gravity). The origin is located at the nominal interaction point.

The spherical coordinates ϕ and θ are defined in the standard way, with ϕ as the angle between the x-axis and the xy-projection of the position vector and θ as the angle between

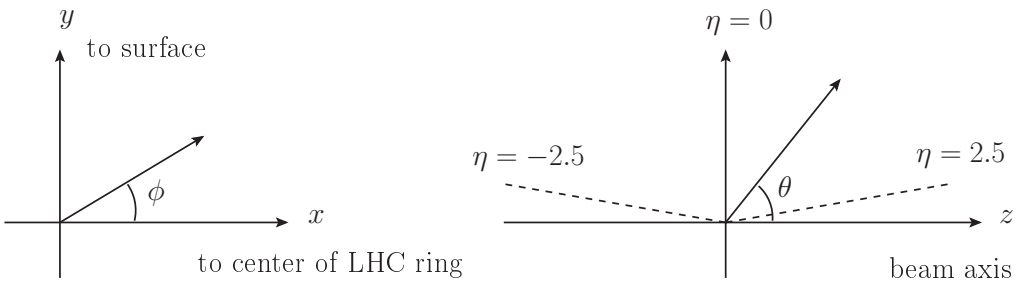

Figure 2.3: Illustration of the ATLAS coordinate system showing two projections. The definitions of the azimuthal and polar angles ϕ and θ are shown, as well as sample values of the pseudorapidity η.

the position vector and the positive z-axis. The angle ϕ increases clock-wise when looking in the positive z direction and is zero on the positive x-axis. The range of θ is $\theta \in [0, \pi]$, while the range of ϕ is chosen as $\phi \in [-\pi, \pi]$. We also define the pseudorapidity

$$\eta = -\ln\left(\tan\frac{\theta}{2}\right), \tag{2.2}$$

which is usually quoted instead of the polar angle θ. The pseudorapidity is zero when $\theta = \pi/2$, i.e. in the direction perpendicular to the beam axis. See figure 2.3 for an illustration of the ATLAS coordinate system.

The transverse component of any vector, e.g. $\mathbf{p}_{\mathrm{T}}$, is defined as its projection in the xy-plane (transverse to the beam axis). To quantify the separation between two directions, the distance ΔR in the $\eta\phi$-plane is used:

$$\Delta R = \sqrt{(\Delta\eta)^2 + (\Delta\phi)^2}\,. \tag{2.3}$$

2.3.2 The magnets

The charge and momentum of a charged particle is measured by determining the curvature of the particle's trajectory in a magnetic field. The stronger the magnetic field, the more the trajectory is bent (smaller radius of curvature), and the better momentum resolution one can obtain. The ATLAS detector therefore uses superconducting electromagnets to produce strong magnetic fields.

The magnetic field configuration of ATLAS consists of the solenoidal magnetic field in the inner detector and the toroidal magnetic field in the muon spectrometer. The geometry of solenoidal and toroidal magnetic fields is illustrated in figure 2.4.

The central solenoid provides a magnetic flux density of 2 T directed along the beam axis in the inner detector. The barrel and end-cap toroids provide the magnetic field for the muon spectrometer. The field is here tangential to a circle parallel to the xy-plane around the beam axis.

2.3.3 The inner detector

The ATLAS inner detector tracking system consists of three separate detectors. From the beam pipe and outwards, these are the pixel detector, the semiconductor tracker (SCT), and the transition radiation tracker (TRT) (see figure 2.5).

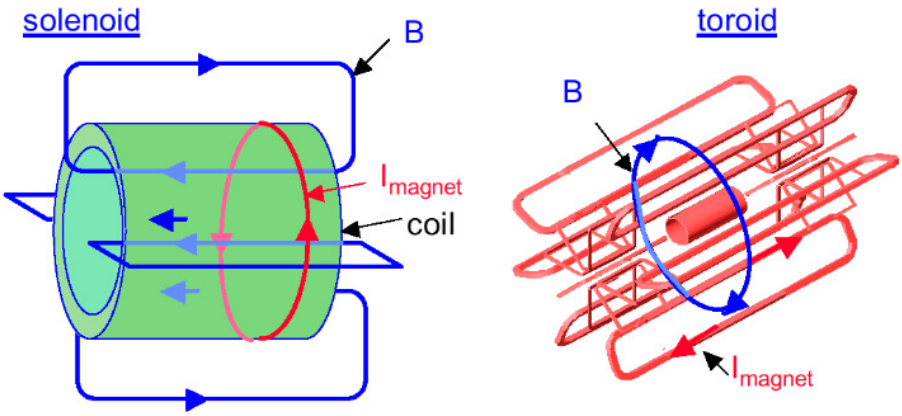

Figure 2.4: Illustration of solenoidal (left) and toroidal (right) magnetic fields. The current loops (red) and the magnetic fields (blue) are shown.

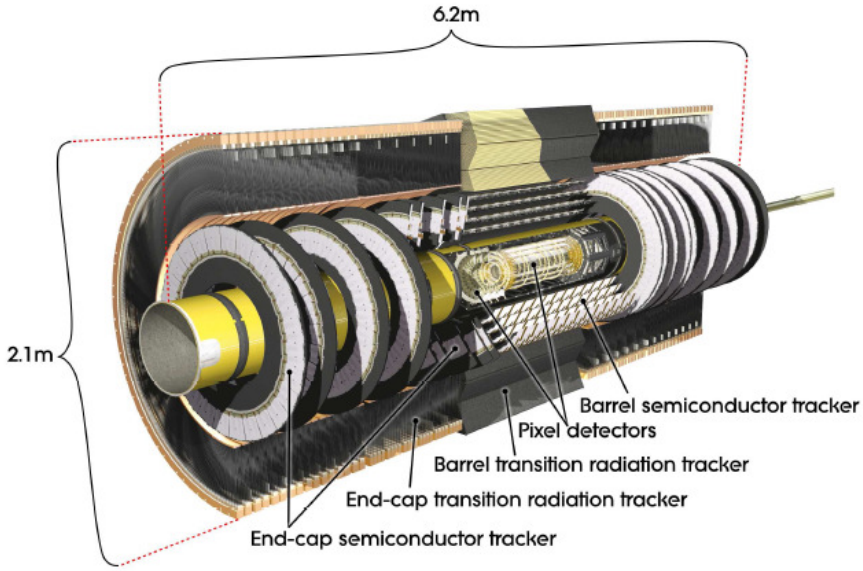

Figure 2.5: Layout of the ATLAS inner detector.

The pixel and SCT detectors are both silicon based semiconductor detectors. In such detectors, p-doped silicon is brought in contact with n-doped silicon, and this results in a p-n junction. The depletion zone, which is almost free of holes and free electrons, is extended by the application of a bias voltage. When a charged particle passes through such a p-n junction, it creates electron-hole pairs, and the electrons and holes drift in opposite directions because of the bias voltage. This creates a measurable pulse on the electrodes.

The basic sensor of the pixel detector is a pixel of size $50 \times 400\,\mu\text{m}^2$ in $R\phi \times z$ where R is the distance from the beam axis. Each hit in a pixel defines a space point. The intrinsic accuracy of the pixel detector barrel is $10\,\mu$m in $R\phi$ and $115\,\mu$m in z. Typically three pixel layers are crossed by each track.

In the SCT, silicon strips are used. The strips are oriented so that they measure either ϕ or z, and two hits are required for one space point. Eight strip layers are crossed by each track (providing four space points). The intrinsic accuracy per module for the SCT in the barrel is $17\,\mu$m in $R\phi$ and $580\,\mu$m in z.

In the TRT, straw tubes of diameter 4 mm are used to provide many measurements of $R\phi$ with an accuracy of $130\,\mu$m per straw. The straw tubes' length direction is parallel to the beam axis in the barrel and radial in the end caps, and the TRT therefore does not provide any measurement of η. The TRT typically provides 36 measurements per track. A straw tube consists of a central anode wire surrounded by a cylindrical tube. When a charged particle ionizes the gas in the TRT tube, the electrons start to drift towards the central wire, where they produce a signal. The drift time, i.e. the time the electrons use to reach the central wire, is measured, and gives a measurement of the radius (distance from central wire) at which the charged particle passed. See the left part of figure 2.8 for an illustration of a charged particle passing through a drift tube (in that case, in the ATLAS muon spectrometer).

Transition radiation is the emission of a photon when a charged particle passes between two media of different dielectric constants. The phenomenon occurs only for particles with very high relativistic factors, i.e. $\beta\gamma \gtrsim 1000$ [9]. In the TRT, there are layers of materials with different dielectric constants, which will cause electrons to emit transition radiation photons. These photons are measured in the TRT tubes, and provide electron identification, since heavier particles will not produce transition radiation because of their smaller relativistic factors. A transition radiation hit in the TRT is identified as a hit where the signal exceeds a higher threshold than for ordinary hits.

2.3.4 The calorimeters

The ATLAS detector uses sampling calorimeters. Such calorimeters consist of layers of active detector material and dead material. The energy measurement is obtained from the samples in the active detector layers, while the dead material (the absorbers) is there only to stop the particles. The ATLAS calorimeter layout is shown in figure 2.6. The calorimeters cover the region $|\eta| < 4.9$.

The ECal of ATLAS uses liquid argon (LAr) as its active detector material, and lead plates as absorbers. The ionization in the LAr is measured directly by electrodes. Over the η range corresponding to that of the inner detector, the ECal has finer granularity, so that precision measurements of photons and electrons can be made. Over the rest of the η range, the granularity is coarser, but still fine enough for jet reconstruction and $\not{E}_{\text{T}}$ measurements (see chapter 4 for explanations of jets and $\not{E}_{\text{T}}$).

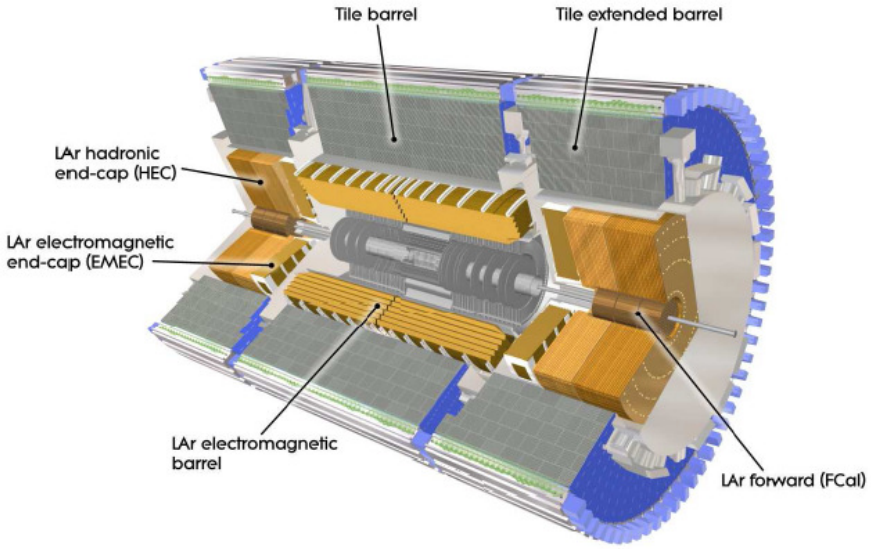

Figure 2.6: Layout of the ATLAS calorimeter system.

The HCal of ATLAS consists of the tile calorimeter in the barrel and extended barrel regions, and the LAr end-cap calorimeters and LAr forward calorimeters. The tile calorimeter uses steel as absorber and scintillators as active detector material. Here, the particles of a hadronic shower produce photons in tiles of scintillating material, and these photons are read out through wavelength shifters and photomultiplier tubes.

The hadronic end-cap calorimeter consists of two wheels for each end-cap, using copper plates as absorbers and LAr as active detector medium. Inside the center of the hadronic end-cap calorimeters, we find the forward calorimeters, covering the region closest to the beam pipe, assuring an as hermetic as possible detector. The detector needs to be as hermetic as possible to do good $\not{E}_{\mathrm{T}}$ measurements. The forward calorimeters use copper and tungsten as absorbers and LAr as active detector material.

2.3.5 The muon spectrometer

The layout of the ATLAS muon spectrometer is shown in figure 2.7. It consists, as the inner detectors and calorimeters, of a barrel part and end-caps. There are different kinds of sensors used in the muon spectrometer, serving different purposes. These are the monitored drift tubes (MDTs), the cathode strip chambers (CSCs), the resistive plate chambers (RPCs), and the thin gap chambers (TGCs).

The main precision tracking sensors in the ATLAS muon spectrometer are the MDTs. These are gaseous ionisation detectors with drift time measurement as in the case of the TRT. An illustration of an MDT is shown in figure 2.8. The tubes are oriented with their length direction tangential to a circle parallel to the xy-plane around the beam axis. They thus provide good precision in η, but not in ϕ. They are oriented in this way because this makes the tube length direction parallel to the toroidal magnetic field, so that the MDTs provide as good as possible momentum resolution.

In the first end-cap layer for $|\eta| > 2$, the particle flux is expected to be too large for the MDTs to cope with. The MDTs are therefore replaced by the CSCs in this region.

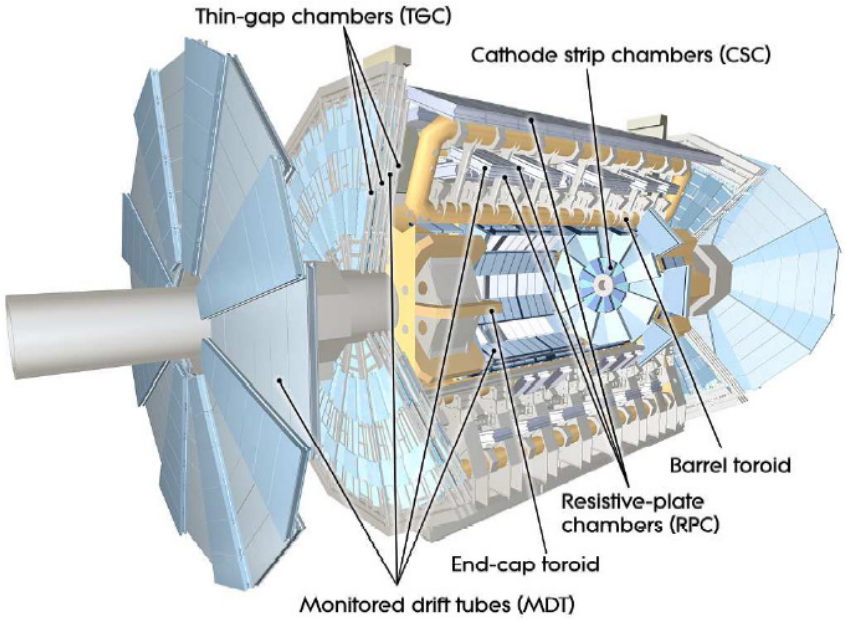

Figure 2.7: Layout of the ATLAS muon spectrometer.

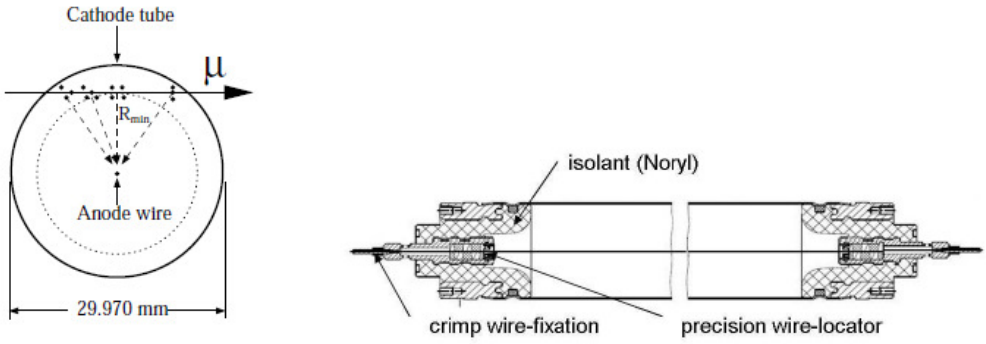

Figure 2.8: Illustration of a monitored drift tube from the ATLAS muon spectrometer.

The CSCs are multiwire proportional chambers, which are gaseous ionization detectors, and they serve the same purpose as the MDTs.

The trigger is the system that, for each collision event, decides whether the data from this particular event should be stored. It is needed because keeping all events is not feasible in terms of bandwidth and data storage. The muon chambers must provide information to the trigger very fast, and the MDTs are not feasible for this. For the trigger, faster detectors are needed, and these are the RPCs in the barrel and the TGCs in the end-caps. The RPCs and TGCs are both gaseous ionization detectors. In addition to trigger information, they provide measurements in ϕ, which is not accurately measured by the MDTs.

Muon reconstruction can in ATLAS be done stand-alone by the muon spectrometer only, or by matching a muon spectrometer track to an inner detector track, giving a combined muon.

2.4 SCT shift training

In October 2009, I went to CERN to take SCT shift training, since this is an activity the Oslo group is involved in. ATLAS was taking cosmic data at the time. I got the qualifications needed to take SCT shifts, both data quality monitoring shifts and detector operations shifts, which included taking three shadow shifts together with an experienced shifter. In Febraury 2010, I went back to CERN and took one block of detector operations shifts (four shifts).

Detector operations shifts consist of monitoring the detector control system (DCS) through a program called FSM (Finite State Machine) and an alarm panel. In the FSM, all cooling loops and detector modules are arranged in a tree structure, and one can navigate down the tree to look at the status or issue commands to specific modules. During my shadow shifts we used the FSM to manually set the bias voltage to lower values than the nominal 150 V for all modules in a specific barrel layer, which was done to allow for certain detector studies. Also, one can restart the bias voltage on modules that have been turned off because the current got too high (known as a module trip). When beam manipulations or beam injection is done, one must assure that the bias voltage is turned down, so that all modules are in standby, and the "safe for beam" flag is active. When the beam is stable, one can ramp up the bias voltage.

Alarms regarding temperatures, dew points, pressures etc. may appear during a shift. Unless the alarm is known and harmless, one should in general notify the expert on call. In addition, one monitors the data acquisition (DAQ) during a detector operations shift.

During data quality monitoring shifts, one looks at histograms produced "online", meaning that they are produced in real time as the data is streamed off the detector. The histograms are used to verify that the detector is performing properly, or detecting problems. A collection of online noise plots for the SCT barrel is shown in figure 2.9.

2.5 Summary

In this chapter, we have described the ATLAS detector at the LHC. We have described the layout of the detector, and how different particles are detected through their interactions with the detector. In the next chapter, an analysis of real data taken by the ATLAS detector is presented.

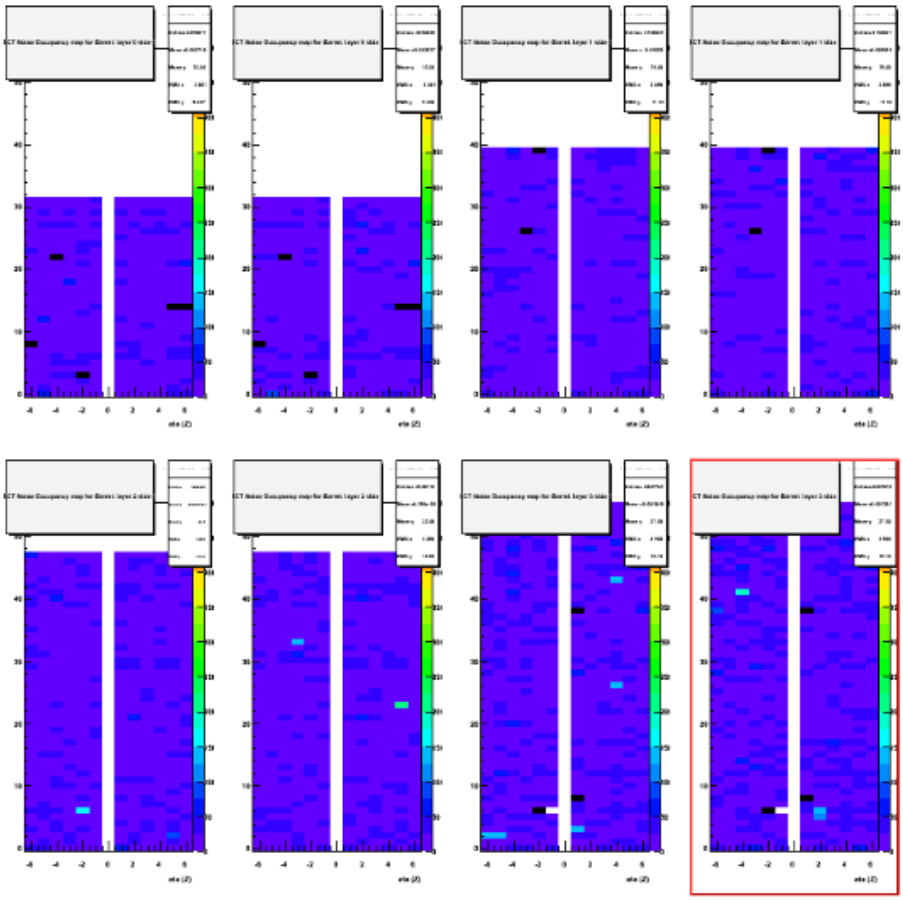

Figure 2.9: Online noise plots for the SCT barrel. The different plots correspond to different layers. Noisy modules will appear as yellow or red. Black modules are out of the configuration.

Chapter 3

Cosmic data analysis

3.1 Cosmic rays

Cosmic rays have played an important role in the history of particle physics. Several particles, such as the pions, the muon, and the positron were first discovered in cosmic ray showers, and cosmic rays were the primary source of experimental particle physics data before accelerators made it possible to study high energy particle interactions under more controlled circumstances.

Cosmic rays are particles of extraterrestrial origin arriving in the earth's atmosphere. The sources of these particles may be within our galaxy or beyond. The particles arriving to the atmosphere are called primary cosmic rays. The primary cosmic rays are typically protons, nuclei, or electrons. Protons dominate, and contribute approximately 85% of the primary cosmic rays [10].

When primary cosmic rays enter the earth's atmosphere, they create showers of secondary particles. A photon will create an electromagnetic shower (as described in section 2.2.1), and protons and nuclei will create hadronic showers when they interact strongly with the nuclei of the air. In the hadronic showers, the secondary particles produced are mostly pions, and to some extent kaons. These mesons will either produce more secondary particles through strong interactions with nuclei, or decay.

A neutral pion will decay to two photons, $\pi^0 \to \gamma\,\gamma$, contributing to the electromagnetic component of the shower. Charged pions decay to muons, $\pi^+ \to \mu^+\,\nu_\mu$ and $\pi^- \to \mu^-\,\overline{\nu_\mu}$. The decays of charged pions to electrons, $\pi^+ \to e^+\,\nu_e$ and $\pi^- \to e^-\,\overline{\nu_e}$, are helicity suppressed because of the maximal parity violation in charged current weak interactions. The decays do not happen because the weakly produced particles (anti-particles) are purely left-handed (right-handed). If the decay products were highly relativistic, this would violate the conservation of angular momentum, since the pion is spin-0. The decays to muons are no problem since the muons are not highly relativistic (the muon mass is comparable to the pion mass).

The muons produced in the decays of pions and kaons may decay to electrons, $\mu^+ \to e^+\,\nu_e\,\overline{\nu_\mu}$ and $\mu^- \to e^-\,\overline{\nu_e}\,\nu_\mu$, but they will mostly arrive to the earth surface because of their relatively long lifetime. We have $c\tau_\mu = 659\,\mathrm{m}$ [4] and the relativistic factor will further extend the range. A cosmic ray shower is illustrated in figure 3.1.

The energy spectrum, i.e. the flux as function of the energy, of primary cosmic rays is shown in figure 3.1. The highest energy cosmic rays have the lowest flux. The most energetic cosmic rays measured have energies exceeding $10^{20}\,\mathrm{eV}$. We have $10^{20}\,\mathrm{eV} = 16\,\mathrm{J}$, which would be the kinetic energy of a mass of 2 kg traveling at the speed 4 m/s ($E_{\mathrm{kin}} =$

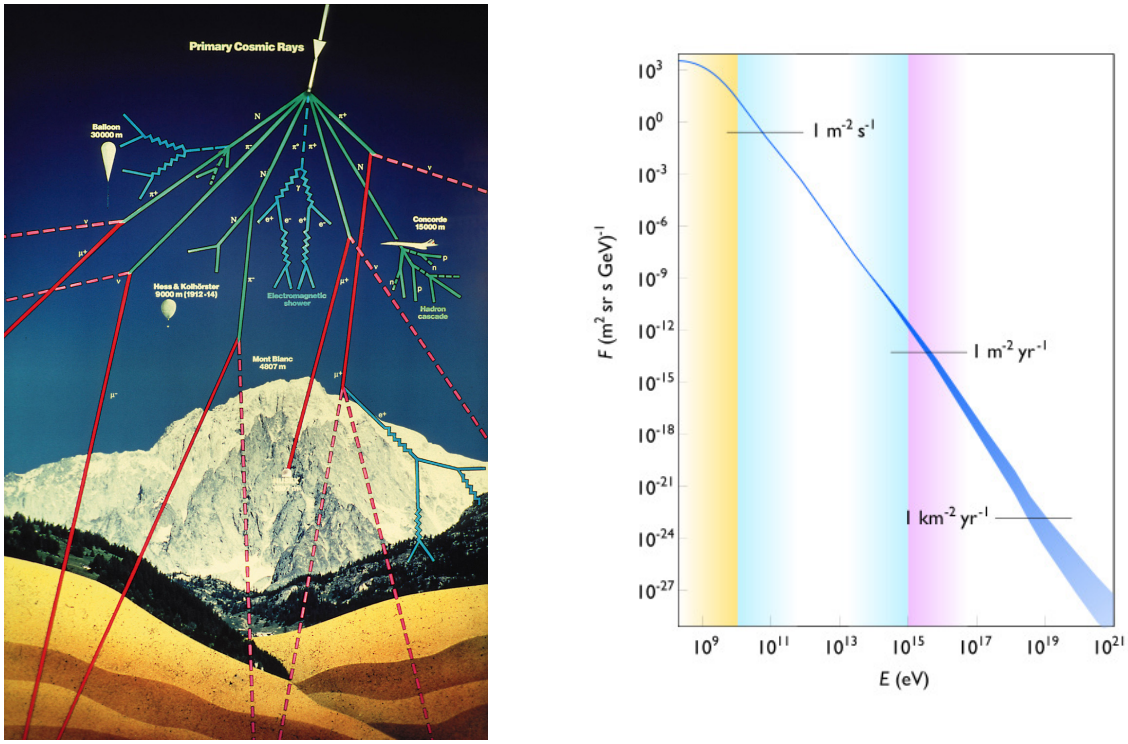

Figure 3.1: Illustration of a cosmic ray shower (left) and the energy spectrum (flux as function of energy) of primary cosmic rays (right).

$mv^2/2$). Really a macroscopic energy!

We can calculate the center of mass energy when a cosmic ray of energy $E \sim 10^{20}\,\text{eV}$ collides with a stationary atmospheric nucleus of mass $m \sim 10\,\text{GeV}$. We have then for the center of mass energy E_{CM}:

$$E_{\text{CM}}^2 = (E+m)^2 - \mathbf{p}^2 = E^2 + 2Em + m^2 - \mathbf{p}^2 \approx 2Em \tag{3.1}$$

where $\mathbf{p}$ is the momentum of the cosmic ray ($|\mathbf{p}| \approx E$). This gives $E_{\text{CM}} = \sqrt{2Em} \sim 10^{15}\,\text{eV}$, which can be compared to the LHC design energy for proton-proton collisions of $E_{\text{CM}} \sim 10^{13}\,\text{eV}$. However, from the flux distribution in figure 3.1, we see that such cosmic rays are very rare, while the LHC will produce collisions at a MHz rate, and in the very center of our detector instead of in the upper atmosphere.

3.2 Cosmic data taking with ATLAS

Since the construction of the ATLAS detector was finished before the LHC actually started with collisions, ATLAS has been taking cosmic data. This means that the detector has been measuring particles from cosmic ray showers. There are several reasons for doing this. It allows one

- to calibrate the different parts of the detector,
- to do alignment studies and improve the alignment,
- and to get a first impression of how the detector is performing, including the complete software chain from data taking to plots and results.

Alignment means the following. All of the different components of the ATLAS detector are mechanically mounted with extremely high precision. We are talking about large objects mounted with precisions of micrometers. This is necessary because to do tracking, hits in different sensors must be translated into points or regions in space, which require precise knowledge of the position of the sensor (relative to the other sensors).

When one does alignment, one improves the knowledge of the position of each detector part. This is done by fitting tracks without considering the hits of the part under study, and comparing the fitted track to the positions of the hits one has taken out. By doing this for many tracks, a residual distribution can be built, which will have a mean different from zero if the considered detector part is not aligned (its position is not precisely known). One can then change alignment constants in the reconstruction software to account for this.

3.3 ATLAS cosmic data simulation

In order to be able to start simulation vs. real data comparisons already before the LHC starts, cosmic data has been simulated for ATLAS. The simulation has been done in the following way. Variations exist between different datasets. Main source is [14].

Single muons are generated at the earth surface within the square

$$-300\,\mathrm{m} < x < +300\,\mathrm{m} \quad \text{and} \quad -300\,\mathrm{m} < z < +300\,\mathrm{m} \tag{3.2}$$

with energies in the range $10\,\mathrm{GeV} < E < 5\,\mathrm{TeV}$ and with an angle $\theta < 70°$ relative to the vertically downward direction. The energy, charge, and direction of the muon is generated according to fits to measured distributions at the earth surface. An extrapolation is then made down to $y = 0$, through the earth above the ATLAS cavern, either using GEANT[1] or simply by a straight line approximation.

At this point, a selection is made, requiring that the muon at $y = 0$ falls within some region in the xy-plane, or that it enters some filter volume, e.g. the TRT. Only muons passing this selection are stored, and for these muons, the full detector response is simulated. If the passage through the earth above ATLAS has not already been simulated with GEANT, this is now done. The detector response simulation results in simulated raw data, which is then passed to the ATLAS reconstruction software in the same way as real data.

The reconstruction software produces tracks, calorimeter clusters, and higher level analysis objects from the raw data. The reconstruction software is "hacked" when used on cosmic data, to be able to cope with tracks not originating from close to the interaction point, and possibly other things that distinguishes cosmic data from collision data in terms of reconstruction. In collision events, all the final state particles originate from close to the interaction point.

The result of the reconstruction is ESD (Event Summary Data) files, where the physicist doing the final analysis can access objects such as tracks, calorimeter clusters, muons etc. Smaller files containing less information can be made from the ESD. Examples are AOD (Analysis Object Data) and DPD (Derived Physics Data) files.

[1] GEANT [11] is a detector simulation framework.

3.4 An analysis of 2008 cosmic ATLAS data

The particles in a cosmic ray shower reaching the ground are mostly muons. In addition, the particles reaching the ATLAS detector have to pass through some material, but not necessarily much material because of the shafts down to the ATLAS cavern. This further reduces the amount of other particles than muons, since muons are much more penetrating than other particles, as described in section 2.2.1. For this reason, cosmic data analysis is to a large extent analysis of muons only. Other particles may be observed in cosmic events, but these are then mostly secondary particles originating from the muon's interactions with the detector material. Secondary electrons and even jets have been observed in ATLAS cosmic data.

3.4.1 The perigee and impact parameters

The perigee of a track is defined as the point on the track closest to the beam axis. The parameters of cosmic muons, such as η, ϕ and p_{T}, are taken at perigee. The so-called impact parameters defined for a track are:

- d_0: the distance from the perigee to the beam axis,
- z_0: the z coordinate of the perigee,
- ϕ_0: the azimuthal angle of the direction of the momentum vector at perigee,
- θ_0: the polar angle of the direction of the momentum vector at perigee.

The sign convention for d_0 is as follows. Let ϕ' be the azimuthal angle of the perigee position. We then define d_0 as positive if

$$\phi' - \phi_0 = \frac{\pi}{2} + 2n\pi \tag{3.3}$$

where n is an integer. Note that the xy-projection of the momentum vector is always perpendicular to the xy-projection of the position vector at perigee, since the perigee is the point of closest approach to the beam axis. This means that we have either $\phi' - \phi_0 = \pi/2 + 2n\pi$ or $\phi' - \phi_0 = 3\pi/2 + 2n\pi$, giving positive or negative d_0 respectively. Note also that the definition implies that the d_0 is positive if the z-projection of the track's angular momentum $\mathbf{L} = \mathbf{r} \times \mathbf{p}$ is negative at perigee. See figure 3.2 for an illustration of the impact parameters.

3.4.2 Data samples used in this analysis

The real data samples used in this analysis are:

1. Run number 91890, year 2008, ESD.
2. Run number 91900, year 2008, ESD.

These are real cosmic data from 2008 with both magnetic fields turned on, so that the muon momentum can be measured in both the inner detector and the muon spectrometer. The data used was reprocessed in spring 2009, with the at that time newest alignment constants and reconstruction software.[2]

The MC (Monte Carlo) data samples used are:

[2]The 2008 cosmic data has later been through additional reprocessings which show improved performance of the muon reconstruction.

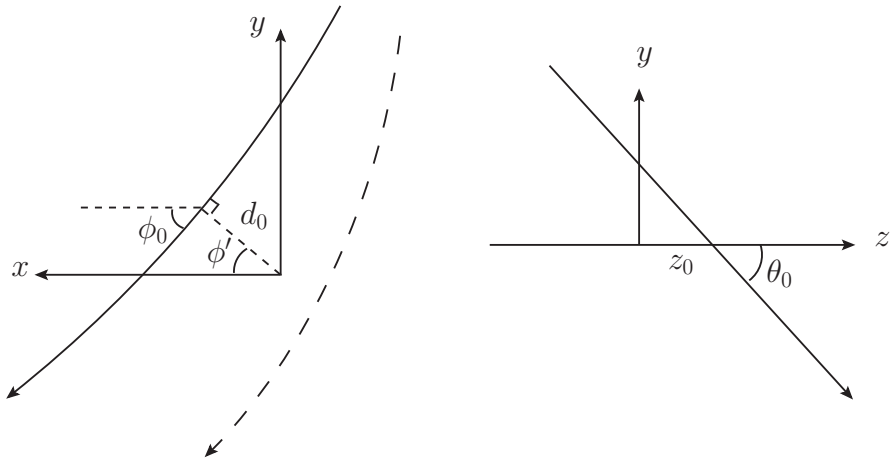

Figure 3.2: Illustration of the impact parameters d_0, ϕ_0, θ_0, and z_0. Two projections of the ATLAS coordinate system are shown. In the yz-projection, the perigee of the track is assumed to be at $y = 0$. The angle ϕ' which is used to determine the sign of d_0 is shown in the transverse projection. In this illustration, we have $\phi_0 < 0$, $d_0 > 0$, and $z_0 > 0$. The dashed track in the transverse projection would have $d_0 < 0$.

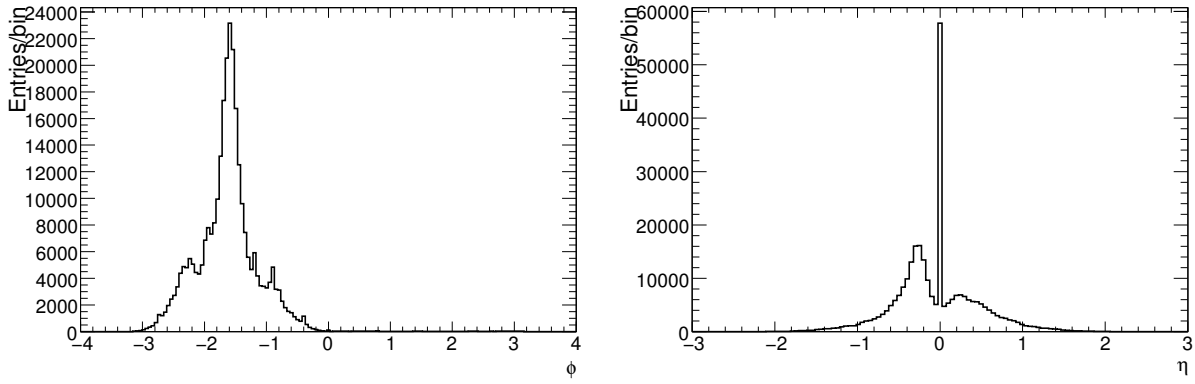

Figure 3.3: The ϕ (left) and η (right) distributions for muons in real data sample 1 with no muon selection criteria.

1. Monte Carlo with toroid and solenoid magnets on, ESD.

2. Monte Carlo with toroid and solenoid magnets off, ESD.

All reconstructed muon objects are accessed through the `MuidMuonCollection` container. Detailed information about the datasets can be found in appendix A.

3.4.3 Basic distributions: η and ϕ

Figure 3.3 shows the η and ϕ distributions obtained by running over all muons (reconstructed muon analysis objects) in data sample 1 with no muon selection criteria.

Practically all the muons have $\phi \in [-\pi, 0]$, which means that they are moving downwards. Actually, the direction of any reconstructed track is ambiguous, since there is no timing information on the separate hits. In collision data, this is not an issue, since the

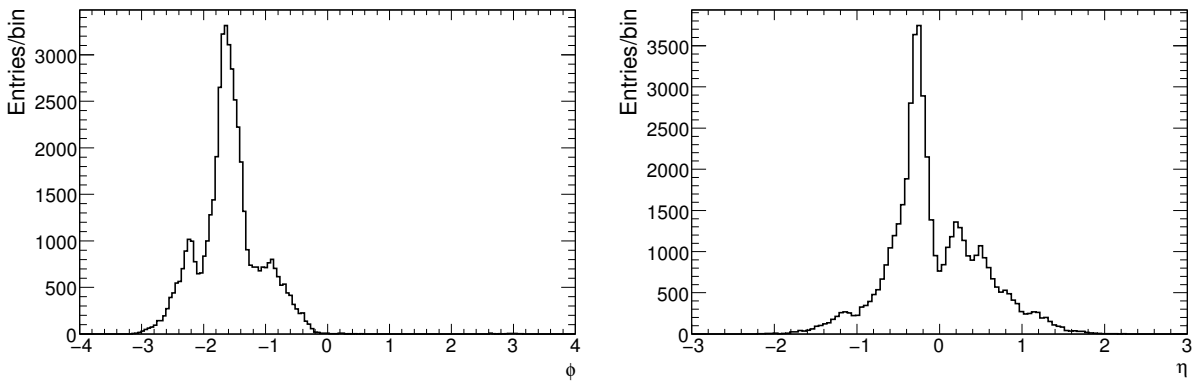

Figure 3.4: The ϕ (left) and η (right) distributions for muons in real data sample 1 with the requirement that the muons must have at least one hit in either the SCT or the pixel detector.

tracking software can take into account that all tracks should originate from the interaction point. Since Athena[3] release 15.0.0, the cosmic analysis track reconstruction software assumes downward direction on all tracks. The data used here was reconstructed with Athena release 14, but almost all tracks have been given the downward direction in these data, as seen in figure 3.3.

The ϕ distribution peaks at $\phi = -\pi/2$, corresponding to the straight downward direction. Note that ϕ in this case is measured at perigee, so that it is the same as the ϕ_0 impact parameter. This means that the ϕ distribution shown is not the distribution that would be obtained if the muons were measured above the detector, since the muons are bent in the solenoidal magnetic field.

For the η distribution, we see a large peak at $\eta = 0$ (corresponding to the direction perpendicular to the beam axis). This peak seems unphysical, since it includes only one bin. The η and ϕ distributions obtained with the requirement of at least one hit in either the SCT or the pixel detector are shown in figure 3.4. Now, the unphysical peak at $\eta = 0$ is gone. This is explained as follows. The η assigned to the muon analysis object is the one from the inner detector track. If the inner detector track has only TRT hits, then no η value is assigned to the track, and the default value is zero. This is because the barrel TRT tubes are oriented parallel to the beam axis, and the TRT therefore provides only ϕ information (see section 2.3.3). The requirement of at least one SCT or pixel hit reduced the number of entries in the histograms from $296 \cdot 10^3$ to $50 \cdot 10^3$.

In the η distribution, we see peaks on either side of $\eta = 0$. These correspond to the big and small shafts leading down to the ATLAS cavern (see figure 3.5). We see that there are more muons on the $\eta < 0$ side. This corresponds to the fact that the bigger shaft is located at $z > 0$. For a muon moving downwards into the inner detector from the big shaft, we will have $\theta > \pi/2$ and therefore $\eta < 0$.

There seems also to be peaks on either side of the large, central peak in the ϕ distribution. These probably correspond to the elevator shafts leading down to the ATLAS cavern, which are situated at $x \approx \pm 30\,\mathrm{m}$.

[3]Athena is the central component of the ATLAS software.

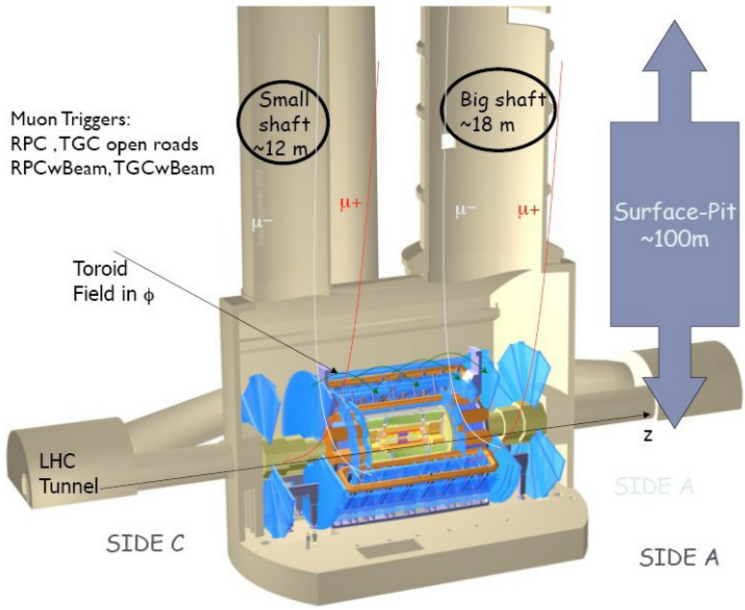

Figure 3.5: Illustration of the ATLAS cavern geometry. The trajectories of positive and negative muons from the two shafts in the toroidal magnetic field are shown.

Cut type	Pixel hits	SCT hits	Silicon hits	TRT hits	d_0 [mm]	p_{T} [GeV]	TRT phase [ns]
Loose			≥ 8	≥ 30	≤ 500	≥ 1	$\in [-10, 40]$
Medium			≥ 10	≥ 20	≤ 250	≥ 1	$\in [5, 30]$
Tight	≥ 4	≥ 12		≥ 50	≤ 40	≥ 1	$\in [5, 30]$

Table 3.1: Recommended inner detector cuts on muons. The loose requirement is 8 silicon hits *or* 30 TRT hits. TRT phase of zero is excluded from the loose TRT phase range. This is beacuse it is a default value.

3.4.4 Inner detector cuts

As seen in the previous section, the selection criteria (cuts) used can significantly change the observed distributions. One should require certain numbers of hits in various subdetectors etc. There exists a set of recommended cuts for inner detector tracks [13]. These are divided into loose, medium, and tight cuts, and they are shown in table 3.1.

The numbers of hits in these cuts refer only to barrel hits, but in this analysis, all hits have been included, i.e. also end-cap hits. Shown in table 3.2 are the numbers of muons after the different inner detector cuts (including the cuts on d_0, p_{T}, and TRT phase). We want to ensure good quality of the muon tracks used in our analysis. On the other hand, we also need to keep enough muons to ensure sufficient statistics. The tight cut seems clearly too restrictive, and does not provide enough statistics. It seems that the medium cut is a good compromise between track quality and statistics. This cut should provide enough statistics to get well defined distributions.

The TRT event phase measures the time of arrival of the cosmic muon relative to the time window when the TRT measures whether or not the signal exceeds the threshold value. The TRT event phase distributions for real data sample 1 and MC data sample

Cut type	Number of muons
Loose	$63 \cdot 10^3$
Medium	$13 \cdot 10^3$
Tight	$0.82 \cdot 10^3$

Table 3.2: Numbers of muons surviving the different inner detector cuts when applied on real data sample 1.

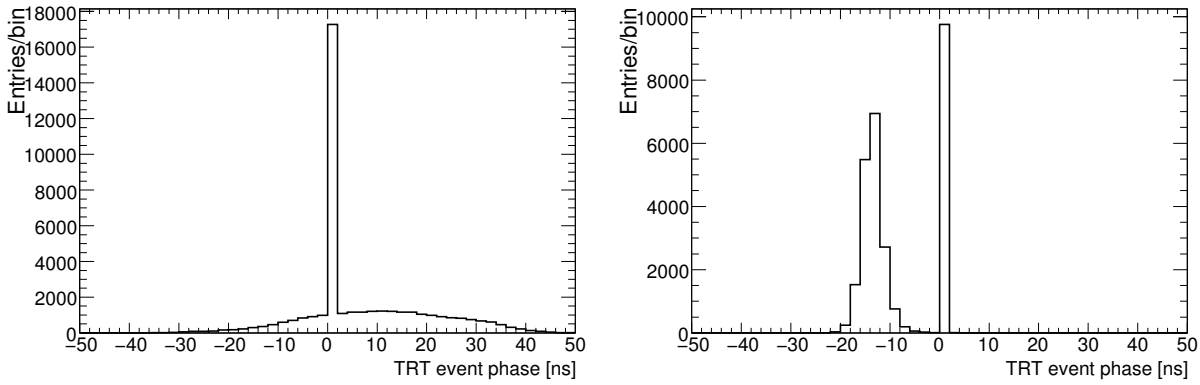

Figure 3.6: TRT event phase distributions for real data sample 1 (left) and MC data sample 1 (right).

1 are shown in figure 3.6. The distributions are very different. It seems that the event phase is not constructed in the MC in such a way that it can be compared to real data. Therefore, the event phase cut is only applied to the real data, not to the MC. This seems to be standard procedure when analysing ATLAS cosmic data. We also see that many events have a default value of zero for the event phase, which explains why this value is excluded from the loose cut region.

3.4.5 Muon spectrometer/inner detector correlations

A muon will typically make three tracks when traversing the ATLAS detector. One track in the muon spectrometer on the muon's way into the detector, one track in the inner detector, and one track in the muon spectrometer on the muon's way out of the detector. One can easily access two tracks, one muon spectrometer track and the inner detector track, from the muon analysis object. The muon analysis object is of course tailored for collision data analyses, and holds therefore only one muon spectrometer track. (A muon originating from the interaction point traverses the muon spectrometer only once.)

If one extrapolates the muon spectrometer track into the inner detector, then one can obtain the expected impact parameters based only on the muon spectrometer track. If these impact parameters are compared with the ones obtained from the inner detector track, one should find a clear correlation. We define the quantity

$$\Delta d_0 = d_0(\text{inner detector}) - d_0(\text{muon spectrometer}). \tag{3.4}$$

The similar quantities $\Delta\phi_0$, $\Delta\theta_0$, and Δz_0 are defined analogously. These quantities are residuals, and we expect them to be distributed approximately normally (Gaussian) around zero. The extrapolation of the muon spectrometer track is done in reconstruction, and the extrapolated track is accessible through the muon analysis object.

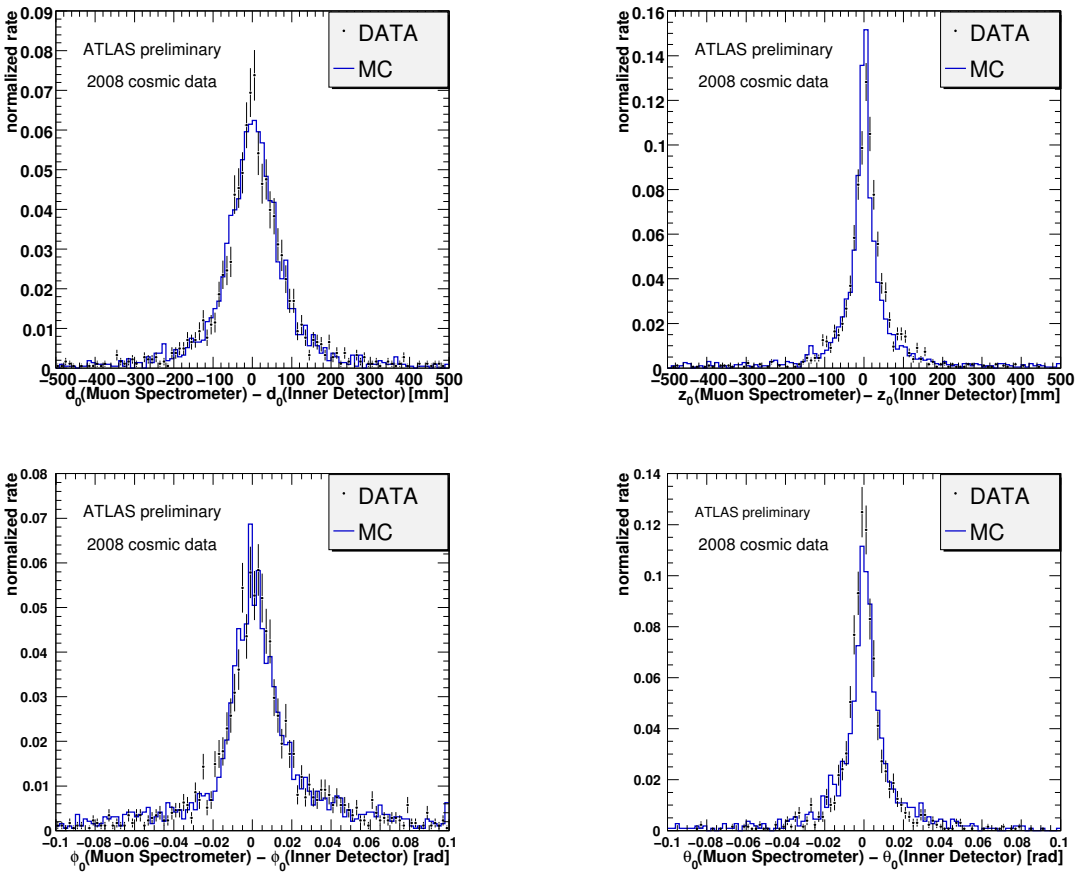

Figure 3.7: Approved ATLAS cosmic analysis plots showing muon spectrometer/inner detector impact parameter residual distributions for 2008 cosmic data and MC.

Figure 3.7 shows approved preliminary ATLAS cosmic analysis plots showing the muon spectrometer/inner detector correlation. These plots are made from 2008 cosmic data, which is also what is used here. We see that the distributions seem more or less Gaussian, and that data and MC seem to agree satisfactory.

The residual distributions were now produced from real data sample 1 and MC data sample 1. These are shown in figure 3.8. Note that the definition of the residuals used here (eq. (3.4)) is opposite of the one used in the approved plots, which has only the effect of reflecting the distributions through zero.

To be able to compare the distributions obtained from different data samples, in our case the real data and the MC data, one must scale the histograms. This is because the histograms from the different data samples in general will contain different number of entries. In all the plots where MC and real data are compared, the histograms are scaled down with the number of entries in the histograms. I.e. a bin in the scaled histogram has content equal to the bin content in the original histogram divided by the total number of entries in the original histogram.

In the plots in figure 3.8, error bars are shown for data. The errors have been obtained from standard ROOT[4] functionality, i.e. `TH1::Sumw2()` has been called for the histograms. ROOT then automatically scales the errors when the histogram is scaled. The error on a bin when the bin has been filled with n entries, all with unit weight, is $\sqrt{n}$.

[4]ROOT [12] is a data analysis framework.

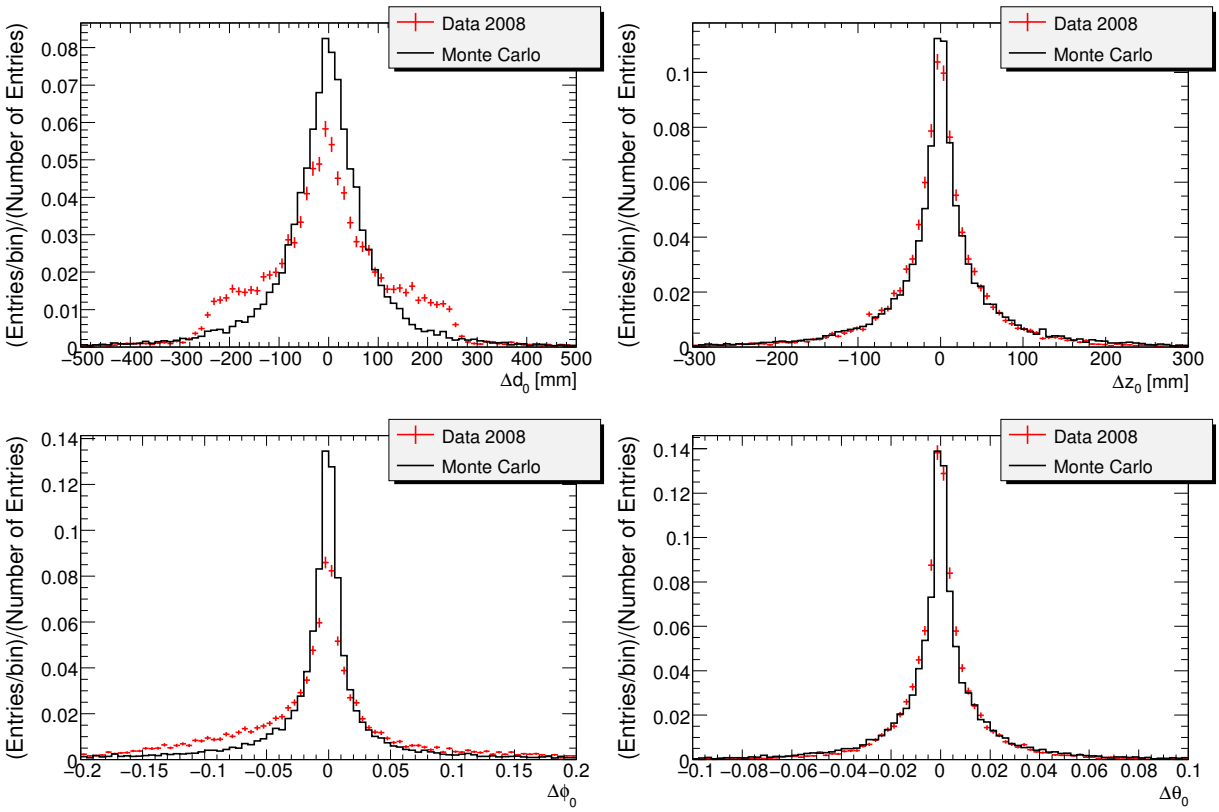

Figure 3.8: Residual distributions obtained from real data sample 1 and MC data sample 1 with medium inner detector cuts.

This corresponds to the fact that a Poisson distribution with mean $\mu = \lambda$ has standard deviation $\sigma = \sqrt{\lambda}$.

The $\Delta\theta_0$ and Δz_0 plots in figure 3.8 seem to agree with the approved cosmic plots. In these plots, the agreement between MC and data is also good. However, in figure 3.8, the Δd_0 and $\Delta\phi_0$ distributions do not agree with the approved plots, and here data and MC do not agree satisfactory. The Δd_0 distribution shows severe non-Gaussian tails on both sides, not reproduced by MC. Furthermore, the $\Delta\phi_0$ distribution is clearly asymmetric, also not reproduced by MC.

Muon spectrometer cuts

The cuts used so far ensure a good inner detector track, but does not ensure good quality of the muon spectrometer track. We should also use some cuts on numbers of hits in the muon spectrometer. The total number of muon spectrometer hits for the muons in real data sample 1 with medium inner detector cuts, is shown in figure 3.9.

We see here that most muons have a substantial number of hits in their muon spectrometer track. Therefore, cutting on total number of muon spectrometer hits is probably not necessary. To remove just the worst muon spectrometer tracks, we now require at least 15 muon spectrometer hits in addition to the inner detector cuts. The resulting Δd_0 and $\Delta\phi_0$ distributions are shown in figure 3.10. The distributions are still bad, with the same non-Gaussian tails and asymmetry.

The number of RPC ϕ hits for muons in real data sample 1 with medium inner detector cuts and at least 15 muon spectrometer hits is shown in figure 3.11. (Note that a bin in

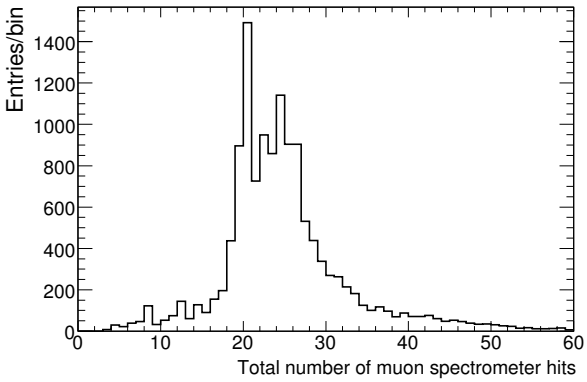

Figure 3.9: Total number of muon spectrometer hits for muons in real data sample 1 with medium inner detector cuts.

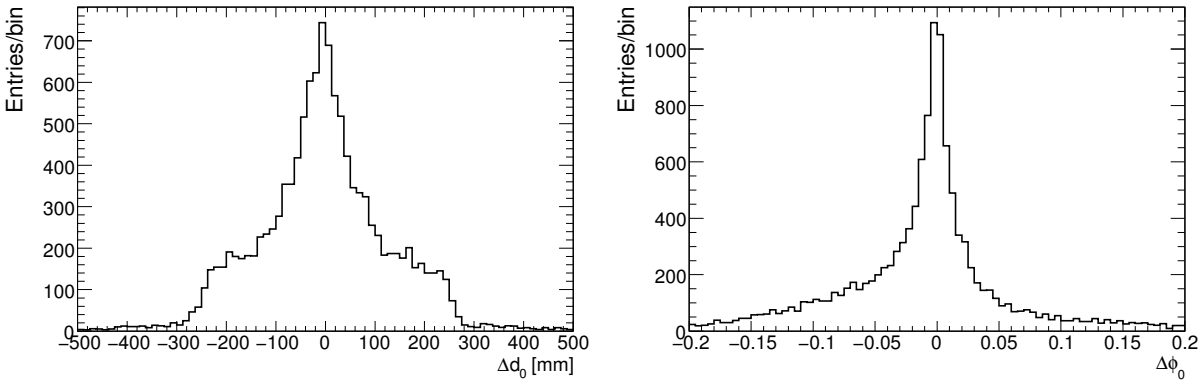

Figure 3.10: Residual distributions obtained from real data sample 1 with medium inner detector cuts and the requirement of at least 15 muon spectrometer hits.

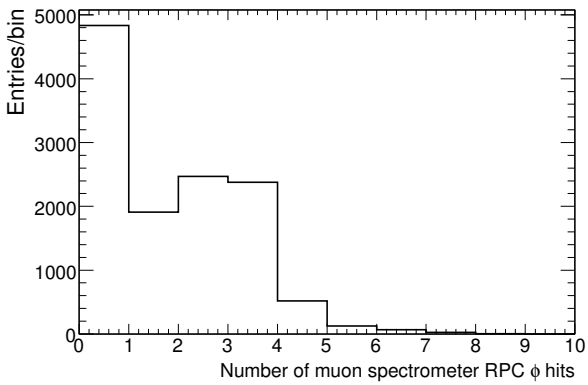

Figure 3.11: Number RPC ϕ hits for muons in real data sample 1 with medium inner detector cuts and requirement of at least 15 muon spectrometer hits in total.

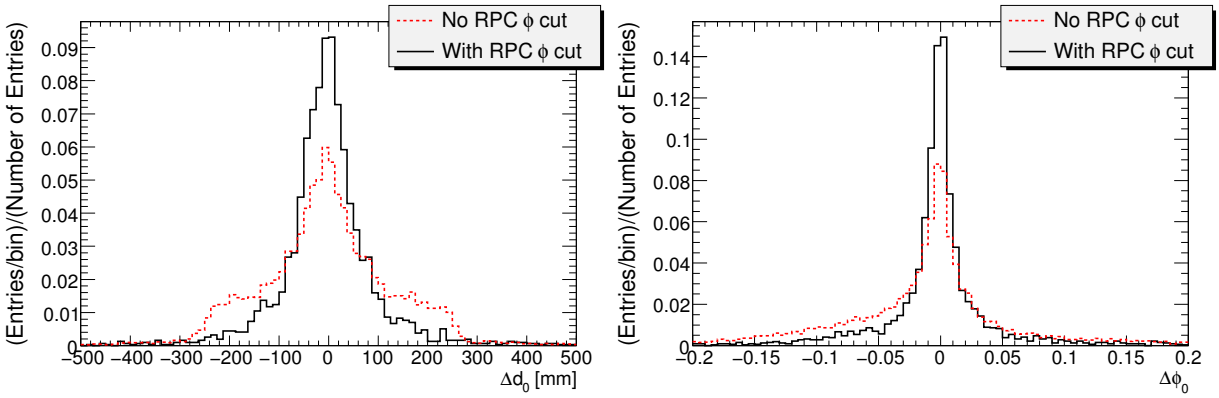

Figure 3.12: Residual distributions obtained from real data sample 1 with medium inner detector cuts and requirement of at least 15 muon spectrometer hits, with and without the requirement of 3 RPC ϕ hits.

this and similar histograms is filled with the number of hits corresponding to the bin's low edge, so that the first bin in figure 3.11 is filled with the muons with zero RPC ϕ hits.) We see that there are many muons with no RPC ϕ hits.

We now add the requirement of at least 3 RPC ϕ hits to the analysis. Figure 3.12 shows the Δd_0 and $\Delta\phi_0$ distributions with and without the RPC ϕ cut. We see that the RPC ϕ cut seems to remove the tails and asymmetry of these distributions.

We can now produce again the residual distributions with our final cuts, which are

- medium inner detector cuts (table 3.1),
- at least 15 muon spectrometer hits in total,
- at least 3 muon spectrometer RPC ϕ hits.

These cuts are used throughout the rest of this analysis, unless stated otherwise. The numbers of muons passing the cuts are $3.1 \cdot 10^3$ for real data sample 1 and $16 \cdot 10^3$ for MC data sample 1. The distributions are shown in figure 3.13. Now these agree well with the approved plots, and MC and real data agree satisfactory.

The reason for the importance of the RPC ϕ hits, is that the MDTs do not measure ϕ well enough (see section 2.3.5). Indeed, one of the purposes of the RPCs is to provide ϕ

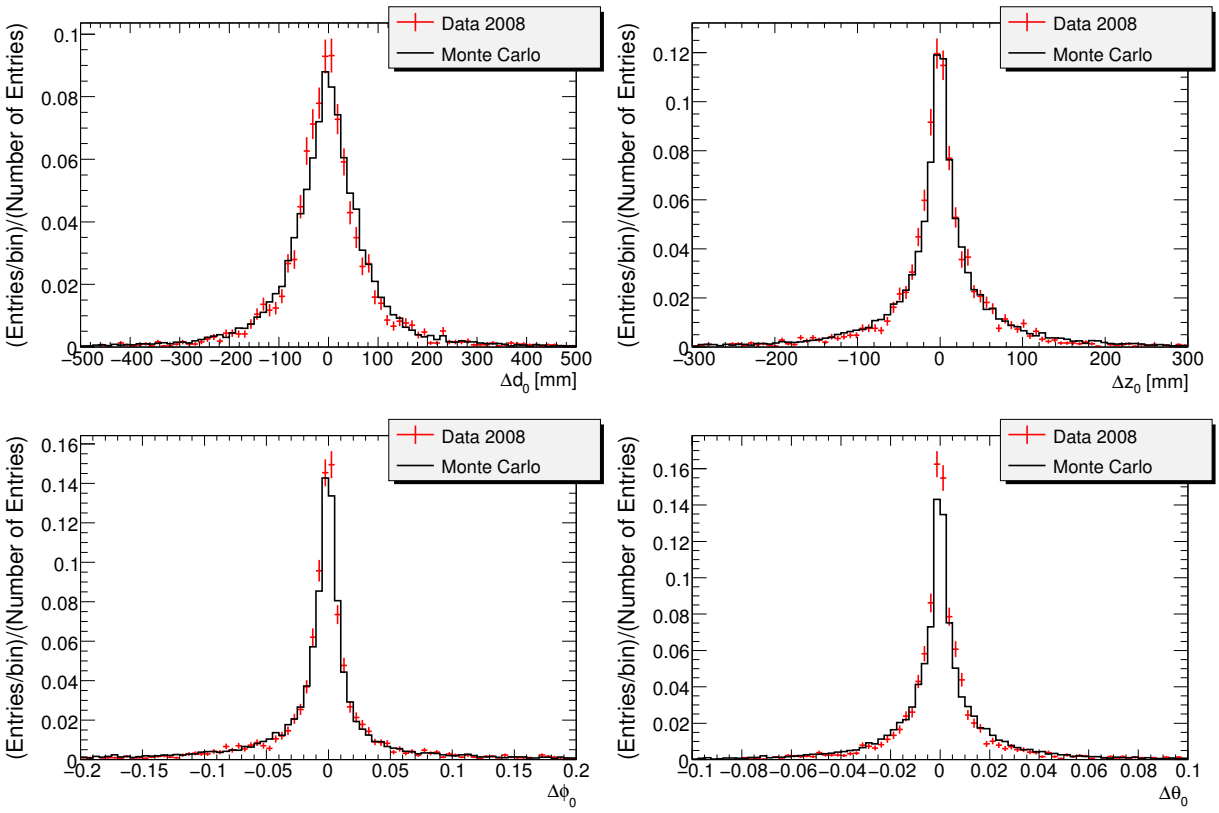

Figure 3.13: Residual distributions obtained from real data sample 1 and MC data sample 1 with final cuts.

measurement. This explains why the Δz_0 and $\Delta\theta_0$ distributions looked fine also without the RPC cut. These impact parameters do not depend on the track's projection in the xy-plane. Hence, accurate ϕ measurement is not required to get these distributions right, and MDT hits suffice.

Figure 3.14 shows correlation plots (two-dimensional histograms) of θ_0 and ϕ_0 for muon spectrometer vs. inner detector. These plots show straight lines with statistical smearing, which is what is expected.

Energy loss in the calorimeters

In the same way as for the impact parameters, we can compare the momentum measurements in the muon spectrometer and in the inner detector by defining the difference:

$$\Delta p = p(\text{inner detector}) - p(\text{muon spectrometer}). \tag{3.5}$$

Here, the momenta are really the momenta of the tracks in the different parts of the detector, i.e. no extrapolation is made. On the muon's way from the muon spectrometer to the inner detector (or vice versa), it traverses the calorimeters. These consist of dense material, and we therefore expect the muon to lose a certain amount of energy. This energy loss should show up as a shift in the Δp distibution, so that it should not be centered around zero. Our cosmic muons all have $p_{\mathrm{T}} > 1\,\mathrm{GeV}$, which makes them highly relativistic. This means that $E = \sqrt{p^2 + m^2} \approx p$, so that the energy loss and the momentum loss in the calorimeters are the same.

The Δp distribution obtained from real data sample 1 is shown in figure 3.15. We see a large peak centered at approximately $-3\,\mathrm{GeV}$, and a smaller peak at $+3\,\mathrm{GeV}$. This is

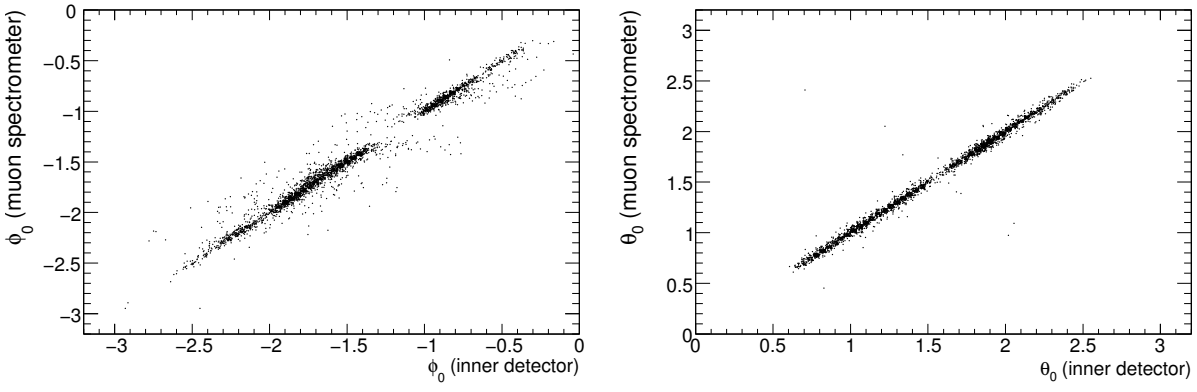

Figure 3.14: Scatterplots of ϕ_0 and θ_0 showing muon spectrometer value vs. inner detector value from real data sample 1.

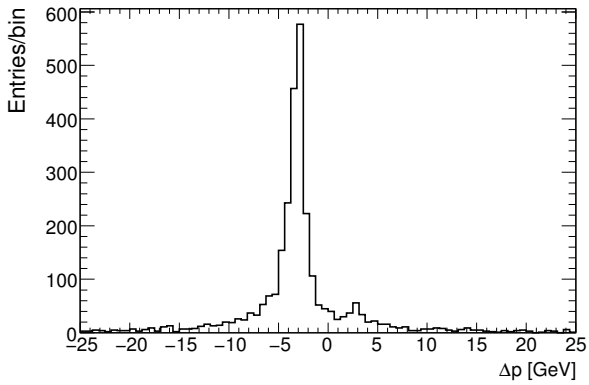

Figure 3.15: Distribution of Δp obtained from real data sample 1 using the definition (3.5).

interpreted in the following way. As mentioned, the muon object holds only one muon spectrometer track. Sometimes this will be the track the muon made on its way into the detector, and sometimes the one it made on its way out.

Since a cosmic muon traverses the detector from top to bottom, we can refer to the different muon spectrometer tracks as "upper" and "lower". The upper muon spectrometer track has y-coordinate $y_{\text{track}} > 0$, while the lower one has $y_{\text{track}} < 0$. Figure 3.16 shows the Δp distribution segmented in the cases $y_{\text{track}} > 0$ and $y_{\text{track}} < 0$ as well as the distribution of y_{track} itself.

We see that the peak at $-3\,\text{GeV}$ corresponds to the $y_{\text{track}} > 0$ (upper muon spectrometer tracks) entries, and that the peak at $+3\,\text{GeV}$ corresponds to $y_{\text{track}} < 0$ (lower muon spectrometer tracks) entries. From the definition (3.5), we see that this means that the muons have more energy in the upper muon spectrometer than in the inner detector, and more energy in the inner detector than in the lower muon spectrometer, as expected. We see also that far more muons have $y_{\text{track}} > 0$, meaning that most of the muon spectrometer tracks associated to the muon objects are upper tracks, which again corresponds to the fact that the peak at $-3\,\text{GeV}$ is far bigger than the one at $+3\,\text{GeV}$.

We can now redefine Δp in such a way that the expected momentum difference will

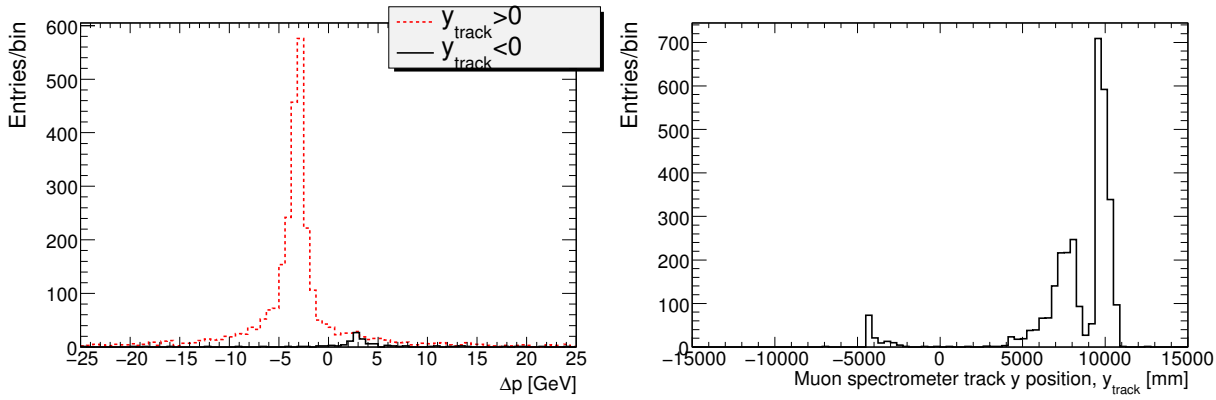

Figure 3.16: The Δp distribution as defined in eq. (3.5) for real data sample 1 segmented into $y_{\text{track}} > 0$ and $y_{\text{track}} < 0$ as well as the distribution of y_{track}.

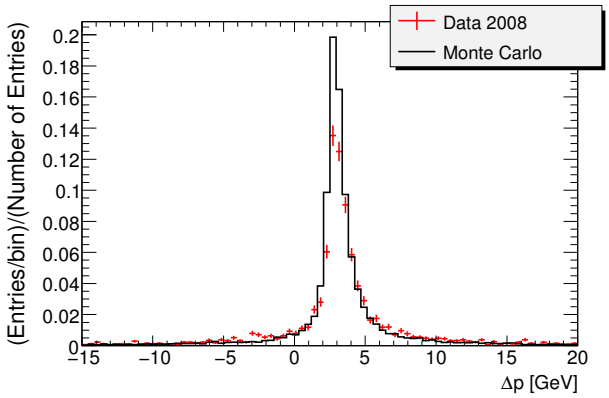

Figure 3.17: Distribution of Δp obtained from real data sample 1 and MC data sample 1 using the definition (3.6).

be the same for upper and lower muon spectrometer tracks, namely:

$$\Delta p = \begin{cases} p(\text{muon spectrometer}) - p(\text{inner detector}) & \text{for } y_{\text{track}} > 0, \\ p(\text{inner detector}) - p(\text{muon spectrometer}) & \text{for } y_{\text{track}} < 0. \end{cases} \tag{3.6}$$

The corrected Δp distribution is shown for real data sample 1 and MC data sample 1 in figure 3.17. Real data and MC are seen to agree reasonably well, although the data apparently has more events out in the tails of the distribution, as seen from the discrepancy at the peak.

The distribution for real data seems to have a small peak at $-3\,\text{GeV}$, even though we have segmented the muon spectrometer tracks according to y-coordinate. This may be explained by the fact that some muon spectrometer tracks apparently extend throughout the detector, and have both "upper" and "lower" hits. It is then possible that the y-coordinate and the momentum are taken at different positions along the track, and that this gives the small peak at $-3\,\text{GeV}$.

We have seen that the cosmic muons lose on average approximately $3\,\text{GeV}$ while traversing the calorimeters, and that the momentum difference distribution shows satisfactory agreement between real data and MC.

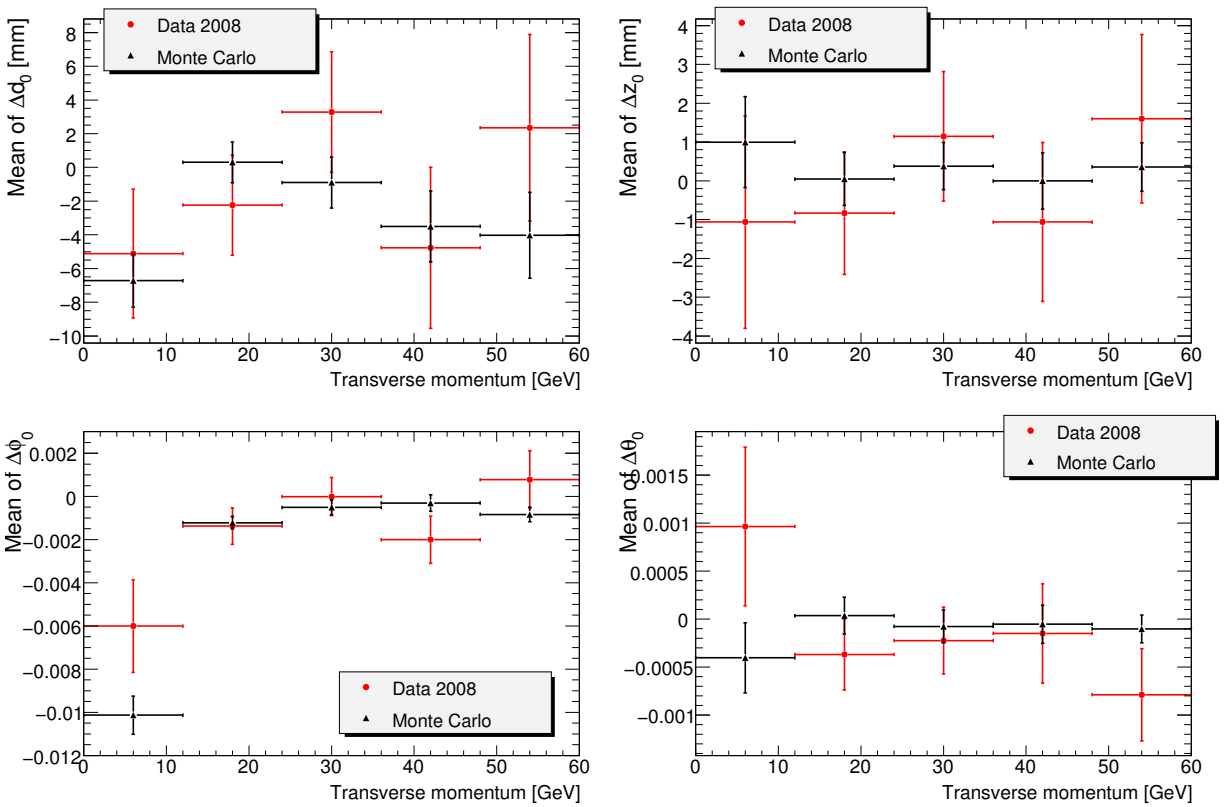

Figure 3.18: Means of residual distributions obtained from real data sample 1 and MC data sample 1 as function of transverse momentum.

Biases of the residual distributions

The inner detector-muon spectrometer residual distributions should be centered around zero. A non-zero mean for a residual distribution means that some systematic effect is seen.

Figure 3.18 shows the means of the residual distributions (corresponding to figure 3.13) as function of transverse momentum. The distributions are built spearately for muons with p_{T} falling in the different bins, and the means are extracted. The p_{T} axis extends only to 60 GeV to ensure enough statistics in each bin. The means seem generally consistent with zero for both real data and MC.

The $\Delta\phi_0$ distribution seems to have a bias at small momenta which is reproduced by MC. If we distinguish between positive and negative muons, the bias is seen to be clearly charge dependent (see figure 3.19). This is also reproduced by MC.

Since the bias at small momenta is charge dependent, is seems that it is related to some systematic effect in the extrapolation of the muon trajectory through the solenoidal magnetic field. For higher momenta, the bias then vanishes because the muon trajectory curves less in the magnetic field. To confirm this hypothesis, we can compare with the results obtained for MC without magnetic field. This is, however, a bit tricky. In the analysis, both the transverse momentum and the charge of the muons is used, neither of which can be measured with magnetic field off. To make the comparison with the MC data sample with magnetic field off, the truth particle charge was used to distinguish between positive and negative muons. Furthermore, no segmentation of the muons according to p_{T} was made, since the truth particle p_{T} is given where the particle is generated, namely

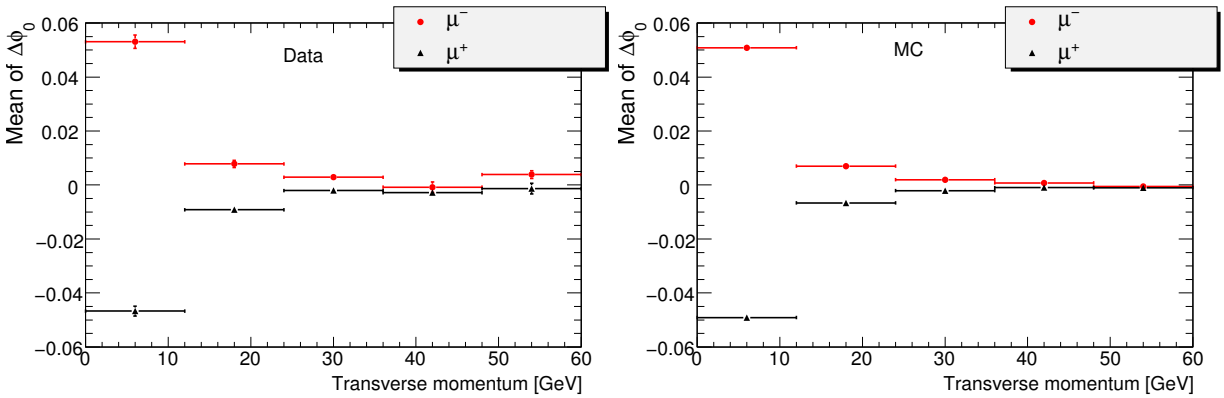

Figure 3.19: Mean of the $\Delta\phi_0$ distribution for positive and negative muons as function of p_{T} for real data sample 1 (left) and MC sample 1 (right).

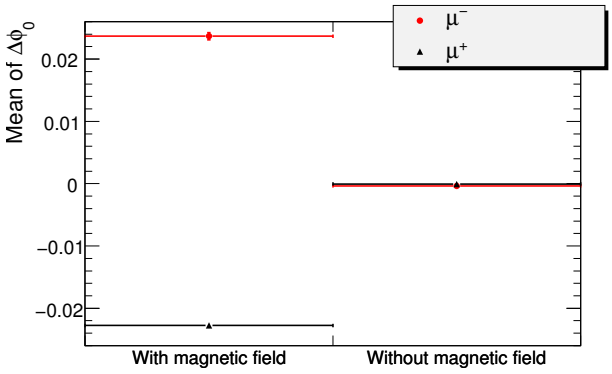

Figure 3.20: Mean of the $\Delta\phi_0$ distribution for positive and negative muons for MC with magnetic field on (MC data sample 1) and for MC with magnetic field off (MC data sample 2).

on the earth surface. Truth particles were accessed through the `INav4MomTruthEvent` container.

The comparison between MC with magnetic field on and off is shown in figure 3.20. Here the means of the $\Delta\phi_0$ for the different charges are obtained in exactly the same way for both MC with magnetic field on and off. This means that the truth particle charge is used for both data samples, so that the difference between them is solely related to the difference in magnetic field configurations.

We see that the charge dependent bias of the $\Delta\phi_0$ distribution vanishes for the MC with magnetic field off. This confirms that the charge dependent bias is due to some systematic effect in extrapolating the muon trajectory through the magnetic field. This could be just that the extrapolation tool uses a somewhat large step length to be able to do the extrapolation relatively fast.

It may seem surprising that the charge dependent bias creates a bias for the total distribution when the biases for positive and negative muons are approximately oppositely equal. It would seem that the biases would cancel. The reason for this is the fact that the number of positive muons is larger than the number of negative ones, as we will come back to in section 3.4.6.

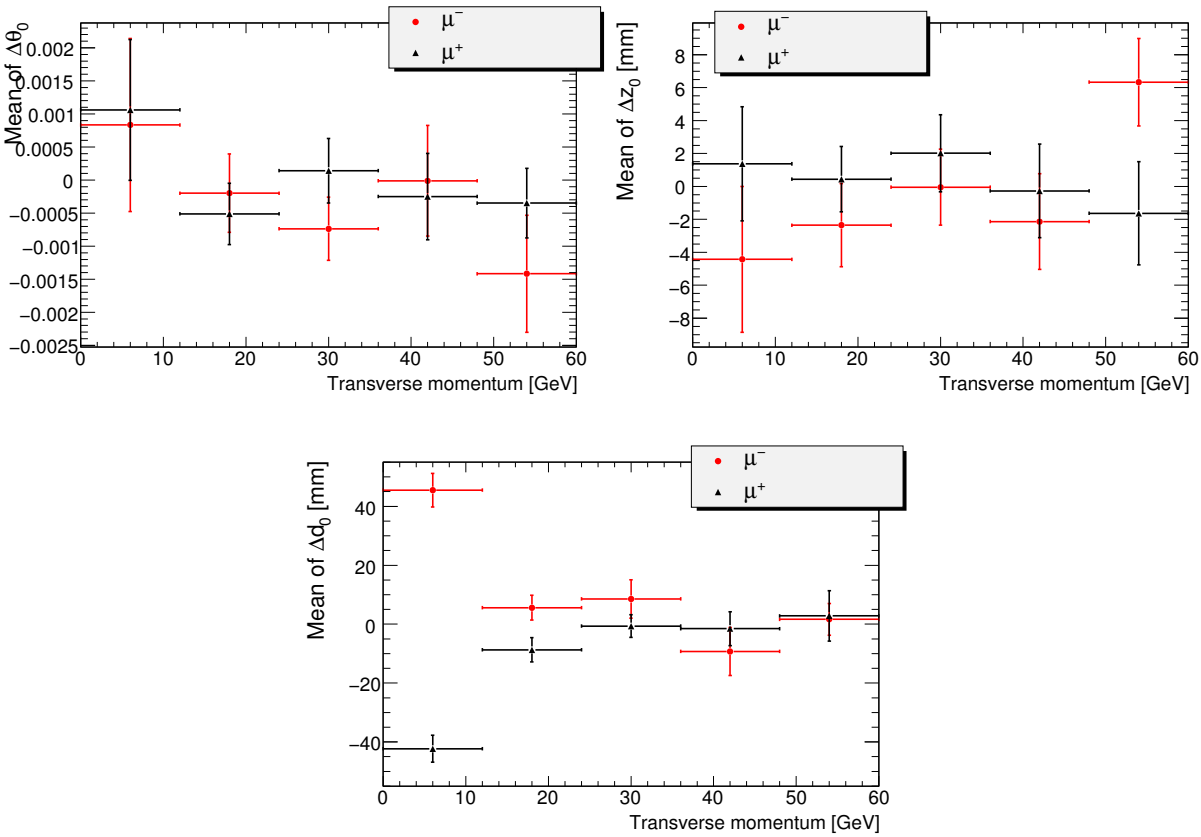

Figure 3.21: Mean of the Δd_0, $\Delta\theta_0$ and Δz_0 distributions for positive and negative muons as function of p_{T} for real data sample 1.

Since the charge dependence of the mean of $\Delta\phi_0$ is related to extrapolation through the solenoidal magnetic field, we would also expect it to be visible in the Δd_0 distribution, since this impact parameter also depends on the transverse projection of the track. We do not expect to see it in the $\Delta\theta_0$ and Δz_0 distributions. The means of Δd_0, $\Delta\theta_0$, and Δz_0 with charge distinction, are shown in figure 3.21. As expected, the charge dependence is visible in the Δd_0 distribution, but not in the $\Delta\theta_0$ or Δz_0 distributions.

The standard deviations of the residual distributions as function of p_{T} were also plotted. These are shown in figure 3.22. The standard deviation increases at small momenta, and this is reproduced by MC, although there seems to be some discrepancy between MC and real data in terms of the absolute numbers. The increased standard deviation at small momenta is probably due to more bending in the magnetic fields and larger effect of multiple scattering.

The error bars on the means and standard deviations in this section were obtained through `TH1::GetMeanError()` and `TH1::GetRMSError()` in ROOT.

Charge mismeasurement rate

We can also study the electric charge as measured in the muon spectrometer and in the inner detector. A comparison was done by looking at the ratio

$$\kappa = \frac{Q_{\text{inner detector}}}{Q_{\text{muon spectrometer}}} = \pm 1. \tag{3.7}$$

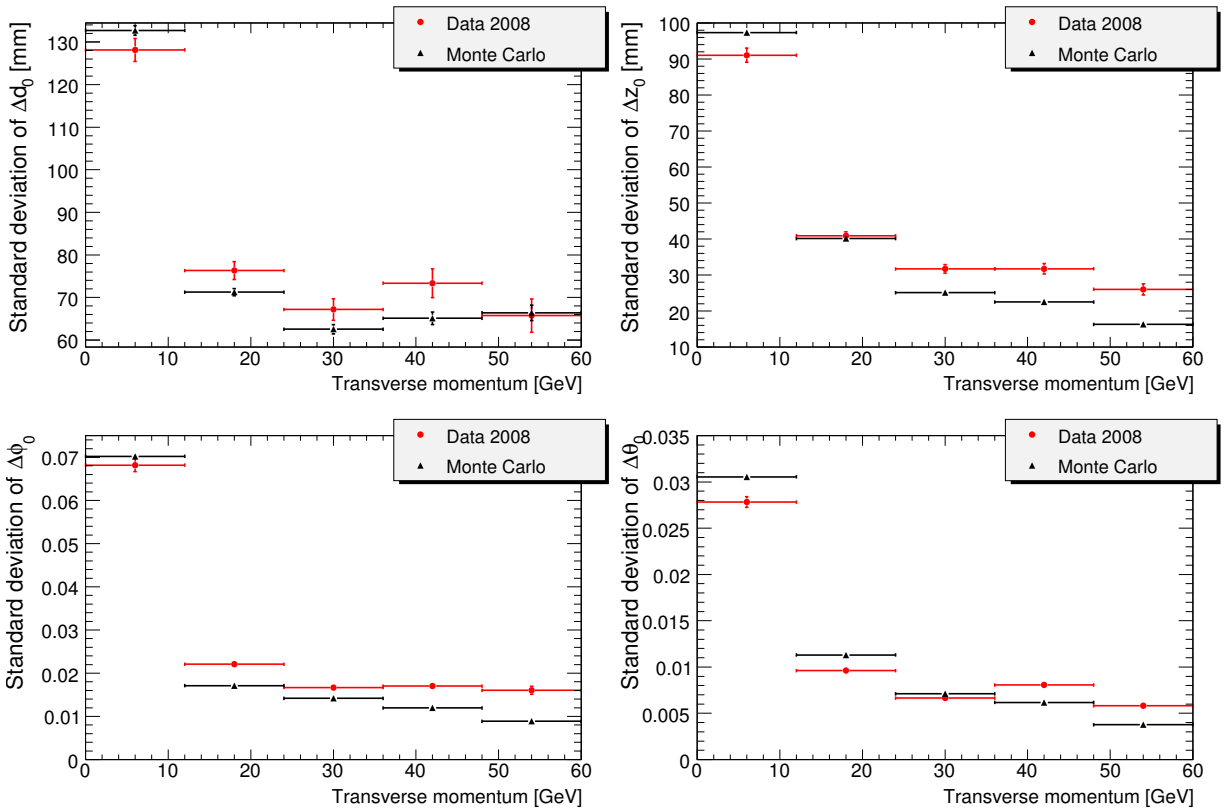

Figure 3.22: Standard deviations of residual distributions obtained from real data sample 1 and MC data sample 1 as function of transverse momentum.

If this ratio is -1, then one of the charge measurements is wrong. If the ratio is $+1$, then the charge measurements are both right or both wrong, but consistent. We define the charge mismeasurement rate as

$$\text{charge mismeasurement rate} = \frac{N(\kappa = -1)}{N(\kappa = -1) + N(\kappa = +1)} \tag{3.8}$$

where $N(\kappa = \pm 1)$ denotes number of muons with $\kappa = \pm 1$. If we assume that the cases where both charge measurements are wrong, are very rare, then the expression (3.8) gives really the precentage of all muons which get a wrong charge measurement. In any case, it gives an idea of how often the charge of a muon is misidentified.

The charge mismeasurement rate as defined in eq. (3.8) is plotted as function of p_{T} for real data sample 1 and MC data sample 1 in figure 3.23. We see here that the charge mismeasurement rate tends to increase as function of the p_{T} (at least for the real data). This is because the tracks curve less for high momentum particles, so that it becomes more difficult to measure the bending, the direction of which gives the charge of the particle.

For the real data, the charge mismeasurement rate ranges from less than one percent at low momenta to a few percent at high momenta.

3.4.6 The muon charge ratio

Cosmic ray showers do not contain equal numbers of positive and negative muons. Because the primary cosmic rays are mostly protons, positive muons dominate in the showers.

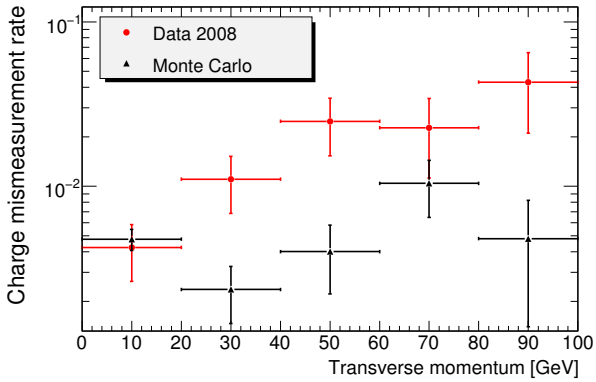

Figure 3.23: The charge mismeasurement rate as defined in eq. (3.8) as function of p_{T} for real data sample 1 and MC data sample 1.

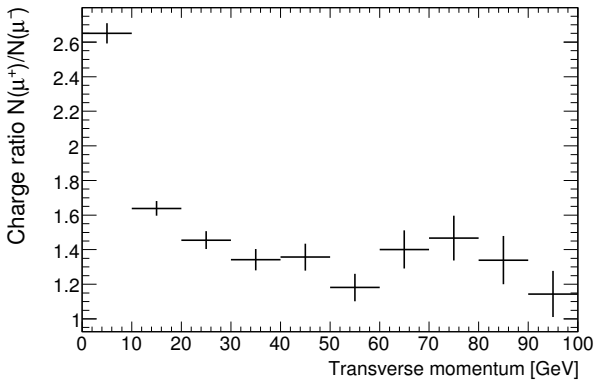

Figure 3.24: The muon charge ratio obtained from real data samples 1 and 2 as function of p_{T}.

Experimentally, the muon charge ratio in cosmic ray showers is

$$R = \frac{N(\mu^+)}{N(\mu^-)} \approx 1.27 \tag{3.9}$$

independent of the muon momentum [10]. Here, $N(\mu^+)$ and $N(\mu^-)$ are the numbers of positive and negative muons respectively.

Figure 3.24 shows the muon charge ratio obtained from real data samples 1 and 2 as function of p_{T}. Note that the RPC ϕ cut has been dropped in producing this plot to increase the statistics, since accurate ϕ measurement is not important here. Here, a momentum dependence is seen. This is related to the geometry of the ATLAS cavern.

Figure 3.5 shows the geometry of the ATLAS cavern. The trajectories of positive and negative muons originating from the big and small shafts in the toroidal magnetic field are shown. We see that:

- of the muons originating from the big shaft, the positive ones are bent into the detector, while the negative ones are bent away,
- of the muons originating from the small shaft, the negative ones are bent into the detector, while the positive ones are bent away.

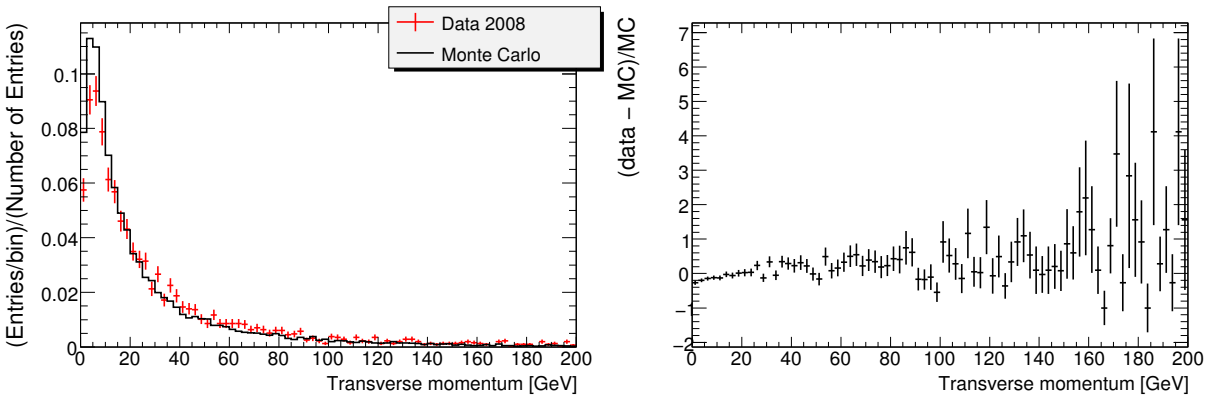

Figure 3.25: The transverse momentum distribution obtained from real data sample 1 and MC data sample 1 (left) and the relative deviation (data – MC)/MC (right).

One can say that the big shaft "favors" positive muons while the small shaft "favors" negative muons. If the shafts were of equal size, this would not affect the charge ratio measured in the detector, but since more muons enter the cavern through the big shaft, positive muons are on average more "favored" than negative ones. This means that the charge ratio R as defined in eq. (3.9) will be larger in the ATLAS detector than on the surface of the earth.

We know, however, that high momentum muons are bent less in the magnetic field. This means that the effect of the toroid field as a "charge selector" will be smaller for higher momenta. This is exactly the p_{T} dependence of the charge ratio seen in figure 3.24. We see that positive muons are favored for small momenta, as expected, and that the charge ratio comes closer to the value at the earth surface for higher momenta.

It should be noted that we have here just a raw distribution of charge measurements in ATLAS. To obtain a measurement of the muon charge ratio R at the earth surface, one would have to correct for the effect of the toroidal magnetic field as "charge selector". Also, effects like charge mismeasurement (section 3.4.5) should be taken into account.

3.4.7 Transverse momentum distribution

Figure 3.25 shows the transverse momentum distribution of muons passing our selection criteria (including the cut on RPC ϕ hits) from real data sample 1 and MC data sample 1, as well as the relative deviation (data – MC)/MC. To be more precise, the content ϵ_i of bin number i in the (data – MC)/MC histogram is calculated as

$$\epsilon_i = \frac{x_i^{\mathrm{data}} - x_i^{\mathrm{MC}}}{x_i^{\mathrm{MC}}} \tag{3.10}$$

where x_i^{MC} and x_i^{data} denote the contents of bin number i in the MC and data histograms respectively.

Real data and MC are seen to agree reasonably well, but the MC distribution shows a shift towards lower momenta compared to the data.

3.4.8 Conclusions

The ATLAS cosmic data is the first real data taken by the ATLAS detector. The performance of the ATLAS detector in searches for various kinds of new physics and mea-

surements of various quantities has been investigated through simulations for a couple of decades. Since also cosmic data taking has been simulated, the cosmic data provide a first possibility to test the actual performance of the ATLAS detector against simulations. The agreement between simulation and real data means in general that the simulation studies of new physics searches etc. with ATLAS can be trusted.

The residual distributions of section 3.4.5 are essentially measures of the track parameter resolution for muons in the ATLAS detector, and the precision of the extrapolation of muons through the detector. That these distributions show close agreement between simulation and real data, shows that the track parameter resolution of the detector is as good as expected from simulation. This is very important for all kinds of studies that will be conducted when the LHC starts. In addition, the close agreement between simulation and data shows that the material of the detector is well known, since this material affects the extrapolation of the muons through the detector.

Although simulation and real data seem to agree well, we have also seen that certain effects are not correctly reproduced by simulation. The $\Delta\phi_0$ and Δd_0 distributions of section 3.4.5 looked fine for the simulated data even without the cut on RPC ϕ hits. The reason for this, is that most of the muons in the simulated data already had at least three RPC ϕ hits, i.e. the distribution of RPC ϕ hits for the cosmic muons was not correctly reproduced by simulation. In this context it should be noted that the configuration of the RPC was not nominal in run 91890 (which was used in the analysis). One sector was not read out at all, and two sectors were read out with non-nominal settings. This could explain the discrepancy in the number of RPC hits between data and simulation.

3.5 Summary

In this section, an analysis of cosmic data taken by ATLAS in 2008 has been presented. The real data has been compared to simulated cosmic data, and it seems that the detector is performing as expected, in particular in terms of muon reconstruction. The precise measurement of muons in the ATLAS detector can contribute to a change in our understanding of the interactions between elementary particles. In the next chapter, the prospects for the discovery of a new charged gauge boson decaying to electrons and muons are evaluated using simulated data.

Chapter 4

Search for W' in lepton and $\not{E}_{\mathrm{T}}$ final state

4.1 Search channel and experimental signature

In this chapter, a search for a heavy, charged gauge boson W' with the ATLAS detector at the LHC using simulated data for $\sqrt{s} = 10\,\mathrm{TeV}$ is presented. The particular W' considered is the SM-like W', which is a carbon copy of the SM W with a larger mass. This means in particular that all the couplings to fermions (vertex factors) are the same as for the SM W (see eq. (1.46)). Furthermore, the decay $W' \to W\,Z$ is forbidden. This is no real BSM model, but rather a benchmark model used to evaluate discovery potentials without considering a particular BSM model.

The decay channels for the SM-like W' are the same as for the SM W. The exception is that an on-shell SM W cannot decay to tb (e.g. $W^+ \to t\,\overline{b}$) since the mass of the top is 171 GeV [4] while the mass of the SM W is 80 GeV. For W' masses above approximately 180 GeV, the additional decay channels $W'^+ \to t\,\overline{b}$ and $W'^- \to \overline{t}\,b$ open up.

In calculating cross sections, the difference between the SM W and the W' will enter through the propagator, which depends on the boson mass. The W boson propagator is [1]

$$D_{\mathrm{F}\alpha\beta} = \frac{-g_{\alpha\beta} + k_\alpha k_\beta / m_W^2}{k^2 - m_W^2 + i\epsilon} \tag{4.1}$$

where k is the 4-momentum transferred by the W boson. The propagator is largest when $k^2 \approx m_W^2$, and the W boson is then said to be on the mass shell. The same is valid for the W' when m_W is replaced by $m_{W'}$.

The search channel considered in this study is $W' \to l\,\nu_l$ where the lepton l is either an electron or a muon. More precisely, the decay channels considered are

$$W'^- \to e^-\,\overline{\nu_e}, \quad W'^+ \to e^+\,\nu_e, \quad W'^- \to \mu^-\,\overline{\nu_\mu}, \quad W'^+ \to \mu^+\,\nu_\mu. \tag{4.2}$$

The experimental signature to look for is thus one high p_{T} lepton and missing transverse energy corresponding to the neutrino (see section 4.1.1). Note that the word lepton will in the following generally be used to refer to the charged lepton, even though the neutrino is of course also a lepton.

A W' may also decay into the τ lepton, but we do not consider this decay channel because the τ decays before reaching the detector, which makes a $W' \to \tau\,\nu_\tau$ study more difficult. The decay of W' into jets, i.e. $W' \to q'\,\overline{q}$ where q and q' are quarks, is another

possible channel. An example of such a decay is $W'^{+} \to u\,\overline{d}$. However, leptons provide a cleaner signature at a hadron collider since there will be a lot of jet activity from various QCD processes. Both the 2 jet channel and the τ channel can be studied, but in this thesis we look only at the electron and muon channels.

4.1.1 The missing transverse energy

At the LHC, the colliding particles are not elementary. A proton consists of three valence quarks, and in high energy collisions, additional quark-anti-quark pairs ("sea quarks") and gluons may be created from the vacuum. The interaction between two colliding protons is really an interaction between the constituent partons (quarks and gluons). In particular, any hard scattering leading to high p_{T} final state particles is an interaction between one parton from one of the protons, and one parton from the other one. This may e.g. be a reaction such as $q\,\overline{q} \to Z \to l^{+}\,l^{-}$ where each initial state quark emerge from one of the colliding protons.

The momenta of the interacting partons are not the full momenta of the colliding protons, but each interacting parton rather takes a momentum fraction $x \in (0, 1)$ of the total momentum of its proton, i.e. it has momentum xp where p is the momentum of the proton. In each collision, for each proton, the momentum fraction x of the colliding parton is a stochastic variable following a probability distribution given by the parton distribution function (PDF) $f(x, q^2)$. Note that the PDF depends on the momentum transfer q of the hard scattering. The different partons have different PDFs, i.e. the function $f(x, q^2)$ looks different for the up quark, the charm quark, and the gluon. The PDFs will also look different if a different hadron than the proton is considered.

When two partons scatter and produce final state particles, the inital state partons, and thus also the final state particles, will have a total momentum

$$p_z = (x_1 - x_2)p \tag{4.3}$$

along the beam axis, where x_1 and x_2 are the momentum fractions of the partons from the two protons. (We have here defined proton 1 to be moving in positive z-direction.) In general $x_1 \neq x_2$, so there is a non-zero total momentum along the beam axis. One can therefore not assume that the total momentum along the beam axis of the final state particles in a proton-proton collision should be zero.

It is, however, a good assumption that the transverse momenta of the interacting partons are small compared to the energy scale of the collision. One can e.g. use the uncertainty principle to get an order of magnitude estimate of the transverse momentum of the partons, using that the proton size is of order 1 fm. One has

$$\Delta x\,\Delta p_x \sim \hbar \quad \Rightarrow \quad \Delta p_x \sim \frac{\hbar}{\Delta x} \approx \frac{0.2\,\mathrm{GeV\,fm}}{1\,\mathrm{fm}} = 0.2\,\mathrm{GeV} \tag{4.4}$$

which is negligible compared to the TeV scale of the collision. Therefore, one can assume that the total momentum in the transverse plane of the final state particles in a proton-proton collision should be zero. This can be used to observe particles which do not interact with the detector, since their existence can be inferred when the total measured final state momentum in the transverse plane is different from zero. One has

$$\sum_{\text{invisible}} \mathbf{p}_{\mathrm{T}} + \sum_{\text{visible}} \mathbf{p}_{\mathrm{T}} = \mathbf{0} \quad \Rightarrow \quad \sum_{\text{invisible}} \mathbf{p}_{\mathrm{T}} = -\sum_{\text{visible}} \mathbf{p}_{\mathrm{T}}, \tag{4.5}$$

therefore the missing transverse momentum, which is supposed to equal the total transverse momentum of invisible particles, is calculated by taking the vector sum of all visible transverse momentum and reversing the sign.

At the LHC, all final state particles will be highly relativistic, since their rest masses are small compared to the energy scale of the collisions. The energy and the magnitude of the momentum for these particles are therefore equal,

$$E = \sqrt{\mathbf{p}^2 + m^2} \approx |\mathbf{p}|\,, \quad |\mathbf{p}| \gg m. \tag{4.6}$$

Most of the measurements of the momenta of final state particles in ATLAS which go into the calculation of the missing transverse momentum, are actually energy measurements from the calorimeters, and therefore the term missing transverse energy is used instead of missing transverse momentum, even though there is physically no such thing as "transverse energy". The missing transverse energy is not constructed *only* from calorimeter measurements. The momenta of any muons must be measured through tracking, since muons are not stopped in the calorimeters.

Missing transverse energy $\not{E}_{\mathrm{T}}$ constitute the only possibility for measuring neutrinos. Within the SM, the neutrinos are the only source of $\not{E}_{\mathrm{T}}$, but in some BSM theories, other sources of $\not{E}_{\mathrm{T}}$ are also present. An example is the lightest supersymmetric particle of supersymmetric models (see section 4.12).

4.1.2 The transverse mass

When searching for a particle decaying to two (or more) visible particles, the invariant mass

$$m = \sqrt{\left(\sum E\right)^2 - \left(\sum \mathbf{p}\right)^2} \tag{4.7}$$

(where the sums run over the decay products) is used. The invariant mass distribution exhibits a peak at the decaying particle's mass (eq. (4.1) leads to resonance for $k^2 \approx m_W^2$). Since the neutrino of the W' decay is only partially reconstructed ($\not{E}_{\mathrm{T}}$), the invariant mass can not be reconstructed.

A much used variable in searches for W' decaying to lepton and neutrino is the transverse mass. We consider an on-shell W' produced at rest and decaying to an electron and a neutrino. The electron and the neutrino can be treated as massless ($m_\nu \ll m_e \ll m_{W'}$). Since the electron and neutrino are both massless we have $p_\nu = E_\nu$ and $p_e = E_e$ where E_e (p_e) and E_ν (p_ν) are the energies (momenta) of the electron and the neutrino respectively. Conservation of momentum requires that the electron and the neutrino go in opposite directions with $p_e = p_\nu$, and we therefore also have $E_e = E_\nu$. Together with conservation of energy,

$$E_e + E_\nu = m_{W'}, \tag{4.8}$$

this gives $E_e = E_\nu = p_e = p_\nu = m_{W'}/2$.

The maximum transverse momentum for the electron is thus $p^e_{\mathrm{T,max}} = m_{W'}/2$. A first definition of the transverse mass could be $m_{\mathrm{T}} = 2p^e_{\mathrm{T}}$, which should exhibit an end point at the W' mass, i.e. the cross section should decrease rapidly for transverse masses above $m_{\mathrm{T}} = m_{W'}$ since this is the largest transverse mass value allowed by an on-shell W'.

With θ as the polar angle of the electron direction of motion, we have

$$m_{\mathrm{T}} = 2p^e_{\mathrm{T}} = 2p_e \sin\theta = m_{W'} \sin\theta. \tag{4.9}$$

Using $\sin^2\theta + \cos^2\theta = 1$, we find the following expression for the differential cross section:

$$\frac{d\sigma}{dm_{\mathrm{T}}} = \frac{d\sigma}{d\cos\theta}\frac{d\cos\theta}{dm_{\mathrm{T}}} \propto \frac{d\sigma}{d\cos\theta}\frac{m_{\mathrm{T}}}{\sqrt{m_{W'}^2 - m_{\mathrm{T}}^2}}. \tag{4.10}$$

The differential cross section should therefore increase towards the end point at $m_{\mathrm{T}} = m_{W'}$, and is said to have a Jacobian peak there.

Since the momenta of the neutrino and the electron are equal (but opposite), we may write the transverse mass as $m_{\mathrm{T}} = \sqrt{4p_{\mathrm{T}}^{e\,2}} = \sqrt{4p_{\mathrm{T}}^e p_{\mathrm{T}}^\nu}$. The transverse momentum of the electron is experimentally measured as its energy deposit in the electromagnetic calorimeter multiplied by $\sin\theta$, and therefore denoted E_{T}. The transverse momentum of the neutrino is meausured as the missing transverse energy $\not{E}_{\mathrm{T}}$. Of course, the missing transverse energy may stem also from other sources than the neutrino, other neutrinos, or mismeasurements. If we want to attribute the $\not{E}_{\mathrm{T}}$ to our neutrino, we should therefore require that it is more or less in the opposite direction of the electron. We thus arrive at an experimentally efficient transverse mass,

$$m_{\mathrm{T}} = \sqrt{2E_{\mathrm{T}}^e \not{E}_{\mathrm{T}}(1 - \cos\Delta\phi_{e,\not{E}_{\mathrm{T}}})}\,, \tag{4.11}$$

where $\Delta\phi_{e,\not{E}_{\mathrm{T}}}$ is the azimuthal angle between the direction of the electron and the direction of the $\not{E}_{\mathrm{T}}$. Note that the factor $(1-\cos\Delta\phi_{e,\not{E}_{\mathrm{T}}}) \in [0,2]$ takes the maximum value 2 when the electron and the $\not{E}_{\mathrm{T}}$ are oppositely directed.

The above considerations apply equally well for W' decaying to muon and neutrino. The transverse mass for muon events is defined analogously,

$$m_{\mathrm{T}} = \sqrt{2p_{\mathrm{T}}^\mu \not{E}_{\mathrm{T}}(1 - \cos\Delta\phi_{\mu,\not{E}_{\mathrm{T}}})}\,, \tag{4.12}$$

where p_{T}^μ is the transverse momentum of the muon. (Here we write p_{T} instead of E_{T} since the momentum of the muon is measured through tracking.)

4.1.3 Relation to the invariant mass

In section 4.1.2, we made plausible the definition

$$m_{\mathrm{T}} = \sqrt{2p_{\mathrm{T}}^l p_{\mathrm{T}}^\nu(1 - \cos\Delta\phi_{l,\nu})} \tag{4.13}$$

for the transverse mass, accentuating the relation to the lepton p_{T} for a W or W' boson produced at rest, at least in the transverse plane. A SM W boson can be produced with significant transverse momentum at the LHC. For the simple definition $m_{\mathrm{T}} = 2p_{\mathrm{T}}$, this could lead to a transverse mass greater than the W invariant mass (invariant mass of the lepton-neutrino pair). We will now show that the definition (4.13) implies $m_{\mathrm{T}} \leq m$ where m is the invariant mass of the decaying particle, so that we are "safe" from overestimating the mass in the case of a boosted W or W'.

The mass of the decaying particle satisfies (for massless decay products)

$$m^2 = \left(|\mathbf{p}^l| + |\mathbf{p}^\nu|\right)^2 - \left(\mathbf{p}^l + \mathbf{p}^\nu\right)^2. \tag{4.14}$$

Analogously, the transverse mass can be written as

$$m_{\mathrm{T}}^2 = \left(|\mathbf{p}_{\mathrm{T}}^l| + |\mathbf{p}_{\mathrm{T}}^\nu|\right)^2 - \left(\mathbf{p}_{\mathrm{T}}^l + \mathbf{p}_{\mathrm{T}}^\nu\right)^2. \tag{4.15}$$

The equivalence of equations (4.13) and (4.15) is easily derived using

$$\mathbf{p}_{\mathrm{T}}^{l} \cdot \mathbf{p}_{\mathrm{T}}^{\nu} = \left|\mathbf{p}_{\mathrm{T}}^{l}\right| \left|\mathbf{p}_{\mathrm{T}}^{\nu}\right| \cos \Delta\phi_{l,\nu}. \tag{4.16}$$

From equations (4.14) and (4.15), some vector algebra leads to the relation

$$m^2 = m_{\mathrm{T}}^2 + 2\left(\left|\mathbf{p}^{l}\right| \left|\mathbf{p}^{\nu}\right| - \left|\mathbf{p}_{\mathrm{T}}^{l}\right| \left|\mathbf{p}_{\mathrm{T}}^{\nu}\right| - p_z^l p_z^\nu\right). \tag{4.17}$$

We must show that the quantity in brackets is always greater than or equal to zero. We write it in terms of the polar angles and use a trigonometric identity:

$$\begin{aligned} \left|\mathbf{p}^{l}\right| \left|\mathbf{p}^{\nu}\right| - \left|\mathbf{p}_{\mathrm{T}}^{l}\right| \left|\mathbf{p}_{\mathrm{T}}^{\nu}\right| - p_z^l p_z^\nu &= \left|\mathbf{p}^{l}\right| \left|\mathbf{p}^{\nu}\right| (1 - \sin\theta_l \sin\theta_\nu - \cos\theta_l \cos\theta_\nu) \\ &= \left|\mathbf{p}^{l}\right| \left|\mathbf{p}^{\nu}\right| [1 - \cos(\theta_l - \theta_\nu)] \geq 0. \end{aligned} \tag{4.18}$$

We have thus $m_{\mathrm{T}} \leq m$, so the end point of the transverse mass distribution stays at the particle mass, regardless of any boost of the particle. We see that $m_{\mathrm{T}} = m$ when the lepton and neutrino are emitted with the same polar angle, $\theta_l = \theta_\nu$. We identify one special case, $\theta_l = \theta_\nu = \pi/2$ (only transverse motion). In this case $m = m_{\mathrm{T}}$ obviously holds since $\mathbf{p}_{\mathrm{T}} = \mathbf{p}$.

4.2 W' production in pp-collisions

The production of a SM-like W' in proton-proton collisions happens through the $q'\,\overline{q}\,W'$ vertex where q and q' are quarks. If q' is an up-type quark, then q is a down-type quark. The non-generation-mixing production reactions for the W' are

$$\begin{aligned} u\,\overline{d} \to W'^{+}, \quad c\,\overline{s} \to W'^{+}, \quad t\,\overline{b} \to W'^{+}, \\ \overline{u}\,d \to W'^{-}, \quad \overline{c}\,s \to W'^{-}, \quad \overline{t}\,b \to W'^{-}. \end{aligned} \tag{4.19}$$

In addition, generation mixing vertices exist. A few examples are

$$u\,\overline{s} \to W'^{+}, \quad u\,\overline{b} \to W'^{+}, \quad \overline{c}\,b \to W'^{-}. \tag{4.20}$$

These vertices arise from the fact that the flavor- and mass quantum mechanical eigenstates for the quarks are not the same. As mentioned in section 1.5, these vertices are suppressed by the smallness of the off-diagonal elements of a 3×3 matrix known as the CKM matrix. (Note that this is true for the SM W boson, and therefore also for the SM-like W'.)

Two Feynman diagrams showing the production and decay of the W' are shown in figure 4.1. The total W' production cross section in pp collisions is dominated by the fusion of light (u and d) quarks.

CompHEP [15] is a program for calculating cross sections and decay widths at tree level. One can edit the Lagrangian used by CompHEP, and thereby add e.g. a SM-like W'. Here, models with a SM-like W' with different masses are used, and with the W' width as the SM W width scaled to the mass of the W', i.e.

$$\Gamma_{W'} = \frac{m_{W'}}{m_W} \Gamma_W. \tag{4.21}$$

The differential cross section $d\sigma/dm_{\mathrm{T}}$ for $d\,\overline{u} \to W'^{-} \to e^{-}\,\overline{\nu_e}$ in pp collisions at $\sqrt{s} = 10\,\mathrm{TeV}$ calculated by CompHEP for a $2\,\mathrm{TeV}$ W' is shown in figure 4.2. Here, the

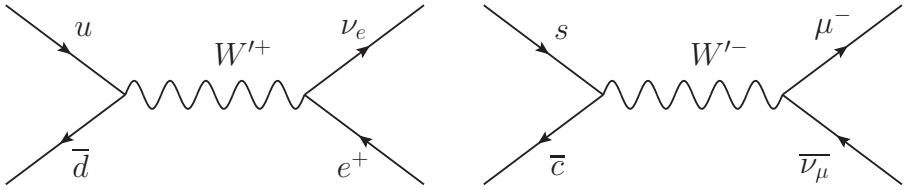

Figure 4.1: Feynman diagrams showing the production of a W' and its subsequent decay to the lepton and neutrino final state.

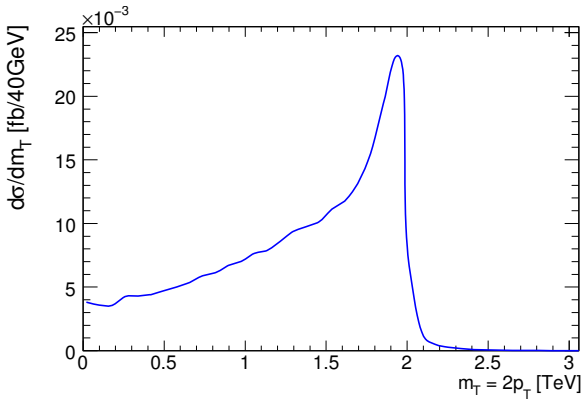

Figure 4.2: The differential cross section $d\sigma/dm_{\mathrm{T}}$ for $d\,\overline{u} \to W'^{-} \to e^-\,\overline{\nu_e}$ in pp collisions at $\sqrt{s} = 10\,\mathrm{TeV}$ as calculated by CompHEP.

simple definition $m_{\mathrm{T}} = 2p_{\mathrm{T}}$ is used, where p_{T} is the transverse momentum of the electron. The Jacobian peak at $m_{\mathrm{T}} = 2\,\mathrm{TeV}$ is clearly seen. For $m_{\mathrm{T}} > m_{W'}$, the cross section decreases rapidly, since the W' then goes off the mass shell.

Figure 4.3 shows the total cross section for $d\,\overline{u} \to W'^{-} \to e^-\,\overline{\nu_e}$ in pp collisions at $\sqrt{s} = 10\,\mathrm{TeV}$ calculated by CompHEP as function of the W' mass. We see that the cross section decreases rapidly (exponentially) as function of the W' mass.

The total cross section for any process in pp collisions is given by an integral over the parton distribution functions. We have [17]

$$\sigma = \int_0^1 dx_1 \int_0^1 dx_2\, f_1(x_1, q^2) f_2(x_2, q^2) \hat{\sigma}(x_1, x_2) \tag{4.22}$$

where f_1 and f_2 are the PDFs of the interacting partons and $\hat{\sigma}$ is the hard scattering cross section (i.e. the cross section at parton level). If one wants the cross section for a given final state, then one must in addition sum over all possible parton level processes giving this final state. Note that the function $f_i(x, q^2)$ is normalized in such a way that it includes the probability of getting the parton type i from the proton (the total probability of getting a u quark will be different from that of getting a gluon, etc.). The parton distribution functions for sea quarks, gluons and valence quarks are shown for low energy and extrapolated to LHC energies in figure 4.4 (taken from ref. [16]). We see for example that the gluon becomes very important at low momentum fractions when going to LHC energies.

If we consider the process $d\,\overline{u} \to W'^{-} \to e^-\,\overline{\nu_e}$ as above, then the partons 1 and 2 are the d and $\overline{u}$ quarks. The hard scattering cross section for this process is largest when the

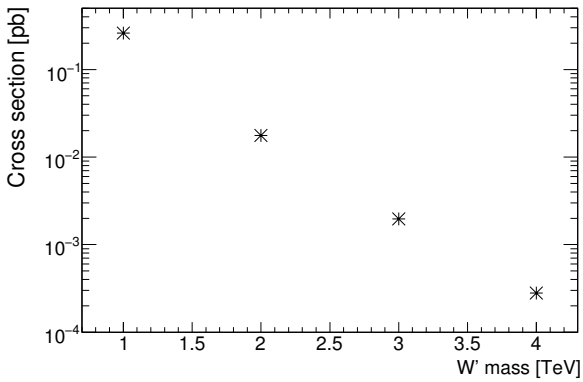

Figure 4.3: The total cross section for $d\,\overline{u} \to W'^{-} \to e^{-}\,\overline{\nu_e}$ in pp collisions at $\sqrt{s} = 10\,\text{TeV}$, calculated by CompHEP, as function of the W' mass.

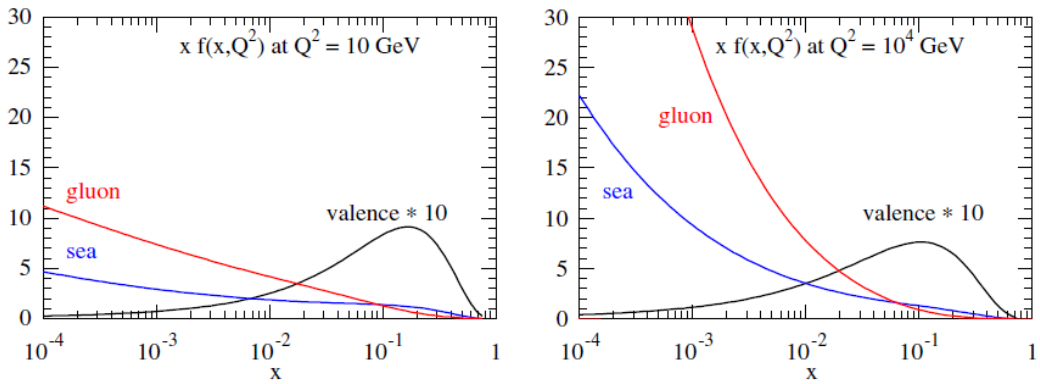

Figure 4.4: Parton distribution functions for the proton for low energy scale (left) and extrapolated to LHC energies (right). (From ref. [16].)

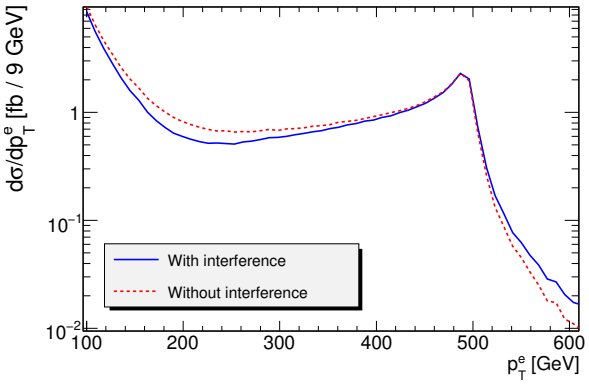

Figure 4.5: The differential cross section $d\sigma/dp_{\mathrm{T}}$ for the process $d\,\overline{u} \to e^+\,\nu_e$ in 10 TeV pp collisions as calculated by CompHEP within the SM-like W' model ($m_{W'} = 1.0\,\mathrm{TeV}$) with and without the interference terms.

invariant mass of the system of the two interacting partons is close to the W' mass (see eq. 4.1). The invariant mass of the two parton system is

$$\begin{aligned} m(x_1, x_2) &= \sqrt{(E_1 + E_2)^2 - (\mathbf{p}_1 + \mathbf{p}_2)^2} \\ &= \sqrt{[(x_1 + x_2)p]^2 - [(x_1 - x_2)p]^2} \\ &= \sqrt{x_1 x_2 s} \end{aligned} \tag{4.23}$$

where $p = \sqrt{s}/2$ is the momentum of the each of the colliding protons and s is the proton-proton center of mass energy squared. The higher the invariant mass of the two parton interaction, the higher the values of x_1 and x_2, the smaller the probability densities $f_1(x_1, q^2)$ and $f_2(x_2, q^2)$.

4.2.1 Interference terms

When calculating the cross section at parton level for a process such as $u\,\overline{d} \to e^+\,\nu_e$ in a model with a SM-like W', the Feynman diagram of figure 4.1 contributes as well as the corresponding diagram with the W' replaced by a SM W. The absolute square of the Feynman amplitude, which enters the cross section calculation, takes the form

$$|\mathcal{M}_W + \mathcal{M}_{W'}|^2 = |\mathcal{M}_W|^2 + |\mathcal{M}_{W'}|^2 + \mathcal{M}_W \mathcal{M}^*_{W'} + \mathcal{M}^*_W \mathcal{M}_{W'} \tag{4.24}$$

where $\mathcal{M}_W$ ($\mathcal{M}_{W'}$) is the Feynman amplitude corresponding to W (W') exchange. The last two terms are called interference terms. Because of these terms, the cross section can not be seen simply as a sum of W and W' contributions.

The last three terms of equation (4.24) all correspond to changes from the SM cross section, and thus constitute signal in a statistical sense. The signal W' samples to be used in this study, which are generated with the event generator Pythia [20], do not include any interference with the SM W for the simplicity of the event generation.

Figure 4.5 shows the differential cross section $d\sigma/dp^e_{\mathrm{T}}$ for the process $d\,\overline{u} \to e^+\,\nu_e$ in 10 TeV pp collisions as calculated by CompHEP within the SM-like W' model with and without the interference terms for a 1.0 TeV W'. We see that the interference terms give a negative contribution decreasing the cross section below the W' peak, while the contribution is positive above the peak. This agrees with the results presented in [18], where the effect of W/W' interference in single top production is investigated.

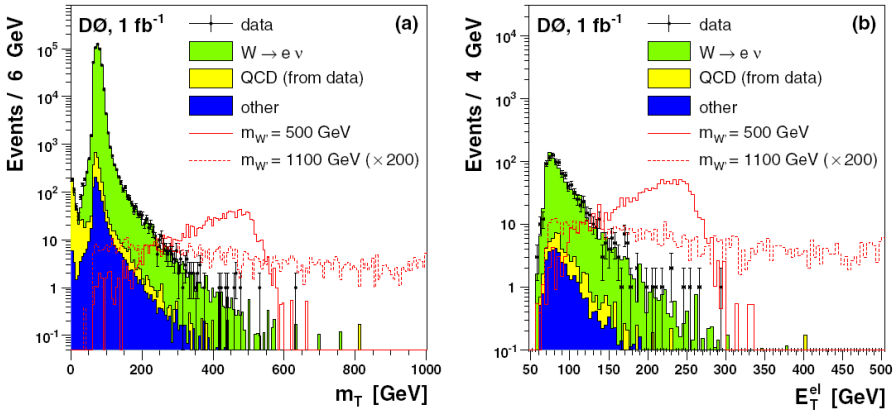

Figure 4.6: Transverse mass and electron transverse energy distributions from the DØ study of the electron plus missing transverse energy final state together with MC predictions.

4.3 Tevatron results on W'

A search for a new charged gauge boson W' decaying to electron and neutrino has been performed by the DØ collaboration using $p\overline{p}$ data with $\sqrt{s} = 1.96\,\text{TeV}$ corresponding to an integrated luminosity of $1\,\text{fb}^{-1}$ [19]. The distributions obtained for the transverse mass (defined as in this thesis) and the electron transverse energy after cuts are shown together with MC predictions in figure 4.6.

The QCD background has been estimated from the data. The spectrum has been scaled to fit the MC prediction in the W peak region $60\,\text{GeV} < m_\text{T} < 140\,\text{GeV}$.

No significant excess of events at high transverse mass or high E^e_T is observed. The DØ collaboration puts a lower limit with 95% confidence level on the SM-like W' mass, $m_{W'} > 1.00\,\text{TeV}$.

4.4 SM backgrounds

We want to perform a search for the SM-like W' decaying to lepton and neutrino. Our experimental signature is one high p_T lepton and missing transverse energy. We now need to find out which other processes can produce this final state, and thus possibly mimic a W' signal.

4.4.1 SM W boson

The Feynman diagrams of figure 4.1 can of course also be drawn with the SM W in place of the W'. The W can therefore produce exactly the same final state as the W'. We will be looking for W' at high values of the transverse mass. For the W to produce events in the signal region, it must be far off the mass shell. The W mass is $m_W = 80.4\,\text{GeV}$ [4], while we will be looking for signals above 1 TeV (the Tevatron limit).

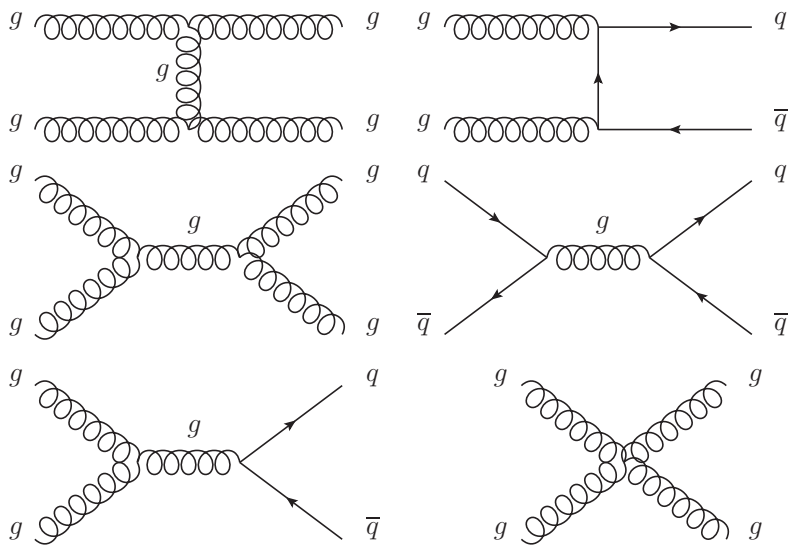

Figure 4.7: Some Feynman diagrams for strong dijet production in pp collisions.

4.4.2 QCD dijets

As mentioned in section 1.4, the strong force becomes stronger at lower energy or larger distances, a phenomenon known as confinement. A colored object, a quark or a gluon, can therefore not exist as a single particle, but is always bound inside a color neutral hadron. In high energy collisions, a quark or a gluon may be produced with high momentum. The strong force will not allow it to escape by itself, so the result is a collection of hadrons all moving in approximately the same direction as the initial quark or gluon. This is known as a jet.

In hadron collisions, the cross section for dijet production is large, because it may proceed through the strong interaction. Some Feynman diagrams for strong interaction dijet production are shown in figure 4.7.

Hadrons in a jet may decay leptonically, for example pions and kaons decay to muons (see section 3.1), or a lepton may be wrongly reconstructed from a jet. Electrons may appear in reconstruction because charged hadrons interact in the electromagnetic calorimeter and also provide inner detector tracks. Muons may appear if a high momentum jet has "punched through" the calorimeters and made tracks in the muon spectrometer. In addition, $\not{E}_{\mathrm{T}}$ may arise from mismeasurements or neutrinos from leptonic decays. Dijets may thus contribute to the lepton and $\not{E}_{\mathrm{T}}$ final state, and because of the large cross section, this contribution should be examined.

4.4.3 Top quark pairs

The top quark is the heaviest discovered particle of the SM with a mass $m_t = 171\,\mathrm{GeV}$ [4]. Top quark pair production will have a relatively high cross section at the LHC. The top quark decays mainly through $t \to W\,b$. The bottom quark gives a b-jet. The W may decay hadronically, giving jets, or leptonically. If the W boson from one of the top quarks decays into an electron or a muon $W \to l\,\nu_l$, and the W from the other top decays hadronically, we get our one lepton and $\not{E}_{\mathrm{T}}$ (neutrino) final state.

Feynman diagrams for the strong production of $t\bar{t}$ pairs in pp collisions are shown in

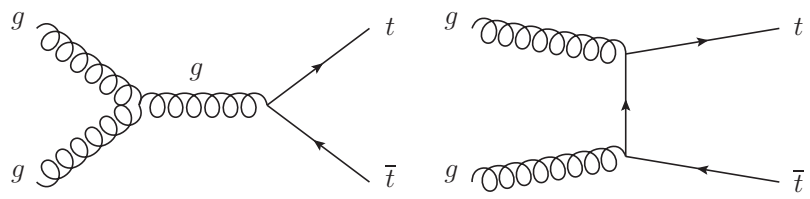

Figure 4.8: Feynman diagrams for the strong production of $t\overline{t}$ pairs in pp collisions. The quark fusion diagram is shown in figure 4.9.

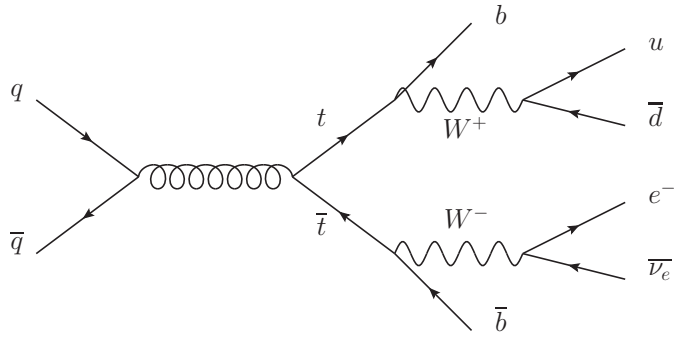

Figure 4.9: The strong production of a $t\overline{t}$ pair and the subsequent decays giving the one lepton and $\not{E}_{\mathrm{T}}$ final state.

figure 4.8. Figure 4.9 shows the strong production of a $t\overline{t}$ pair and the subsequent decays into the one lepton and $\not{E}_{\mathrm{T}}$ final state.

4.4.4 Dibosons

Diboson production is the production of two SM gauge bosons, such as WZ, $W\gamma$, $Z\gamma$, WW or ZZ. Various decays of these gauge boson pairs may give the one lepton and $\not{E}_{\mathrm{T}}$ final state, such as e.g. $W\gamma \to l\,\nu_l\,\gamma$, $WZ \to l\,\nu_l\,\nu\,\overline{\nu}$, and $WW \to l\,\nu_l\,q'\,\overline{q}$.

Some Feynman diagrams for diboson production in pp collisions are shown in figure 4.10.

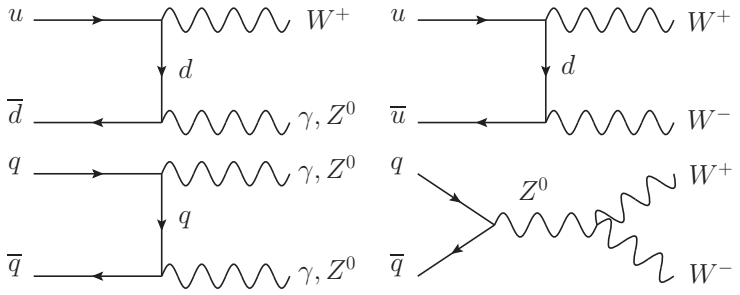

Figure 4.10: Some Feynman diagrams for diboson production in pp collisions.

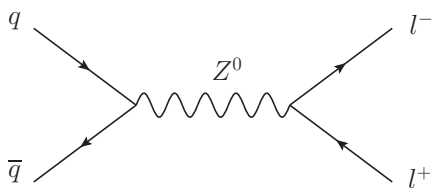

Figure 4.11: Feynman diagram for Z production and leptonic decay in pp collisions.

4.4.5 SM Z boson

SM Z^0 bosons may produce high p_{T} leptons through the Feynman diagram of figure 4.11. We get two leptons, but if one of these leptons does not meet our lepton selection criteria, or if it is not reconstructed at all, then the Z may lead to a measured one lepton and $\not{E}_{\mathrm{T}}$ final state, since missing transverse energy may arise from mismeasurements.

The muon case can be especially dangerous if one of the muons is not reconstructed at all. The lost muon will then show up as $\not{E}_{\mathrm{T}}$ pointing in the opposite direction of the measured muon, balancing its momentum, which is exactly the W' signature (see section 4.12). The same goes for electrons if one of the electrons hits a gap in the calorimeter coverage, but a misidentified electron is not so problematic, since its momentum will still be taken into account when calculating $\not{E}_{\mathrm{T}}$ as long as the electron has hit the calorimeters.

The Z^0 boson must be off-shell or produced with significant transverse momentum to produce leptons with p_{T} corresponding to our search region, since its mass is $m_Z = 91.19\,\mathrm{GeV}$ [4].

4.5 Monte Carlo simulation

MC simulation for ATLAS is done in two steps: event generation and detector simulation. First, events are generated using an event generator such as Pythia or MC@NLO [21]. Here, the simulation of the dynamics of the collision is made, and the result is a set of final state particles. These particles are then propagated through the ATLAS detector using GEANT. The particles' interactions with the detector are then translated into simulated raw data in the digitization step. The simulated raw data are finally passed to reconstruction in the same way as real data.

One could in principle imagine implementing a given physics model, and then simply generating without constraints events corresponding to a given integrated luminosity. This would result in a data sample resembling a real data sample of the same integrated luminosity, containing all kinds of events. This is not practically possible because of the huge number of events this would correspond to.

What is instead done, is that certain kinds of events of interest are generated. One dataset then contains one specific kind of events, e.g. $t\bar{t}$ events or dijet events, often also with specific kinematical constraints. For a simulation study of a given final state, one then uses only datasets that are expected to contribute to this final state. To obtain a distribution as it is expected to appear in real data with a given integrated luminosity, all relevant datasets must be scaled according to their cross section and their contributions added.

Consider a process with cross section σ. Assume that we have a data sample with N_{gen} generated events, and that we want to obtain the expected distribution of any variable x

for the process given an integrated luminosity $\int L\,dt$. We must then make a histogram of x from the generated events and scale it with a factor k satisfying

$$kN_{\text{gen}} = N_{\text{exp}} = \sigma \int L\,dt \tag{4.25}$$

where N_{exp} is the number of expected events. The scale factor is thus

$$k = \frac{\sigma}{N_{\text{gen}}} \int L\,dt. \tag{4.26}$$

The cross section of the process is calculated by the event generator.

4.6 Datasets and cross sections

Since the cross section for SM W production decreases exponentially after the Jacobian peak at $m_{\text{T}} \approx 80\,\text{GeV}$, generating W events without kinematical constraints requires generating an enormous amount of events to obtain good statistics in the high m_{T} signal region. Therefore, W events have been generated with two different cuts on the W invariant mass (invariant mass of the lepton-neutrino system), $200\,\text{GeV} < m_{l\nu} < 500\,\text{GeV}$ and $m_{l\nu} > 500\,\text{GeV}$. The cross section used for such a dataset is of course

$$\sigma = \int_{m_{l\nu}^{\min}}^{m_{l\nu}^{\max}} \frac{d\sigma}{dm_{l\nu}}\,dm_{l\nu} \tag{4.27}$$

which in both cases is orders of magnitude smaller than the total W cross section. SM Z samples used have a cut $m_{ll} > 200\,\text{GeV}$ where m_{ll} is the dilepton invariant mass.

Similar considerations apply to dijet production. To obtain good statistics for hard jets without generating billions of softer jets, events must be generated with different kinematical constraints. In the dijet case, the cut is made on the transverse momentum $\hat{p}_{\text{T}}$ of each parton in the two parton center of mass frame. The datasets J0 to J8 have $\hat{p}_{\text{T}}$ cuts ranging from 8 GeV to 2.24 TeV. The datasets do not overlap, in the sense that $\hat{p}_{\text{T}}$ has upper limits in each dataset J0 to J7 corresponding to the lower limit in the next dataset.

We do not expect the W to contribute significantly to the signal region when $m_{l\nu} < 200\,\text{GeV}$. It could, however, contribute because of the large cross section for on-shell W production and the possibility of mismeasurements. For completeness, it would therefore be good to include also a W sample with $m_{l\nu} < 200\,\text{GeV}$. For this purpose, a bulk W sample (with no cut on $m_{l\nu}$) was used, and the cut $m_{l\nu} < 200\,\text{GeV}$ was made in the analysis code. The invariant mass of the W is reconstructed from the truth information about the lepton and the neutrino with the W as "mother". To verify the correctness of the implementation, histograms of the invariant mass $m_{l\nu}$ for the two W samples described above were made, and $m_{l\nu}$ fell exactly in the regions corresponding to the cut in the event generation (see figure 4.12).

For the scale factor of the low mass data sample, the total cross section and the total number of generated events was used (see eq. 4.26), which is equivalent to using the cross section

$$\sigma = \int_{0}^{200\,\text{GeV}} \frac{d\sigma}{dm_{l\nu}}\,dm_{l\nu} \tag{4.28}$$

and the number of events passing the $m_{l\nu} < 200\,\text{GeV}$ cut.

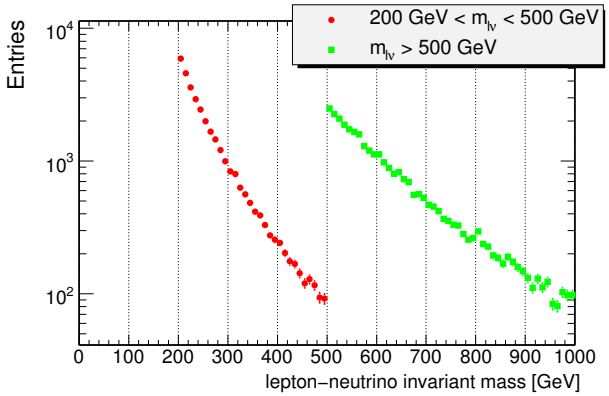

Figure 4.12: Invariant mass distributions obtained for the W boson for the two W samples with different generator level mass cuts. The plot verifies the correctness of the calculation of the true lepton-neutrino invariant mass.

The signal samples contain W' of different masses decaying to lepton and neutrino, where lepton also includes τ. The $t\bar{t}$ sample contains only events in which at least one of the Ws from the top quarks decays leptonically. The diboson samples used are also filtered to include at least one lepton. All datasets and cross sections used are shown in tables 4.1 and 4.2. The cross sections have been obtained from AMI[1]. To the extent possible the `r808_r838`[2] reconstruction tags are used for all datasets, but if a dataset is not available with this tag, an older tag is used. The cuts referred to in table 4.2 are

1. $200\,\text{GeV} < m_{l\nu} < 500\,\text{GeV}$,
2. $m_{l\nu} > 500\,\text{GeV}$,
3. $m_{ll} > 200\,\text{GeV}$.

Note also that the $t\bar{t}$ events are generated with the event generator MC@NLO, and come therefore with weights ± 1. This is because the distributions are calculated as sums of different separately finite contributions where some contributions may be negative [21]. With the exception of $t\bar{t}$, all cross sections are calculated to leading order.

4.7 Trigger

The concept of the trigger was briefly introduced in section 2.3.5. The trigger is the system that determines, for each event, whether to keep the data from this event, since recording all events is not feasible in terms of bandwidth and data storage. The trigger therefore needs to quickly identify objects which could identify an event as "interesting". The trigger consists of three levels, level 1, level 2, and the event filter, with increasingly complex algorithms and decreasing rates. The trigger menu is the collection of all triggers used.

The ATLAS simulation includes simulation of the trigger system. This means that, for each event, the trigger decision is stored in the output data. When analysing the

[1] AMI [22] is the ATLAS Metadata Interface, which gives the user access to information about ATLAS datasets.

[2] This tag corresponds to datasets reconstructed with Athena release 15.3.1.6.

Process	Run no.	Recon. tag	MC events	Cross section [fb]
$W' \to l\,\nu_l$, 1.0 TeV	105610	r808_r838	$60 \cdot 10^3$	4678
$W' \to l\,\nu_l$, 1.5 TeV	105626	r808_r838	$35 \cdot 10^3$	720.6
$W' \to l\,\nu_l$, 2.0 TeV	105611	r808_r838	$20 \cdot 10^3$	155.4
$W' \to l\,\nu_l$, 2.5 TeV	105662	r808_r838	$20 \cdot 10^3$	39.8
$W' \to l\,\nu_l$, 3.0 TeV	105663	r808_r838	$20 \cdot 10^3$	11.7
$W' \to l\,\nu_l$, 3.5 TeV	105664	r808_r838	$20 \cdot 10^3$	4.02

Table 4.1: Signal samples used in the W' search analysis. For the cases where a generator level event selection is made, the cross section quoted is $\sigma \times \epsilon$ where ϵ is the generator level selection efficiency.

Process	Run no.	Recon. tag	MC events	Cross section [fb]
$t\,\bar{t} \to l + X$	105200	r808_r838	$1.7 \cdot 10^6$	$205.5 \cdot 10^3$
Dijets J0	105009	r808_r838	$1.0 \cdot 10^6$	$1.17 \cdot 10^{13}$
Dijets J1	105010	r808_r838	$0.99 \cdot 10^6$	$8.67 \cdot 10^{11}$
Dijets J2	105011	r808_r838	$0.94 \cdot 10^6$	$5.60 \cdot 10^{10}$
Dijets J3	105012	r808_r838	$1.4 \cdot 10^6$	$3.28 \cdot 10^9$
Dijets J4	105013	r808_r838	$1.0 \cdot 10^6$	$1.52 \cdot 10^8$
Dijets J5	105014	r808_r838	$1.2 \cdot 10^6$	$5.12 \cdot 10^6$
Dijets J6	105015	r808_r838	$0.39 \cdot 10^6$	$1.12 \cdot 10^5$
Dijets J7	105016	r808_r838	$0.37 \cdot 10^6$	$1.08 \cdot 10^3$
Dijets J8	105017	r586	$0.37 \cdot 10^6$	1.11
$W \to e\,\nu_e$	106020	r809_r838	$5.1 \cdot 10^6$	$10.35 \cdot 10^6$
$W \to \mu\,\nu_\mu$	106021	r808_r838	$5.0 \cdot 10^6$	$10.35 \cdot 10^6$
$W \to l\,\nu_l$, cut 1	106604	r808_r838	$50 \cdot 10^3$	12705.8
$W \to l\,\nu_l$, cut 2	106605	r808_r838	$50 \cdot 10^3$	405.1
$Z \to e^+\,e^-$, cut 3	105121	r808_r838	$15 \cdot 10^3$	1622
$Z \to \mu^+\,\mu^-$, cut 3	105122	r808_r838	$15 \cdot 10^3$	1621
$WW \to l + X$	105985	r808_r838	$50 \cdot 10^3$	$15.61 \cdot 10^3$
$WZ \to l + X$	105987	r808_r838	$1.0 \cdot 10^5$	$4.87 \cdot 10^3$
$ZZ \to l + X$	105986	r808_r838	$50 \cdot 10^3$	$1.36 \cdot 10^3$
$Z\gamma \to l\,l\,\gamma$	105120	r808_r838	$24 \cdot 10^3$	$11.09 \cdot 10^3$
$W\gamma \to l\,\nu_l\,\gamma$	006540	r474	$80 \cdot 10^3$	$52.32 \cdot 10^3$

Table 4.2: Background samples used in the W' search analysis. Note that number of MC events quoted for the $t\bar{t}$ sample is $n_+ - n_-$ where n_+ (n_-) is the number of events with positive (negative) weights. The total number of events for this sample is $n_+ + n_- = 2.3 \cdot 10^6$. For the cases where a generator level event selection is made, the cross section quoted is $\sigma \times \epsilon$ where ϵ is the generator level selection efficiency.

data, one can then access the trigger decision using the Trigger Decision Tool, and find out for example whether the trigger system has identified a high p_{T} electron or muon, large missing transverse energy etc.

The sum of the rates of all triggers can not exceed the total bandwidth of the data taking infrastructure. If the rate of a certain trigger, for example an electron trigger with a certain p_{T} threshold, is expected to exceed the bandwidth which can be allocated to this trigger, a prescaling is imposed on the trigger. This means that only a certain fraction of the events fulfilling the requirements of this trigger is stored.

If one wants to obtain a distribution from MC data which as closely as possible reproduces the corresponding distribution from real data, one should apply the trigger decision in the analysis code for the MC data, so that only events which fired the trigger appear in the final distributions. Events which did not fire the trigger should not be included in the distributions, since these would be lost from the real data. A signal with a low trigger efficiency (low probability to fire the trigger) will give many signal events which are not stored. If a trigger decision cut is not imposed in an MC study, the expected number of reconstructed signal events will be overestimated, and MC data and real data will not agree.

For this W' study, an electron or muon trigger with a p_{T} threshold of 10 GeV is required to pass through all trigger levels. The triggers used are called `e10_medium` and `mu10` respectively. According to the ATLAS TWiki [23], these triggers are expected to run without prescale at a luminosity $L = 10^{31}\,\mathrm{cm}^{-2}\,\mathrm{s}^{-1}$. It is important to use a trigger without prescale, since we do not want to throw away any W' events. When the luminosity is increased, the 10 GeV electron and muon triggers may be prescaled. In this case, it will be necessary to use triggers with higher p_{T} thresholds to avoid a prescale. For the $W\gamma$ diboson dataset, the `e10i` trigger is used as electron trigger, since this dataset has a different "trigger menu" (the `e10_medium` trigger information is not accessible).

4.8 Event selection

We must now find out how to select the events interesting for a W' study from all the events coming off the ATLAS detector.

4.8.1 Lepton selection

A reconstructed electron or muon is an object created by the ATLAS software from hits and energy deposits. It may or may not correspond to an actual electron or muon. When doing analysis, one may select leptons fulfilling certain quality criteria, which typically depend on the analysis. In selecting electrons, cuts on the shape of the shower in the electromagnetic calorimeter are central. Furthermore, cuts on transition radiation hits in the TRT and on the association of the electromagnetic calorimeter shower to a track in the inner detector may improve the electron quality. For muons an important quality cut is to require a track in the inner detector to be matched to the muon spectrometer track. The muon is then called a combined muon.

An electron candidate is built from a cluster in the electromagnetic calorimeter if an inner detector track can be extrapolated to match the cluster within a $\Delta\eta \times \Delta\phi$ window of 0.05×0.10 and if the ratio of cluster energy to track momentum satisfies $E/p < 10$. The ATLAS software divides electrons into loose, medium, and tight categories based on various cuts. Detailed information about the cuts can be found in [25]. For loose electrons,

cuts are made on the shape of the electromagnetic cluster and on the leakage of energy into the hadronic calorimeter. For medium electrons, further cuts are made on shower shapes, and cuts are made on number of hits of the inner detector track and the track d_0. Fake electrons from $\pi^0 \to \gamma\,\gamma$ are reduced by cutting on the secondary maximum of the cluster. For tight electrons, tighter cuts are imposed on the track/cluster matching $(\Delta\eta, \Delta\phi, E/p)$, and a cut is made on the ratio of high threshold (transition radiation) hits to total number of TRT hits. Note that the loose, medium, and tight electron definitions are not related to and should not be confused with the loose, medium, and tight inner detector cuts used for cosmic muons in section 3.4.

For the analysis, the following requirements are made on electrons:

- Medium electron
- $|\eta| < 2.5$
- $p_{\mathrm{T}} > 50\,\mathrm{GeV}$

For muons, the following criteria are imposed:

- Combined muon
- $\chi^2_{\mathrm{match}} < 100$ (inner detector-muon spectrometer)
- $|z_0| < 200\,\mathrm{mm}$
- $|\eta| < 2.5$
- $p_{\mathrm{T}} > 50\,\mathrm{GeV}$

The variable χ^2_{match} is the χ^2 of the matching between the muon spectrometer and inner detector tracks. The lepton selection used is based on the one found in [24]. A similar selection is also used for W' search in [26].

The electrons used are taken from the `ElectronAODCollection` while muons are taken from the `StacoMuonCollection`.

4.8.2 Event preselection

As an initial event selection, we now require:

- exactly one high-p_{T} lepton (as defined in section 4.8.1),
- missing transverse energy $\not{E}_{\mathrm{T}} > 50\,\mathrm{GeV}$,
- trigger `mu10` or `e10_medium`.

For the $\not{E}_{\mathrm{T}}$, the `MET_RefFinal` container is used.

We require exactly one high p_{T} lepton since we do not expect the W' decay products to be accompanied by high p_{T} activity from other processes. Note that we accept other reconstructed electrons or muons in the event as long as their p_{T} is below 50 GeV.

Figure 4.13 shows the reconstructed transverse mass spectra in the electron and muon channels for 1 TeV and 2 TeV W's after event preselection. We see clearly in both electron and muon channels the decrease of the differential cross section above the W' mass. The

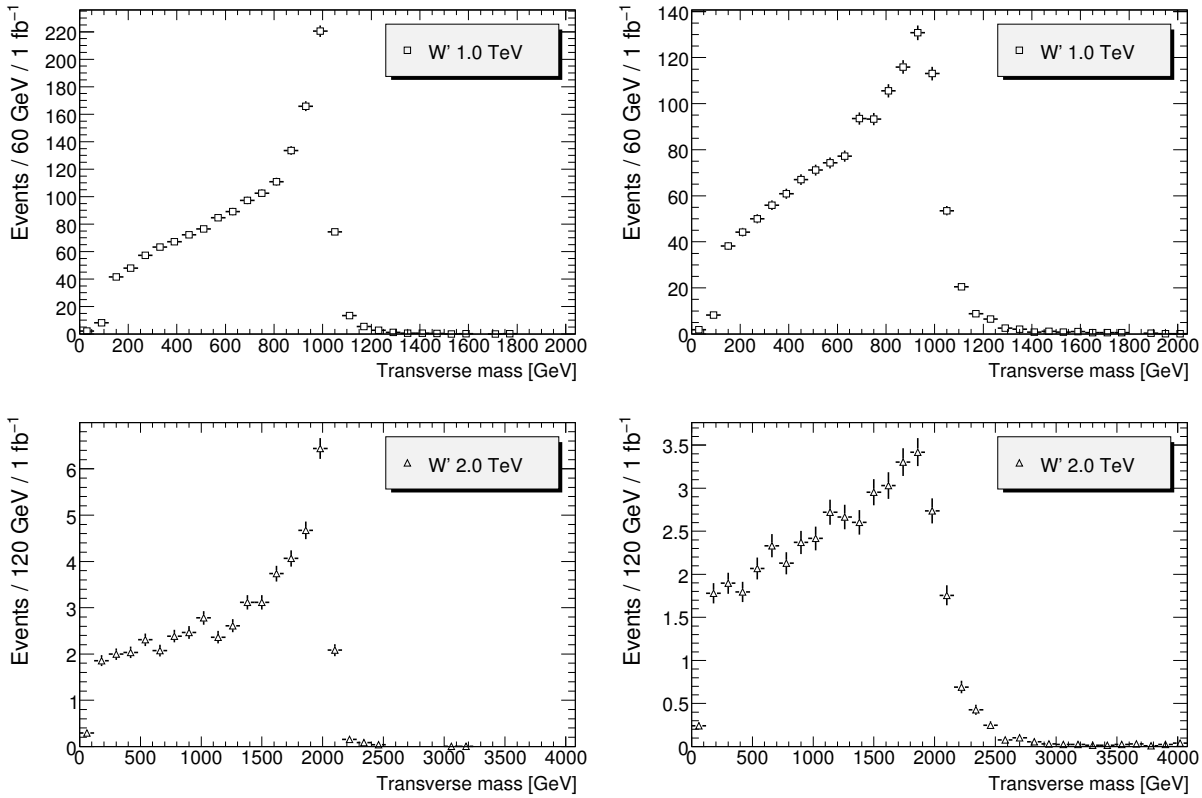

Figure 4.13: Reconstructed transverse mass spectra after event preselection in electron (left) and muon (right) channels for 1 TeV and 2 TeV W' bosons.

W' mass	Electron channel	Muon channel
1 TeV	$(86.3 \pm 0.2)\%$	$(85.2 \pm 0.3)\%$
2 TeV	$(85.0 \pm 0.4)\%$	$(84.3 \pm 0.4)\%$
3 TeV	$(82.5 \pm 0.5)\%$	$(80.2 \pm 0.5)\%$

Table 4.3: Reconstruction efficiencies for W' events at three different masses.

Jacobian peak looks especially nice in the electron channel, since calorimeter measurements are more precise than tracking at such high p_{T}. The Jacobian peak seems also to be more washed out in the muon channel for the 2 TeV W' than for the 1 TeV W'. This is probably because the tracking momentum accuracy decreases with momentum.

Table 4.3 shows the W' event reconstruction efficiency in electron and muon channels for three different W' masses. The numbers quoted in this table are $n_l^{\mathrm{presel}}/n_l$ where n_l is the number of $W' \to l\,\nu_l$ events (from truth), and n_l^{presel} is the number of these events which pass the one lepton and $\not\!\!E_{\mathrm{T}}$ requirements (trigger not required at this point). Note that these efficiencies are not pure electron and muon reconstruction efficiencies, but include detector acceptance, $\not\!\!E_{\mathrm{T}}$ reconstruction, and all quality criteria imposed on the leptons. The efficiencies are all above 80%, and somewhat higher in the electron channel than in the muon channel. Note that the geometrical acceptance ($|\eta| < 2.5$) is about 96% in both channels.

Around 10% to 15% of reconstructed events which pass the one lepton and $\not\!\!E_{\mathrm{T}}$ requirements in both electron and muon channels are actually $W' \to \tau\,\nu_\tau$ events where the

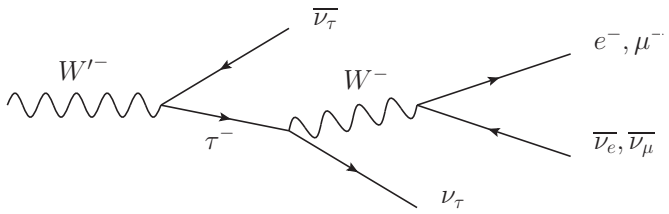

Figure 4.14: Feynman diagram for W' decay to τ lepton which in turn decays to electron or muon.

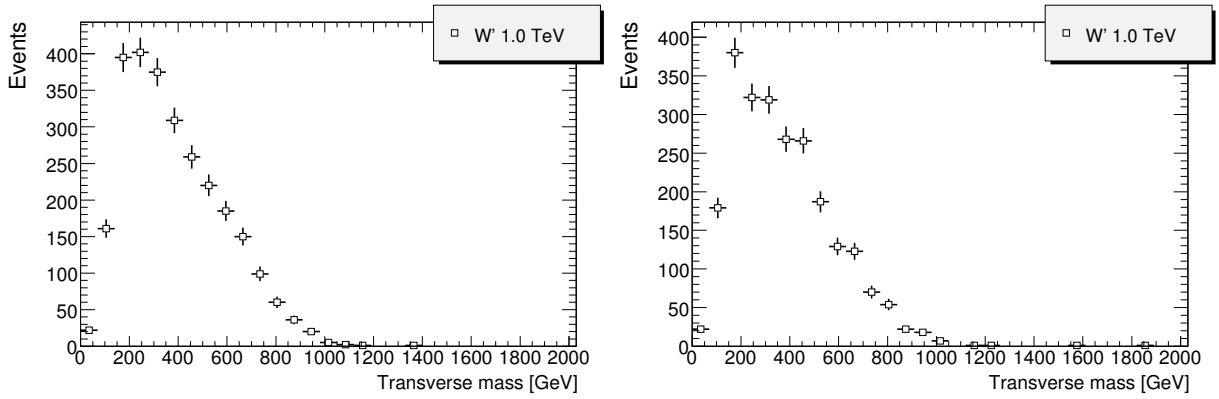

Figure 4.15: Reconstructed transverse mass distributions in electron (left) and muon (right) channels after one lepton and $\not\!\!E_{\mathrm{T}}$ requirements for events where the W' decays to $\tau\nu_\tau$. In these events, the τ lepton has decayed according to eq. (4.29), or it has decayed hadronically and produced a fake lepton.

τ decays to electron or muon, for example

$$W'^- \to \overline{\nu_\tau}\,\tau^- \to \overline{\nu_\tau}\,\nu_\tau\,l^-\,\overline{\nu_l} \tag{4.29}$$

where $l = e, \mu$ as shown in figure 4.14, or where a hadronic τ decay produces a fake electron or muon. The reconstructed transverse mass spectra for such events after one lepton and $\not\!\!E_{\mathrm{T}}$ requirements are shown in figure 4.15 for the 1 TeV W'. The distribution tends to low values of the transverse mass, since the τ momentum taken by the neutrinos is not measured, but contributes to the $\not\!\!E_{\mathrm{T}}$ predominantly in the opposite direction of the τ neutrino from the W' decay. Note that the events where the W' decays to τ lepton have not been counted when the efficiencies of table 4.3 have been calculated. I.e., the τ events contribute neither to n_l or to n_l^{presel} in this calculation.

Table 4.4 shows the trigger efficiency for three different W' masses. The trigger efficiency is defined here as $n_{\mathrm{trig}}/n_{\mathrm{offline}}$ where n_{offline} is the number of events passing the one lepton and $\not\!\!E_{\mathrm{T}}$ requirements, and n_{trig} is the number of these events which have been triggered. The trigger efficiency is around 99% for electron events and 85% for muon events, more or less independently of the W' mass. We see that some few events are picked up only by the "wrong" trigger (i.e. some muon events are picked up only by the electron trigger and vice versa).

Figure 4.16 shows the reconstructed p_{T}, $\not\!\!E_{\mathrm{T}}$, and m_{T} spectra for two W' masses and backgrounds. The most important backgrounds are seen to be dijets, $t\bar{t}$ and the SM W boson. The bins with large statistical errors in the SM W distributions correspond to

W' mass	Offline lepton	Electron trigger	Muon trigger	Total efficiency
1 TeV	Electron	$(98.8 \pm 0.08)\%$	$(0.3 \pm 0.04)\%$	$(98.8 \pm 0.08)\%$
1 TeV	Muon	$(1.5 \pm 0.09)\%$	$(85.7 \pm 0.3)\%$	$(85.9 \pm 0.2)\%$
2 TeV	Electron	$(98.8 \pm 0.1)\%$	$(0.4 \pm 0.08)\%$	$(98.9 \pm 0.1)\%$
2 TeV	Muon	$(1.7 \pm 0.2)\%$	$(85.8 \pm 0.4)\%$	$(86.1 \pm 0.4)\%$
3 TeV	Electron	$(98.8 \pm 0.1)\%$	$(0.5 \pm 0.09)\%$	$(98.8 \pm 0.1)\%$
3 TeV	Muon	$(1.7 \pm 0.2)\%$	$(84.4 \pm 0.5)\%$	$(84.7 \pm 0.5)\%$

Table 4.4: Trigger efficiencies for W' events at three different masses.

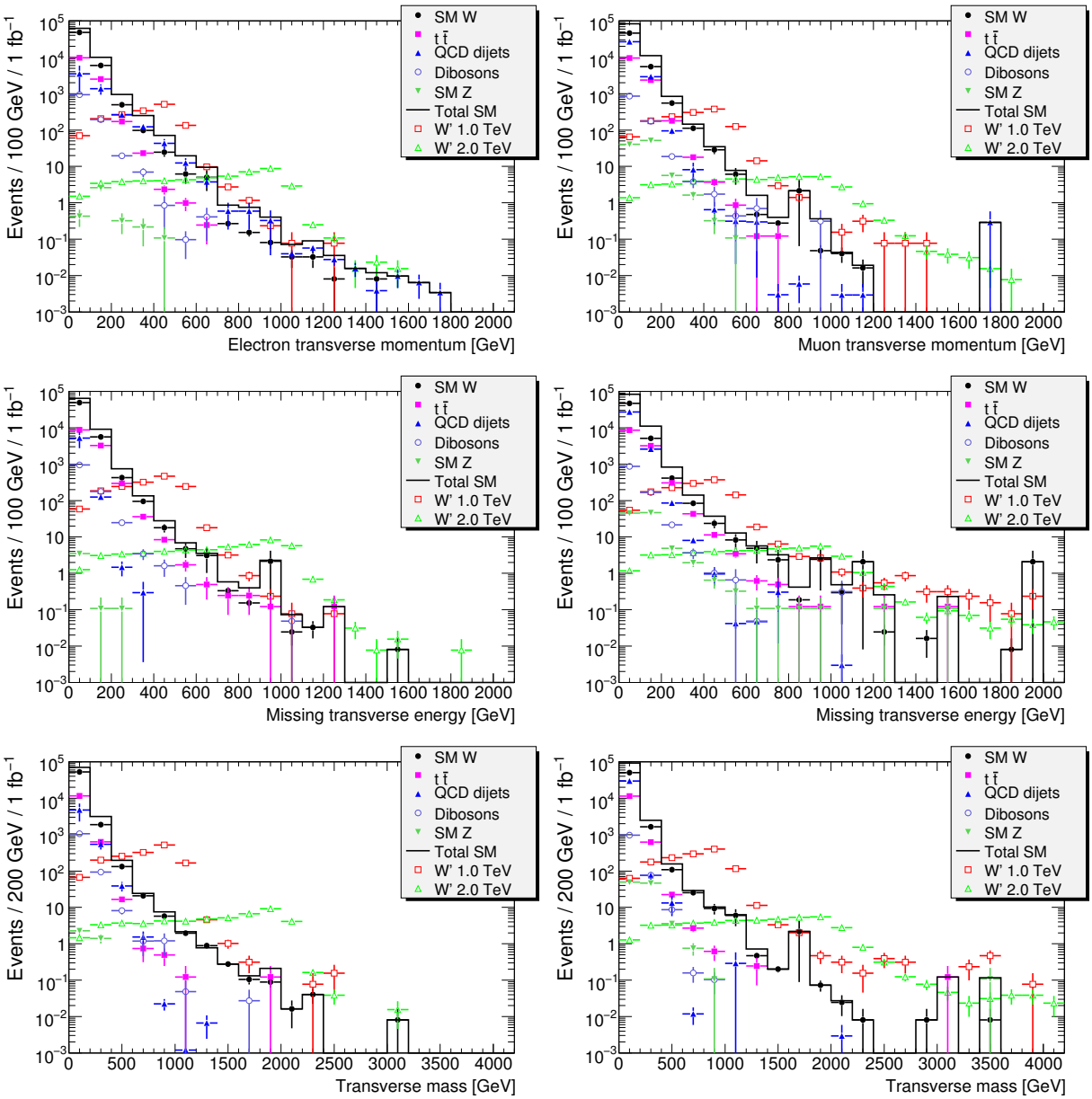

Figure 4.16: Reconstructed p_{T}, $\not{E}_{\mathrm{T}}$, and m_{T} spectra after event preselection in electron (left) and muon (right) channels for 1 TeV and 2 TeV W' bosons and backgrounds.

events from the low mass ($m_{l\nu} < 200\,\text{GeV}$) sample, which has a larger scale factor than the high mass samples.

If the electron p_{T} distribution in figure 4.16 is compared to the one in reference [24], the present dijet contribution is seen to be much smaller. In [24], the dijet contribution is far above the SM W. This is because older reconstructions were used in [24]. When the present analysis was run with the `r635` reconstruction tags, the dijet contribution to the electron p_{T} spectrum was much larger. This is probably because of an improvement in the electron identification algorithms.

In terms of the transverse mass, some backgrounds are already reduced at high transverse mass compared to the p_{T} distribution, and the high mass tail of the SM W is seen to be the dominant background. Note that the total SM background actually goes below the SM W for the transverse mass histogram in the electron channel just below 1500 GeV (the same effect is seen more clearly in figure 4.22). This is because the corresponding bin in the $t\bar{t}$ histogram has negative content, which can happen in the tail of a distribution when the only event in a bin has negative weight.

We now want to look at some variables to reduce the $t\bar{t}$ and dijet backgrounds. Note that the high mass tail of the SM W represents irreducible background, since it has the exact same event topology as the W'.

4.8.3 Lepton isolation

If a jet leads to the reconstruction of a fake lepton, or if a real lepton exists within a jet, the reconstructed lepton is likely to be surrounded by a lot of activity in the detector (tracks and energy deposits). For leptons from W' decay, there is no reason to expect significant activity in their vicinity. They are expected to be isolated.

We define the isolation variable given by the sum of all transverse energy (calorimeter measurements) in the vicinity of our reconstructed lepton:

$$E_{\text{T}}^{\Delta R<x} = \sum_{\Delta R<x} E_{\text{T}} \tag{4.30}$$

where ΔR is relative to the reconstructed lepton's direction of motion. The region given by $\Delta R < x$ is a circle in the η, ϕ-plane. In three dimensions x, y, z, it corresponds to a cone-like volume, and the isolation variables are therefore referred to as "E_{T}-cone" variables.

Figure 4.17 shows the distributions of $E_{\text{T}}^{\Delta R<0.3}$ for signals and backgrounds in the electron and muon channels. The jet background is represented by the J5-J7 samples, since these samples give enough events passing the event preselection to define relatively smooth distributions. (The J8 sample is excluded because this sample has an older reconstruction tag.) We see that the dijet samples tend to higher values of $E_{\text{T}}^{\Delta R<0.3}$ than the signal samples, so the variable can be used for jet background reduction. Note that the signal samples tend to higher values of the variable (less isolation) in the electron channel than in the muon channel. This is probably because the electrons have a relatively high probability to do bremsstrahlung in the material preceding the calorimeters at such high momentum. The effect is less important in the muon channel because of the mass. Electrons from W' appear to be less isolated than both electrons from the SM W and electrons from $t\bar{t}$.

To account for bremsstrahlung, we can make the isolation cut p_{T} dependent, since the bremsstrahlung probability increases with momentum. We therefore consider also the normalized isolation $E_{\text{T}}^{\Delta R<0.3}/p_{\text{T}}$. The signal and background distributions for this

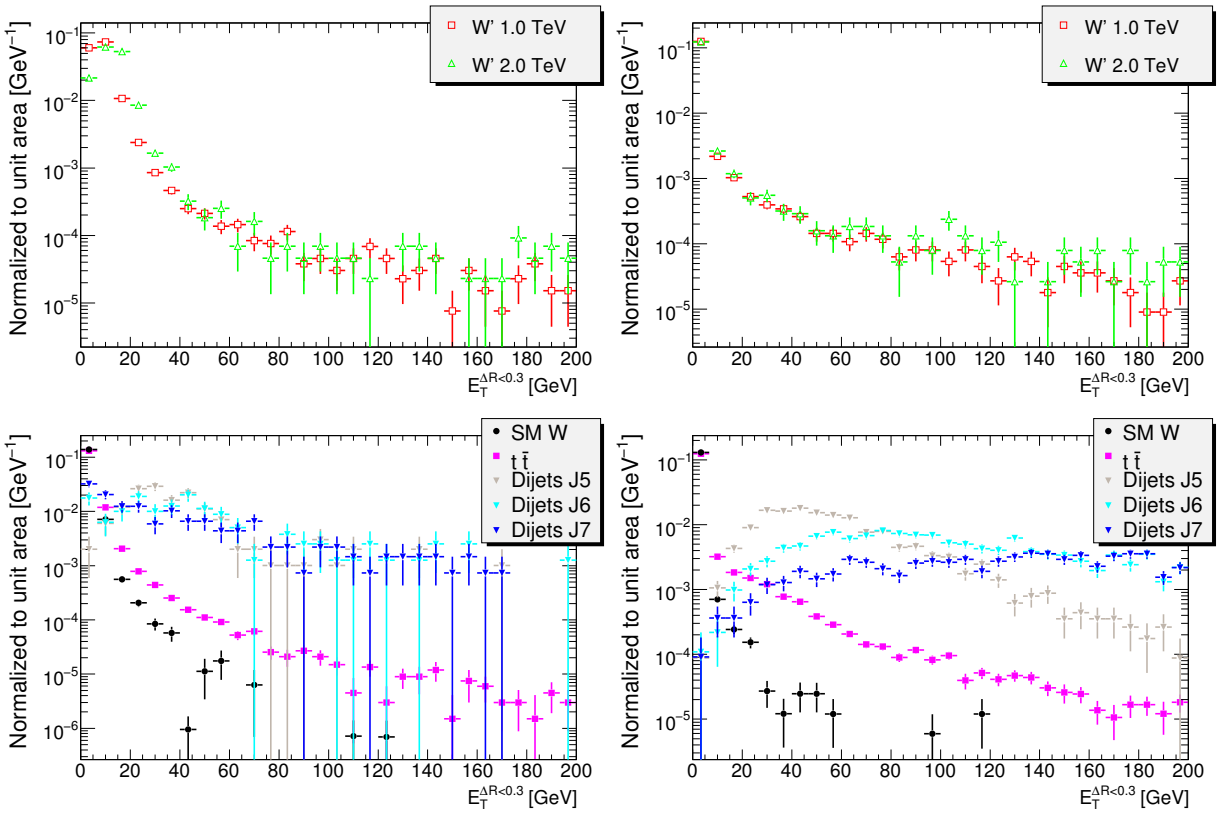

Figure 4.17: The distributions of the isolation variable $E_{\mathrm{T}}^{\Delta R<0.3}$ for signals (top) and backgrounds (bottom) in the electron (left) and muon (right) channels.

variable are shown in figure 4.18. The electrons from W' appear as more isolated than those from $t\bar{t}$ in terms of the normalized isolation.

Just by looking at the isolation distributions, one can get an idea of where to make the cut to reject the jets. Since jets are not our dominant background in terms of the transverse mass, it is not possible to optimize the cut value for significance. However, to make an argument for the choice of cut value, we can try to maximize the product of signal efficiency and background rejection, $\epsilon_{\mathrm{sgn}} r_{\mathrm{bkg}}$. The signal efficiency is defined as the fraction of signal events passing the cut, $\epsilon_{\mathrm{sgn}} = n^{\mathrm{sgn}}_{\mathrm{after}}/n^{\mathrm{sgn}}_{\mathrm{before}}$ and the background rejection is defined as $r_{\mathrm{bkg}} = 1 - n^{\mathrm{bkg}}_{\mathrm{after}}/n^{\mathrm{bkg}}_{\mathrm{before}}$. This approach also allows the comparison of cut variables, since the best variable can be defined as the one giving the largest $\epsilon_{\mathrm{sgn}} r_{\mathrm{bkg}}$.

Figure 4.19 shows the value of $\epsilon_{\mathrm{sgn}} r_{\mathrm{bkg}}$ as function of the cut value for $E_{\mathrm{T}}^{\Delta R<0.3}$ and $E_{\mathrm{T}}^{\Delta R<0.3}/p_{\mathrm{T}}$ as cut variables in the electron and muon channels. The background is here the jet samples J5-J7 merged according to cross section, and the signal is the 1 TeV W'. We see that the maximum value is higher in the muon channel than in the electron channel, as expected because of bremsstrahlung. The maximum value is slightly higher in the normalized isolation than in standard E_{T}-cone.

For this analysis, we proceed with a cut $E_{\mathrm{T}}^{\Delta R<0.3}/p_{\mathrm{T}} < 0.05$, which gives a close to maximum value of $\epsilon_{\mathrm{sgn}} r_{\mathrm{bkg}}$ in both channels. In the electron channel we obtain $\epsilon_{\mathrm{sgn}} = 92.3\%$ and $r_{\mathrm{bkg}} = 96.1\%$ (for J5-J7). In the muon channel, the corresponding numbers are $\epsilon_{\mathrm{sgn}} = 97.3\%$ and $r_{\mathrm{bkg}} = 99.9\%$.

Because of bremsstrahlung, it could be an improvement to consider track based isolation "p_{T}-cone" (photons do not make tracks), or to consider calorimeter measurements with a wider inner cone subtracted (the deposits assumed to be from the lepton are al-

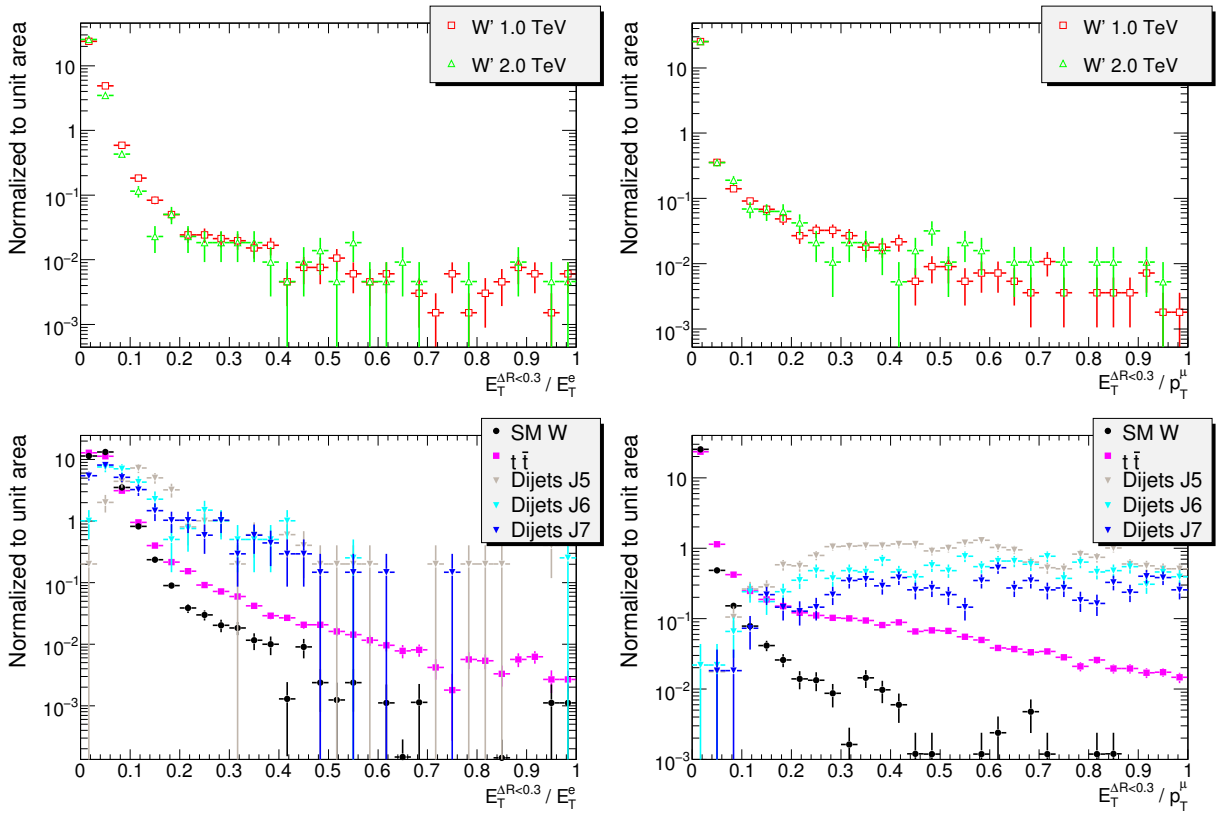

Figure 4.18: The distributions of the normalized isolation $E_{\mathrm{T}}^{\Delta R<0.3}/p_{\mathrm{T}}$ for signals (top) and backgrounds (bottom) in the electron (left) and muon (right) channels.

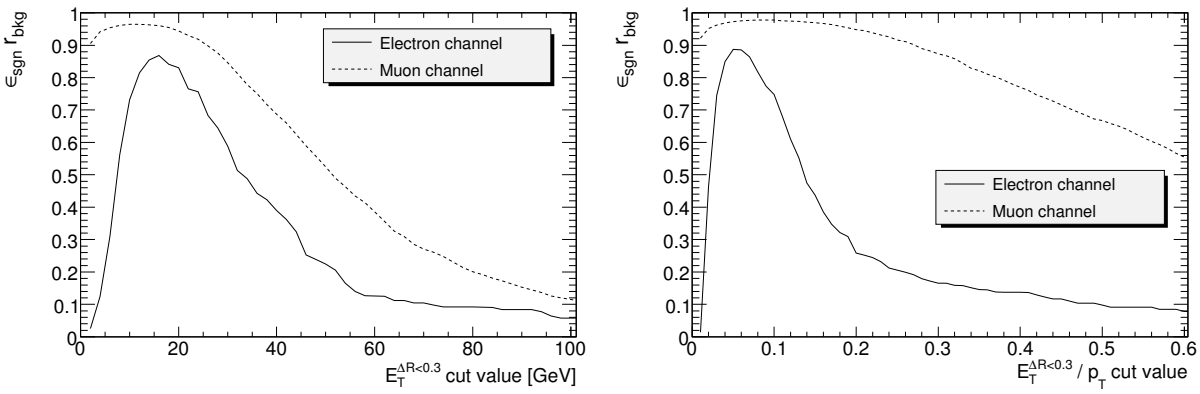

Figure 4.19: The product $\epsilon_{\mathrm{sgn}} r_{\mathrm{bkg}}$ as function of the cut value used for $E_{\mathrm{T}}^{\Delta R<0.3}$ and $E_{\mathrm{T}}^{\Delta R<0.3}/p_{\mathrm{T}}$ in electron and muon channels.

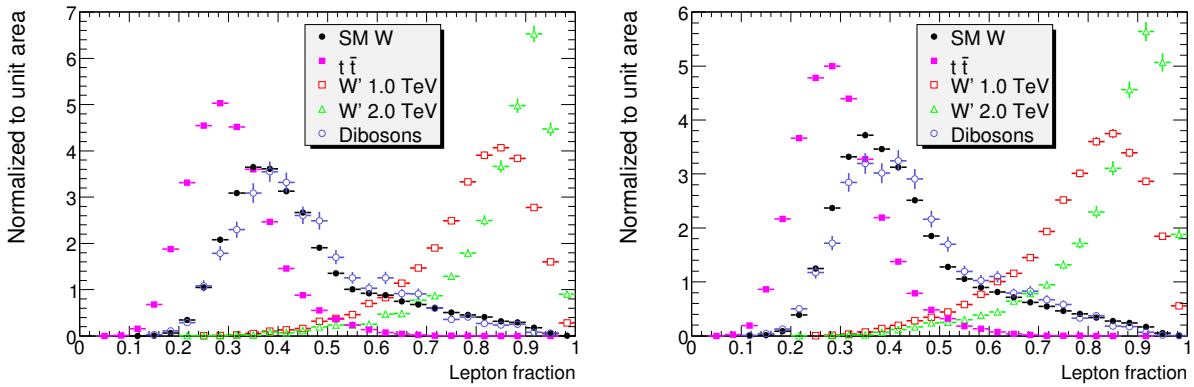

Figure 4.20: Lepton fraction distributions for signals and backgrounds in the electron (left) and muon (right) channels.

ways subtracted when calculating an E_{T}-cone). Isolation requirements using calorimeter measurements in a region $0.1 < \Delta R < 0.3$ (a so-called "E_{T}-ring") or tracks in a region $\Delta R < 0.3$ were explored, but neither option seemed to give better signal/background separation.

4.8.4 The Lepton Fraction

As seen in figure 4.18, the $t\bar{t}$ background is not significantly reduced by the cut on normalized isolation. We therefore look at a different variable for $t\bar{t}$ rejection.

For a W' signal, we expect the event to be dominated by the lepton and neutrino from the W' decay. There is no reason to expect significant jet activity. For the typical $t\bar{t}$ event depicted in figure 4.9, the final state lepton and neutrino will be accompanied by four jets, including two b-jets.

We define the lepton fraction by

$$f_{\mathrm{lep}} = \frac{E_{\mathrm{T}}^{e} + \not{E}_{\mathrm{T}}}{\sum E_{\mathrm{T}} + \not{E}_{\mathrm{T}}} \tag{4.31}$$

for electron events and

$$f_{\mathrm{lep}} = \frac{p_{\mathrm{T}}^{\mu} + \not{E}_{\mathrm{T}}}{\sum E_{\mathrm{T}} + p_{\mathrm{T}}^{\mu} + \not{E}_{\mathrm{T}}} \tag{4.32}$$

for muon events. (Note that the sums are scalar sums.) It measures the fraction of transverse momentum in the event which can be attributed to the charged lepton and the neutrino. The $\sum E_{\mathrm{T}}$ is the scalar sum of E_{T} from calorimeter measurements. The denominator in the lepton fraction definition looks different for electron and muon events, since the muon p_{T} is not counted in $\sum E_{\mathrm{T}}$, while the electron p_{T} (or E_{T}) is.

The lepton fraction distributions for signal and background in the muon and electron channels are shown in figure 4.20. Note that the isolation cut is already imposed when producing these plots. We see that $t\bar{t}$ events tend to low values of the lepton fraction and that the signal tends to high values, as expected.

We now look at the product $\epsilon_{\mathrm{sgn}} r_{\mathrm{bkg}}$ as function of the lepton fraction cut value, which is shown in figure 4.21. Here, the background is $t\bar{t}$, while the signal is again the 1 TeV W'. For the analysis, a cut $f_{\mathrm{lep}} > 0.5$ is made in both electron and muon channels. In the electron channel, this cut achieves $\epsilon_{\mathrm{sgn}} = 97.3\%$ and $r_{\mathrm{bkg}} = 97.0\%$, while the numbers in the muon channel are $\epsilon_{\mathrm{sgn}} = 96.4\%$ and $r_{\mathrm{bkg}} = 97.4\%$.

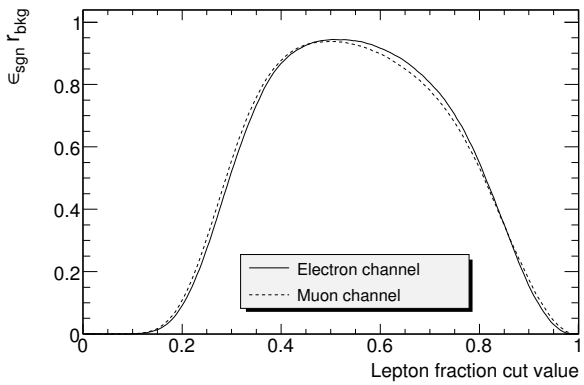

Figure 4.21: The product $\epsilon_{\mathrm{sgn}} r_{\mathrm{bkg}}$ as function of the lepton fraction cut value in the electron and muon channels.

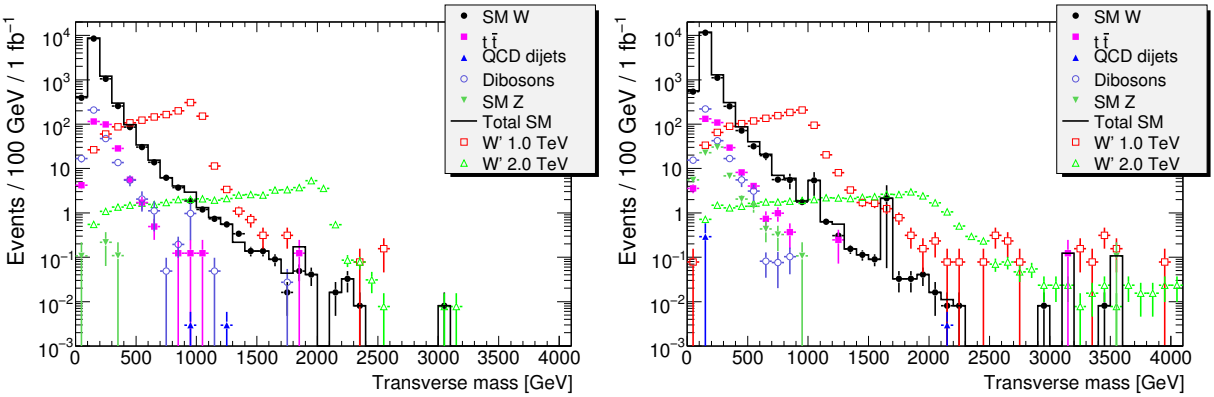

Figure 4.22: Transverse mass distributions for signals and backgrounds in the electron (left) and muon (right) channels after cuts on normalized isolation and lepton fraction.

Note that the SM W lepton fraction distribution is made by combining the different mass ranges according to cross section. While it may seem that the SM W is reduced by the lepton fraction cut, the reduction is mainly in the low mass end of the spectrum. The high mass SM W tail is irreducible.

4.8.5 The momentum ratio $p_{\mathrm{T}}/\not{E}_{\mathrm{T}}$

We have now rejected most of the $t\bar{t}$ and jet background. Figure 4.22 shows the transverse mass distributions obtained with cuts on normalized isolation and the lepton fraction. We see some "stray" $t\bar{t}$, diboson, and SM Z events at very high transverse mass. We see also a couple of spikes in the SM W distribution in the muon channel, corresponding to events from the low mass ($m_{l\nu} < 200\,\mathrm{GeV}$) sample which have been wrongly reconstructed with large transverse mass.

To further clean our transverse mass distributions, we consider one additional cut variable. In a W' event, the transverse momentum of the W' is expected to be small. This means that the charged lepton p_{T} must be balanced by the neutrino p_{T} due to conservation of momentum. Experimentally, this means that the lepton p_{T} should be balanced by the $\not{E}_{\mathrm{T}}$ for a W' event.

Figure 4.23 shows the distribution of the momentum ratio $p_{\mathrm{T}}/\not{E}_{\mathrm{T}}$, where p_{T} is the

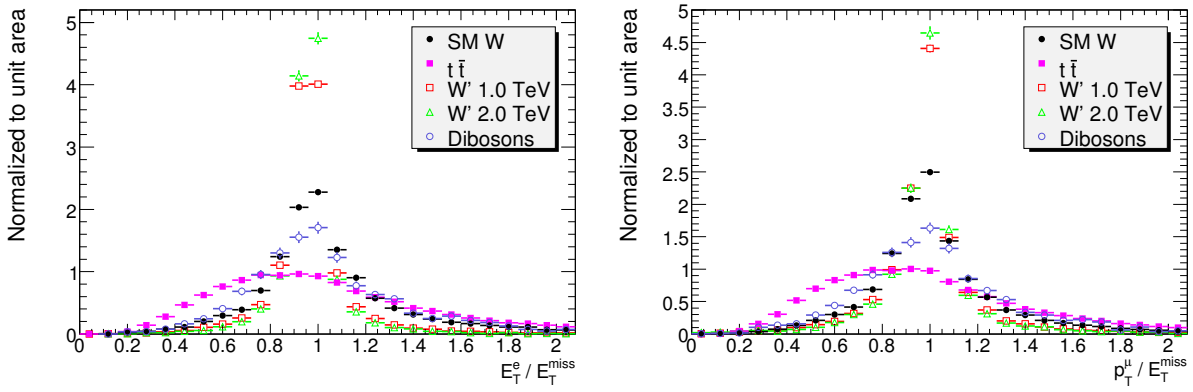

Figure 4.23: Momentum ratio $p_{\mathrm{T}}/\not{E}_{\mathrm{T}}$ distributions for signals and backgrounds in the electron (left) and muon (right) channels.

transverse momentum of the lepton, for signals and backgrounds in the electron and muon channels. Note that the isolation cut has been applied, but not the lepton fraction cut, in producing these distributions. We see that the signal distributions are peaked around 1 as expected. The $t\bar{t}$ distribution is wider, probably partly due to the fact that the W bosons from top decays can have significant transverse momentum.

We proceed with a loose cut $0.5 < p_{\mathrm{T}}/\not{E}_{\mathrm{T}} < 1.5$. A cut on the momentum ratio $p_{\mathrm{T}}/\not{E}_{\mathrm{T}}$ is not used in any of the ATLAS W' studies (references [24] and [26]), but such a cut is used in the Tevatron study [19].

4.8.6 Lepton fraction vs. $p_{\mathrm{T}}/\not{E}_{\mathrm{T}}$ correlation

Figure 4.24 shows two-dimensional histograms of the lepton fraction vs. the momentum ratio $p_{\mathrm{T}}/\not{E}_{\mathrm{T}}$ for the 1 TeV W' signal and for $t\bar{t}$ and dijet backgrounds. For the dijets, the J5 to J7 samples are merged according to cross section. No cuts have been applied other than event preselection (section 4.8.2).

No obvious correlation is seen between the variables for signal or for these backgrounds. We do see, however, that the lepton fraction cut alone reduces these backgrounds effectively, and that the $p_{\mathrm{T}}/\not{E}_{\mathrm{T}}$ cut quantitatively does not add much in terms of reduction. The $p_{\mathrm{T}}/\not{E}_{\mathrm{T}}$ cut is more of a cleaning cut. Events where the $\not{E}_{\mathrm{T}}$ and the lepton p_{T} differ significantly are not good W' candidates, and we have seen that a very small fraction of low mass W events can contribute at high transverse mass because of $\not{E}_{\mathrm{T}}$ mismeasurements. These events, and similar misreconstructions from other kinds of events, should not be included in the transverse mass spectrum. For the analysis, we proceed with cuts on both the lepton fraction and the momentum ratio $p_{\mathrm{T}}/\not{E}_{\mathrm{T}}$.

4.8.7 Distributions after cuts and the cut flow

The p_{T}, $\not{E}_{\mathrm{T}}$, and m_{T} distributions after all cuts have been applied are shown in figure 4.25. As a reminder, these cuts are now:

- preselection,
- normalized isolation $E_{\mathrm{T}}^{\Delta R<0.3}/p_{\mathrm{T}} < 0.05$,
- lepton fraction $f_{\mathrm{lep}} > 0.5$,

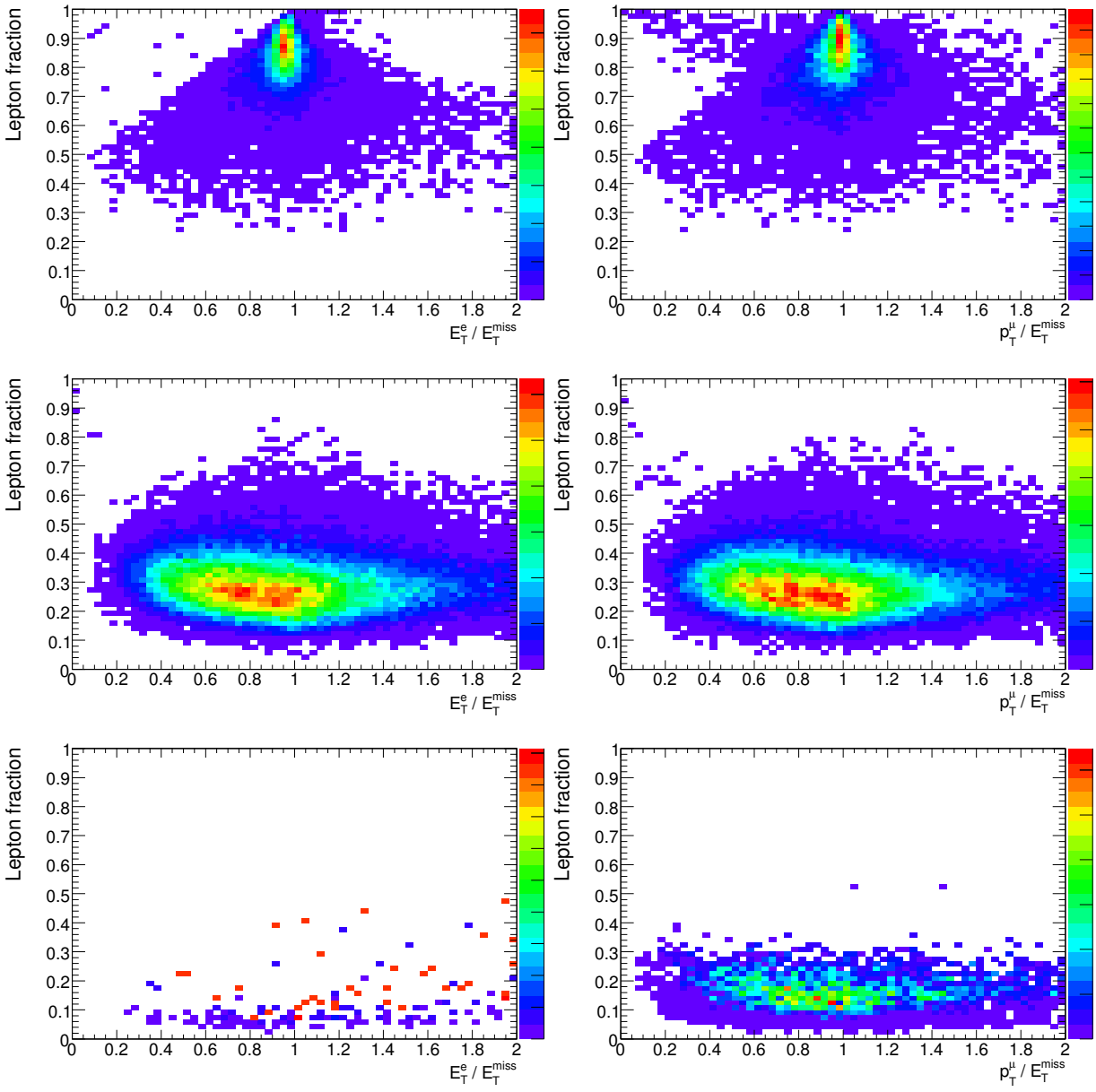

Figure 4.24: Correlation plots of lepton fraction vs. $p_{\mathrm{T}}/\not{E}_{\mathrm{T}}$ for 1 TeV W' signal (top), $t\bar{t}$ background (middle) and dijet background (bottom) in electron (left) and muon (right) channels.

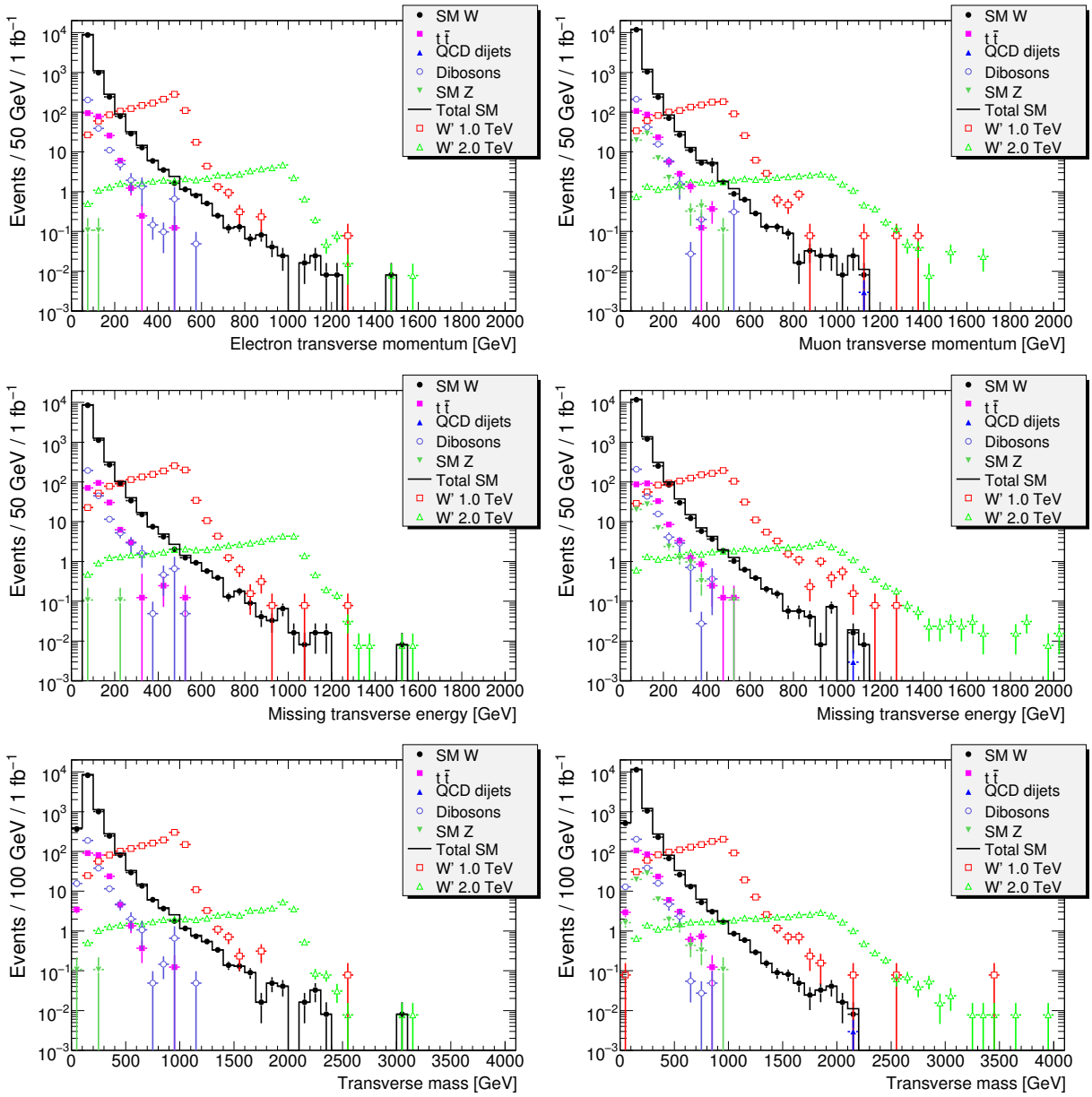

Figure 4.25: Distributions of p_{T}, $\not{E}_{\mathrm{T}}$, and m_{T} in electron (left) and muon (right) channels after isolation, lepton fraction, and $p_{\mathrm{T}}/\not{E}_{\mathrm{T}}$ cuts.

- $0.5 < p_{\mathrm{T}}/\not{E}_{\mathrm{T}} < 1.5$.

We see that the high mass tail of the SM W is the clearly dominant background, and that this background is statistically well defined up to transverse masses above 1.5 TeV. The transverse mass distributions shown in figure 4.25 will be used for the evaluation of the W' discovery potential.

The mismeasured SM W events giving the spikes in the m_{T} distribution in the muon channel have been removed by the $p_{\mathrm{T}}/\not{E}_{\mathrm{T}}$ cut. These events all have $\not{E}_{\mathrm{T}} > 2p_{\mathrm{T}}^{\mu}$ due to $\not{E}_{\mathrm{T}}$ mismeasurements. A single dijet event has survived all cuts in the muon channel. This event has a lepton fraction $f_{\mathrm{lep}} = 0.53$, so we could remove it by increasing the lepton fraction cut value slightly. Tuning a cut to remove a single MC event would, however, not be very well motivated.

	Preselection	Isolation	Lepton fraction	$p_T/\not{E}_T$	$m_T > 700\,\text{GeV}$
W' 1 TeV	1540 ± 11	1422 ± 11	1384 ± 10	1344 ± 10	823 ± 8.0
W' 1.5 TeV	245 ± 2.2	228 ± 2.2	223 ± 2.1	218 ± 2.1	172 ± 1.9
W' 2 TeV	50.7 ± 0.63	47.9 ± 0.61	47.1 ± 0.60	46.2 ± 0.60	39.0 ± 0.55
W' 2.5 TeV	13.2 ± 0.16	12.4 ± 0.16	12.2 ± 0.16	12.0 ± 0.15	10.1 ± 0.14
W' 3 TeV	3.74 ± 0.047	3.50 ± 0.045	3.43 ± 0.045	3.36 ± 0.044	2.75 ± 0.040
W' 3.5 TeV	1.23 ± 0.016	1.15 ± 0.015	1.11 ± 0.015	1.09 ± 0.015	0.811 ± 0.013
SM W	55202 ± 327	36760 ± 265	10303 ± 132	10055 ± 130	16.9 ± 2.1
Dijets	5317 ± 2428	26.2 ± 9.6	0.00590 ± 0.0042	0	0
Dibosons	1159 ± 21	944.0 ± 20	294.4 ± 11	262.3 ± 10	0.898 ± 0.66
$t\bar{t}$	12324 ± 45	8447 ± 37	254 ± 6.4	206 ± 5.7	0.246 ± 0.246
SM Z	3.68 ± 0.63	2.27 ± 0.50	0.433 ± 0.22	0.216 ± 0.15	0

Table 4.5: Signal and background cut flow in the electron channel. The numbers shown are expected events per $1\,\text{fb}^{-1}$ with statistical errors.

	Preselection	Isolation	Lepton fraction	$p_T/\not{E}_T$	$m_T > 700\,\text{GeV}$
W' 1 TeV	1303 ± 10	1268 ± 9.9	1222 ± 9.8	1161 ± 9.5	655 ± 7.1
W' 1.5 TeV	200 ± 2.0	194 ± 2.0	189 ± 2.0	179 ± 1.9	136 ± 1.7
W' 2 TeV	44.2 ± 0.59	42.8 ± 0.58	41.9 ± 0.57	39.6 ± 0.55	32.0 ± 0.50
W' 2.5 TeV	10.8 ± 0.15	10.5 ± 0.14	10.2 ± 0.14	9.62 ± 0.14	7.89 ± 0.13
W' 3 TeV	3.06 ± 0.042	2.97 ± 0.042	2.88 ± 0.041	2.70 ± 0.040	2.11 ± 0.035
W' 3.5 TeV	1.01 ± 0.014	0.977 ± 0.014	0.935 ± 0.014	0.876 ± 0.013	0.618 ± 0.011
SM W	52342 ± 322	51446 ± 319	13537 ± 156	13213 ± 154	12.2 ± 0.31
Dijets	29956 ± 3714	2359 ± 2354	0.293 ± 0.290	0.00295 ± 0.00295	0.00295 ± 0.00295
Dibosons	1058 ± 20	1003 ± 19	302.7 ± 10	276.1 ± 9.7	0.0760 ± 0.056
$t\bar{t}$	12108 ± 44	10925 ± 42	288 ± 6.6	227 ± 5.9	0.860 ± 0.33
SM Z	100 ± 3.3	95.7 ± 3.2	69.9 ± 2.7	60.1 ± 2.5	0.432 ± 0.22

Table 4.6: Signal and background cut flow in the muon channel. The numbers shown are expected events per $1\,\text{fb}^{-1}$ with statistical errors.

The signal and background cut flow in the electron channel is shown in table 4.5, and the cut flow in the muon channel is shown in table 4.6. The numbers in the tables are expected events per $1\,\text{fb}^{-1}$ with statistical errors. For the number of expected events before any event selection (i.e. the cross section) consult tables 4.1 and 4.2. The last cut, $m_T > 700\,\text{GeV}$, is the transverse mass cut that will be used for calculating the significance for a 1 TeV W'.

The event numbers quoted here can not be compared to the corresponding ones in reference [24], since [24] is a 14 TeV study. The numbers for the muon channel show reasonable agreement with the talk [27] on W' search in the muon channel at 10 TeV, although one must note that the trigger requirement is applied after the other cuts in this talk.

4.9 The statistics of discovery and exclusion

4.9.1 The significance

We will search for the W' by looking for an excess of events at high transverse mass. If the number of observed events is significantly greater than the expected background b, we claim to have discovered something. The observed excess is said to be significant when the probability of observing it given only background is sufficiently small.

Consider the number of events n in a given data sample satisfying some criteria, for example that the transverse mass falls within some range. Since each bunch crossing in our detector has a certain (very small) probability of producing such an event, independent of all other bunch crossings, we conclude that n follows a binomial distribution. For any intereseting data sample, the number of bunch crossings will be huge. In this limit, where number of trials is large and the success probability is small, the binomial distribution approaches the Poisson distribution. The probability for $n = k$ is thus

$$P(k|\lambda) = \frac{\lambda^k e^{-\lambda}}{k!} \tag{4.33}$$

where λ is the expectation (average) value of n, which can be written as $\lambda = \epsilon\sigma \int L\, dt$ where σ is the cross section for the particular kind of event considered and ϵ is the reconstruction efficiency.

Let now n be the number of signal-type events (number of events above some cut value of the transverse mass) observed, and b be the expected number of background events in this transverse mass region. The probability of observing an excess as great as or greater than what we are seeing given only background, known as the p value, is

$$p = \sum_{k=n}^{\infty} P(k|b) = \sum_{k=n}^{\infty} \frac{b^k e^{-b}}{k!}. \tag{4.34}$$

The p value is converted to a significance Z by requiring

$$p = \int_Z^{\infty} \frac{e^{x^2/2}}{\sqrt{2\pi}}\, dx = 1 - \Phi(Z) \tag{4.35}$$

where the integrand is the probability density function (PDF) of the standard normal distribution (with zero mean and unit variance) and Φ is its cumulative distribution function. I.e. Z is the number of standard deviations a Gaussian has to fluctuate to give the p value in its tail. In particle physics, a significance $Z = 5$ ("5σ"), corresponding to a p value $p = 2.87 \cdot 10^{-7}$ is required to claim discovery. This means that the probability for claiming discovery if there is only background is as small as $2.87 \cdot 10^{-7}$.

4.9.2 Likelihood ratio based significance

Instead of using n as test statistic, we could make a different choice. Let s be the expected number of signal events for some discovery. We write the expectation for the observation n as

$$E[n] = \mu s + b \tag{4.36}$$

where the parameter μ measures whether or not the signal is present. We estimate the expected background b by a MC experiment where m signal-type events are observed.

The expectation for m is $E[m] = \tau b$ where τ is the ratio of integrated luminosity for the MC sample to that of the data:

$$\tau = \frac{(\int L\,dt)_{\text{MC}}}{(\int L\,dt)_{\text{data}}}. \tag{4.37}$$

We define the joint likelihood function for the observations n and m:

$$L(\mu, b) = \frac{(\mu s + b)^n e^{-(\mu s+b)}}{n!} \times \frac{(\tau b)^m e^{-\tau b}}{m!}. \tag{4.38}$$

Note that b is taken as a free parameter, so this approach takes into account statistical uncertainty in the background estimate, instead of assuming $b = m/\tau$ without uncertainty.

Our test statistic is now taken to be $q_\mu = -2 \ln \lambda(\mu)$ where

$$\lambda(\mu) = \frac{L(\mu, \tilde{b})}{L(\hat{\mu}, \hat{b})}. \tag{4.39}$$

Here $L(\mu, \tilde{b})$ is the maximum of L with μ fixed and $L(\hat{\mu}, \hat{b})$ is the global maximum of L. If we calculate this test statistic for a value μ which is realized in the data, we expect $\hat{\mu} \approx \mu$ and therefore $q_\mu \approx 0$. For any observation $q_\mu^{\text{obs}} > 0$ (an excess in the data), the p value can be calculated as

$$p = \int_{q_\mu^{\text{obs}}}^{\infty} f(q_\mu|\mu)\, dq_\mu \tag{4.40}$$

where $f(q_\mu|\mu)$ is the PDF of q_μ. Note that the integral (4.40) is in principle a sum over discrete possible values of q_μ, since the outcomes n and m of the experiment are discrete.

When we test the background hypothesis, we calculate q_0. The background only PDF for q_0, $f(q_0|0)$, can be calculated by MC sampling. However, for a large enough dataset, and if certain conditions are fulfilled, $f(q_0|0)$ approximates a χ^2 PDF with one degree of freedom (DOF) [28]. Since a χ^2 distributed variable with 1 DOF is just the square of a standard normal distributed variable, the significance becomes in this case

$$Z = \sqrt{q_0} = \sqrt{-2 \ln \lambda(0)}. \tag{4.41}$$

(Here the observation is assumed to fluctuate above and below its expectation with equal probability, details in [28].)

One can analytically find that $\hat{\mu} = (n - m/\tau)/s$ for $n \geq m/\tau$. In the limit of large τ, then $\tilde{b} = \hat{b} = m/\tau = b$. The log-likelihood ratio is then

$$\ln \lambda(0) = -n \ln \frac{n}{b} + n - b. \tag{4.42}$$

Combined with equation (4.41), this gives a significance

$$Z = \sqrt{2 \left[n \ln \frac{n}{b} - n + b \right]}. \tag{4.43}$$

The expected significance in the presence of signal is obtained by inserting the expected observation $n = s + b$:

$$Z = \sqrt{2 \left[(s+b) \ln \left(1 + \frac{s}{b} \right) - s \right]}. \tag{4.44}$$

Note that we have assumed large τ, so we do not take the statistical uncertainty in the background estimate into account now. The large τ limit should however be appropriate

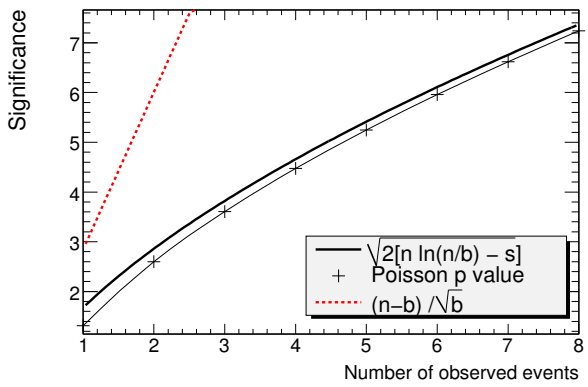

Figure 4.26: The significance as function of the number of observed events n for an expected background $b = 0.1$ calculated using different formulae. "Poisson p value" refers to equations (4.34) and (4.35).

in our case, since the highest mass SM W sample has been generated equivalent to more than $100\,\mathrm{fb}^{-1}$. Equation (4.44) is used to calculate significances in [24].

Figure 4.26 shows the significance as function of the observation n calculated according to equation (4.43) and equations (4.34) and (4.35) for an expected background $b = 0.1$. This is a typical value of b for a 5σ discovery of a W'. For comparison, the widely used formula $Z = s/\sqrt{b} = (n-b)/\sqrt{b}$ is also plotted. We see that the approximation (4.43) agrees reasonably well with the straight forward p value calculation, although equation (4.43) has a constant offset towards higher significance. The formula $Z = s/\sqrt{b}$ is seen to make no sense in this low statistics regime. This formula should be used when b is large.

4.9.3 Exclusion

If no excess of events at high transverse mass is observed, we would like to put a limit on the W' mass with some confidence level. We could then calculate a p value, not as the tail of the background distribution above the observation (as in the case of significance), but rather as the tail of a signal plus background distribution below the observation. More precisely,

$$p = \sum_{k=0}^{n} P(k|s+b) = \sum_{k=0}^{n} \frac{(s+b)^k e^{-(s+b)}}{k!}. \tag{4.45}$$

This p value is the probability of observing as few as or fewer events than we did, given an expected signal s and expected background b. The signal plus background $(s+b)$ hypothesis is then excluded at confidence level (CL) $1-p$. Usually, one requires $p = 5\%$, corresponding to a 95% CL exclusion. This means that the probability of excluding the $s+b$ hypothesis if it is true is 5%.

It should be noted that this exclusion is a statement about the $s+b$ hypothesis, not the signal hypothesis itself. Such an approach can give some strange results. In particular, one can obtain very strong limits if the observation falls significantly below the background expectation. In this case, the background hypothesis may itself be excluded at rather high confidence level, and one could question whether the background is really understood. Intuitively, a limit from an experiment where the observation agrees well with the expected background should carry more weight than one from an experiment

where the observation falls significantly below the expected background, but the latter experiment can put a stronger limit on s if the above described procedure is followed.

The CL_s method [29] is an approach in which one can try to make a statement about the signal hypothesis itself rather than only about the signal plus background hypothesis. We define

$$\mathrm{CL}_{s+b} = \sum_{k=0}^{n} P(k|s+b) = \sum_{k=0}^{n} \frac{(s+b)^k e^{-(s+b)}}{k!} \tag{4.46}$$

(the same as the previously defined p value), and

$$\mathrm{CL}_b = \sum_{k=0}^{n} P(k|b) = \sum_{k=0}^{n} \frac{b^k e^{-b}}{k!}. \tag{4.47}$$

Finally, we define CL_s as

$$\mathrm{CL}_s = \frac{\mathrm{CL}_{s+b}}{\mathrm{CL}_b}. \tag{4.48}$$

The quantity CL_s is thus the p value for the $s+b$ hypothesis increased by a factor $1/\mathrm{CL}_b$ which depends on the level of agreement between the observation and the background prediction. It can be thought of as the p value for the signal hypothesis itself, and the signal s is within the CL_s approach excluded at confidence level $1 - \mathrm{CL}_s$.

For the case of no observed events, $n = 0$, we find

$$\mathrm{CL}_s = e^{-s} \quad \Rightarrow \quad s = -\ln \mathrm{CL}_s \approx 3 \tag{4.49}$$

for $\mathrm{CL}_s = 5\%$, i.e. 95% CL exclusion. If no events are observed, any model predicting 3 signal events is excluded at 95% CL.

4.10 Expectations for discovery and exclusion potentials with early 10 TeV data

We now want to evaluate the potential for discovery and exclusion of a SM-like W' with early ATLAS data at $\sqrt{s} = 10\,\mathrm{TeV}$. The "cut and count" approach is used, in which we make a cut at some value of the transverse mass, and count the number of expected signal and background events above the cut value. The expected signal s and background b are then inserted into equation (4.44) for the significance.

4.10.1 Optimizing the transverse mass cut

Where to make the transverse mass cut for significance calculations should be determined by optimizing the significance. A low cut gives more signal, but also more background, while a high cut gives less background, but also less signal. Figure 4.27 shows the significance as function of the transverse mass cut value for three W' masses with an integrated luminosity of $10\,\mathrm{pb}^{-1}$. The significance is shown independently for electron and muon channels.

We see that the optimal cut value is independent of the channel considered. In reference [24] it is claimed that a cut value $m_\mathrm{T} = 0.7 m_{W'}$ optimizes the significance, and this cut value is there used for significance calculations. From figure 4.27, it is clear that $m_\mathrm{T} = 0.7 m_{W'}$ is a very good approximation to the optimal cut value also in this study, and this cut will therefore be used in the following significance calculations.

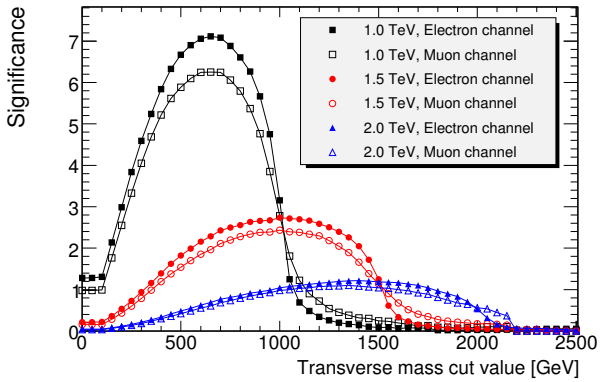

Figure 4.27: Significance as function of the transverse mass cut value for three W' masses in electron and muon channels for $10\,\mathrm{pb}^{-1}$ of integrated luminosity.

Note that the optimal cut value is clearly independent of the integrated luminosity considered, since an increase of the integrated luminosity by a factor α corresponds to increases of both s and b by this factor, and therefore an increase of the significance by a factor $\sqrt{\alpha}$, as seen from equation (4.44).

4.10.2 Discovery limits with early data

To estimate the highest possible mass of a W' which can be discovered with a given integrated luminosity, we make a plot of the number of expected events from a W' and the number of signal events which is needed for discovery as functions of the W' mass. The intersection of these functions gives approximately the heaviest W' which can be discovered with this integrated luminosity. (The reason for the dependence of the required number of signal events for discovery on the W' mass is that the expected background depends on the transverse mass cut.) By discovery, we mean $Z = 5$ (5σ).

The discovery limit plot is shown for $10\,\mathrm{pb}^{-1}$ in the electron and muon channels in figure 4.28. The discovery limit is $m_{W'} = 1.15\,\mathrm{TeV}$ in the electron channel and $m_{W'} = 1.1\,\mathrm{TeV}$ in the muon channel. In both single channels, a W' barely beyond the Tevatron 95% CL exclusion limit ($m_{W'} > 1.0\,\mathrm{TeV}$) can be discovered.

For the significance of the combined search, we use simply $s = s_e + s_\mu$ and $b = b_e + b_\mu$ where s_e (b_e) and s_μ (b_μ) are the expected signals (backgrounds) in the electron and muon channels respectively. Note that the sum of two Poisson distributed variables is itself Poisson distributed. Simply summing the events of the two channels is not the optimal way of doing a combined search, but the gain of a more sophisticated approach is expected to be small when the channels are as similar as in this case.

The discovery limit plots for the combined search with $10\,\mathrm{pb}^{-1}$ and $100\,\mathrm{pb}^{-1}$ of integrated luminosity are shown in figure 4.29. We see that a W' of mass 1.3 TeV can be discovered with $10\,\mathrm{pb}^{-1}$ and that the limit with $100\,\mathrm{pb}^{-1}$ is $m_{W'} = 2\,\mathrm{TeV}$. With $1\,\mathrm{fb}^{-1}$ of integrated luminosity (figure 4.30), a W' of mass 2.8 TeV can be discovered in the combined search.

We see from the various discovery limit plots that a 5σ excess typically corresponds to 4 or 5 signal events. It is common convention within ATLAS to require 10 signal events for any discovery. The corresponding discovery limits can be read off from the discovery

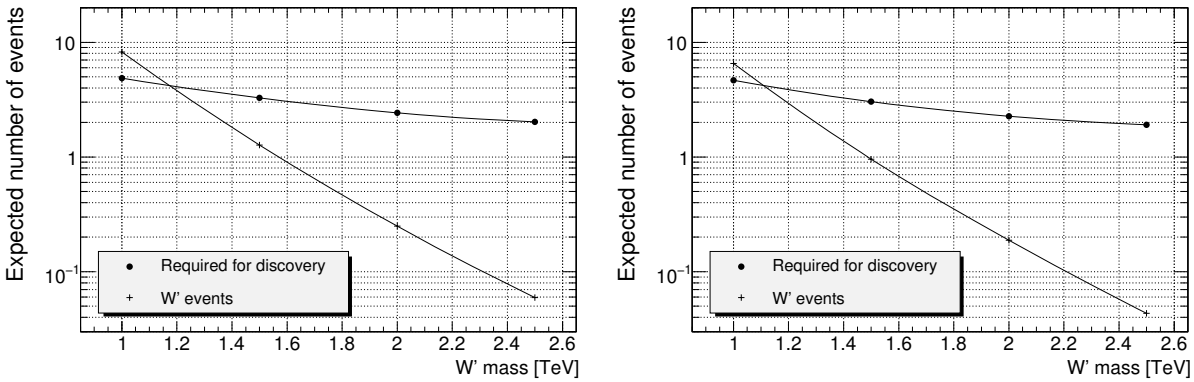

Figure 4.28: Expected number of W' events and number of signal events needed for discovery as functions of the W' mass for $10\,\mathrm{pb}^{-1}$ in the electron (left) and muon (right) channels.

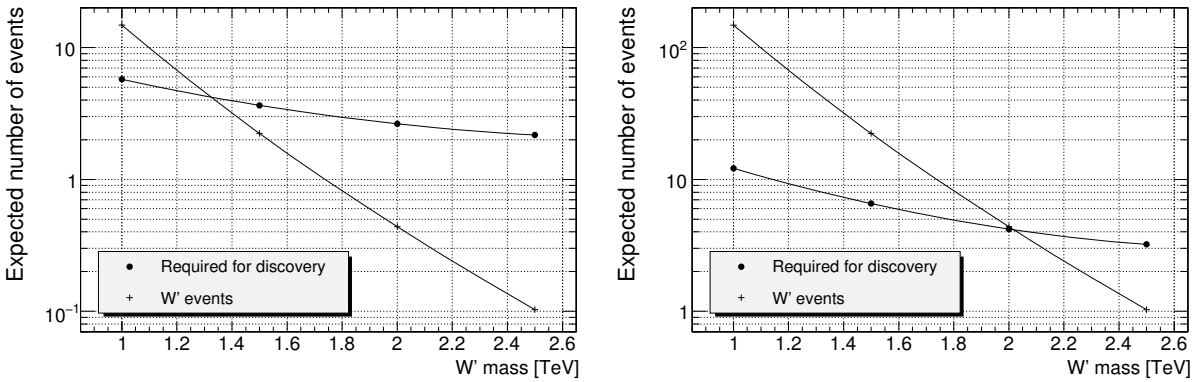

Figure 4.29: Expected number of W' events and number of signal events needed for discovery as functions of the W' mass for the combined search with $10\,\mathrm{pb}^{-1}$ (left) and $100\,\mathrm{pb}^{-1}$ (right) of integrated luminosity.

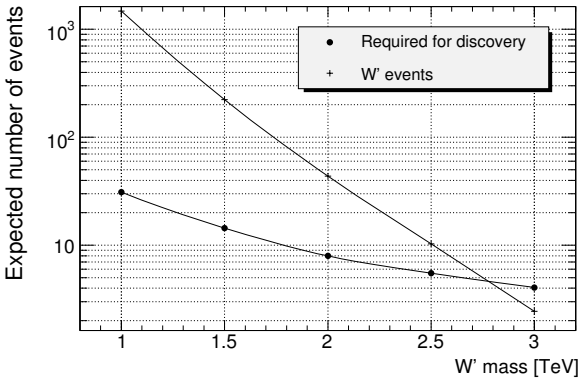

Figure 4.30: Expected number of W' events and number of signal events needed for discovery as functions of the W' mass for the combined search with $1\,\mathrm{fb}^{-1}$ of integrated luminosity.

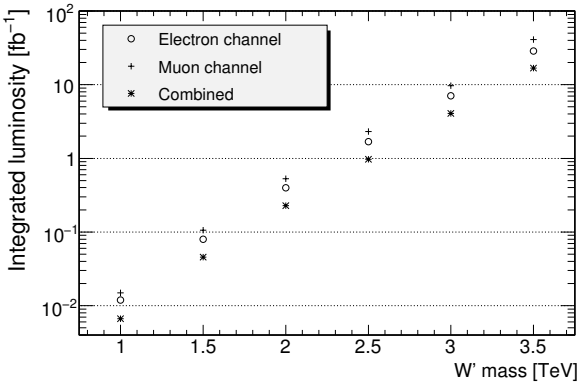

Figure 4.31: Integrated luminosity required for 10 signal events as function of the W' mass for electron and muon channels and the combined search.

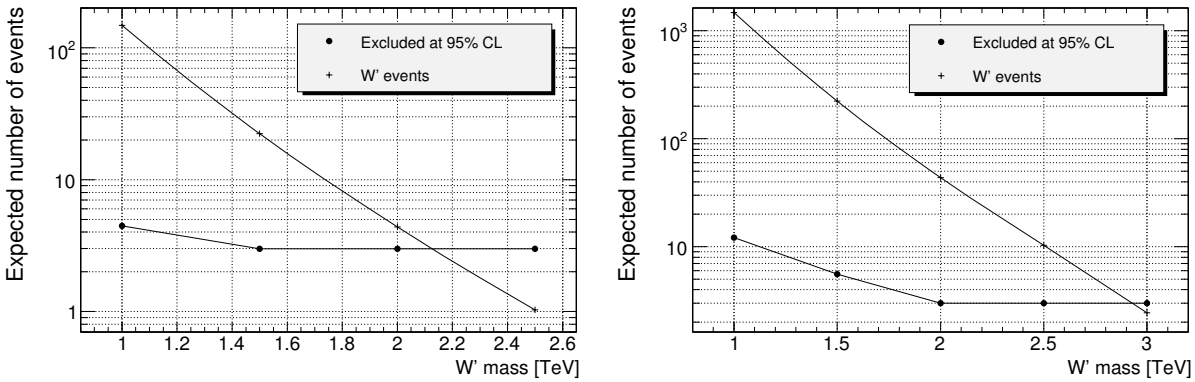

Figure 4.32: Expected number of W' events and number of signal events excluded at 95% CL as functions of the W' mass for the combined search with $100\,\mathrm{pb}^{-1}$ (left) and $1\,\mathrm{fb}^{-1}$ (right).

limit plots. For $10\,\mathrm{pb}^{-1}$, $100\,\mathrm{pb}^{-1}$, and $1\,\mathrm{fb}^{-1}$ in the combined search, the 10 event limits are respectively 1.1 TeV, 1.75 TeV, and 2.5 TeV.

Figure 4.31 shows the integrated luminosity required for 10 signal events as function of the W' mass for electron and muon channels and the combined search for all the simulated W' masses. For the heaviest simulated mass, $m_{W'} = 3.5\,\mathrm{TeV}$, the required integrated luminosity for 10 signal events in the combined search is just below $20\,\mathrm{fb}^{-1}$.

4.10.3 Exclusion potential

To find which limit can be put on the W' mass at 95% CL for a given integrated luminosity, we make a plot of expected number of events from the W' and the excluded value of s as functions of the W' mass. The excluded value of s is calculated as described in section 4.9.3. For this calculation, the observation n is required. It is here set equal to the most probable value of the background distribution, since exclusion is relevant when no hint of signal is seen.

Figure 4.32 shows the exclusion limit plots for the combined search with $100\,\mathrm{pb}^{-1}$ and $1\,\mathrm{fb}^{-1}$ of integrated luminosity. We obtain the constraints $m_{W'} > 2.1\,\mathrm{TeV}$ and $m_{W'} > 2.9\,\mathrm{TeV}$ at 95% CL for these integrated luminosities respectively.

We note that since the W' search corresponds to a case where $s \gg b$, the exclusion limit is exactly where the expected signal is three events. Note that the integrated luminosity required to exclude any of the W' masses can thus be read from figure 4.31 by scaling the integrated luminosity for 10 events by a factor 3/10.

4.11 Expectations for discovery and exclusion potentials with early 7 TeV data

At the time of this writing, it has become clear that the first high energy running of the LHC will take place with a proton-proton center of mass energy $\sqrt{s} = 7\,\text{TeV}$. It was earlier believed that this energy would be 10 TeV, and that is why all existing MC production consists of events generated at $\sqrt{s} = 10\,\text{TeV}$, including the samples used in this W' study. The fact that the LHC will run first at $\sqrt{s} = 7\,\text{TeV}$ leaves the early 10 TeV data study (section 4.10) as a rather academic exercise. The corresponding mass limits at $\sqrt{s} = 7\,\text{TeV}$ are more interesting.

While generating events is a rather quick process, simulating the particles' interactions with the ATLAS detector takes a lot of CPU time. No fully simulated W' signal samples and high mass W background samples exist for $\sqrt{s} = 7\,\text{TeV}$ at the time of this writing. There are (at least) three ways of estimating the discovery/exclusion potential at 7 TeV without running full detector simulation:

- generating events at 7 TeV and running fast detector simulation (AtlFast [30]),
- using the simulated events at 10 TeV and changing the cross section of each data sample to the 7 TeV cross section,
- using the simulated events at 10 TeV and reweighting from 10 TeV to 7 TeV on an event by event basis.

The event by event rescaling technique is used in this study.

The idea of event by event reweighting (PDF reweighting) is that any hard scattering process (where both partons have momentum $p < 3.5\,\text{GeV}$) occuring in 10 TeV proton-proton collisions with differential cross section

$$\frac{d\sigma}{dp_1\,dp_2}(10\,\text{TeV}) = f_1(x_1, q^2) f_2(x_2, q^2)\, d\hat{\sigma}(p_1, p_2)\, \frac{dx_1}{dp_1}\, \frac{dx_2}{dp_2} \tag{4.50}$$

could also occur in 7 TeV proton-proton collisions with differential cross section

$$\frac{d\sigma}{dp_1\,dp_2}(7\,\text{TeV}) = f_1(x_1', q^2) f_2(x_2', q^2)\, d\hat{\sigma}(p_1, p_2)\, \frac{dx_1'}{dp_1}\, \frac{dx_2'}{dp_2}. \tag{4.51}$$

Here p_i are the parton momenta, f_i are the proton PDFs for the interacting partons 1 and 2, q is the momentum transfer of the interaction, and $d\hat{\sigma}$ is the hard scattering cross section element within some infinitesimal variation of the final state. The hard scattering cross section element is independent of the proton-proton center of mass energy. The momentum fractions of the partons in 10 TeV pp collisions are x_1 and x_2, and the corresponding momentum fractions at 7 TeV are $x_i' = 10x_i/7$. For the event scale factor w, we have thus

$$w = \frac{d\sigma/(dp_1\,dp_2)(7\,\text{TeV})}{d\sigma/(dp_1\,dp_2)(10\,\text{TeV})} = \left(\frac{10}{7}\right)^2 \frac{f_1(x_1', q^2) f_2(x_2', q^2)}{f_1(x_1, q^2) f_2(x_2, q^2)}, \tag{4.52}$$

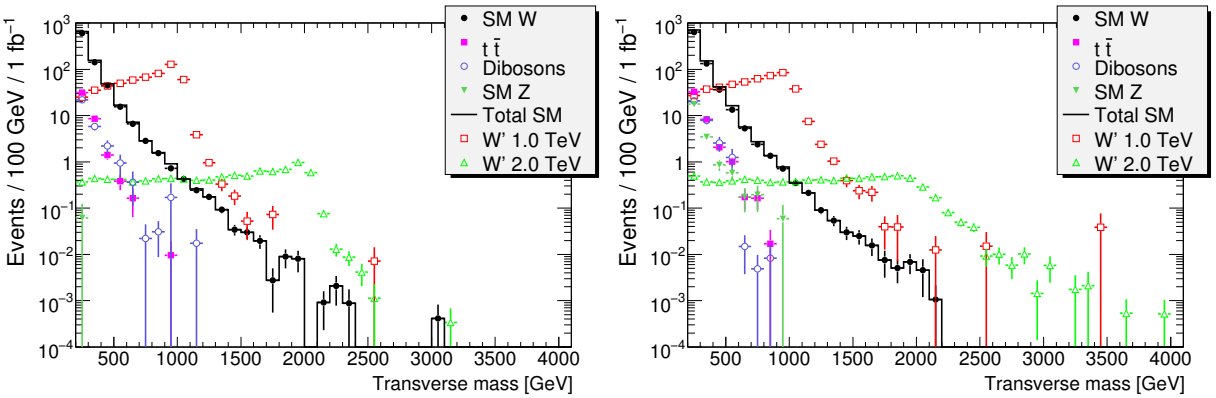

Figure 4.33: Transverse mass distributions at $\sqrt{s} = 7\,\text{TeV}$ in electron (left) and muon (right) channels.

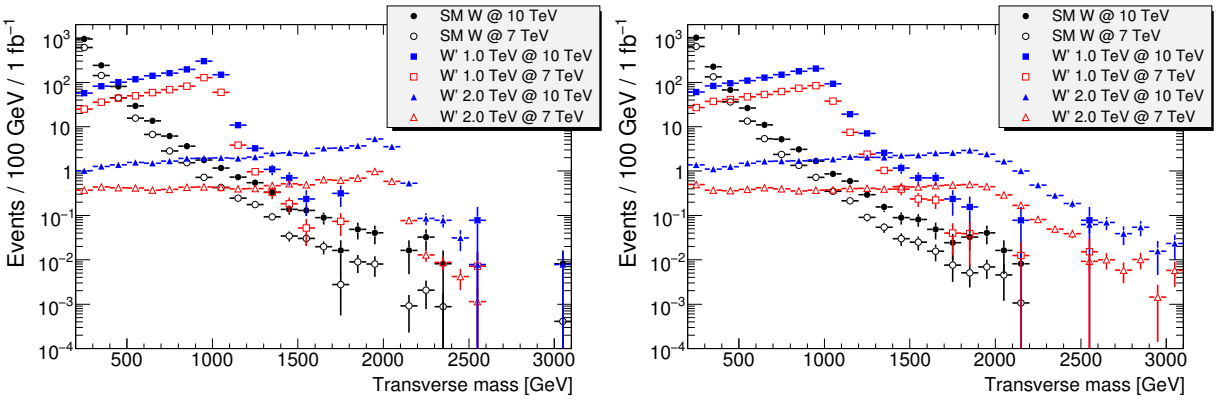

Figure 4.34: Transverse mass distributions at $\sqrt{s} = 7\,\text{TeV}$ and $\sqrt{s} = 10\,\text{TeV}$ in electron (left) and muon (right) channels for signals and high mass W background.

where we have used that $dx_i/dp_i = 2/(10\,\text{TeV})$ and $dx_i'/dp_i = 2/(7\,\text{TeV})$ ($x_i = 2p_i/\sqrt{s}$).

For this study, PDF reweighting is done using the `PDFTool` [31].

4.11.1 Transverse mass distributions at 7 TeV

Figure 4.33 shows the transverse mass distributions of signals and backgrounds after cuts reweighted to $\sqrt{s} = 7\,\text{TeV}$. The shapes of the distributions are very similar to the 10 TeV case, but the cross sections are decreased. The $m_{l\nu} < 200\,\text{GeV}$ SM W sample has not been rerun with reweighting, since this sample did not contribute any events in the signal region after cuts. Note that this will necessarily also be the case at 7 TeV when we are using reweighting, since we are then using exactly the same events as in the 10 TeV study. Also, the dijet background has not been rerun since only one event contributed in the signal region after cuts.

Figure 4.34 shows the 7 TeV and 10 TeV transverse mass distributions after cuts together for signals and the dominant SM W background. We see that the relative decrease in cross section is larger for the higher mass interactions. This is seen both from the difference between the decreases of the 1 TeV and 2 TeV W' distributions, and from the continously increasing difference between the SM W distributions as function of the transverse mass.

The ratio of 10 TeV to 7 TeV number of expected events for signal and background at

W' mass	1.0 TeV	1.5 TeV	2.0 TeV	2.5 TeV
Signal $N(10\,\text{TeV})/N(7\,\text{TeV})$	2.41	3.47	5.43	9.34
Background $N(10\,\text{TeV})/N(7\,\text{TeV})$	2.43	3.08	4.26	6.47

Table 4.7: Ratios between number of expected events N at 10 TeV and 7 TeV for signal and background at different W' masses.

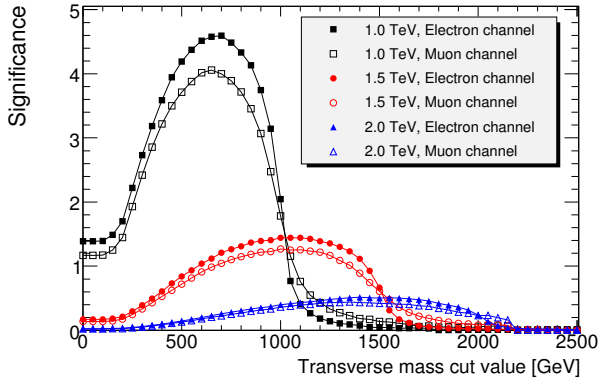

Figure 4.35: Significance as function of the transverse mass cut value for three W' masses in electron and muon channels for $10\,\text{pb}^{-1}$ of integrated luminosity at $\sqrt{s} = 7\,\text{TeV}$.

the different W' masses after cuts are shown in table 4.7. The background is the sum of all background, but it is of course dominated by the SM W. The numbers of events are calculated with the cut $m_\text{T} > 0.7 m_{W'}$. Again we see that the higher mass interactions are reduced by a greater factor, and that this is the case both for signal and background. The different reductions of the background for different transverse mass cuts could not be reproduced by a global dataset reweighting (i.e. using the 7 TeV cross section). In this case, the high mass W sample would get one global factor, and this factor would be the reduction of the background regardless of the transverse mass region considered.

4.11.2 Discovery and exclusion limits

The significance as function of the transverse mass cut value at $\sqrt{s} = 7\,\text{TeV}$ is shown in figure 4.35. We see that the cut $m_\text{T} > 0.7 m_{W'}$ is still a good approximation to the optimal cut value at this energy.

Figure 4.36 shows the discovery limit plots (as described in section 4.10.2) for $10\,\text{pb}^{-1}$, $100\,\text{pb}^{-1}$, and $1\,\text{fb}^{-1}$ at $\sqrt{s} = 7\,\text{TeV}$. The corresponding largest discoverable W' masses are 1.1 TeV, 1.6 TeV, and 2.15 TeV respectively. We can still go barely beyond the Tevatron limit with $10\,\text{pb}^{-1}$. The 10 event limits for $100\,\text{pb}^{-1}$ and $1\,\text{fb}^{-1}$ are 1.4 TeV and 1.95 TeV respectively. Figure 4.37 shows the integrated luminosity for 10 signal events as function of the W' mass.

The exclusion limit plots (as described in section 4.10.3) for $100\,\text{pb}^{-1}$ and $1\,\text{fb}^{-1}$ are shown in figure 4.38. The limits on the W' mass at 95% CL are 1.65 TeV and 2.25 TeV respectively. The latter limit is particularly interesting, since $1\,\text{fb}^{-1}$ is the integrated luminosity which is expected to be accumulated before the LHC is shut down and prepared for higher energies.

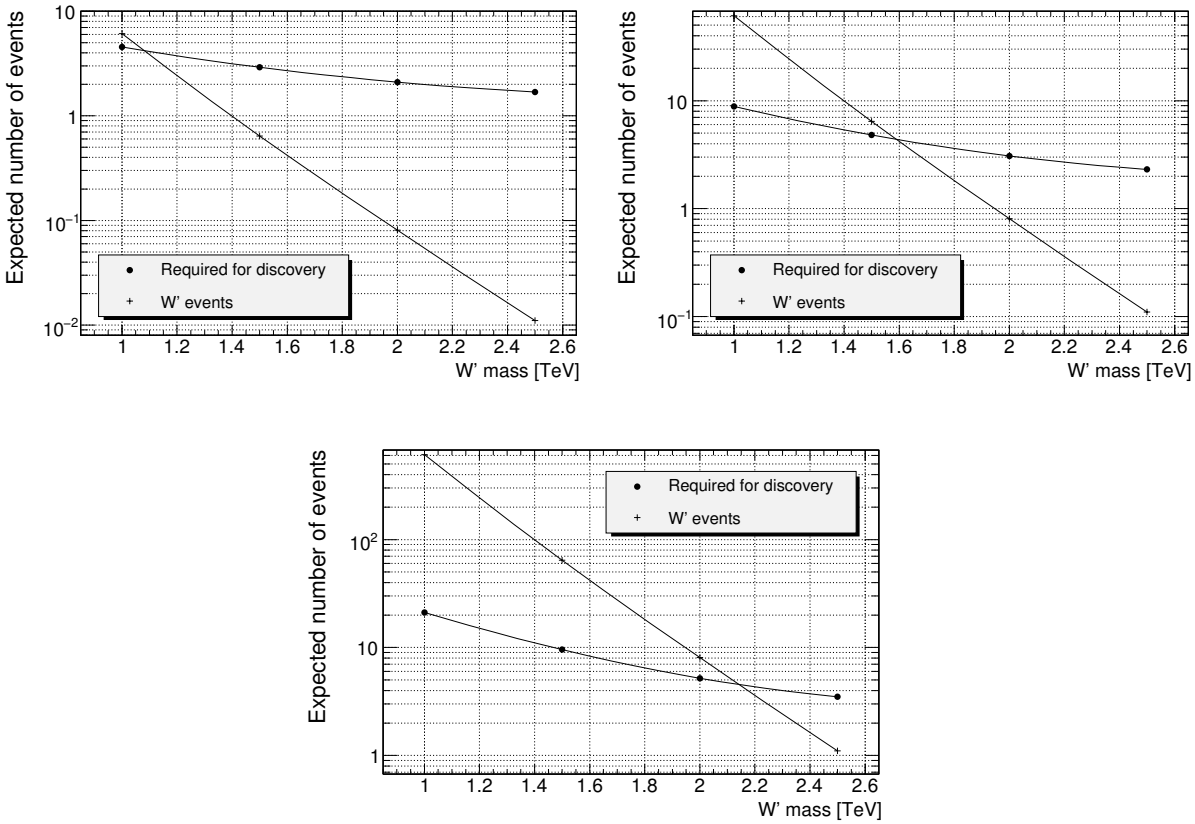

Figure 4.36: Expected number of W' events and number of signal events needed for discovery as functions of the W' mass for the combined search with $10\,\mathrm{pb}^{-1}$ (top left), $100\,\mathrm{pb}^{-1}$ (top right), and $1\,\mathrm{fb}^{-1}$ (bottom) of integrated luminosity.

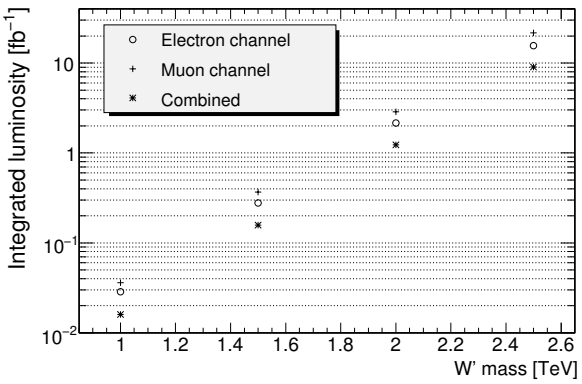

Figure 4.37: Integrated luminosity required for 10 signal events as function of the W' mass.

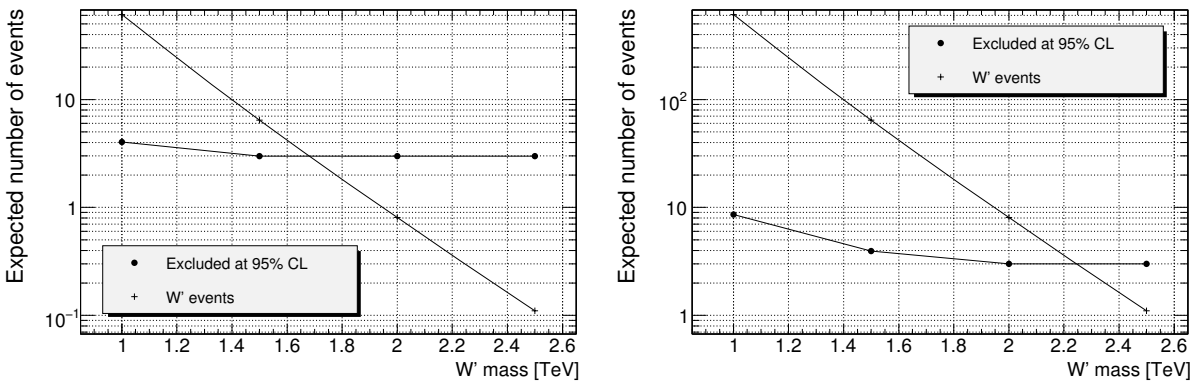

Figure 4.38: Expected number of W' events and number of signal events excluded at 95% CL as functions of the W' mass for the combined search with $100\,\mathrm{pb}^{-1}$ (left) and $1\,\mathrm{fb}^{-1}$ (right).

4.12 Supersymmetry and Z' contributions to the transverse mass spectrum

It is interesting to examine how processes beyond the Standard Model (BSM) other than a W' may contribute to the transverse mass spectrum. In particular, to see whether other BSM processes may produce an excess of events at high transverse mass, and thus possibly mimic a W' signal. We consider here possible contributions from supersymmetry (SUSY) and Z'. These contributions are examined at $\sqrt{s} = 10\,\mathrm{TeV}$.

SUSY models postulate supersymmetric partners of all SM particles. A SM fermion has a bosonic partner, while a SM boson has a fermionic partner. A theoretically pleasing consequence of SUSY is that loop diagram contributions to the Higgs mass from a SM particle is partially cancelled (exactly cancelled if SUSY were not broken) by its superpartner. This solves the hierarchy problem (section 1.7). An overview of the particle content of SUSY models is shown in figure 4.39. One should note that the Higgs sector is extended compared to the SM. Furthermore, the SUSY partners of the Higgs sector and the SUSY partners of the electroweak gauge bosons mix to form the mass eigenstates (physical particles) called charginos and neutralinos, as depicted in figure 4.39.

Within the SM, the running of the coupling constants with energy does not cause them

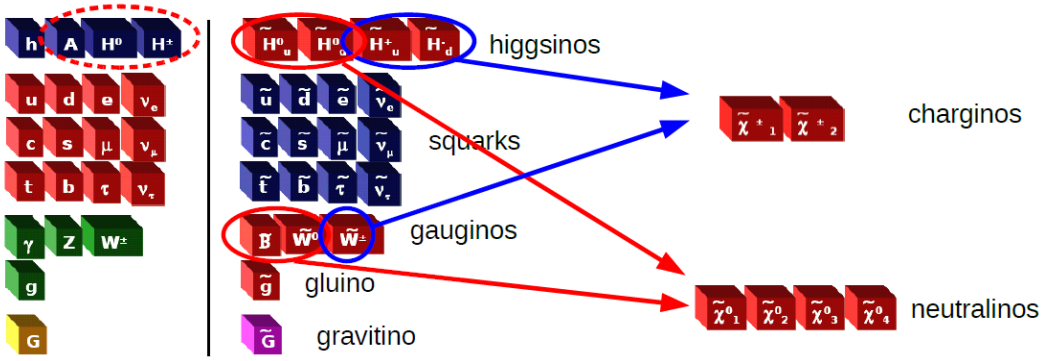

Figure 4.39: Overview of the particle content in SUSY models.

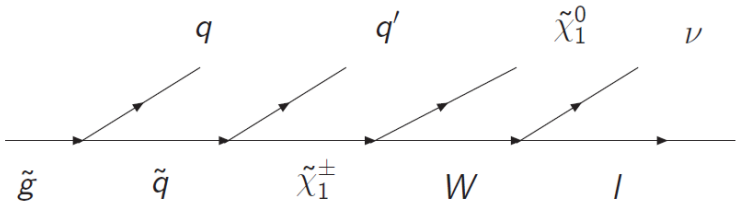

Figure 4.40: Gluino decay chain leading to one lepton and $\not{E}_{\mathrm{T}}$. Here the LSP is the neutralino $\tilde{\chi}_1^0$.

to meet (become equal) at some high energy. Within SUSY models, the coupling constants do meet at high energy, so that grand unification[3] becomes possible. Furthermore, SUSY may provide an explanation for the shape of the Higgs potential.

If so-called R-parity is conserved, then sparticles (SUSY partners of SM particles) must couple to SM particles in pairs. This means that sparticles are produced in pairs, and that the lightest sparticle must be stable. The lightest sparticle (LSP) is thus a candidate to explain dark matter. In an experimental context, the LSP is a source of missing transverse momentum. Various decay chains of sparticles may give a one lepton final state. With the addition of $\not{E}_{\mathrm{T}}$ from the LSP, SUSY events may give a W'-like signature. Figure 4.40 shows an illustration of a gluino decay chain leading to one lepton and $\not{E}_{\mathrm{T}}$ (both LSP and neutrino).

The Z' is a generic name of neutral gauge bosons appearing in BSM theories. As in the case of the W', the Z' properties are also model dependent. Considered here is the SM-like Z', which is a heavier copy of the SM Z^0 boson. The Z' may, as the SM Z boson, decay into two leptons, $Z' \to l^+ l^-$. The Z' may thus contribute to the one lepton final state if one of the leptons is not reconstructed.

It is interesting to examine the Z' because a Z' may appear together with a W' in some models. Their masses could be related, such as the masses of the SM Z and W bosons.

SUSY and Z' datasets and cross sections are shown in table 4.8. The SUSY models used are minimal supergravity (mSUGRA) models, and the different models SUX correspond to different points in mSUGRA parameter space. The particular SUX models used are arbitrarily chosen.

4.12.1 Distributions before cuts

Figures 4.41 and 4.42 show the p_{T}, $\not{E}_{\mathrm{T}}$, and m_{T} distributions after event preselection with non-SM contributions. Note that we now plot the 1.5 TeV W' instead of the 2.0 TeV one, since we consider Z' bosons of 1.0 TeV and 1.5 TeV. However, this is somewhat arbitrary, since in a model with both a W' and a Z', their masses are not necessarily equal.

We see that the SUSY models have many events with large $\not{E}_{\mathrm{T}}$, as expected because of the LSP. The lepton p_{T} in SUSY events is generally not so large, and therefore neither is the transverse mass.

For the Z' distributions, we note the very different contributions in the electron and muon channels. The contribution from Z' is much greater in the muon channel. This is

[3]Grand unification is the idea that the electroweak and strong forces are unified with a single coupling constant at some high energy scale.

Process	Run no.	Recon. tag	MC events	Cross section [fb]
$Z' \to e^+ e^-$, 1.0 TeV	105603	r808_r838	$42 \cdot 10^3$	251
$Z' \to \mu^+ \mu^-$, 1.0 TeV	105601	r808_r838	$30 \cdot 10^3$	254
$Z' \to e^+ e^-$, 1.5 TeV	105624	r808_r838	$15 \cdot 10^3$	76.1
$Z' \to \mu^+ \mu^-$, 1.5 TeV	105625	r808_r838	$15 \cdot 10^3$	77.8
SU1	105401	r808_r838	$10 \cdot 10^3$	2414
SU3	105403	r808_r838	$15 \cdot 10^3$	5477
SU6	105404	r808_r838	$9.0 \cdot 10^3$	1246
SU8	105406	r808_r838	$9.0 \cdot 10^3$	1806

Table 4.8: Non-SM background samples used in the analysis.

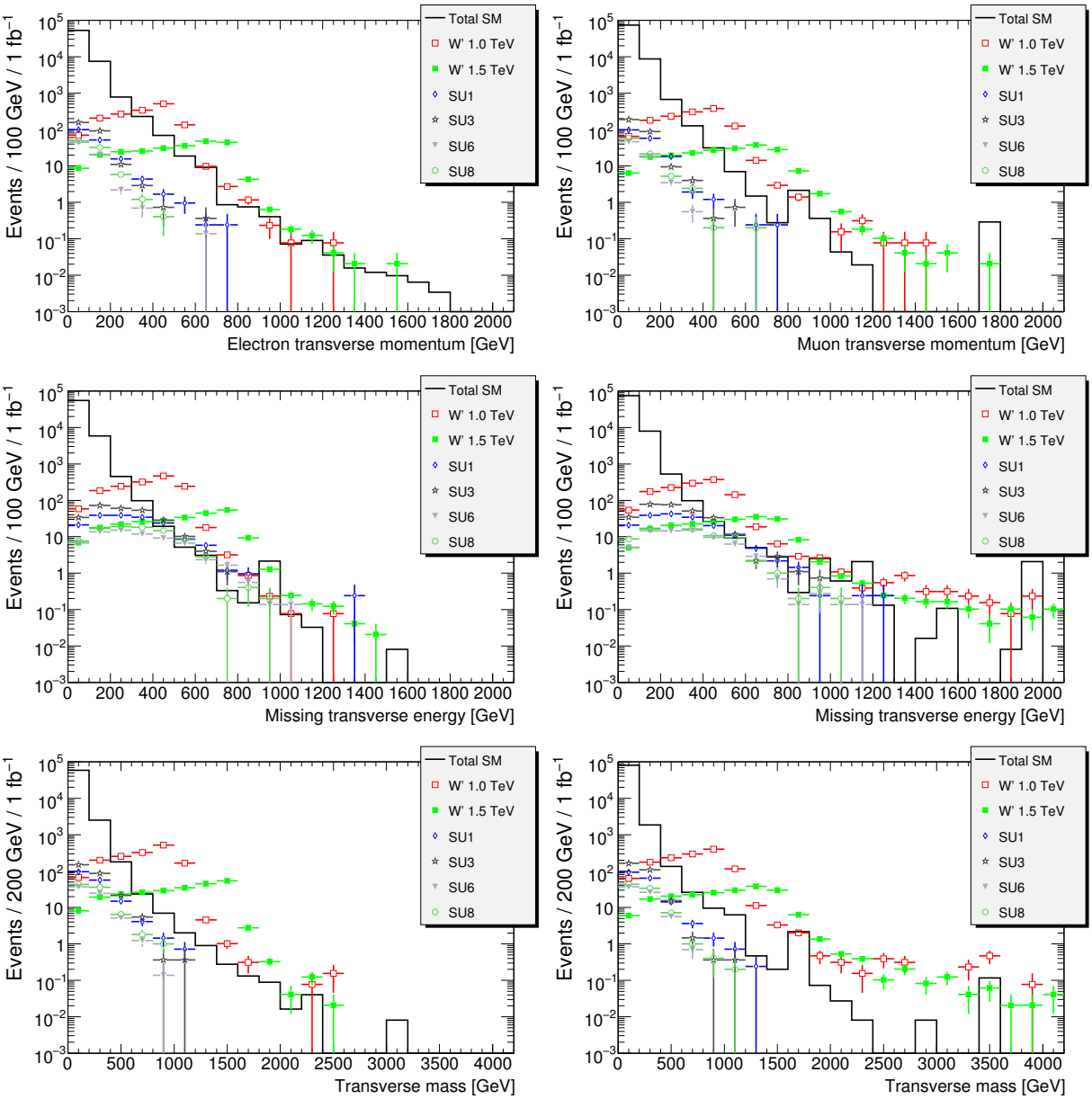

Figure 4.41: Distributions of p_{T}, $\not{E}_{\mathrm{T}}$, and m_{T} in electron (left) and muon (right) channels after event preselection.

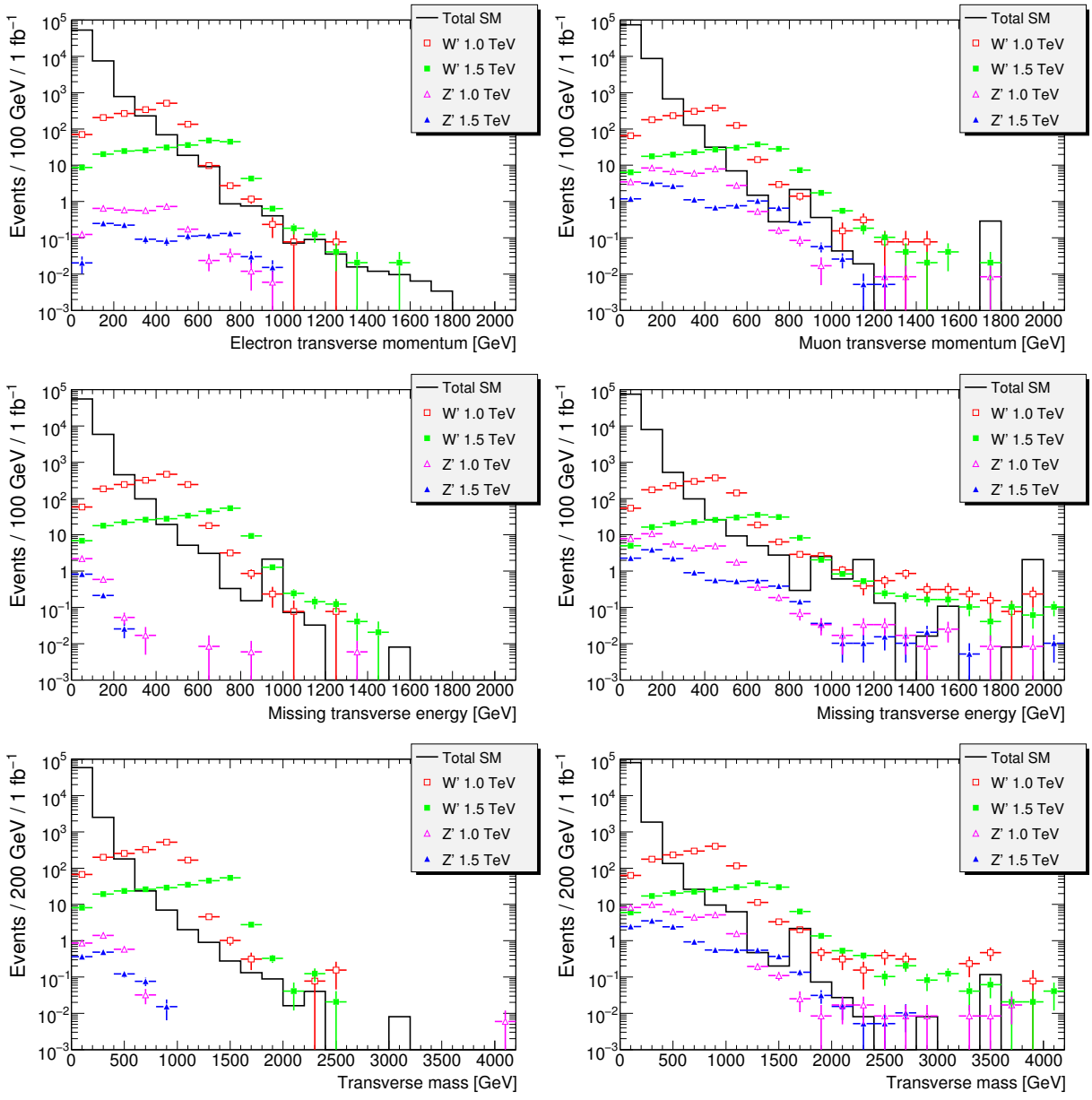

Figure 4.42: Distributions of p_{T}, $\not{E}_{\mathrm{T}}$, and m_{T} in electron (left) and muon (right) channels after event preselection.

explained as follows. In the event preselection, we cut not only on the leading lepton p_{T}, but also on the missing transverse energy. If a muon is not reconstructed, this means that its momentum will not be taken into account when the $\not{E}_{\mathrm{T}}$ is calculated. The result is that the non-reconstructed muon shows up as $\not{E}_{\mathrm{T}}$. (More precisely, if no other sources of $\not{E}_{\mathrm{T}}$ are present, the $\not{E}_{\mathrm{T}}$ will equal the transverse component of the muon's momentum.) A $Z' \to \mu^+ \mu^-$ event where one muon is lost, is thus reconstructed as a one muon event with $\not{E}_{\mathrm{T}}$ balancing the muon p_{T}, i.e. it looks exactly like a W' event.

The same will happen in the electron channel in the rare case where one electron hits a crack in the calorimeter coverage. In the more usual case, when both electrons hit the calorimeters, but only one of them are identified as an electron, the non-reconstructed electron will still enter in the $\not{E}_{\mathrm{T}}$ calculation, and thus the event will have negligible $\not{E}_{\mathrm{T}}$ unless another source of $\not{E}_{\mathrm{T}}$ is present.

The result of this is that $Z' \to e^+ e^-$ events rarely pass the $\not{E}_{\mathrm{T}}$ requirement in the cases when one electron is not reconstructed, but the $Z' \to \mu^+ \mu^-$ events do pass the $\not{E}_{\mathrm{T}}$ requirement in the cases when one muon is not reconstructed. This gives rise to the larger contribution from Z' in the muon channel.

4.12.2 Cut variable distributions

We now examine how the lepton fraction and $p_{\mathrm{T}}/\not{E}_{\mathrm{T}}$ cuts affect the SUSY and Z' contributions. The lepton fraction distributions for Z', W', and SUSY models are shown in figure 4.43.

For SUSY events, the lepton fraction tends to low values, as for the $t\bar{t}$ events. The reason is that SUSY decay chains typically involve several hard jets. In fact, the denominator in the lepton fraction is very similar to the so-called effective mass,

$$M_{\mathrm{eff}} = \not{E}_{\mathrm{T}} + \sum_{\mathrm{jets}} p_{\mathrm{T}}, \tag{4.53}$$

which is used as search variable in SUSY searches, since SUSY events tend to high values of this variable.

For Z' in the electron channel, the lepton fraction distribution is peaked just below 1/2. This is easy to understand. In $Z' \to e^+ e^-$ events, the electrons go back to back with equal momenta. The two electrons are expected to dominate the event, and we thus have $\sum E_{\mathrm{T}} \approx 2E_{\mathrm{T}}^e$ (the unidentified electron also contributes to $\sum E_{\mathrm{T}}$). Furthermore, the $\not{E}_{\mathrm{T}}$ for these events is expected to be small. We thus have

$$f_{\mathrm{lep}} = \frac{E_{\mathrm{T}}^e + \not{E}_{\mathrm{T}}}{\sum E_{\mathrm{T}} + \not{E}_{\mathrm{T}}} \approx \frac{1}{2}. \tag{4.54}$$

The reason why the peak is just below 1/2 is because some other softer activity in the event also contributes to $\sum E_{\mathrm{T}}$. For Z' in the muon channel, the lepton fraction distribution looks very much like the one from W' events, as expected from the discussion in section 4.12.1.

The $p_{\mathrm{T}}/\not{E}_{\mathrm{T}}$ distributions for Z', W', and SUSY models are shown in figure 4.44. Also here, SUSY events tend to lower values than signal events. Again, the Z' looks different in the electron and muon channels. The momentum ratio $p_{\mathrm{T}}/\not{E}_{\mathrm{T}}$ tends to high values for $Z' \to e^+ e^-$ events, since these events have low $\not{E}_{\mathrm{T}}$. The Z' events in the muon channel look very much like W' events also in terms of $p_{\mathrm{T}}/\not{E}_{\mathrm{T}}$.

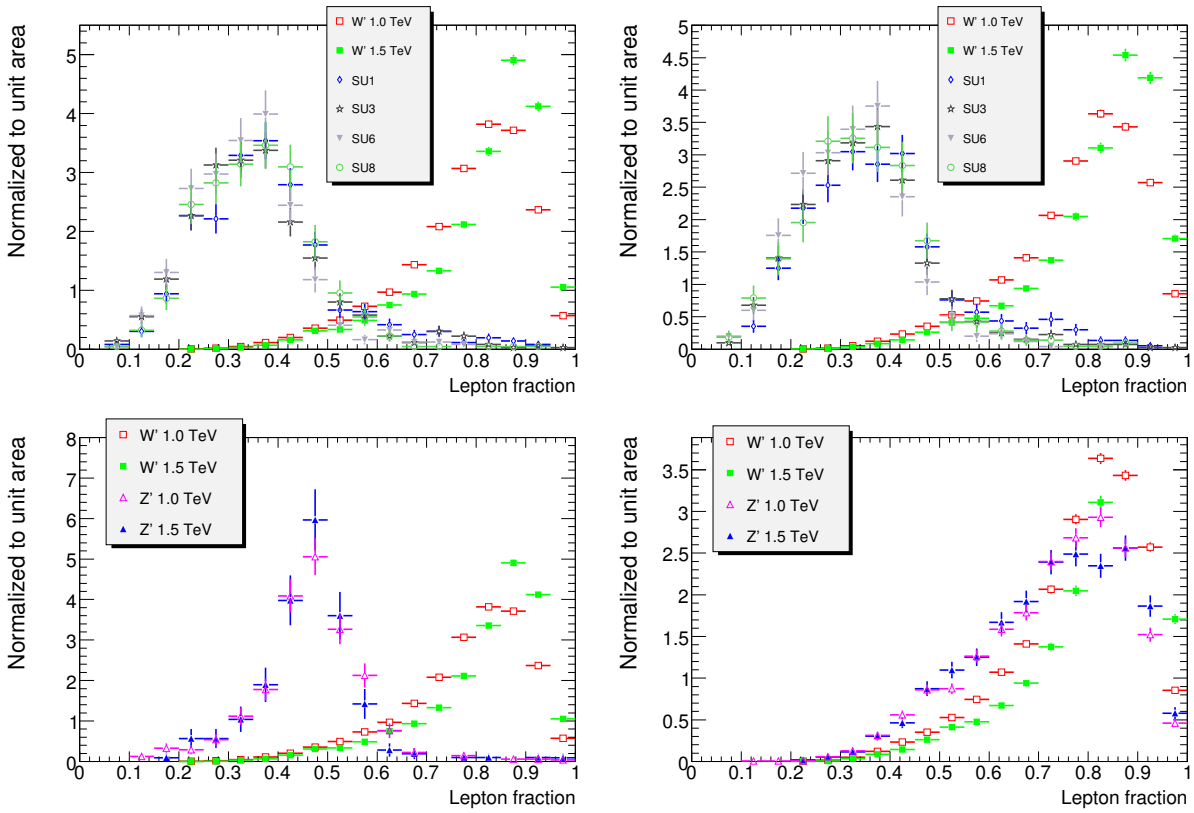

Figure 4.43: Lepton fraction distributions in the electron (left) and muon (right) channels.

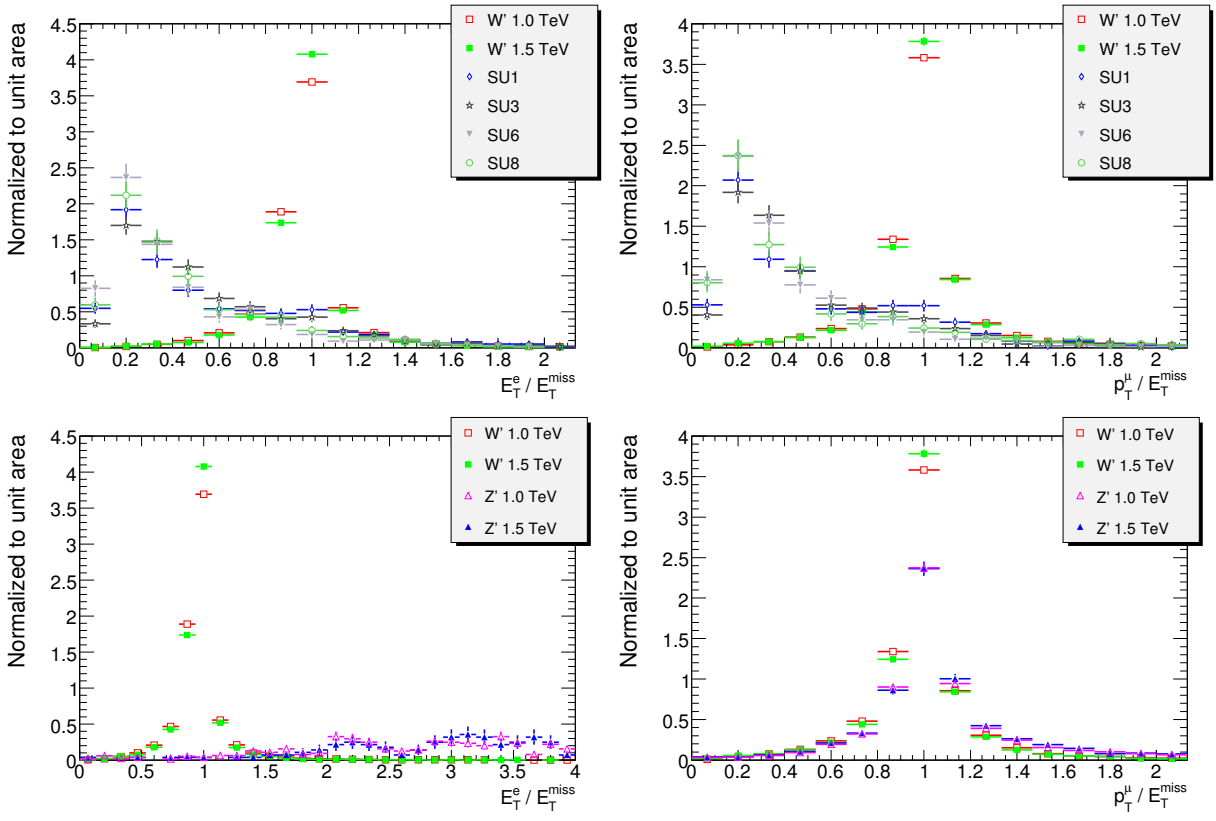

Figure 4.44: Distributions of $p_{\mathrm{T}}/\not{E}_{\mathrm{T}}$ in the electron (left) and muon (right) channels.

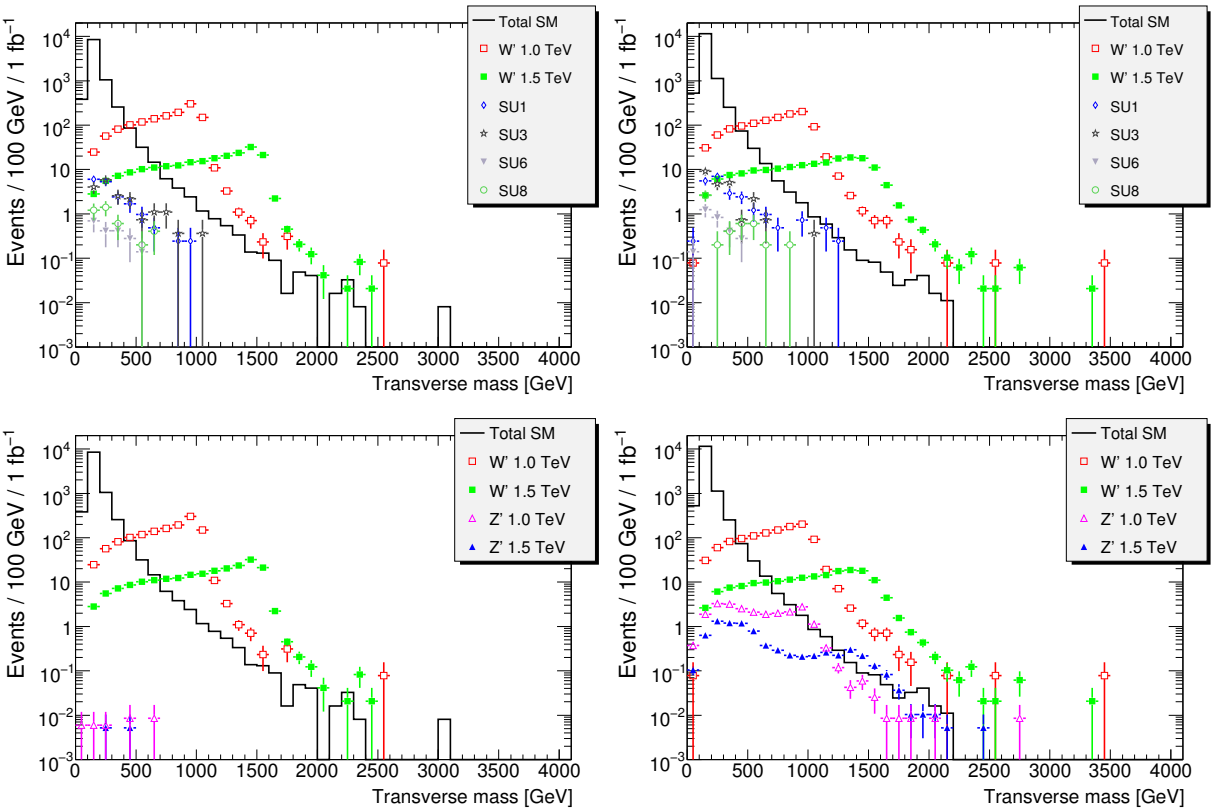

Figure 4.45: Transverse mass distributions in the electron (left) and muon (right) channels after cuts.

4.12.3 Transverse mass distributions after cuts

The transverse mass distributions after cuts are shown in figure 4.45. There are some SUSY events at high transverse mass in both electron and muon channels. The magnitude of this contribution is really not determined by the available statistics, but it seems to be less than the SM W contribution. In any case, an excess of high transverse mass events due to SUSY can be distinguished from one due to a W' by looking at the lepton fraction and $p_{\mathrm{T}}/\not{E}_{\mathrm{T}}$ distributions of the signal events.

In the muon channel, the Z' transverse mass distributions look similar to the W' distributions in shape. With the SM-like Z' cross section, the distributions go just barely above the SM background for some transverse mass ranges. The Z' cross section is of course model dependent, and if the Z' cross section is higher than that of the SM-like Z', a Z' could really produce a W'-like excess of events at high transverse mass.

One could imagine a scenario with a Z' with high enough cross section and no W'. In this case, one would start to see an excess of events at high transverse mass in the muon channel, which could be interpreted as a W' signal. The Z' would of course already at this point be discovered in the dilepton channels. The conclusion is that an excess of high transverse mass events in the muon channel could be from a Z' if such a neutral boson exists. So if a Z' has been discovered and one starts to see an excess of high transverse mass events in the muon channel, one should be aware that this excess may be from the Z'.

4.13 Conclusions

The potential for discovery of a new charged gauge boson W' decaying to lepton and neutrino, where lepton means muon or electron, has been investigated using simulated data at $\sqrt{s} = 10\,\text{TeV}$. As reference model, the SM-like W' has been used. It has been shown that such a boson is detectable by ATLAS as an excess of events at high transverse mass. QCD dijet and $t\bar{t}$ backgrounds have been shown to be reducible, and the dominating background has been identified as the SM W high mass tail.

We have used PDF reweighting to find that the signal cross section is reduced by a factor 2.4 for the 1 TeV W' when the center of mass energy is reduced from 10 TeV to 7 TeV, and higher factors for the larger W' masses. The high mass SM W background is reduced by comparable factors when considering the relevant transverse mass ranges.

For the SM-like W', we have seen that ATLAS becomes sensitive beyond the Tevatron 95% CL exclusion limit even with $10\,\text{pb}^{-1}$ of integrated luminosity at 7 TeV proton-proton center of mass energy. With the $1\,\text{fb}^{-1}$ which is expected to be accumulated at 7 TeV, ATLAS can put a limit on the SM-like W' mass $m_{W'} > 2.25\,\text{TeV}$ at 95% CL. It should be noted that these limits will depend on how well the data is understood. In particular, the $\not{E}_{\text{T}}$ can be a challenge to understand in early data.

Finally, the contributions to the transverse mass spectrum from Z' and SUSY models has been examined. It has been shown that a Z' decaying to two muons may give a W'-like signature when one of the muons is not reconstructed.

4.14 Summary

In this chapter, the prospects for the discovery of a new charged gauge boson decaying to electrons and muons with ATLAS have been investigated using simulated data. In the next chapter, we return to the analysis of real ATLAS data, and look at the very first LHC collision data taken by ATLAS.

Chapter 5

The first LHC collisions in ATLAS

5.1 The 900 GeV minimum bias data

In December 2009, ATLAS saw the first LHC proton-proton collision events. The collisions were made with the injection energy from the SPS, i.e. $\sqrt{s} = 900\,\text{GeV}$. Some collisions were also made with the energy ramped to $\sqrt{s} = 2.36\,\text{TeV}$, thus proving the LHC to be the most powerful particle accelerator ever built. In this section, we look at the 900 GeV collisions, since these constitute a much larger data sample than the $\sqrt{s} = 2.36\,\text{TeV}$ collisions.

The data samples used are all the 900 GeV minimum bias data samples with reconstruction tag `r988`. For MC the 900 GeV minimum bias MC with reconstruction tag `r1023` is used. (A complete list of datasets can be found in appendix A.)

5.1.1 Event selection

When looking at real data, the configuration of the detector in the run considered is of importance. The configuration means in this context the currents in the magnets and the status of the various subdetectors. For example, parts of the 900 GeV minimum bias data was taken with the pixel and SCT detectors at low bias voltage because the LHC had not declared stable beam. For a study of muons, the toroid magnet is crucial, while for a study of electrons, this is not the case. Therefore, the requirements made on the detector configuration depends on the analysis. In ATLAS, one can select "good" luminosity blocks based on any detector configuration requirements using a good runs list (GRL).

When looking at minimum bias data, cuts should also be made to ensure that the event is really a collision event. In this analysis, the files of type `DESD_COLLCAND` are used. These include only events that have been selected as collision candidates based on the timing of the liquid argon end cap calorimeters and the minimum bias trigger scintillators (MBTS). For this analysis, the following additional selection is made to ensure collision events:

- trigger `MBTS_1_1` at level 1,
- $|\Delta t| < 7.5\,\text{ns}$ (defined below),
- reconstructed primary vertex.

The `MBTS_1_1` trigger means that the MBTS has given a signal at both end caps. In addition, we would like these signals to appear at approximately the same time at both

end caps. Therefore the cut on Δt, defined as the difference between the average signal times in end caps A and C, $\Delta t = t_{\mathrm{A}} - t_{\mathrm{C}}$, is made.

5.1.2 V^0 vertices in the inner detector

Masses and lifetimes quoted in this section are from reference [4].

A V^0 particle is a neutral particle decaying to two charged particles, thus drawing a V in a bubble chamber or an event display. Identifying V^0 vertices in the ATLAS inner detector, one can look for known signals as a test of the tracking performance.

The K^0_{S} meson is a mixture of the strangeness eigenstates $K^0 = d\overline{s}$ and $\overline{K^0} = \overline{d}s$. It decays mainly to two pions, $K^0_{\mathrm{S}} \to \pi^+\pi^-$. With a lifetime of $\tau = 0.896 \cdot 10^{-10}\,\mathrm{s}$ giving $c\tau = 2.68\,\mathrm{cm}$, the K^0_{S} is likely to give a secondary vertex in the inner detector. The K^0_{S} mass is $m_{K^0_{\mathrm{S}}} = 497.6\,\mathrm{MeV}$.

Another candidate to provide secondary vertices in the inner detector is the $\Lambda = uds$ strange baryon. The decays $\Lambda \to p\,\pi^-$ and $\overline{\Lambda} \to \overline{p}\,\pi^+$ provide the V^0 signature. The lifetime of the Λ is $\tau = 2.63{\cdot}10^{-10}\,\mathrm{s}$ giving $c\tau = 7.89\,\mathrm{cm}$, and its mass is $m_\Lambda = 1115.7\,\mathrm{MeV}$.

For this study, a standard GRL is used requiring the solenoid magnet and the inner detector to be on (see appendix A). For vertex fitting, the `TrkVKalVrtFitter` tool is used. This tool requires the track masses to be set, and they are here set to the pion mass, $m_\pi = 139.57\,\mathrm{MeV}$, for both tracks. The effect of the track masses on the vertexing procedure should be minimal in any case, so we expect this approach to give good results also for Λ decaying to proton and pion. As input to the vertexing, track pairs are formed from tracks from the `TrackParticleCandidate` container satisfying:

- at least 6 silicon (SCT and pixel) hits,
- at least one pixel hit,
- $p_{\mathrm{T}} > 100\,\mathrm{MeV}$.

If the vertex fit is successful, the vertex fitter returns a χ^2 and a number of degrees of freedom N_{dof} of the fit. A cut $p > 0.1$ is made on the p value of the fit (fit probability)

$$p = \int_{\chi^2_{\mathrm{fit}}}^{\infty} f_{\chi^2}(x; N_{\mathrm{dof}})\,dx \tag{5.1}$$

where $f_{\chi^2}(x; N_{\mathrm{dof}})$ is the PDF of the χ^2 distribution with N_{dof} degrees of freedom. This means that there is in principle a 10% probability to reject a vertex fit of two tracks coming from an actual vertex.

To calculate the invariant mass of the decaying particle,

$$m = \sqrt{(E_1 + E_2)^2 - (\mathbf{p}_1 + \mathbf{p}_2)^2}, \tag{5.2}$$

we must assume some values for the masses m_1 and m_2 of the decay products since

$$E_i = \sqrt{\mathbf{p}_i^2 + m_i^2} \tag{5.3}$$

(the particles can not be assumed to be highly relativistic). The momenta $\mathbf{p}_1$ and $\mathbf{p}_2$ must be taken at the reconstructed vertex position.

Figure 5.1 (left) shows the invariant mass distribution of vertices under the assumption that both decay products are pions. The distributions are shown both for opposite sign

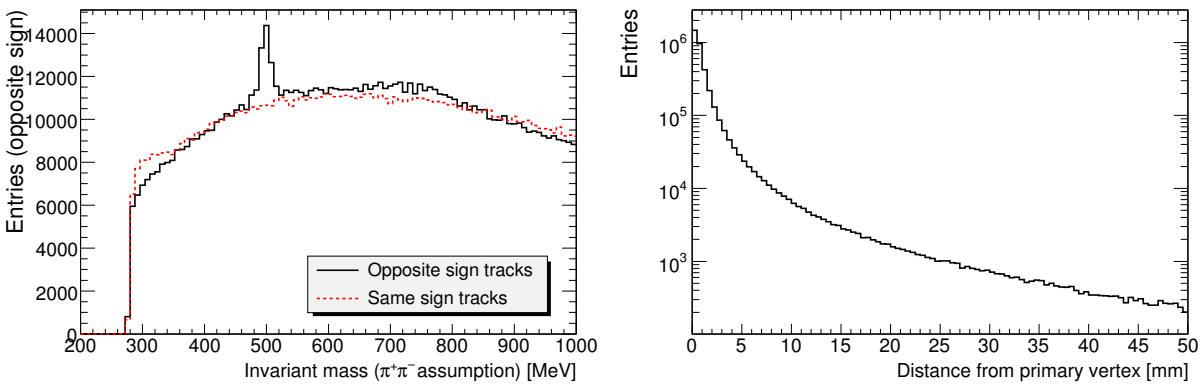

Figure 5.1: Invariant mass of tracks from reconstructed vertices under the assumption that both tracks are pions (left) and the distance of the vertices from the reconstructed primary vertex (right).

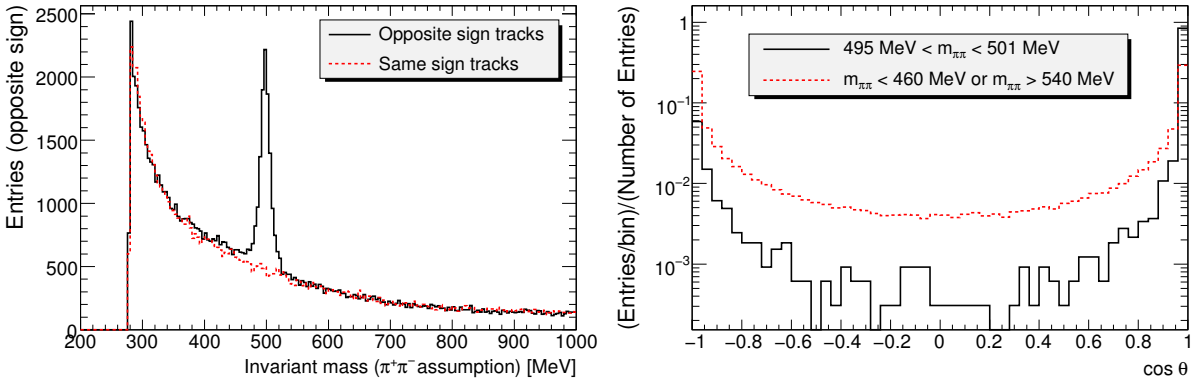

Figure 5.2: Invariant mass of tracks from reconstructed vertices under the assumption that both tracks are pions with the cut $|\mathbf{x}_{\text{sec}} - \mathbf{x}_{\text{prim}}| > 5\,\text{mm}$ (left) and the distribution of $\cos\theta$ for signal dominated and background dominated mass regions for opposite sign tracks (right).

tracks and same sign tracks. The K^0_S peak is clearly seen around 500 MeV for the opposite sign tracks, but not for the same sign tracks, as expected. The same sign distribution has been normalized to the opposite sign distribution to give the same integral in the region $m_{\pi\pi} \notin [400\,\text{MeV}, 600\,\text{MeV}]$. The numbers on the y axis thus correspond only to the number of entries in the opposite sign histogram.

Shown in figure 5.1 (right) is the distribution of the distance from the reconstructed primary vertex to the secondary vertex. The combinatorial background from fake vertices is expected to be larger closer to the primary vertex. We make a cut that the distance to the primary vertex, $|\mathbf{x}_{\text{sec}} - \mathbf{x}_{\text{prim}}|$ where $\mathbf{x}_{\text{sec(prim)}}$ is the position of the secondary (primary) vertex, be greater than 5 mm.

Figure 5.2 (left) shows the invariant mass distribution of track pairs after the cut $|\mathbf{x}_{\text{sec}} - \mathbf{x}_{\text{prim}}| > 5\,\text{mm}$, as well as the distribution of $\cos\theta$ for opposite sign tracks for signal- and background dominated mass regions (right). The angle θ is defined as the angle between the sum of the momenta of the decay products and the vector pointing

from the primary to the secondary vertex, i.e.

$$\cos\theta = \frac{(\mathbf{p}_1 + \mathbf{p}_2) \cdot (\mathbf{x}_{\text{sec}} - \mathbf{x}_{\text{prim}})}{|\mathbf{p}_1 + \mathbf{p}_2|\,|\mathbf{x}_{\text{sec}} - \mathbf{x}_{\text{prim}}|}. \tag{5.4}$$

Since $\mathbf{p}_1 + \mathbf{p}_2 = \mathbf{p}_{V^0}$ for real V^0 vertices, we will have $\cos\theta \approx 1$ for these. This is because the V^0 is coming from the primary vertex and is not bent by the magnetic field. This is clearly seen in figure 5.2 (right), where the signal dominated sample has about ten times more entries in the last bin than in the first bin, while the background dominated sample has approximately equal number of entries in the first and last bins.

Figure 5.3 shows invariant mass distributions under $\pi^+\pi^-$, $p\pi^-$, and $\overline{p}\pi^+$ assumptions for track pairs with final cuts:

- fit p value $p > 0.1$,
- $|\mathbf{x}_{\text{sec}} - \mathbf{x}_{\text{prim}}| > 5\,\text{mm}$,
- $\cos\theta > 0.98$.

The plots on the right hand side show fits to a second degree polynomial plus a Gaussian in the region around the mass peak. Fit parameters with only the statistical uncertainties of the fits are shown in the plot frames. The means are close to the K^0_{S} and Λ masses. For the $p\pi^-$ and $\overline{p}\pi^+$ hypotheses, the assigment of masses to the tracks is done using the measured charges of the tracks. This means that the positive track is given the proton mass for the $p\pi^-$ hypothesis, while it is given the pion mass for the $\overline{p}\pi^+$ hypothesis.

Figure 5.4 shows the Armenteros-Podolanski plot, $p_\perp$ vs. longitudinal asymmetry $(p^+_{\text{L}} - p^-_{\text{L}})/(p^+_{\text{L}} + p^-_{\text{L}})$. Here, $p_\perp$ is the momentum of the decay products in the direction orthogonal to the V^0 direction of motion, and $p^{+(-)}_{\text{L}}$ is the momentum of the positive (negative) track along the V^0 direction of motion, i.e.

$$p^\pm_{\text{L}} = \mathbf{p}^\pm \cdot \mathbf{n}_{V^0} \quad \text{and} \quad p_\perp = \left|\mathbf{p}^\pm - \left(\mathbf{p}^\pm \cdot \mathbf{n}_{V^0}\right)\mathbf{n}_{V^0}\right| \tag{5.5}$$

where $\mathbf{n}_{V^0} = \mathbf{p}_{V^0}/\,|\mathbf{p}_{V^0}|$ is the unit vector along the V^0 direction of motion. (Note that $p^+_\perp = p^-_\perp \equiv p_\perp$ since $\mathbf{p}_{V^0} = \mathbf{p}^+ + \mathbf{p}^-$).

The visible arc in the Armenteros-Podolanski plot is due to K^0_{S} decays. Smaller arcs due to Λ and $\overline{\Lambda}$ decays are not visible over the background.

5.1.3 Electron candidates

The study of V^0 vertices in the inner detector provides "standard candles" for testing the tracking performance, since the masses of the V^0 particles are already known. For the study of electrons, "standard candles" are for example the decays $J/\psi \to e^+\,e^-$ and $Z^0 \to e^+\,e^-$. However, the 900 GeV minimum bias data does not constitute a large enough data sample to see these decays. For example, the cross section for $p\,p \to Z^0 + X \to e^+e^- + X$ at $\sqrt{s} = 900\,\text{GeV}$ is of order 10 pb, while the integrated luminosity of the December 2009 minimum bias 900 GeV data is estimated to be of order $10\,\mu\text{b}^{-1}$. In fact, almost no real electrons, except for some secondaries and conversion electrons, exist in these data. What is done in this section is therefore a data/MC comparison for electron candidates, which are mainly hadronic fakes, to see whether the ATLAS electron reconstruction is performing as expected from MC.

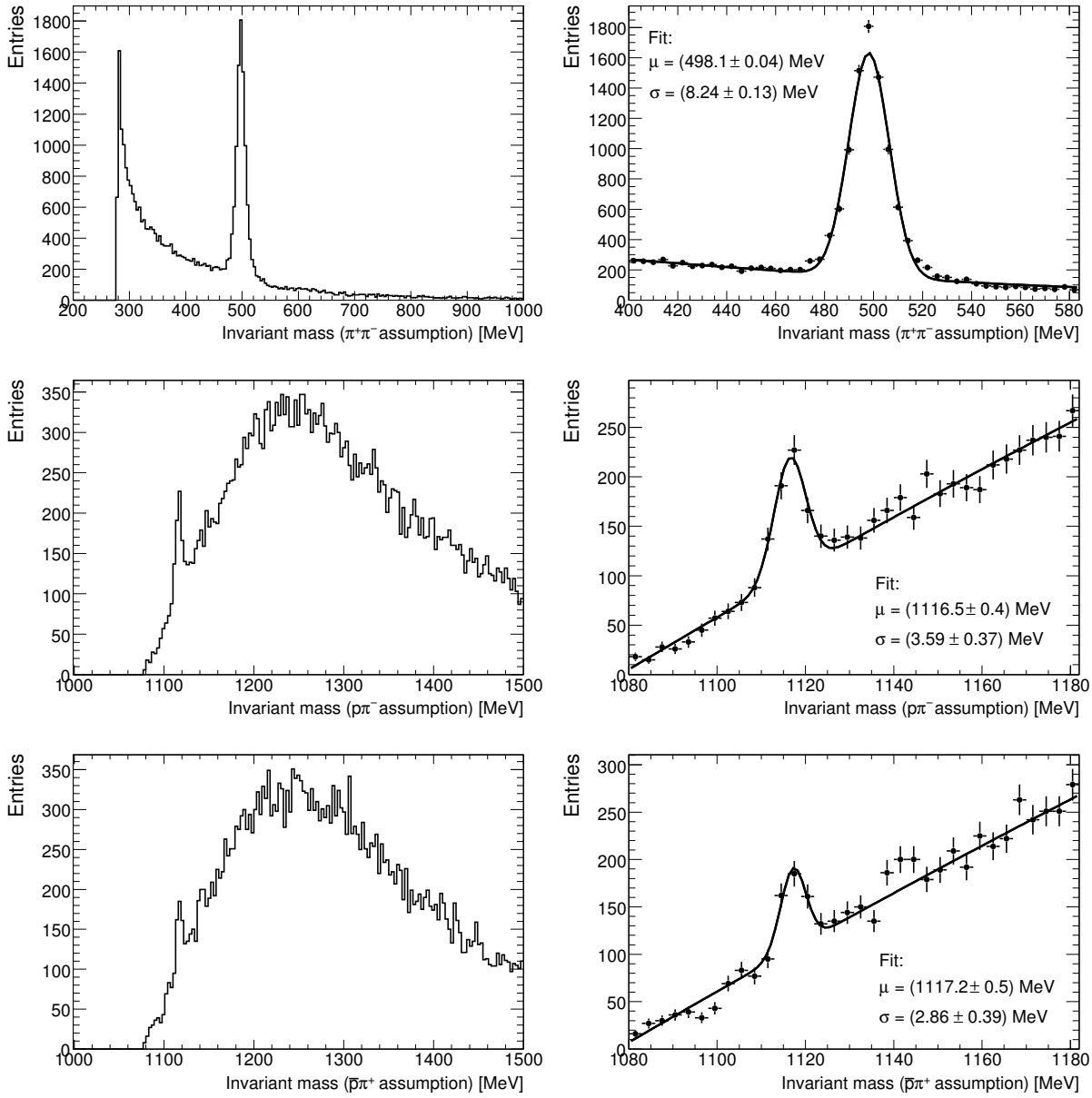

Figure 5.3: Invariant mass distributions with different decay product hypotheses (left) and fits to second degree polynomials plus Gauss peaks around the peak regions (right). Only opposite sign track pairs are used for the plots. The decay product hypotheses are $\pi^+\pi^-$ (top), $p\pi^-$ (middle), and $\overline{p}\pi^+$ (bottom).

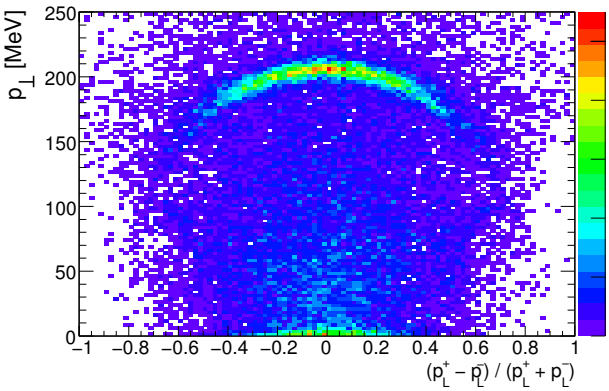

Figure 5.4: Armenteros-Podolanski plot. The perpendicular and longitudinal directions are defined relative to the V^0 direction of motion.

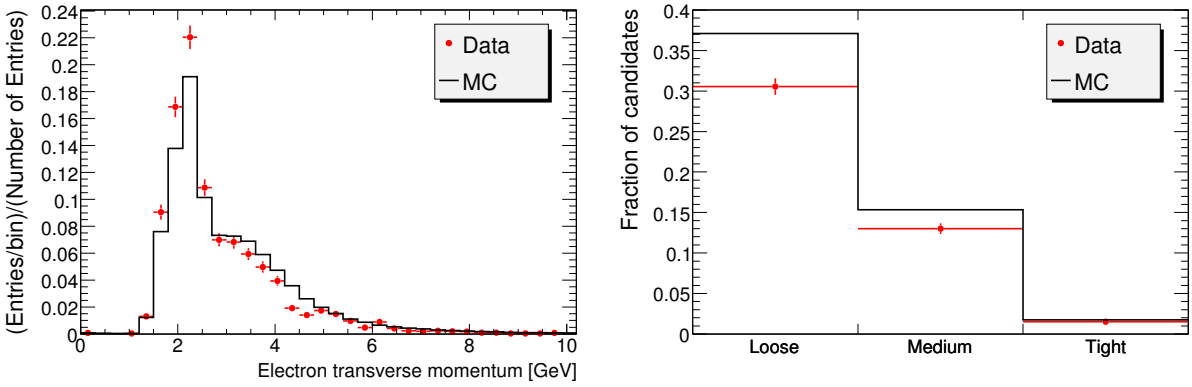

Figure 5.5: Transverse momentum distribution for all electron candidates within $|\eta| < 2.5$ (left) and fractions of these candidates satisfying loose, medium, and tight selection criteria (right).

Electrons are selected from the `ElectronAODContainer`. For the study of electron candidates, the status of the inner detector, solenoid magnet, and calorimeters is important. The performance of these systems in the events used for the study is assured using a GRL from the e/γ combined performance group.

Electron candidates are only considered in the pseudorapidity region $|\eta| < 2.5$. The transverse momentum distribution of all electron candidates is shown in figure 5.5 (left). Figure 5.5 (right) shows the fractions of electron candidates satisfying the loose, medium, and tight electron selection criteria (see section 4.8.1). The η and ϕ distributions of all electron candidates are shown in figure 5.6.

For the p_{T} distribution, reasonable agreement is seen between data and MC, although the MC is somewhat shifted towards higher p_{T} relative to the data. For the fractions of loose, medium, and tight electrons, we see that the MC has more loose and medium electrons compared to the data. The angular distributions η and ϕ show good agreement between data and MC.

In the following, only electron candidates satisfying the loose criteria are used for the data/MC comparison. Figure 5.7 shows the transverse momentum and E/p distributions for these electron candidates. Good agreement is seen in both distributions, although the

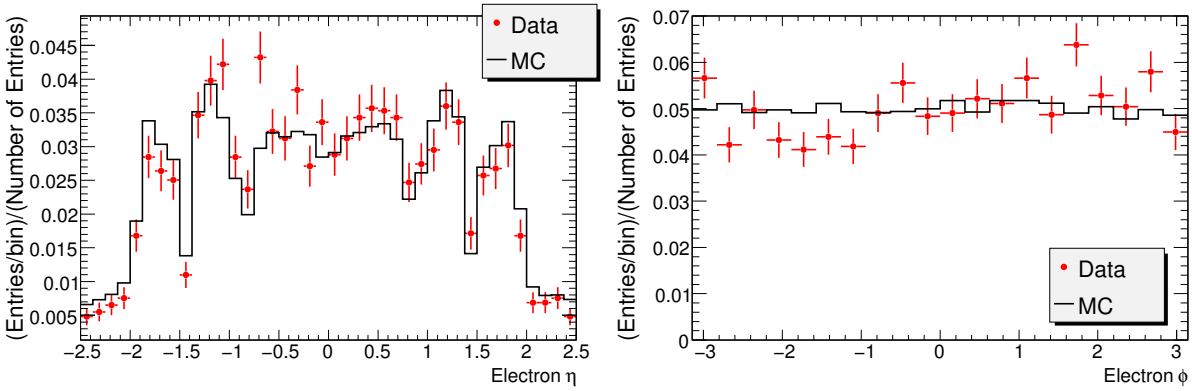

Figure 5.6: Distributions of η (left) and ϕ (right) for all electron candidates within $|\eta| < 2.5$.

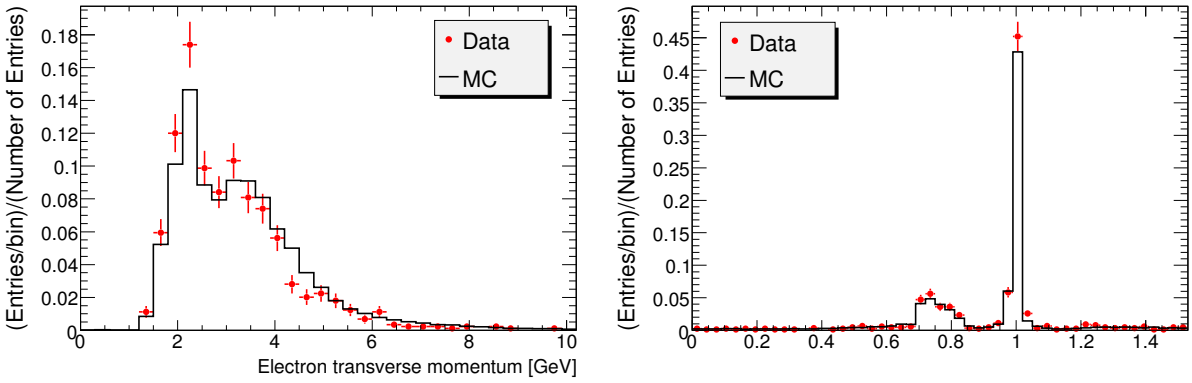

Figure 5.7: Transverse momentum distribution for loose electron candidates within $|\eta| < 2.5$ (left) and the distribution of E/p for these candidates (right).

p_{T} spectrum shows the same shift to higher values for MC as seen in figure 5.5 for all candidates. The real data sample used contains 2916 electron candidates within $|\eta| < 2.5$ after cuts, and 891 of these satisfy the loose selection.

Figure 5.8 shows the distributions of the impact parameters d_0 and z_0. The impact parameters are taken with respect to the reconstructed primary vertex using a track-to-vertex tool. Good agreement between data and MC is seen in both distributions.

Figure 5.9 shows the distributions of the isolation variable $E_{\mathrm{T}}^{\Delta R<0.3}$ and the normalized isolation $E_{\mathrm{T}}^{\Delta R<0.3}/p_{\mathrm{T}}$ (defined in section 4.8.3). Isolation variables are central in all studies of prompt electrons, and was used to reject jet background to our W' study. Reasonable agreement between data and MC is seen in both distributions.

5.1.4 Muon candidates

For muons, as for electrons, "standard candles" are typically Z^0 and J/ψ. Therefore, only a data/MC comparison is performed also for muons. Muons are selected from the `StacoMuonCollection`. Only muons within $|\eta| < 2.5$ are considered. A GRL from the muon combined performance group is used. The real data contains 194 muon candidates within $|\eta| < 2.5$ after cuts.

Figure 5.10 shows the muon p_{T} distribution, as well as the fractions of standalone and combined muons. The distributions of ϕ and η for the muon candidates are shown

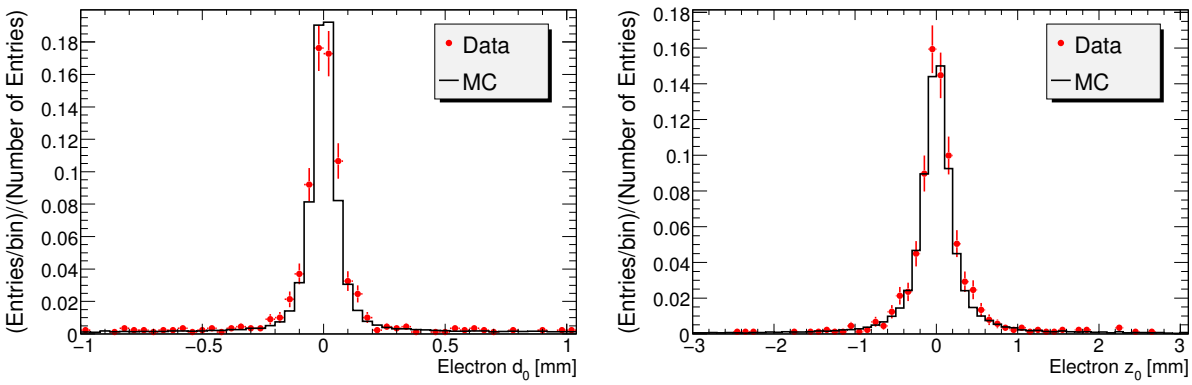

Figure 5.8: Distributions of the impact parameters d_0 (left) and z_0 (right) for loose electron candidates within $|\eta| < 2.5$. The impact parameters are taken with respect to the reconstructed primary vertex.

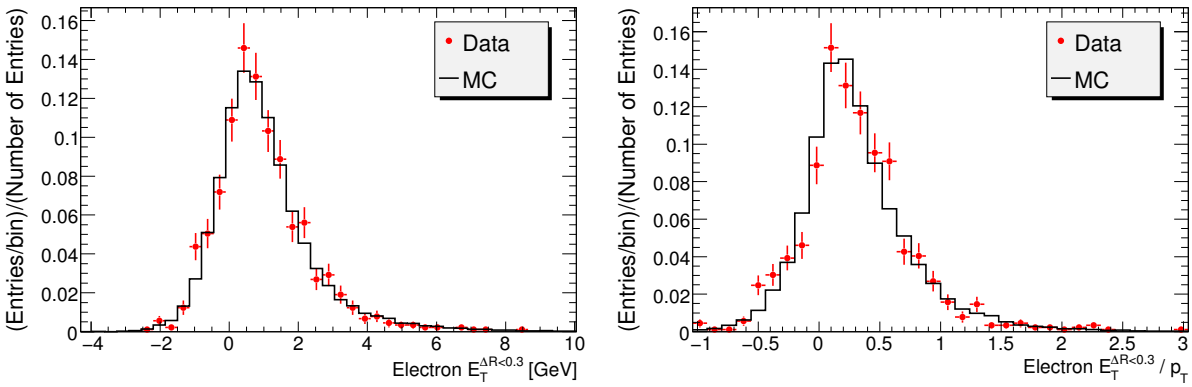

Figure 5.9: Isolation $E_{\mathrm{T}}^{\Delta R<0.3}$ (left) and normalized isolation $E_{\mathrm{T}}^{\Delta R<0.3}/p_{\mathrm{T}}$ (right) for loose electron candidates within $|\eta| < 2.5$.

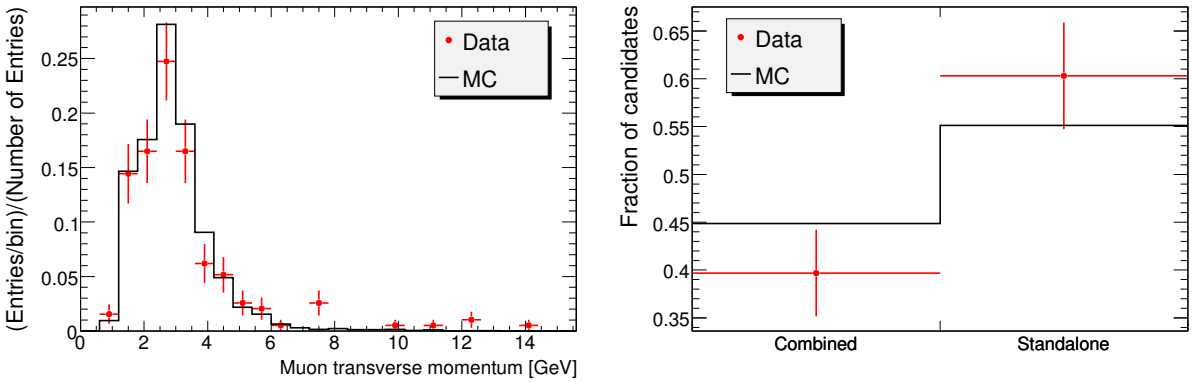

Figure 5.10: Transverse momentum distribution for all muon candidates within $|\eta| < 2.5$ (left) and fractions of these candidates which are standalone and combined muons (right).

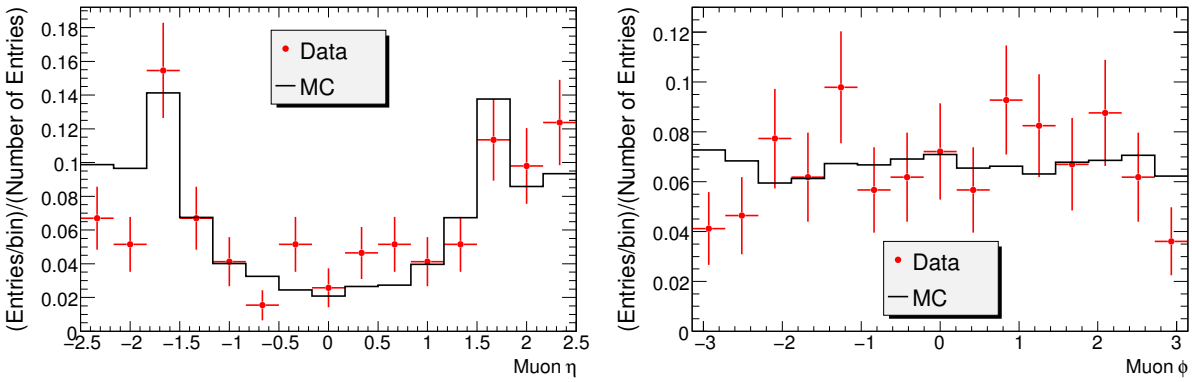

Figure 5.11: Distributions of η (left) and ϕ (right) for all muon candidates within $|\eta| < 2.5$.

in figure 5.11. All the plots show good agreement between data and MC, although the statistics is limited.

Figure 5.12 shows the impact parameters d_0 and z_0 with respect to the reconstructed primary vertex, while figure 5.13 shows $E_{\mathrm{T}}^{\Delta R<0.3}$ and $E_{\mathrm{T}}^{\Delta R<0.3}/p_{\mathrm{T}}$. Both the impact parameters and isolation variables plots show reasonable agreement between data and MC, except possibly for the $E_{\mathrm{T}}^{\Delta R<0.3}/p_{\mathrm{T}}$ distribution. However, the statistics in the real data is very limited.

5.1.5 Jets and $\not{E}_{\mathrm{T}}$

As we have seen, the missing transverse energy is central in any study of the W or a W' boson. It is therefore interesting to check the performance of the $\not{E}_{\mathrm{T}}$ reconstruction in the minimum bias data by comparing to MC. When studying $\not{E}_{\mathrm{T}}$, it is often a good idea to look also at jet reconstruction, since jet energies must be properly reconstructed in order to get a good $\not{E}_{\mathrm{T}}$ reconstruction.

For the study of the $\not{E}_{\mathrm{T}}$ a "jet/$\not{E}_{\mathrm{T}}$ with inner detector" GRL is used. This leaves $329 \cdot 10^3$ events in the real data after cuts. The corresponding number of MC events after cuts are $6.1 \cdot 10^6$.

Figure 5.14 shows the jet p_{T} (left) and jet multiplicity (right) distributions. The jets are taken from the `AntiKt4H1TowerJets` container (jets reconstructed with the anti-k_{T} algorithm from calorimeter towers). The agreement in the p_{T} spectrum between data

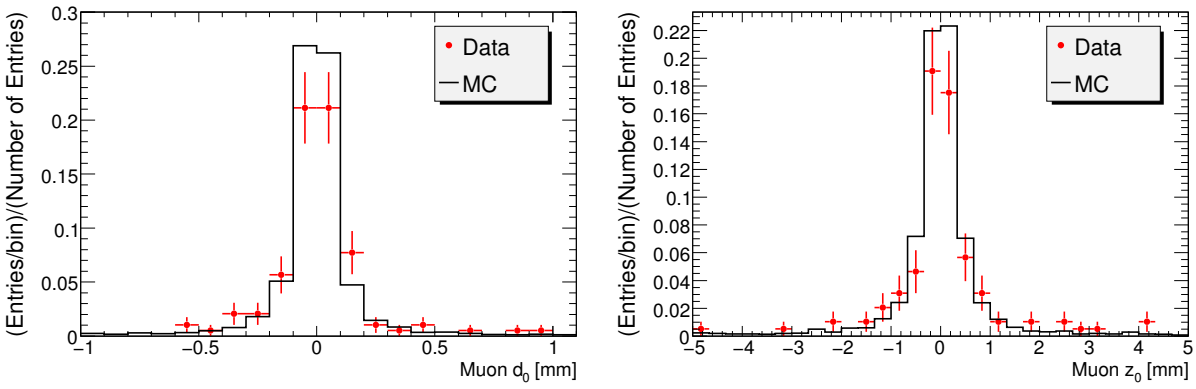

Figure 5.12: Distributions of d_0 (left) and z_0 (right) for all muon candidates within $|\eta| < 2.5$.

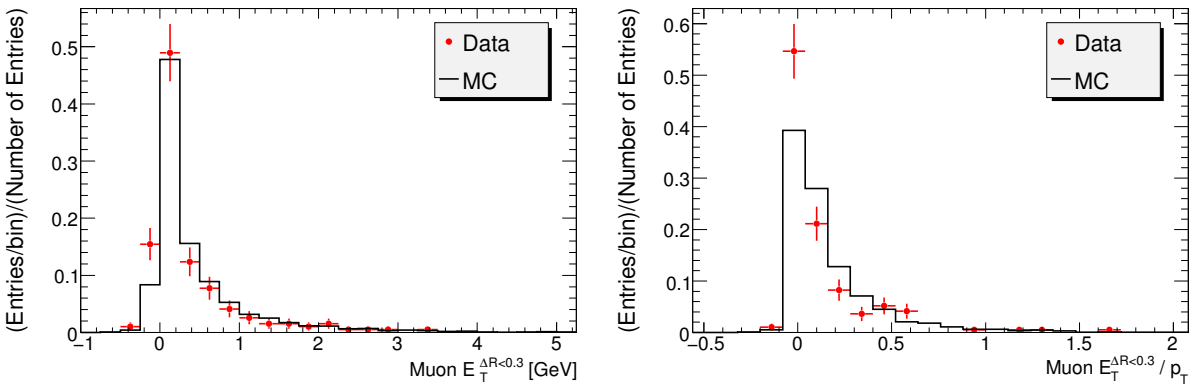

Figure 5.13: Isolation $E_{\mathrm{T}}^{\Delta R<0.3}$ (left) and normalized isolation $E_{\mathrm{T}}^{\Delta R<0.3}/p_{\mathrm{T}}$ (right) for all muon candidates within $|\eta| < 2.5$.

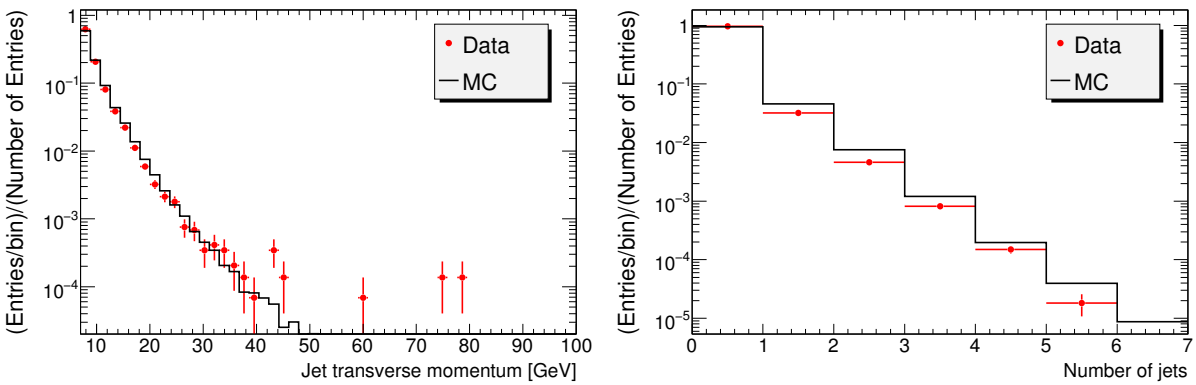

Figure 5.14: Distributions of jet p_{T} (left) and number of jets (right).

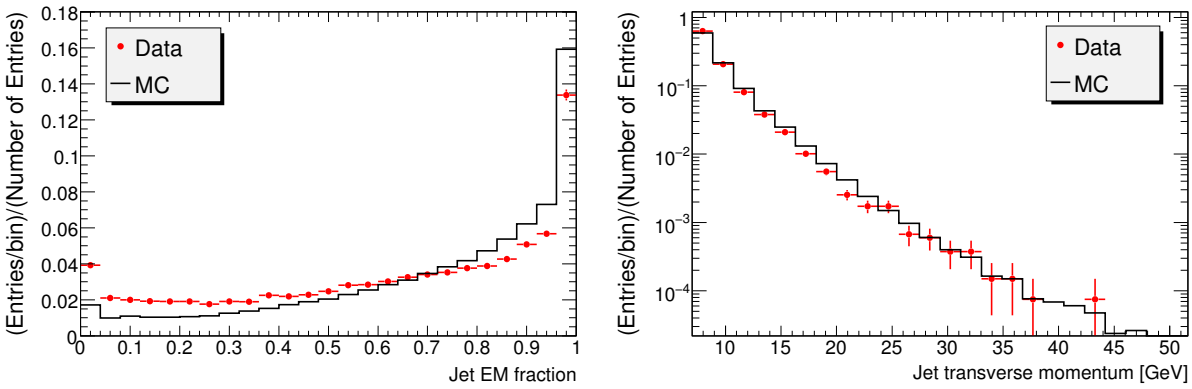

Figure 5.15: Distribution of the jet EM fraction (left) and the jet p_{T} distribution after the cut $f_{\mathrm{EM}} > 0.1$ (right).

and MC seems fairly good at low p_{T}, but the real data has stray events at high p_{T} not reproduced by MC. It should be noted that there are even 5 jets with $p_{\mathrm{T}} > 100\,\mathrm{GeV}$ in the real data. For the jet multiplicity, a slight tendency towards higher jet multiplicity is seen in the MC compared to data.

The jets with very high p_{T} are likely to be fake jets due to calorimeter noise. To distinguish such jets from real jets, one can look at the electromagnetic fraction (EM fraction) f_{EM} of the jet. The EM fraction is defined as the ratio of the energy deposit of the jet in the electromagnetic calorimeter to the total jet energy. Any real jet will deposit a significant part of its energy in the electromagnetic calorimeter.

The distribution of the jet EM fraction is shown in figure 5.15 (left). A quite clear discrepancy between data and MC is seen. Of the 10 jets with $p_{\mathrm{T}} > 50\,\mathrm{GeV}$ in the real data, 9 fall in the first bin of the EM fraction histogram, and the remaining jet falls in the underflow bin. Figure 5.15 (right) shows the jet p_{T} distribution with the cut $f_{\mathrm{EM}} > 0.1$. This cut removes the high p_{T} noise jets, so that there are no jets with $p_{\mathrm{T}} > 45\,\mathrm{GeV}$ in the real data.

When high p_{T} noise jets exist in an event, the $\not{E}_{\mathrm{T}}$ of the event will be large. To clean the $\not{E}_{\mathrm{T}}$ distribution, we can therefore make the cleaning cut that we veto any events with at least one jet with $f_{\mathrm{EM}} < 0.1$. Figure 5.16 shows the $\not{E}_{\mathrm{T}}$ distributions obtained with (left) and without (right) this cleaning cut. The distribution without the cut has several events with very high $\not{E}_{\mathrm{T}}$, including 4 events with $\not{E}_{\mathrm{T}} > 100\,\mathrm{GeV}$. The distribution with

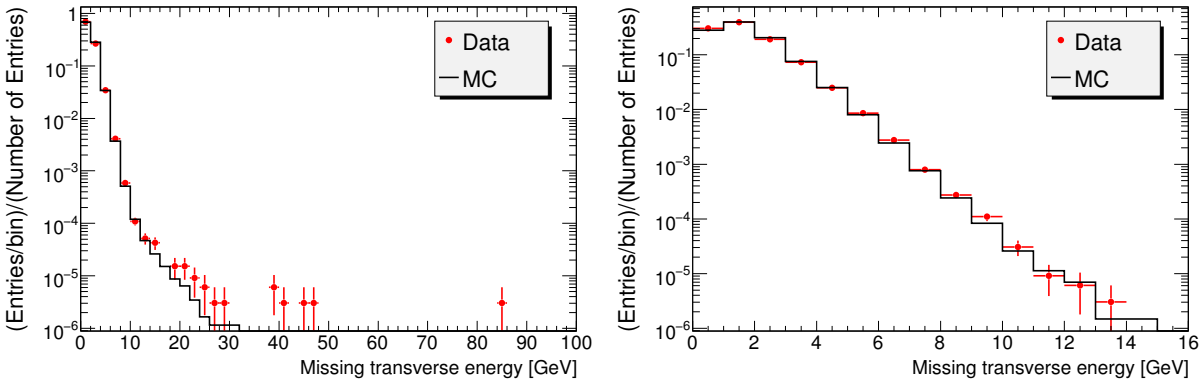

Figure 5.16: Distributions of $\not\!\!E_{\mathrm{T}}$ (left) and the same distribution with the requirement that no jets with $f_{\mathrm{EM}} < 0.1$ exist in the event (right).

Process	Run no.	Recon. tag	MC events	Cross section [pb]
$W \to e\,\nu_e$	106020	`r1205_r1210`	$997 \cdot 10^3$	$7.78 \cdot 10^3$
$W \to \mu\,\nu_\mu$	106021	`r1085_r1113`	$990 \cdot 10^3$	$7.78 \cdot 10^3$
Dijets J0	105009	`r1085_r1113`	$390 \cdot 10^3$	$9.75 \cdot 10^9$
Dijets J1	105010	`r1085_r1113`	$400 \cdot 10^3$	$6.73 \cdot 10^8$
Dijets J2	105011	`r1085_r1113`	$400 \cdot 10^3$	$4.12 \cdot 10^7$
Dijets J3	105012	`r1206_r1210`	$370 \cdot 10^3$	$2.19 \cdot 10^6$
Dijets J4	105013	`r1206_r1210`	$399 \cdot 10^3$	$8.79 \cdot 10^4$
Dijets J5	105014	`r1085_r1113`	$399 \cdot 10^3$	$2.33 \cdot 10^3$
Dijets J6	105015	`r1085_r1113`	$366 \cdot 10^6$	33.8
$t\,\bar{t} \to l + X$	105200	`r1085_r1113`	$200 \cdot 10^3$	80.4

Table 5.1: MC datasets used in the analysis. For the cases where a generator level event selection is made, the cross section quoted is $\sigma \times \epsilon$ where ϵ is the generator level selection efficiency.

the cleaning cut has no events with $\not\!\!E_{\mathrm{T}} > 15\,\mathrm{GeV}$. The $\not\!\!E_{\mathrm{T}}$ used in these plots is the `MET_Topo`, which is $\not\!\!E_{\mathrm{T}}$ calculated from so-called topo clusters. This $\not\!\!E_{\mathrm{T}}$ reconstruction has been shown to perform better than final and refined $\not\!\!E_{\mathrm{T}}$ in these early data.

5.2 Lepton and $\not\!\!E_{\mathrm{T}}$ event selection in the first 7 TeV data

On the 30th of March 2010, ATLAS saw the first proton-proton collisions at $\sqrt{s} = 7\,\mathrm{TeV}$. Since then, around $1\,\mathrm{nb}^{-1}$ of data has been accumulated at this energy (at the time of this writing). In this section, we perform a loosened W' event selection in these data, and compare to MC.

Table 5.1 shows the MC datasets and cross sections used for this analysis. The processes considered are SM W production, QCD dijet production, and $t\bar{t}$ pair production. Names of the datasets used for both real and simulated data can be found in appendix A.

5.2.1 Lepton selection

The lepton selection used for this analysis is the same as in the W' MC analysis with only small alterations, in particular with a lowered p_{T} threshold, in order to increase the real data statistics. For electrons, we require:

- Medium electron (see section 4.8.1)
- $|\eta| < 2.5$
- $p_{\mathrm{T}} > 10\,\mathrm{GeV}$

For muons, we require:

- Combined muon
- $\chi^2_{\mathrm{match}} < 100$ (inner detector-muon spectrometer)
- $|\eta| < 2.5$
- $|d_0| < 0.2\,\mathrm{mm}$
- $|z_0| < 1.0\,\mathrm{mm}$
- $p_{\mathrm{T}} > 10\,\mathrm{GeV}$

Note that the transverse and longitudinal impact parameters d_0 and z_0 are taken relative to the reconstructed primary vertex, and that we can for this reason apply tight cuts on them to reject secondary muons and cosmics. Rejection of cosmic muons using the timing information of the TRT is also possible, but has not been implemented yet.

5.2.2 Event selection

We now select events satisfying the following criteria:

- reconstructed primary vertex,
- $f_{\mathrm{EM}} > 0.1$ and $n_{90} > 5$ for all jets (see below),
- exactly one high-p_{T} lepton (as defined in section 5.2.1),
- $\not{E}_{\mathrm{T}} > 10\,\mathrm{GeV}$.

To reject events with noisy jets, we use now not only the f_{EM} variable discussed in section 5.1.5, but also the variable n_{90}, which is defined as the smallest number of calorimeter cells containing at least 90% of the jet's energy. If n_{90} is small, so that most of the jet's energy is measured in only a few cells, the jet is likely to be noise-induced.

For the missing transverse energy, the container `MET_Topo` is used for electron events, since this is performing well in the early data. In events with high-p_{T} muons, using a purely cluster based $\not{E}_{\mathrm{T}}$ does not make sense, since the muons will then not be taken into account. For the muon events, the `MET_Final` container is used for $\not{E}_{\mathrm{T}}$.

Good luminosity blocks are selected using GRLs from the e/γ and Muon Combined Performance groups.

5.2.3 Trigger

To treat the data and the MC equally, we should make some requirement on the trigger decision. In the 7 TeV data used for this analysis, the high level trigger (level 2 and the event filter) has not been used to reject events, since the rate has been relatively low. We should therefore require a trigger decision at level 1.

In section 5.1, we required a minimum bias trigger at level 1. This was appropriate, since we were running on the minimum bias stream. In fact, most of the data used for the present analysis is also the minimum bias stream, but for the runs where this is the case, the minimum bias triggers were not prescaled, so that this stream contains more or less all the events recorded. However, for the last two runs used in this analysis, 153565 and 153599, the instantaneous luminosity was so high that the minimum bias triggers were prescaled. This means that, when looking for high-p_{T} muons or electrons in this run, the minimum bias stream should not be used. For these runs, the `MuonswBeam` and `L1CaloEM` streams are used for the muon analysis and the electron analysis respectively. The events in these streams have passed level 1 muon or electron triggers respectively, and a corresponding requirement should be made for the MC.

For the electron analysis, the level 1 electromagnetic calorimeter trigger `L1_EM3` is required to pass for both MC and real data. This trigger has not been prescaled in any of the runs used. Similarily, one could imagine using the level 1 muon trigger `L1_MU0` for the muon analysis. This does, however, provide a problem. In some early 7 TeV runs, there was a problem with the RPC trigger timing. As a result, some of the level 1 muon triggers from these runs are associated to the wrong bunch crossing, and imposing a trigger requirement rejects perfectly good events. Therefore, for the muon analysis, no trigger requirement is made. Note that this means that the MC and the real data are not treated completely equally, as the level 1 muon trigger requirement has already been imposed on the real data in the runs 153565 and 153599 at the time of data taking. The effect should not be large, as the level 1 muon triggers should have high efficiency.

5.2.4 Transverse mass distributions

Figure 5.17 shows the transverse mass distributions obtained in the electron and muon channels with the event selection described in section 5.2.2. The MC has been scaled to the "ATLAS Rec." integrated luminosity from the ATLAS data summary web page [32], which is for these data $892\,\mu\mathrm{b}^{-1}$. The "ATLAS Rec." integrated luminosity corresponds to luminosity blocks in which the whole detector is at nominal voltages etc. A more detailed integrated luminosity determination based on the selected luminosity blocks in the applied GRLs has not been done. An uncertainty of about 20% should be assumed for the online luminosity measurement.

Good agreement is seen between data and MC in both channels. In particular, the rate of the jet contribution in the low transverse mass region is as expected from MC. Note that since we are scaling to the measured integrated luminosity, the agreement is in terms of absolute rate, not just in terms of the shape of the distribution. One should note that the statistical uncertainty on the jet contribution is non-negligible, and that for the most statistically well defined bins in the data in the electron channel, the uncertainty is larger on the MC than on the data.

We now make similar cuts as for the W' analysis, but with cut values tuned to observe the SM W boson rather than some heavy W' boson. These cuts are:

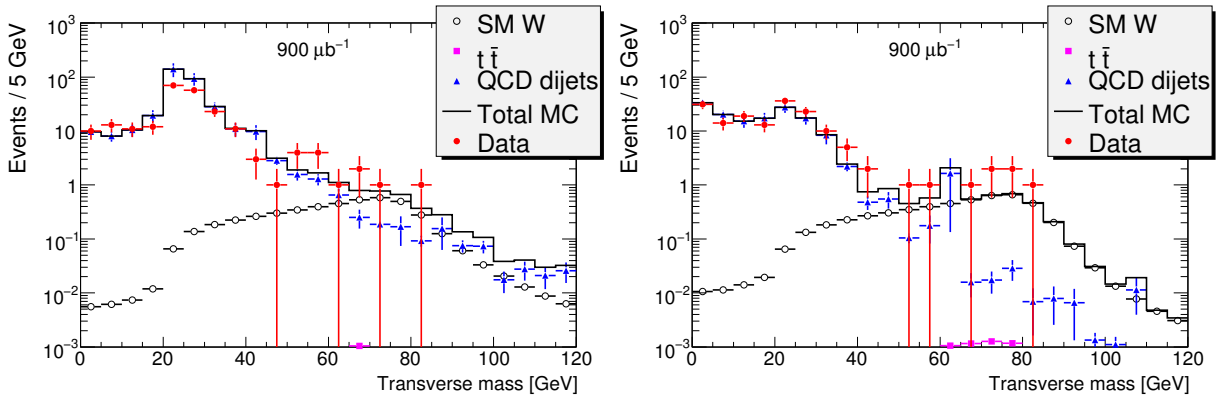

Figure 5.17: Transverse mass distributions in the electron (left) and muon (right) channels in the 7 TeV data after the event selection described in section 5.2.2. The MC has been scaled to the measured integrated luminosity.

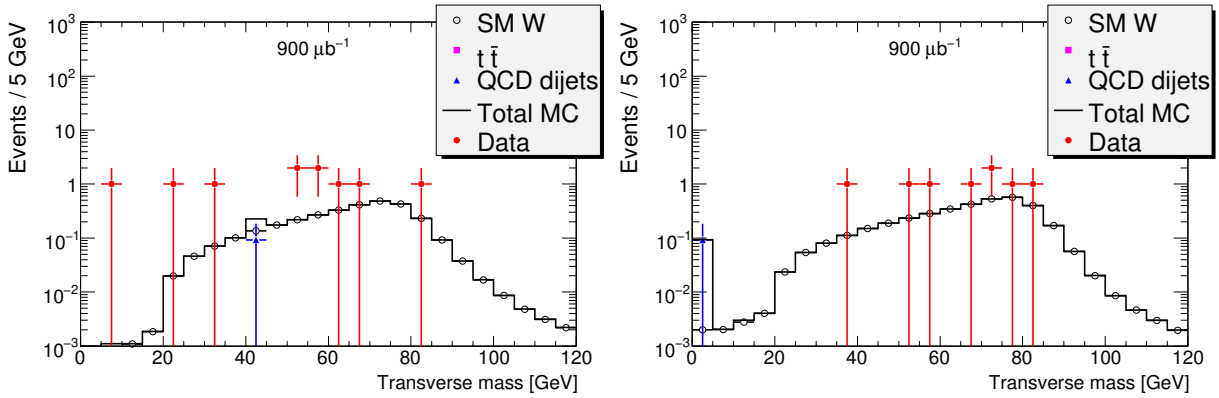

Figure 5.18: Transverse mass distributions in the electron (left) and muon (right) channels in the 7 TeV data after the event selection described in section 5.2.2 and loosened W' cuts. The MC has been scaled to the measured integrated luminosity.

- normalized isolation $E_{\mathrm{T}}^{\Delta R<0.3}/p_{\mathrm{T}} < 0.1$,
- lepton fraction $f_{\mathrm{lep}} > 0.3$,
- $0.5 < p_{\mathrm{T}}/\not{E}_{\mathrm{T}} < 1.5$.

The transverse mass distributions obtained after these cuts are shown in figure 5.18.

With these cuts, the dominating MC contribution is seen to be the SM W, and the events that are left in the data with high transverse mass are good W candidates. Typically, the number of W candidates is counted with a transverse mass cut $m_{\mathrm{T}} > 40\,\mathrm{GeV}$. Using this cut to count W candidates, we are observing 7 W candidates in each of the channels in these data. In the range $40\,\mathrm{GeV} < m_{\mathrm{T}} < 100\,\mathrm{GeV}$, 2.8 W events in the electron channel and 3.4 W events in the muon channel are expected from MC. The observed 7 events in each channel correspond to approximately 1.6σ and 2.1σ deviations. These are not statistically significant deviations, and in any case this is a very preliminary study. Next-to-leading order corrections to the cross section have for example not been taken into account.

Among the 14 good W candidates that are left in the data, we find the first official ATLAS W candidate events. In the electron channel, the first official ATLAS W candidate

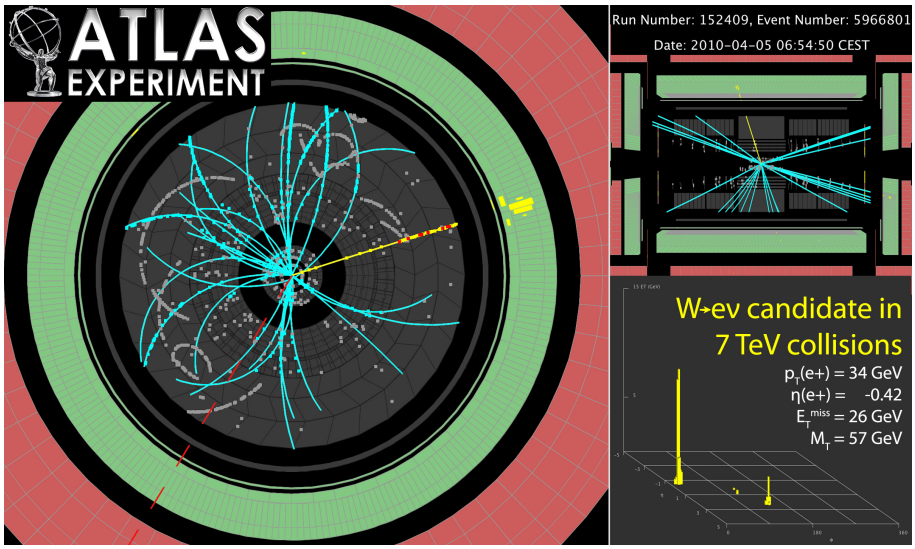

Figure 5.19: Event display of the first official ATLAS W candidate in the electron channel.

was found in run 152409. An event display of this event is shown in figure 5.19. In the transverse projection, the electron is highlighted with yellow, and the direction of the $\not{E}_{\mathrm{T}}$ is shown as a dashed red line. The first candidate in the muon channel was found in run 152221. An event display of this candidate is shown in figure 5.20.

5.3 Conclusions

In this chapter, we have looked at real LHC collision data taken by ATLAS. The study of V^0 vertices in the 900 GeV minimum bias data provides standard candles for testing the tracking performance. We have seen that we can obtain mass peaks for the K^0_{S}, Λ, and $\overline{\Lambda}$ particles, and that fits to these peaks give masses close to the established values. This shows that the ATLAS tracking system is performing well, and that the magnetic field configuration in the inner detector is known to good precision.

The reconstruction of electrons and muons has been tested against simulation for the first 900 GeV minimum bias data. Reasonable agreement between simulation and real data is seen in most distributions.

Finally, we have performed a loosened W' event selection in the first 7 TeV data, in particular with a lowered p_{T} threshold. Good agreement has been shown between simulation and real data in the low mass jet dominated part of the spectrum, not only in terms of shape, but in terms of absolute rate.

With the application of loosened cuts on normalized isolation, lepton fraction, and $p_{\mathrm{T}}/\not{E}_{\mathrm{T}}$, the jet contribution has been reduced. These cuts leave 7 good W candidates above $m_{\mathrm{T}} = 40$ GeV in each channel, 14 good W candidates in total.

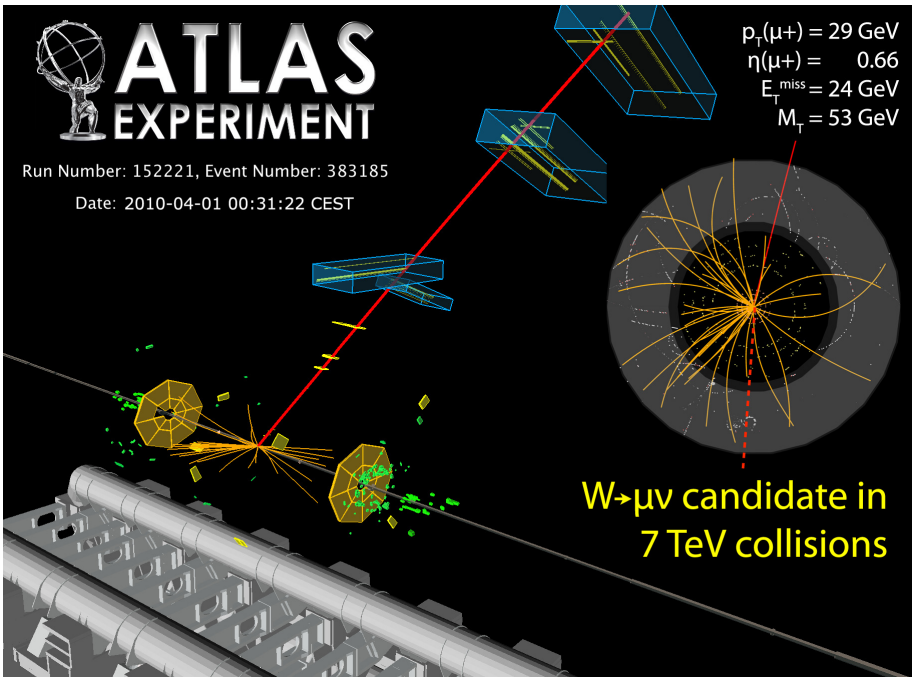

Figure 5.20: Event display of the first official ATLAS W candidate in the muon channel.

Conclusions and outlook

In this thesis, we have investigated the possibility for discovery of a new charged gauge boson W' decaying to charged lepton and neutrino with the ATLAS detector at the LHC. We have seen that such a boson with a mass beyond the Tevatron exclusion limit may be discovered with only of order $10\,\mathrm{pb}^{-1}$ of data at $\sqrt{s} = 7\,\mathrm{TeV}$.

Other possible new physics contributions to the one lepton and missing transverse energy final state have also been considered, in particular supersymmetry and Z'. We have seen that the contributions to the transverse mass spectrum from such processes is at most comparable to the SM background for the models considered.

As this thesis has been written in parallel with the startup of the LHC, a large part has been devoted to the analysis of real ATLAS data, both cosmic data and the first LHC collision data. These data show in general promising results in terms of detector performance and understanding. In particular, a loosened W' event selection was performed in the first 7 TeV data, and good agreement was seen between MC and real data in the low mass part of the spectrum. The first good W candidates have been observed in both electron and muon channels.

The LHC is now running at $\sqrt{s} = 7\,\mathrm{TeV}$, which is the energy that will be used for the collection of the first $1\,\mathrm{fb}^{-1}$ of data. This first data sample will open up a vast range of possible physics discovery. In our W' analysis, we saw that $1\,\mathrm{fb}^{-1}$ of 7 TeV data is enough to discover or exclude a SM-like W' boson with a mass above 2 TeV.

The luminosity of the LHC is increasing week by week, and a very exciting time lies ahead of the particle physics community!

Appendix A

Detailed information about data sets used

A.1 Cosmic data

The names of the data sets (containers) used in the cosmic analysis are, following the same ordering as in section 3.4.2, for real data:

1. `data08_cosmag.00091890.physics_IDCosmic.recon.ESD.o4_r653/`
2. `data08_cosmag.00091900.physics_IDCosmic.recon.ESD.o4_r653/`

and for simulated data:

1. `valid2.108867.CosSimIDVolSolOnTorOn.recon.ESD.s533_d167_r676/`
2. `valid2.108866.CosSimIDVolSolOffTorOff.recon.ESD.s534_d168_r677/`

A.2 10 TeV MC data

The names of the data sets (containers) used for the W' MC study are:

- `mc08.106020.PythiaWenu_1Lepton.merge.AOD.e352_s462_s520_r809_r838`
- `mc08.106021.PythiaWmunu_1Lepton.merge.AOD.e352_s462_s520_r808_r838`
- `mc08.106604.PythiaWemutau_200M500.merge.AOD.e384_s462_s520_r808_r838`
- `mc08.106605.PythiaWemutau_Mg500.merge.AOD.e384_s462_s520_r808_r838`
- `mc08.105610.Pythia_Wprime_emutau_1000.merge.AOD.e352_s462_s520_r808_r838`
- `mc08.105626.Pythia_Wprime_emutau_1500.merge.AOD.e357_s462_s520_r808_r838`
- `mc08.105611.Pythia_Wprime_emutau_2000.merge.AOD.e363_s462_s520_r808_r838`
- `mc08.105662.Pythia_Wprime_emutau_2500.merge.AOD.e363_s462_s520_r808_r838`
- `mc08.105663.Pythia_Wprime_emutau_3000.merge.AOD.e363_s462_s520_r808_r838`
- `mc08.105664.Pythia_Wprime_emutau_3500.merge.AOD.e363_s462_s520_r808_r838`

- mc08.105985.WW_Herwig.merge.AOD.e379_s462_s520_r808_r838
- mc08.105987.WZ_Herwig.merge.AOD.e368_s462_s520_r808_r838
- mc08.105986.ZZ_Herwig.merge.AOD.e379_s462_s520_r808_r838
- mc08.105120.PythiaZgam_allLep.merge.AOD.e347_s462_s520_r808_r838
- mc08.006540.PythiaWgam_allLep.recon.AOD.e327_s400_d99_r474
- mc08.105121.PythiaDYee_200M.merge.AOD.e355_s462_s520_r808_r838
- mc08.105122.PythiaDYmumu_200M.merge.AOD.e355_s462_s520_r808_r838
- mc08.105200.T1_McAtNlo_Jimmy.merge.AOD.e357_s462_s520_r809_r838
- mc08.105009.J0_pythia_jetjet.merge.AOD.e344_s479_s520_r809_r838
- mc08.105010.J1_pythia_jetjet.merge.AOD.e344_s479_s520_r809_r838
- mc08.105011.J2_pythia_jetjet.merge.AOD.e344_s479_s520_r809_r838
- mc08.105012.J3_pythia_jetjet.merge.AOD.e344_s479_s520_r809_r838
- mc08.105013.J4_pythia_jetjet.merge.AOD.e344_s479_s520_r809_r838
- mc08.105014.J5_pythia_jetjet.merge.AOD.e344_s479_s520_r809_r838
- mc08.105015.J6_pythia_jetjet.merge.AOD.e344_s479_s520_r809_r838
- mc08.105016.J7_pythia_jetjet.merge.AOD.e344_s479_s520_r809_r838
- mc08.105017.J8_pythia_jetjet.recon.AOD.e344_s475_r586
- mc08.105624.Pythia_Zprime_ee_SSM1500.merge.AOD.e357_s462_s520_r808_r838
- mc08.105625.Pythia_Zprime_mumu_SSM1500.merge.AOD.e357_s462_s520_r808_r838
- mc08.105603.Pythia_Zprime_ee_SSM1000.merge.AOD.e352_s462_s520_r808_r838
- mc08.105601.Pythia_Zprime_mumu_SSM1000.merge.AOD.e352_s462_s520_r808_r838
- mc08.105401.SU1_jimmy_susy.merge.AOD.e352_s462_s520_r808_r838
- mc08.105403.SU3_jimmy_susy.merge.AOD.e352_s462_s520_r808_r838
- mc08.105404.SU6_jimmy_susy.merge.AOD.e352_s462_s520_r808_r838
- mc08.105406.SU8_jimmy_susy.merge.AOD.e357_s462_s520_r808_r838

A.3 900 GeV minimum bias data

Datasets used for the 900 GeV real collision data:

- data09_900GeV.00142392.physics_MinBias.merge.DESD_COLLCAND.r988_p62/
- data09_900GeV.00141398.physics_MinBias.merge.DESD_COLLCAND.r988_p62/
- data09_900GeV.00141746.physics_MinBias.merge.DESD_COLLCAND.r988_p62/
- data09_900GeV.00141565.physics_MinBias.merge.DESD_COLLCAND.r988_p62/
- data09_900GeV.00141270.physics_MinBias.merge.DESD_COLLCAND.r988_p62/
- data09_900GeV.00142171.physics_MinBias.merge.DESD_COLLCAND.r988_p62/
- data09_900GeV.00142042.physics_MinBias.merge.DESD_COLLCAND.r988_p62/
- data09_900GeV.00141691.physics_MinBias.merge.DESD_COLLCAND.r988_p62/
- data09_900GeV.00142397.physics_MinBias.merge.DESD_COLLCAND.r988_p62/
- data09_900GeV.00140541.physics_MinBias.merge.DESD_COLLCAND.r988_p62/
- data09_900GeV.00141234.physics_MinBias.merge.DESD_COLLCAND.r988_p62/
- data09_900GeV.00142159.physics_MinBias.merge.DESD_COLLCAND.r988_p62/
- data09_900GeV.00140955.physics_MinBias.merge.DESD_COLLCAND.r988_p62/
- data09_900GeV.00141707.physics_MinBias.merge.DESD_COLLCAND.r988_p62/
- data09_900GeV.00141403.physics_MinBias.merge.DESD_COLLCAND.r988_p62/
- data09_900GeV.00141534.physics_MinBias.merge.DESD_COLLCAND.r988_p62/
- data09_900GeV.00142383.physics_MinBias.merge.DESD_COLLCAND.r988_p62/
- data09_900GeV.00140822.physics_MinBias.merge.DESD_COLLCAND.r988_p62/
- data09_900GeV.00141562.physics_MinBias.merge.DESD_COLLCAND.r988_p62/
- data09_900GeV.00141994.physics_MinBias.merge.DESD_COLLCAND.r988_p62/
- data09_900GeV.00142161.physics_MinBias.merge.DESD_COLLCAND.r988_p62/
- data09_900GeV.00142189.physics_MinBias.merge.DESD_COLLCAND.r988_p62/
- data09_900GeV.00141266.physics_MinBias.merge.DESD_COLLCAND.r988_p62/
- data09_900GeV.00141999.physics_MinBias.merge.DESD_COLLCAND.r988_p62/
- data09_900GeV.00141702.physics_MinBias.merge.DESD_COLLCAND.r988_p62/
- data09_900GeV.00141721.physics_MinBias.merge.DESD_COLLCAND.r988_p62/
- data09_900GeV.00141704.physics_MinBias.merge.DESD_COLLCAND.r988_p62/

- data09_900GeV.00142395.physics_MinBias.merge.DESD_COLLCAND.r988_p62/
- data09_900GeV.00142394.physics_MinBias.merge.DESD_COLLCAND.r988_p62/
- data09_900GeV.00141226.physics_MinBias.merge.DESD_COLLCAND.r988_p62/
- data09_900GeV.00142065.physics_MinBias.merge.DESD_COLLCAND.r988_p62/
- data09_900GeV.00141748.physics_MinBias.merge.DESD_COLLCAND.r988_p62/
- data09_900GeV.00141209.physics_MinBias.merge.DESD_COLLCAND.r988_p62/
- data09_900GeV.00142149.physics_MinBias.merge.DESD_COLLCAND.r988_p62/
- data09_900GeV.00141561.physics_MinBias.merge.DESD_COLLCAND.r988_p62/
- data09_900GeV.00142165.physics_MinBias.merge.DESD_COLLCAND.r988_p62/
- data09_900GeV.00142190.physics_MinBias.merge.DESD_COLLCAND.r988_p62/
- data09_900GeV.00141755.physics_MinBias.merge.DESD_COLLCAND.r988_p62/
- data09_900GeV.00142192.physics_MinBias.merge.DESD_COLLCAND.r988_p62/
- data09_900GeV.00142155.physics_MinBias.merge.DESD_COLLCAND.r988_p62/
- data09_900GeV.00141203.physics_MinBias.merge.DESD_COLLCAND.r988_p62/
- data09_900GeV.00140571.physics_MinBias.merge.DESD_COLLCAND.r988_p62/
- data09_900GeV.00142174.physics_MinBias.merge.DESD_COLLCAND.r988_p62/
- data09_900GeV.00142191.physics_MinBias.merge.DESD_COLLCAND.r988_p62/
- data09_900GeV.00141387.physics_MinBias.merge.DESD_COLLCAND.r988_p62/
- data09_900GeV.00141718.physics_MinBias.merge.DESD_COLLCAND.r988_p62/
- data09_900GeV.00141998.physics_MinBias.merge.DESD_COLLCAND.r988_p62/
- data09_900GeV.00142193.physics_MinBias.merge.DESD_COLLCAND.r988_p62/
- data09_900GeV.00141401.physics_MinBias.merge.DESD_COLLCAND.r988_p62/
- data09_900GeV.00142154.physics_MinBias.merge.DESD_COLLCAND.r988_p62/
- data09_900GeV.00142144.physics_MinBias.merge.DESD_COLLCAND.r988_p62/
- data09_900GeV.00142390.physics_MinBias.merge.DESD_COLLCAND.r988_p62/
- data09_900GeV.00140974.physics_MinBias.merge.DESD_COLLCAND.r988_p62/
- data09_900GeV.00141563.physics_MinBias.merge.DESD_COLLCAND.r988_p62/
- data09_900GeV.00142400.physics_MinBias.merge.DESD_COLLCAND.r988_p62/
- data09_900GeV.00141238.physics_MinBias.merge.DESD_COLLCAND.r988_p62/

- data09_900GeV.00141749.physics_MinBias.merge.DESD_COLLCAND.r988_p62/
- data09_900GeV.00142406.physics_MinBias.merge.DESD_COLLCAND.r988_p62/
- data09_900GeV.00142166.physics_MinBias.merge.DESD_COLLCAND.r988_p62/
- data09_900GeV.00142391.physics_MinBias.merge.DESD_COLLCAND.r988_p62/
- data09_900GeV.00142194.physics_MinBias.merge.DESD_COLLCAND.r988_p62/
- data09_900GeV.00142195.physics_MinBias.merge.DESD_COLLCAND.r988_p62/
- data09_900GeV.00141811.physics_MinBias.merge.DESD_COLLCAND.r988_p62/
- data09_900GeV.00142157.physics_MinBias.merge.DESD_COLLCAND.r988_p62/
- data09_900GeV.00141695.physics_MinBias.merge.DESD_COLLCAND.r988_p62/

For 900 GeV minimum bias MC

- mc09_900GeV.105001.pythia_minbias.recon.ESD.e500_s655_s657_d257_r1023/

is used.

A.3.1 GRLs

Queries to generate the GRLs used for the various 900 GeV collision data studies are given here.

- V^0 study:

```
find run 140541+ and partition ATLAS and db DATA and lhc stablebeams
T and st physics_MinBias and ptag data09_900GeV and dq ATLGL green
LBSUMM#DetStatusLBSUMM-December09-01 and dq L1CTP green
LBSUMM#DetStatusLBSUMM-December09-01 and dq atlsol green
LBSUMM#DetStatusLBSUMM-December09-01 and dq pix green
LBSUMM#DetStatusLBSUMM-December09-01 and dq sct green
LBSUMM#DetStatusLBSUMM-December09-01 and dq trtb,trte green
LBSUMM#DetStatusLBSUMM-December09-01
```

- Electron study:

```
f r 141000+ and events 100000+ and dq
LBSUMM#DetStatusLBSUMM-December09-00 pix,sct,lar,trtb,trte,til g and dq
LBSUMM#DetStatusLBSUMM-December09-00 atlsol,atlgl,l1ctp g and
lhc beamenergy 449-451 and lhc stablebeams true
```

- Muon study:

```
f r 141749+ and dq atlgl LBSUMM#DetStatusLBSUMM-December09-01 g and dq pix
LBSUMM#DetStatusLBSUMM-December09-01 g and dq sct
LBSUMM#DetStatusLBSUMM-December09-01 g and dq mdt
LBSUMM#DetStatusLBSUMM-December09-01 g and dq tgc
LBSUMM#DetStatusLBSUMM-December09-01 g  and dq rpc
LBSUMM#DetStatusLBSUMM-December09-01 g and lhc stablebeams true
and mag t >20000 and mag s
```

- $\not\!\!E_{\mathrm{T}}$ study:

```
find run 140541+ and partition ATLAS and db DATA and lhc stablebeams
T and st physics_MinBias and ptag data09_900GeV and dq ATLGL green
LBSUMM#DetStatusLBSUMM-December09-01 and dq L1CTP green
LBSUMM#DetStatusLBSUMM-December09-01 and dq atlsol green
LBSUMM#DetStatusLBSUMM-December09-01 and dq lar green
LBSUMM#DetStatusLBSUMM-December09-01 and dq tile green
LBSUMM#DetStatusLBSUMM-December09-01 and dq pix green
LBSUMM#DetStatusLBSUMM-December09-01 and dq sct green
LBSUMM#DetStatusLBSUMM-December09-01 and dq trtb,trte green
LBSUMM#DetStatusLBSUMM-December09-01
```

A.4 7 TeV MC data

The MC datasets used for the 7 TeV analysis are:

- mc09_7TeV.106020.PythiaWenu_1Lepton.merge.AOD.e468_s765_s767_r1205_r1210/
- mc09_7TeV.106021.PythiaWmunu_1Lepton.merge.AOD.e468_s624_s633_r1085_r1113/
- mc09_7TeV.105009.J0_pythia_jetjet.merge.AOD.e468_s624_s633_r1085_r1113/
- mc09_7TeV.105010.J1_pythia_jetjet.merge.AOD.e468_s624_s633_r1085_r1113/
- mc09_7TeV.105011.J2_pythia_jetjet.merge.AOD.e468_s624_s633_r1085_r1113/
- mc09_7TeV.105012.J3_pythia_jetjet.merge.AOD.e468_s766_s767_r1206_r1210/
- mc09_7TeV.105013.J4_pythia_jetjet.merge.AOD.e468_s766_s767_r1206_r1210/
- mc09_7TeV.105014.J5_pythia_jetjet.merge.AOD.e468_s624_s633_r1085_r1113/
- mc09_7TeV.105015.J6_pythia_jetjet.merge.AOD.e468_s624_s633_r1085_r1113/
- mc09_7TeV.105200.T1_McAtNlo_Jimmy.merge.AOD.e510_s624_s633_r1085_r1113/

A.5 7 TeV real data

The datasets used for real 7 TeV collision data are:

- data10_7TeV.00152221.physics_MinBias.merge.AOD.f238_m427
- data10_7TeV.00152273.physics_MinBias.merge.AOD.f238_m427
- data10_7TeV.00152346.physics_MinBias.merge.AOD.f238_m427
- data10_7TeV.00152272.physics_MinBias.merge.AOD.f238_m427
- data10_7TeV.00152270.physics_MinBias.merge.AOD.f238_m427
- data10_7TeV.00152222.physics_MinBias.merge.AOD.f238_m427
- data10_7TeV.00152174.physics_MinBias.merge.AOD.f238_m427
- data10_7TeV.00152399.physics_MinBias.merge.AOD.f238_m427
- data10_7TeV.00152371.physics_MinBias.merge.AOD.f238_m427
- data10_7TeV.00152372.physics_MinBias.merge.AOD.f238_m427
- data10_7TeV.00152409.physics_MinBias.merge.AOD.f238_m427
- data10_7TeV.00152214.physics_MinBias.merge.AOD.f238_m427
- data10_7TeV.00152223.physics_MinBias.merge.AOD.f238_m427
- data10_7TeV.00152175.physics_MinBias.merge.AOD.f238_m427

- data10_7TeV.00152373.physics_MinBias.merge.AOD.f238_m427
- data10_7TeV.00152343.physics_MinBias.merge.AOD.f238_m427
- data10_7TeV.00152182.physics_MinBias.merge.AOD.f238_m427
- data10_7TeV.00152374.physics_MinBias.merge.AOD.f238_m427
- data10_7TeV.00152168.physics_MinBias.merge.AOD.f238_m427
- data10_7TeV.00152345.physics_MinBias.merge.AOD.f238_m427
- data10_7TeV.00152220.physics_MinBias.merge.AOD.f238_m427
- data10_7TeV.00152844.physics_MinBias.merge.AOD.f243_m435
- data10_7TeV.00152777.physics_MinBias.merge.AOD.f243_m435
- data10_7TeV.00152774.physics_MinBias.merge.AOD.f243_m435
- data10_7TeV.00152778.physics_MinBias.merge.AOD.f243_m435
- data10_7TeV.00152779.physics_MinBias.merge.AOD.f243_m435
- data10_7TeV.00152776.physics_MinBias.merge.AOD.f243_m435
- data10_7TeV.00152809.physics_MinBias.merge.AOD.f243_m435
- data10_7TeV.00152490.physics_MinBias.merge.AOD.f241_m433
- data10_7TeV.00152489.physics_MinBias.merge.AOD.f241_m433
- data10_7TeV.00152508.physics_MinBias.merge.AOD.f241_m433
- data10_7TeV.00152441.physics_MinBias.merge.AOD.f238_m433
- data10_7TeV.00152166.physics_MinBias.merge.AOD.f239_m427
- data10_7TeV.00152549.physics_MinBias.merge.AOD.f242_m435
- data10_7TeV.00152160.physics_MinBias.merge.AOD.f236_m427
- data10_7TeV.00152845.physics_MinBias.merge.AOD.f243_m435
- data10_7TeV.00152772.physics_MinBias.merge.AOD.f242_m435
- data10_7TeV.00152163.physics_MinBias.merge.AOD.f236_m427
- data10_7TeV.00152159.physics_MinBias.merge.AOD.f236_m427
- data10_7TeV.00152877.physics_MinBias.merge.AOD.f243_m435
- data10_7TeV.00152545.physics_MinBias.merge.AOD.f242_m435
- data10_7TeV.00152766.physics_MinBias.merge.AOD.f242_m435
- data10_7TeV.00152767.physics_MinBias.merge.AOD.f242_m435

- data10_7TeV.00152539.physics_MinBias.merge.AOD.f241_m435
- data10_7TeV.00152768.physics_MinBias.merge.AOD.f242_m435
- data10_7TeV.00152164.physics_MinBias.merge.AOD.f236_m427
- data10_7TeV.00152716.physics_MinBias.merge.AOD.f242_m435
- data10_7TeV.00152165.physics_MinBias.merge.AOD.f236_m427
- data10_7TeV.00152878.physics_MinBias.merge.AOD.f243_m440
- data10_7TeV.00152933.physics_MinBias.merge.AOD.f244_m440
- data10_7TeV.00152935.physics_MinBias.merge.AOD.f244_m440
- data10_7TeV.00153028.physics_MinBias.merge.AOD.f246_m445
- data10_7TeV.00153030.physics_MinBias.merge.AOD.f247_m450
- data10_7TeV.00152994.physics_MinBias.merge.AOD.f244_m450
- data10_7TeV.00153029.physics_MinBias.merge.AOD.f247_m445
- data10_7TeV.00153159.physics_MinBias.merge.AOD.f249_m455
- data10_7TeV.00153200.physics_MinBias.merge.AOD.f249_m455
- data10_7TeV.00153135.physics_MinBias.merge.AOD.f249_m455
- data10_7TeV.00153191.physics_MinBias.merge.AOD.f249_m455
- data10_7TeV.00153136.physics_MinBias.merge.AOD.f249_m455
- data10_7TeV.00153134.physics_MinBias.merge.AOD.f249_m455
- data10_7TeV.00153226.physics_MinBias.merge.AOD.f249_m455
- data10_7TeV.00153410.physics_MinBias.merge.AOD.f250_m462
- data10_7TeV.00153350.physics_MinBias.merge.AOD.f250_m460
- data10_7TeV.00153291.physics_MinBias.merge.AOD.f250_m460
- data10_7TeV.00153405.physics_MinBias.merge.AOD.f250_m462
- data10_7TeV.00153474.physics_MinBias.merge.AOD.f250_m462
- data10_7TeV.00153351.physics_MinBias.merge.AOD.f250_m462
- data10_7TeV.00153406.physics_MinBias.merge.AOD.f250_m462
- data10_7TeV.00153288.physics_MinBias.merge.AOD.f250_m460
- data10_7TeV.00153407.physics_MinBias.merge.AOD.f250_m462
- data10_7TeV.00153376.physics_MinBias.merge.AOD.f250_m462

- data10_7TeV.00153459.physics_MinBias.merge.AOD.f250_m462
- data10_7TeV.00153292.physics_MinBias.merge.AOD.f250_m460
- data10_7TeV.00153295.physics_MinBias.merge.AOD.f250_m460
- data10_7TeV.00153408.physics_MinBias.merge.AOD.f250_m462
- data10_7TeV.00153476.physics_MinBias.merge.AOD.f250_m462
- data10_7TeV.00153477.physics_MinBias.merge.AOD.f250_m462
- data10_7TeV.00153294.physics_MinBias.merge.AOD.f250_m460
- data10_7TeV.00153473.physics_MinBias.merge.AOD.f250_m462
- data10_7TeV.00153290.physics_MinBias.merge.AOD.f250_m460
- data10_7TeV.00153349.physics_MinBias.merge.AOD.f250_m460
- data10_7TeV.00153565.physics_L1CaloEM.merge.AOD.f251_m466
- data10_7TeV.00153599.physics_L1CaloEM.merge.AOD.f251_m466
- data10_7TeV.00153565.physics_MuonswBeam.merge.AOD.f251_m466
- data10_7TeV.00153599.physics_MuonswBeam.merge.AOD.f251_m466

A.5.1 GRLs

The queries used to generate the GRLs were for the

- electron channel:

```
find run 152166+ and ready and dq atlgl g and dq cp_eg_electron_barrel y+
and dq cp_eg_electron_endcap y+ and dq tigb g
```

- muon channel:

```
find r 152166+ and lhc stablebeams true and dq atlgl g and dq mdt g and
dq csc g and dq tgc g and dq rpc g and dq pix g and dq sct g and mag s
and mag t > 20000
```

Appendix B

Pauli matrices

The Pauli matrices used in the development of the standard electroweak theory are

$$\tau_1 = \begin{pmatrix} 0 & 1 \\ 1 & 0 \end{pmatrix}, \quad \tau_2 = \begin{pmatrix} 0 & -i \\ i & 0 \end{pmatrix}, \quad \tau_3 = \begin{pmatrix} 1 & 0 \\ 0 & -1 \end{pmatrix}. \tag{B.1}$$

They are Hermitian, $\tau_i^\dagger = \tau_i$, and satisfy the commutation relation

$$[\sigma_k, \sigma_l] = 2i\varepsilon_{klm}\sigma_m \tag{B.2}$$

where ε_{klm} is the fully antisymmetric Levi-Civita tensor, which enters in the transformation rule for the W fields, eq. (1.40).

Since τ_3 is diagonal, it gives neutral current terms:

$$\overline{\chi_L}\gamma^\mu\tau_3\chi_L = \overline{\psi_L^\nu}\gamma^\mu\psi_L^\nu - \overline{\psi_L^e}\gamma^\mu\psi_L^e. \tag{B.3}$$

Charged currents are obtained through linear combinations of the τ_1 and τ_2 matrices.

Bibliography

[1] F. Mandl and G. Shaw, *Quantum field theory*, Revised Edition, WILEY

[2] D. Griffiths, *Introduction to Elementary Particles*, Second Edition, WILEY-VCH

[3] Quang Ho-Kim, Xuam-Yem Pham, *Elementary Particles and Their Interactions: Concepts and Phenomena*, Springer

[4] C. Amsler et al., *Review of Particle Physics*, Physics Letters B 667, 1 (2008)

[5] Andreas Hoecker, *Status of the global electroweak fit of the Standard Model*, arXiv:0909.0961v2

[6] G. Senjanovic, R.N. Mohapatra, Phys. Rev. D12, 1502 (1975)

[7] R.N. Mohapatra, G. Senjanovic, Phys. Rev. Lett. 44, 912 (1980)

[8] ATLAS collaboration, *The ATLAS Experiment at the CERN Large Hadron Collider*, 2008 JINST 3 S08003

[9] ATLAS collaboration, *ATLAS detector and physics performance, Technical Design Report*, Volume I, ATLAS TDR 14, CERN/LHCC 99-14

[10] C. Grupen, *Astroparticle Physics*, Springer

[11] S. Agostinelli et al., GEANT4 Collaboration, *GEANT4: A simulation toolkit*, Nucl. Instr. Meth. A506 (2003) 250-303

[12] R. Brun and F. Rademakers, Nucl. Instrum. Meth. A 389, 81 (1997)

[13] `https://twiki.cern.ch/twiki/bin/view/Atlas/InDetCosmic08Analyses` (ATLAS TWiki)

[14] M. Boonekamp et al., *Cosmic Ray, Beam-Halo and Beam-Gas Rate Studies for ATLAS Commissioning*, ATL-GEN-2004-001

[15] A.Pukhov et al., *CompHEP - a package for evaluation of Feynman diagrams and integration over multi-particle phase space. User's manual for version 3.3*, INP MSU report 98-41/542, Website: `http://comphep.sinp.msu.ru`

[16] S. Moch, *Expectations at LHC from hard QCD*, J. Phys. G: Nucl. Part. Phys. 35 (2008) 073001

[17] D. Green, *High P_{T} Physics at Hadron Colliders*, Cambridge

[18] E. Boos et al., *Interference between W' and W in single-top quark production processes*, Physics Letters B 655 (2007) 245-250

[19] V.M. Abazov et al., Phys. Rev. Lett. 100, 031804 (2008)

[20] T. Sjostrand, S. Mrenna, P. Skands, *PYTHIA 6.4 physics and manual*, JHEP 05 (2006) 026

[21] S. Frixione and B.R. Webber, *Matching NLO QCD computations and parton shower simulations*, JHEP 0206 (2002) 029

[22] `http://ami.in2p3.fr/opencms/opencms/AMI/www`
(ATLAS Metadata Interface)

[23] `https://twiki.cern.ch/twiki/bin/view/Atlas/L31TriggerMenu`
(ATLAS TWiki)

[24] ATLAS collaboration, *Expected Performance of the ATLAS Experiment, Detector, Trigger and Physics*, CERN-OPEN-2008-020, pp. 1726-1749: *Lepton Plus Missing Transverse Energy Signals at High Mass*

[25] ATLAS collaboration, *Expected Performance of the ATLAS Experiment, Detector, Trigger and Physics*, CERN-OPEN-2008-020, pp. 72-93: *Reconstruction and Identification of Electrons*

[26] N. Vranjes, *Search for W' in Lepton+Missing E_{T} Final State With Early Data at ATLAS*, ATL-PHYS-PROC-2008-085

[27] N. Vranjes et al., *$W' \rightarrow \mu\nu$ event selection @ 10 TeV*, talk given at the ATLAS Lepton+X Exotics meeting on March 23rd 2009, slides available from `http://indico.cern.ch/conferenceDisplay.py?confId=54989`

[28] G. Cowan, E. Gross, *Discovery significance with statistical uncertainty in the background estimate*, Available from:
`https://twiki.cern.ch/twiki/pub/AtlasProtected/ATLASStatisticsFAQ/SigCalcNote.pdf`

[29] A. L. Read, *Presentation of search results: the* CL_s *technique*, J. Phys. G: Nucl. Part. Phys. 28 (2002) 2693-2704

[30] E. Richter-Was, D. Froidevaux and L. Poggioli, ATLAS Internal Note, PHYS-No-079 (1996)

[31] `https://twiki.cern.ch/twiki/bin/view/AtlasProtected/PDFReweight`
(ATLAS TWiki)

[32] `https://atlas.web.cern.ch/Atlas/GROUPS/DATAPREPARATION/DataSummary/run-summary.html`
(ATLAS Data Summary web page)